

**HYDRODYNAMIC AND MASS TRANSFER PARAMETERS IN LARGE-SCALE
SLURRY BUBBLE COLUMN REACTORS**

by

Arsam Behkish

B.S. in Chemical Engineering, University of Pittsburgh, 1997

Submitted to the Graduate Faculty of
the School of Engineering in partial fulfillment
of the requirements for the degree of
Doctor of Philosophy

University of Pittsburgh

2004

UNIVERSITY OF PITTSBURGH

SCHOOL OF ENGINEERING

This dissertation was presented by

by

Arsam Behkish

It was defended on

December 6, 2004

and approved by

Shiao-Hung Chiang, Professor Emeritus, Chemical and Petroleum Engineering Department

Robert Enick, Professor, Chemical and Petroleum Engineering Department

George Klinzing, Professor, Chemical and Petroleum Engineering Department

Badie I. Morsi, Professor, Chemical and Petroleum Engineering Department

Patrick Smolinski, Associate Professor, Mechanical Engineering Department

Dissertation Director: Badie I. Morsi, Professor, Chemical and Petroleum Engineering
Department

ABSTRACT

HYDRODYNAMIC AND MASS TRANSFER PARAMETERS IN LARGE-SCALE SLURRY BUBBLE COLUMN REACTORS

Arsam Behkish, Ph.D.

University of Pittsburgh, 2004

The hydrodynamic (gas holdup, ϵ_G , bubble size distribution, d_b , and the Sauter-mean bubble diameter, d_{32}), gas solubility (C^*) and mass transfer parameters (gas-liquid interfacial area, a , and volumetric liquid-side mass transfer coefficient, $k_L a$) were measured for various gases (H_2 , CO , N_2 , CH_4 and He) in an organic liquid (Isopar-M) in the absence and presence of two different solids (glass beads and alumina powder) in two large-scale SBCRs of 0.316 and 0.289 m ID. The data were obtained under wide ranges of pressures (1-27 bar), superficial gas velocities (0.08-0.4 m/s), temperatures (323-453K), and solid concentrations (0-36 vol.%).

The experimental data obtained showed that ϵ_G and $k_L a$ increased with pressure due to the increase of small gas bubbles holdup; increased with superficial gas velocity due to the increase of the gas momentum; and significantly decreased with solid concentration due to a reduction of small gas bubble population. ϵ_G and $k_L a$ values were found to increase with temperature due to the decrease of the Sauter mean bubble diameter and increase of the mass transfer coefficient (k_L). The gas holdup, however, was found to decrease with temperature when the solid

concentration was greater or equal 15 vol.% due to the reduction of froth stability under such conditions.

Empirical and back propagation neural network (BPNN) models were developed to correlate the hydrodynamic and mass transfer parameters in BCRs and SBCRs obtained in our laboratory and those from the literature. The developed models were then used to predict the effects of pressure, superficial gas velocity, temperature and catalyst loading on the total syngas holdup and mass transfer coefficients for the Low-Temperature Fischer-Tropsch (LTFT) synthesis carried out in a 5 m ID SBCR with iron oxides and cobalt-based catalysts. Under typical LTFT operating conditions (30 bar, 513 K, 30 and 50 wt%), the total syngas holdup and mass transfer coefficients predicted for H₂/CO ratio of 2:1 with cobalt-based catalyst were consistently lower than those obtained for H₂/CO ratio of 1:1 with iron oxide catalyst in the superficial gas velocity range from 0.005 to 0.4 m/s.

DESCRIPTORS

Absorption

Artificial Neural Network

Axial solid dispersion

Back Propagation Neural Network

Bubble column reactor

Bubble size distribution

Central Composite Statistical Design

Dynamic Gas Disengagement

Fischer-Tropsch

Gas holdup

Gas-liquid interfacial area

Hydrodynamic

Mass transfer

Sauter-mean bubble diameter

Slurry bubble column reactor

Solubility

Stirred reactor

Syngas

TABLE OF CONTENTS

ABSTRACT.....	iii
DESCRIPTORS.....	v
TABLE OF CONTENTS.....	vi
LIST OF TABLES.....	xii
LIST OF FIGURES.....	xv
NOMENCLATURE.....	xxii
ACKNOWLEDGMENT.....	xxix
1.0 INTRODUCTION.....	1
2.0 LITERATURE REVIEW AND BACKGROUND.....	5
2.1 Hydrodynamics.....	5
2.1.1 Flow Regimes.....	5
2.1.2 Gas Holdup, ε_G	8
2.1.3 Effect of the Superficial Gas Velocity on ε_G	9
2.1.4 Effect of Pressure and Gas Density on ε_G	11
2.1.5 Effect of the Physical Properties of the Liquid on ε_G	12
2.1.6 Effect of Solids on ε_G	15
2.1.7 Effect of Reactor Size on ε_G	20
2.1.8 Effect of Gas Distributor on ε_G	22

2.1.9	Empirical Correlations for ϵ_G	28
2.2	Dynamics of Gas Bubbles.....	28
2.2.1	Gas Bubble Formation.....	34
2.2.2	Gas Bubble Coalescence.....	36
2.2.3	Gas Bubble Breakup.....	39
2.2.4	Gas Bubble Rise Velocity.....	43
2.3	Dynamics of Dispersed Solids.....	49
2.3.1	Particle Settling Velocity.....	50
2.3.2	The Axial Dispersion-Sedimentation Model.....	51
2.4	Mass Transfer Characteristics.....	54
2.4.1	Gas/Liquid/Solid Transport.....	54
2.4.2	Volumetric Liquid-Side Mass Transfer Coefficient, $k_L a$	58
3.0	OBJECTIVE.....	65
4.0	EXPERIMENTAL.....	67
4.1	The Gas-Phase.....	67
4.2	The Liquid Phase.....	68
4.2.1	Composition.....	68
4.2.2	Vapor Pressure.....	68
4.2.3	Density.....	69
4.2.4	Viscosity.....	70
4.2.5	Surface Tension.....	70
4.2.6	Gas-Liquid Diffusivity.....	71

4.3	The Solid Phase.....	71
4.3.1	Particle Size Analysis	71
4.3.2	Particle Density.....	72
4.3.3	Slurry Density	74
4.3.4	Slurry Viscosity	74
4.4	Experimental Setup.....	74
4.4.1	Cold SBCR.....	75
4.4.2	Hot SBCR	79
4.4.3	Gas Sparger.....	82
4.4.4	High-Speed Camera.....	82
4.5	Statistical Experimental Design.....	93
4.5.1	CCSD for the Cold SBCR.....	94
4.5.2	CCSD for the Hot SBCR	94
4.6	Experimental Procedures	97
4.6.1	k_La Measurement	97
4.6.2	ϵ_G Measurement	98
4.6.3	Bubble Size Distribution Measurement.....	98
4.6.4	Sampling of the Solid Particles.....	99
5.0	CALCULATIONS.....	100
5.1	Peng-Robinson Equation of State.....	100
5.2	Calculation of Equilibrium Solubility, C^*	102
5.3	Calculation of k_La	103

5.3.1	The Integral Method	104
5.3.2	The Differential Method	105
5.3.3	The Multiple Linear Regression Method	105
5.4	Calculation of the Gas Holdup, ϵ_G	106
5.5	Calculation of the Sauter-Mean Bubble Diameter Using DGD Technique.....	107
5.6	Calculation of the Bubble Size Distribution Using Photographic Method.....	110
6.0	RESULTS AND DISCUSSION	114
6.1	Solubility of Gases in Isopar-M.....	114
6.2	Gas Holdup in the Cold and Hot SBCRs	120
6.2.1	Effect of Pressure and Solid Concentration on ϵ_G	122
6.2.2	Effect Gas Velocity on ϵ_G	139
6.2.3	Effect of Temperature on ϵ_G	141
6.2.4	Effect of Gas Nature on ϵ_G	147
6.2.5	Comparison of ϵ_G with Literature Data.....	151
6.3	Bubbles Size Distribution in the Cold and Hot SBCRs.....	154
6.3.1	Effect of Gas Nature on the d_{32}	160
6.3.2	Effect of P, U_G , T and C_V on the Bubble Size Distribution.....	160
6.3.3	Effect of P, T, U_G , and C_V on d_{32}	166
6.4	Mass Transfer in the Cold and Hot SBCRs	173
6.4.1	Effect of Pressure and Gas Velocity on $k_L a$	186
6.4.2	Effect of Solid Concentration and Temperature on $k_L a$	195

6.4.3	Effect of Gas Nature on $k_L a$	212
6.4.4	Effect of Solid Nature on $k_L a$	213
6.5	Solid Phase Hydrodynamics in the Cold and Hot SBCR	213
6.5.1	Dispersion Model	213
6.5.2	Axial Solid Distribution in the Cold and Hot SBCR	218
7.0	CORRELATION OF THE HYDRODYNAMIC AND MASS TRANSFER DATA	222
7.1	Empirical Correlations	222
7.1.1	Gas Holdup Correlation	228
7.1.2	Sauter-Mean Bubble Diameter Correlation	231
7.1.3	Mass Transfer Correlation	232
7.1.4	Comparison of the Data with the Available Literature Correlations	233
7.2	Artificial Neural Network Model	239
7.2.1	Construction of the BPNNs	240
7.2.2	Gas Holdup Prediction by BPNN	241
7.2.3	Sauter-Mean Bubble Diameter Prediction by BPNN	241
7.2.4	Volumetric Liquid-Side Mass Transfer Coefficient Prediction by BPNN	245
7.3	Case Study: Modeling of the Hydrodynamic and Mass Transfer Parameters in Fischer-Tropsch Synthesis	245
7.3.1	Effect of P, T, and C_W on the Hydrodynamic and Mass Transfer Parameters	252
7.3.2	Effect of U_G and D_C on the Hydrodynamic and Mass Transfer Parameters	258
7.3.3	Comparison between Coal-to-Liquid (CTL) and Gas-to-Liquid (GTL) Processes	263
7.3.4	Effect of the Number of Orifices in the Gas Sparger on ϵ_G	264

7.3.5	Effect of the Gas Sparger Type on ε_G	266
8.0	CONCLUSIONS.....	270
	APPENDIX A. CURRENT TREND IN THE SLURRY PHASE FISCHER-TROPSCH PROCESS.....	275
	APPENDIX B. CALCULATION OF THE PHYSICAL PROPERTIES OF THE GAS-LIQUID..	280
	APPENDIX C. ARTIFICIAL NEURAL NETWORK.....	283
	BIBLIOGRAPHY.....	292

LIST OF TABLES

Table 1 Available literature studies on high temperature bubble and slurry bubble column reactors.....	18
Table 2 Available correlations for predicting slurry viscosity.....	20
Table 3 Correlations for gas holdup predictions in bubble column reactors.....	29
Table 4 Correlations for gas holdup predictions in slurry bubble column reactors.....	32
Table 5 Correlation for the terminal rise velocity of a single bubble.....	45
Table 6 Correlation for small and large bubble rise velocity in the swarm.....	48
Table 7 Available models for predicting the axial solid dispersion coefficient and particle settling velocity.....	53
Table 8 Steps in three-phase reaction and parameters involved.....	55
Table 9 Literature survey on a and k_L in bubble and slurry bubble columns.....	61
Table 10 Correlations for volumetric mass transfer coefficients in bubble and slurry bubble columns.....	62
Table 11 Thermodynamic properties of gases.....	67
Table 12 Physical properties of Isopar-M.....	69
Table 13 Composition of Isopar-M.....	69
Table 14 Characteristics of the pipes.....	75
Table 15 Values of the coded variables for the experimental design in the cold SBCR.....	95
Table 16 Value of the coded variables for the experimental design in the hot SBCR.....	95
Table 17 Henry's Law constants for gases in Isopar-M at 298 K.....	115

Table 18 Values of the Henry's Law constant for the gases.....	116
Table 19 Coefficients for the ε_G correlation using Equation (6-1).....	120
Table 20 Coefficients for the $\varepsilon_{G\text{-Small}}$ and $\varepsilon_{G\text{-Large}}$ correlation using Equation (6-1).....	121
Table 21 Coefficients for the ε_G , $\varepsilon_{G\text{-Small}}$ and $\varepsilon_{G\text{-Large}}$ correlation using Equation(6-2).....	122
Table 22 Coefficients for the d_{32} correlation using Equation (6-5).....	158
Table 23 Coefficients for the $d_{32\text{-Small}}$ and $d_{32\text{-Large}}$ correlation using Equation (6-5).....	158
Table 24 Coefficients for the $d_{32\text{-Small}}$ and $d_{32\text{-Large}}$ correlation using Equation (6-6).....	159
Table 25 Coefficients for Equation (6-12) used for $k_L a$ correlation in the cold SBCR.....	184
Table 26 Coefficients for Equation (6-13) used for $k_L a$ correlation in the hot SBCR.....	184
Table 27 Coefficients for Equation (6-12) used for k_L correlation in the cold SBCR.....	185
Table 28 Coefficients for Equation (6-13) used for k_L correlation in the hot SBCR.....	185
Table 29 Available literature data in BCRs used in the development of the correlations.....	223
Table 30 Available literature data in SBCRs used in the development of the correlations.....	226
Table 31 Values of K_d used in Equation (7-2).....	229
Table 32 Value of α used in Equation (7-2).....	230
Table 33 Upper and lower limits of the variables involved in Equation (7-1).....	230
Table 34 Upper and Lower limits of the variables involved in Equations (7-6) and (7-7).....	233
Table 35 Upper and lower limits of the variables involved in Equation (7-10).....	233
Table 36 Values of the sparger type (S_T).....	240
Table 37 Ranges of the input and output parameters of the BPNN for total gas holdup (ε_G)	242
Table 38 Ranges of the input and output parameters of the BPNN for large bubbles holdup ($\varepsilon_{G\text{-Large}}$).....	242

Table 39 Weights and biases for the [14,9-7,1] BPNN for ε_G	243
Table 40 Weights and biases for the [14,8,1] BPNN for $\varepsilon_{G-Large}$	244
Table 41 Ranges of the input and output parameters of the BPNN for d_{32}	246
Table 42 Ranges of the input and output parameters of the BPNN for $d_{32-Large}$	246
Table 43 Weights and biases for the [15,9-7,1] BPNN for d_{32}	247
Table 44 Weights and biases for the [15,7-5,1] BPNN for $d_{32-Large}$	248
Table 45 Ranges of the input and output parameters of the BPNN for $k_L a$	249
Table 46 Weights and biases for the [13,8-6,1] BPNN for $k_L a$	250
Table 47 Conditions Selected for the modeling of the hydrodynamics and mass transfer parameters in Low-Temperature Fischer-Tropsch (LTFT) Synthesis using SBCRs.....	253

LIST OF FIGURES

Figure 1 Flow-Regime Map for the Bubble Column Reactor ^(2,11)	8
Figure 2 Parameters influencing the Performance of the Slurry Bubble Column Reactor.....	10
Figure 3 Different Types of Gas Distributors employed in Bubble and Slurry Bubble Column Reactors.....	26
Figure 4 Air Bubble Formations at the Orifice in Water Based on the Experiments of Heijnen and Van't Riet ⁽¹¹²⁾	37
Figure 5 Balance and Expression of all Forces acting on the Gas Bubble at its Formation in SBCRs ⁽²⁸⁾	38
Figure 6 Prediction of the Terminal Rise Velocity of N ₂ Gas Bubble in Isopar-M at 7 bar and 298 K Using the Correlation in Table 5.....	47
Figure 7 Concentration Profile for a Three-Phase System with Chemical Reaction inside the Pores of the Catalyst	56
Figure 8 Viscosities of the Gases used	72
Figure 9 Properties of Isopar-M.....	73
Figure 10 SEM of Glass Beads and Alumina Particles	76
Figure 11 Glass Beads and Alumina Powder Particle Size Distribution	77
Figure 12 Correlations for Predicting Slurry Viscosity in Isopar-M	77
Figure 13 Mechanical Specifications of the Cold SBCR.....	83
Figure 14 Part 1 of Mechanical Specifications of the Hot SBCR.....	84
Figure 15 Part 2 of the Mechanical Specifications of the Hot SBCR.....	85
Figure 16 Schematic of the Cold Slurry Bubble Column Reactor Setup	86

Figure 17 Schematic of the Hot Slurry Bubble Column Reactor Setup	87
Figure 18 Pictures of the Cold Slurry Bubble Column Reactor	88
Figure 19 Pictures of the Hot Slurry Bubble Column Reactor	89
Figure 20 The Mechanical Specifications of The Spider-Type Gas Sparger	90
Figure 21 Pictures of the Spider-Type Gas Sparger and its Distance from the Bottom of the Column.....	91
Figure 22 Picture of the Setup for the High-Speed Phantom Camera used with the Hot SBCR..	92
Figure 23 Central Composite Statistical Design Matrixes.....	96
Figure 24 Dynamic Gas Disengagement in the Slurry Bubble Column Reactor	112
Figure 25 a) Snap shot using Phantom High-Speed Camera through the Jerguson Site- windows of the bubble column reactor, b) The digitalized image of the same shot using Adobe Photoshop software.....	113
Figure 26 Solubility of Gases in Isopar-M at 298K.....	116
Figure 27 Comparison of C* Values obtained in Cold SBCR and STR	117
Figure 28 Solubility of N ₂ and He in Isopar-M as a Function of Temperature	118
Figure 29 Henry's Law Constant for N ₂ and He in Isopar-M.....	119
Figure 30 Comparison between the Experimental and predicted Holdup Values of the Gases in Isopar-M using Equation (6-1) and (6-2).....	123
Figure 31 Effect of pressure on the ϵ_G and $\epsilon_{G-large}$ in the Cold SBCR	124
Figure 32 Effect of pressure on the ϵ_G and $\epsilon_{G-large}$ in the Hot SBCR	125
Figure 33 Effect of Operating Variables on ϵ_G of H ₂ /Isopar-M/Glass Beads in the Cold SBCR	127
Figure 34 Effect of Operating Variables on ϵ_G of CO/ Isopar-M/Glass Beads in the Cold SBCR	128
Figure 35 Effect of Operating Variables on ϵ_G of N ₂ / Isopar-M/Glass Beads in the Cold SBCR	129

Figure 36 Effect of Operating variables on ϵ_G of CH ₄ / Isopar-M/Glass Beads in the Cold SBCR	130
Figure 37 Effect of Operating variables on ϵ_G of He/ Isopar-M/Alumina in the Cold SBCR....	131
Figure 38 Effect of Operating variables on ϵ_G of N ₂ and He/ Isopar-M/Alumina in the Hot SBCR	132
Figure 39 Effect of Glass Beads Particles on the $\epsilon_{G-Small}$ and $\epsilon_{G-large}$ of CO and H ₂ in the Cold SBCR	135
Figure 40 Effect of Glass Beads Particles on the $\epsilon_{G-Small}$ and $\epsilon_{G-large}$ of N ₂ and CH ₄ in the Cold SBCR	136
Figure 41 Effect of Alumina Particles on the $\epsilon_{G-Small}$ and $\epsilon_{G-large}$ of N ₂ and He in the Cold SBCR	137
Figure 42 Effect of Alumina Particles on the $\epsilon_{G-Small}$ and $\epsilon_{G-large}$ of N ₂ and He in the Hot SBCR	138
Figure 43 Effect of U _G on the $\epsilon_{G-Small}$ and $\epsilon_{G-large}$ of H ₂ and CO in the Cold SBCR.....	143
Figure 44 Effect of U _G on the $\epsilon_{G-Small}$ and $\epsilon_{G-large}$ of CH ₄ and N ₂ in the Cold SBCR.....	144
Figure 45 Effect of U _G on the ϵ_G of N ₂ and He/Isopar-M/Alumina in the Hot SBCR	145
Figure 46 Effect of T on the ϵ_G of N ₂ and He/Isopar-M/Alumina in the Hot SBCR.....	146
Figure 47 Effect of T on the $\epsilon_{G-Small}$ and $\epsilon_{G-Large}$ of N ₂ and He in Isopar-M in the Hot SBCR...	148
Figure 48 Effect of T on the $\epsilon_{G-Small}$ and $\epsilon_{G-Large}$ of N ₂ and He at 10 vol.% Alumina in the Hot SBCR	149
Figure 49 Effect of T on the ϵ_G of N ₂ and He at 15 vol.% Alumina in the Hot SBCR.....	150
Figure 50 Effect of Gas Nature on the Gas Holdup in the Cold SBCR.....	152
Figure 51 Effect of Gas Nature on ϵ_G , $\epsilon_{G-Small}$, and $\epsilon_{G-Large}$ in the Cold SBCR.....	153
Figure 52 Comparison with the Literature Data on Gas Holdup obtained with low Viscosity Liquid.....	155

Figure 53 Comparison of ε_G Data with the Literature Values obtained with comparable Liquids	155
Figure 54 Comparison between Photographic Method and the DGD Technique	161
Figure 55 Comparison between the Experimental and predicted d_{32} Values of the Gases in Isopar-M using Equation (6-5) and (6-6).....	162
Figure 56 Effect of the Gas Nature on d_{32} , d_{32} -Small, d_{32} -Large in the Cold SBCR.....	164
Figure 57 Effect of Gas Nature on d_{32} of N_2 and He obtained using the DGD and the Photographic Techniques in the Hot SBCR.....	165
Figure 58 Effect of pressure on the Bubbles Size Distribution of the Gases in Isopar-M in the Cold SBCR.....	167
Figure 59 Effect of Gas Velocity on Bubbles Size Distribution of the Gases in Isopar-M in the Cold SBCR.....	168
Figure 60 Effect of Solid Concentration on the Bubbles Size Distribution of the Gases in Isopar-M in the Cold SBCR.....	169
Figure 61 Effect of P, T and C_V on the Bubble Size Distribution of N_2 and He in the Hot SBCR	170
Figure 62 Effect of P and U_G on d_{32} of the Gases in the Cold SBCR.....	174
Figure 63 Effect of P, C_V and T on d_{32} of the N_2 and He in the Hot SBCR	175
Figure 64 Effect of Temperature on the foaming of the Isopar-M/Alumina slurry in the Hot SBCR	176
Figure 65 Effect of Solid Concentration on the Froth Characteristics of Isopar-M/Alumina Slurry Observed in the Hot SBCR.....	177
Figure 66 Effect of Glass Beads Concentration on d_{32} , d_{32} -Small, and d_{32} -Large of H_2 and CO in the Cold SBCR.....	178
Figure 67 Effect of Glass Beads Concentration on d_{32} , d_{32} -Small, and d_{32} -Large of N_2 and CH_4 in the Cold SBCR.....	179
Figure 68 Effect of Alumina Powder Concentration on d_{32} , d_{32} -Small, and d_{32} -Large of N_2 and He in the Cold SBCR.....	180

Figure 69 Effect of Alumina Powder Concentration on d_{32} , $d_{32\text{-Small}}$, and $d_{32\text{-Large}}$ of N_2 and He in the Hot SBCR	181
Figure 70 Comparison between the Experimental and Predicted k_{La} and k_L Values for the Gases Using Equation (6-12) and (6-13).....	187
Figure 71 Effect of Operating Variables on k_{La} of H_2 /Isopar-M/Glass Beads in the Cold SBCR	189
Figure 72 Effect of Operating Variables on k_{La} of CO/Isopar-M/Glass Beads in the Cold SBCR	190
Figure 73 Effect of Operating Variables on k_{La} of N_2 /Isopar-M/Glass Beads in the Cold SBCR	191
Figure 74 Effect of Operating variables on k_{La} of CH_4 /Isopar-M/Glass Beads in the Cold SBCR	192
Figure 75 Effect of Operating variables on k_{La} of He/Isopar-M/Alumina in the Cold SBCR ...	193
Figure 76 Effect of U_G on k_{La} of N_2 and He/Isopar-M/Alumina in the Hot SBCR	194
Figure 77 Effect of P, U_G , and C_V on a of H_2 /Isopar-M/Glass Beads in the Cold SBCR	196
Figure 78 Effect of P, U_G , and C_V on a of CO/Isopar-M/Glass Beads in the Cold SBCR	197
Figure 79 Effect of P, U_G , and C_V on a of N_2 /Isopar-M/Glass Beads in the Cold SBCR	198
Figure 80 Effect of P, U_G , and C_V on a of CH_4 /Isopar-M/Glass Beads in the Cold SBCR.....	199
Figure 81 Effect of P, U_G , and C_V on a of He/Isopar-M/Alumina in the Cold SBCR.....	200
Figure 82 Effect of P and T on a of N_2 and He/Isopar-M/Alumina in the Hot SBCR	201
Figure 83 Effect of the Operating Variables on k_L of H_2 /Isopar-M/Glass Beads in the Cold SBCR	203
Figure 84 Effect of the Operating Variables on k_L of CO/Isopar-M/Glass Beads in the Cold SBCR	204
Figure 85 Effect of the Operating Variables on k_L of N_2 /Isopar-M/Glass Beads in the Cold SBCR	205

Figure 86 Effect of the Operating Variables on k_L of CH ₄ /Isopar-M/Glass Beads in the Cold SBCR	206
Figure 87 Effect of the Operating Variables on k_L of He/Isopar-M/Alumina in the Cold SBCR	207
Figure 88 Effect of the Operating Variables on k_L of N ₂ and He/Isopar-M/Alumina in the Hot SBCR	208
Figure 89 Effect of C_V and P on $k_{L,a}$ of N ₂ and He/Isopar-M/Alumina in the Hot SBCR.....	210
Figure 90 Effect of Temperature on $k_{L,a}$ of N ₂ and He/Isopar-M/Alumina in the Hot SBCR....	211
Figure 91 Effect of Gas Nature on $k_{L,a}$, a and k_L in Isopar-M in the Cold SBCR	214
Figure 92 Effect of Gas Nature on $k_{L,a}$ of N ₂ and He in Isopar-M/Alumina in the Hot SBCR ..	215
Figure 93 Effect of Solid Nature on $k_{L,a}$, ϵ_G , and d_{32} Values of N ₂ /Isopar-M in the Cold SBCR	216
Figure 94 Axial Solid Distribution for N ₂ and He in Isopar-M/Alumina in the Cold SBCR.....	220
Figure 95 Axial Solid Distribution for N ₂ and He in Isopar-M/Alumina in the Hot SBCR.....	221
Figure 96 Comparison Between Experimental and Predicted ϵ_G , $\epsilon_{G-Large}$, and d_{32} Values from Equations (7-1), (7-4), and (7-6).....	235
Figure 97 Comparison Between Experimental and Predicted $k_{L,a}$ and Sherwood Values from Equations (7-9) and (7-10).....	236
Figure 98 Prediction of the Holdup of H ₂ in Isopar-M/Glass Beads Slurry using Available Literature Correlations and Equation (7-1).....	237
Figure 99 Prediction of $k_{L,a}$ and Sh using Available Literature Correlations and Equations (7-9) and (7-10).....	238
Figure 100 Comparison Between Experimental and Predicted ϵ_G , $\epsilon_{G-Large}$, d_{32} , and $k_{L,a}$ Values Using BPNN Models	251
Figure 101 Effect of P and T on Predicted ϵ_G , d_{32} and $k_{L,a}$ of Syngas in Wax/Alumina Using BPNNs	255
Figure 102 Effect of P and T on ϵ_G , $\epsilon_{G-Small}$ and $\epsilon_{G-Large}$ of the Syngas in wax/Alumina.....	256

Figure 103 Effect of T and C_W on Predicted ϵ_G , d_{32} and k_{La} of Syngas in Wax/Alumina Using BPNNs	259
Figure 104 Effect of T and C_W on ϵ_G , $\epsilon_{G-Small}$ and $\epsilon_{G-Large}$ of the Syngas in wax/Alumina.....	260
Figure 105 Effect of U_G and D_C on ϵ_G , d_{32} and k_{La} of the Syngas in Wax/Alumina.....	262
Figure 106 Effect of H_2/CO Ratio on ϵ_G , d_{32} and k_{La} of the Syngas in Wax/Alumina and Wax/Iron Oxide	265
Figure 107 Effect of N_O and C_W on ϵ_G of Syngas in wax/Alumina.....	267
Figure 108 Effect of Gas Sparger on the Total Gas Holdup of Syngas in Wax using Equation (7-1).....	269

NOMENCLATURE

a	Gas-liquid interfacial area per unit volume of liquid (solid free), m^{-1}
A_C	Cross sectional area of the reactor column, m
a_i	Constants of the statistical correlations, Equation (4-11)
a_p	Solid-Liquid interfacial area, m^{-1}
C^*	Solubility of the gas at equilibrium, $kmol\ m^{-3}$
C_L	Concentration of the gas in the liquid bulk, $kmol\ m^{-3}$
C_S	Average Solid concentration in gas-free slurry, $kg\ m^{-3}$
C_{S0}	Solid concentration at the bottom of the reactor, $kg\ m^{-3}$
$C_S(z)$	Solid concentration at height z in the column, $kg\ m^{-3}$
C_V	Volumetric solid concentration, vol. %
C_W	Concentration of solid in the slurry, wt. %
d_{32}	Sauter-mean bubble diameter, m
D_{AB}	Diffusivity of gas A in the liquid B, $m^2\ s^{-1}$
d_b	Gas bubble diameter, m
d_b^*	Initial bubble diameter at formation, m
D_C	Diameter of the reactor column, m
D_{eff}	Effective diffusivity, $m^2\ s^{-1}$
D_L	Liquid dispersion coefficient, $m^2\ s^{-1}$

d_o	Orifice diameter, m
d_p	Particle diameter, m
D_s	Solid dispersion coefficient, $m^2 s^{-1}$
e	Restitution coefficient, -
F	Force, N
g	Gravitational constant, $m^2 s^{-1}$
H_C	Height of the reactor column, m
H_e	Henry's Law Constant, $bar m^3 kmol^{-1}$
k	Phase mass transfer coefficient, $m s^{-1}$
k_0	Reaction rate constant, m/s
$k_{L,a}$	Volumetric liquid-side mass transfer coefficient, s^{-1}
M_A	Gas molecular weight, $kg kmol^{-1}$
M_B	Liquid molecular weight, $kg kmol^{-1}$
N	Number of moles, kmol
N_0	Total number of gas moles in the reactor, kmol
$n_{1,L}$	Number of moles of component 1 in the liquid phase, kmol
$N_{1,T}$	Total number of mole of component 1, kmol
$N_{G,T}$	Remaining number of gas moles after equilibrium, kmol
N_o	Number of opening on the gas sparger, -
p	Specific power input, $kg m^{-1} s^{-3}$
P	Pressure, bar

$P_{1,F}$	Equilibrium partial pressure of component 1, bar
P_C	Critical pressure, bar
P_i	Parachor contribution group, -
P_m	Mean partial pressure, bar
P_S	Saturated vapor pressure of the liquid, bar
P_T	Total pressure, bar
Q	Phase flow rate, $m^3 s^{-1}$
R^2	Regression coefficient = $\frac{\sum(\Omega_{Exp.} - \bar{\Omega}_{Exp.})(\Omega_{Pred.} - \bar{\Omega}_{Pred.})}{\sqrt{\sum(\Omega_{Exp.} - \bar{\Omega}_{Exp.})^2 \sum(\Omega_{Pred.} - \bar{\Omega}_{Pred.})^2}} \times 100, \%$
R_C	Radius of curvature of a spherical bubble cap, m
R_S	Overall rate of reaction, $kmol m^{-3} s^{-1}$
T	Temperature, K
t	Time, s
T_C	Critical temperature, K
U	Superficial velocity, $m s^{-1}$
U_b	Bubble rise velocity, $m s^{-1}$
$U_{b,0}$	Rise velocity of bubble base, $m s^{-1}$
$U_{b,\infty}$	Terminal rise velocity of a single gas bubble, $m s^{-1}$
U_e	Bubble expansion velocity, $m s^{-1}$
U_F	Frictional velocity at the gas-liquid interface, $m s^{-1}$
$U_{G,O}$	Gas velocity at the orifice, $m s^{-1}$

U_L	Superficial liquid velocity, $m\ s^{-1}$
U_P	Particle settling velocity, $m\ s^{-1}$
U_r	Relative velocity between the gas and liquid phase, $m\ s^{-1}$
\overline{U}_{rms}^2	Average value of square of difference in turbulence velocity, $m^2\ s^{-2}$
U_S	Slip Velocity, $m\ s^{-1}$
U_{SL}	Superficial slurry velocity, $m\ s^{-1}$
$U_{t\infty}$	Single particle settling velocity in infinite liquid medium, $m\ s^{-1}$
V	Volume, m^3
V_b	Volume of the gas bubble, m^3
X_i	Coded variable for the i th variable in Equation (4-11), -
X_W	Liquid composition, wt. %
z	Column axial position, m
Z	Gas deviation factor, -

Greek symbols

δ	Film thickness, m
ε	Phase holdup, -
λ	Constant in Equation (4-7), -
μ	Phase viscosity, $kg\ m^{-1}\ s^{-1}$
ν	Kinematic viscosity, $m^2\ s^{-1}$
ρ	Phase density, $kg\ m^{-3}$

$$\sigma \quad \text{Standard of deviation} = \sqrt{\frac{1}{n-1} \sum_1^n \left(\left| \frac{\text{Pr ed.} - \text{Exp.}}{\text{Exp.}} \right| - AARE \right)^2} \times 100, \%$$

σ_L Surface tension of the liquid, Nm^{-1}

υ Molar volume, $\text{m}^3 \text{kmol}^{-1}$

ω Accentric factor, -

ψ_L Liquid volume fraction in gas-free slurry, $V_L/(V_L+V_S)$, -

Ω Parameter in Equation (4-11)

τ Viscous stress tensor

Subscripts

A Gas specie

B Liquid specie

F Final conditions

FT Feed tank

G Gas phase

I Initial condition

L Liquid phase

O Orifice

S Solid phase

SL Slurry phase

Dimensional numbers

Ar	Archimedes number, $d_p^3 g(\rho_{SL} - \rho_L)\rho_L / \mu_L^2$
Bo	Bond number, $gD_C^2 \rho_L / \sigma$
Eo	Eötvös number, $g(\rho_L - \rho_G)d_b^2 / \sigma_L$
Eu	Euler number, $P / \rho_L U_b d_b^2$
Fr	Froude number, gas: $U_G / \sqrt{gD_C}$, liquid: $gD_C^2 \rho_L / \sigma$
Ga	Galileo number, $g\rho_L^2 D_C^3 / \mu_L^2$
Mo	Morton number, $g\mu_L^4 / \rho_L \sigma^3$
Pe	Peclet number for solid particle, $U_p z / D_S$
Re	Reynolds number, gas: $U_G D_C \rho_L / \mu_L$, particle: $d_p U_{\infty} \rho_L / \mu_L$ gas bubble: $U_b d_b \rho_L / \mu_L$
Sc	Schmidt number, $\mu_L / \rho_L D_{AB}$
Sh	Sherwood number, $k_L d_{32} / D_{AB}$
We	Webber number, $\rho_L U_{G,O}^2 d_O / \sigma$

Abbreviations

AARE	Absolute average relative error = $\frac{1}{n} \sum_1^n \left \frac{Pr ed. - Exp.}{Exp.} \right \times 100, \%$
ANN	Artificial neural network
BC	Bubble cap gas distributor

BCR	Bubble Column Reactor
BPNN	Back propagation neural network
FB	Feed Back
FF	Feed Forward
FT	Fischer-Tropsch
HLN	Hidden layer node(s)
ILN	Input layer node(s)
LTFT	Low temperature Fischer Tropsch
M-ON	Multiple-orifice gas distributor
MSE	Mean square error
OLN	Output layer node(s)
PfP	Perforated plate gas distributor
PoP	Porous plate gas distributor
R	Perforated ring gas distributor
S	Spider type gas distributor
SBCR	Slurry Bubble Column Reactor
S-ON	Single-orifice nozzle gas distributor
SP	Sintered plate gas distributor
TSBC	Tapered slurry bubble column

ACKNOWLEDGMENT

I would like to express my sincere gratitude to Professor Badie I. Morsi for his valuable guidance and support throughout this study. I am grateful to Professor Shiao-Hung Chiang, Professor George Klinzing, Professor Robert Enick, and Professor Patrick Smolinski for serving at my committee.

I would like to acknowledge the financial support of ChevronTexaco ERTC and Exxon Research and Engineering Co. I extend my thanks to Micro Motion Inc. and Mr. Tom Kuny for providing the Coriolis mass flow meter. The technical support of the Chemical and Petroleum Engineering faculty, Mr. Ron Bartlett, Mr. Bob Maniet and the School of Engineering Machine Shop is greatly appreciated.

I am thankful to the member of my research group: Dr. Romain Lemoine, Dr. Benoit Fillion, Mr. Yannick Heintz, Mr. Abdul Karim Alghamdi, Mr. Laurent Sehabiague, Mr. Jean-Philippe Soriano, and Dr. Juan Inga, for their valuable contribution, help, and constructive criticism during this research project.

I am eternally indebted to my parents, sister, brother, family, and friends for their support and encouragement throughout this endeavor. I am especially grateful to my father Dr. Ali Reza Behkish, M.D. for his immense and unconditional assistance.

I dedicate this thesis to my parents.

1.0 INTRODUCTION

Multiphase reactions such as gas/solid, gas/liquid or gas/liquid/solid are widely used in chemical, petroleum and biological processes. Some examples of such reactions are production of cyclohexanol/cyclohexanone from cyclohexane and Benzoic acid/benzaldehyde from toluene by DSM, production of styrene via MBA by Arco, oxidation of propylene by Aristech, Fischer-Tropsch synthesis by SASOL^{(1)*}, and hydro-cracking, hydro-isomerization processes by many petrochemical companies. For specific processes, the three-phase (gas/liquid/solid) reaction is often preferred over the conventional two-phase (gas/solid) reaction because the presence of the liquid has several advantages⁽²⁾:

- It is essential to maintain volatile reactants and products,
- It saves energy generally used in vaporization,
- It allows better temperature control because of the high heat capacity of the liquid.

There are several types of multiphase reactors available in the industry which could be classified in two groups: fixed beds and slurry phase reactors.

The fixed beds or the packed beds are reactors in which the solid phase is stationary. One type of such reactors is the trickle bed where the gas and liquid flow downward through the catalytic packing. The main advantages of fixed bed reactors are⁽²⁾:

* Parenthetical references placed superior to the line of the text refer to the bibliography.

- High selectivity due to the residence time distribution;
- Low capital cost due to easy construction;
- Commercial scaleup is possible; and
- Large volume reactors are available (up to 300 m³).

The disadvantages associated with these reactors are:

- Mal-distribution of the liquid;
- Poor thermal recovery due to difficult temperature control;
- High pressure drop when using small particles;
- Catalyst should have high thermal stability and high crushing strength.

The second group of multiphase reactors is mainly the Stirred tank reactors (STR) and the Slurry Bubble Column Reactors (SBCRs). In the latter, the solid phase consists of fine catalyst particles, which are suspended in the liquid phase due to the gaseous reactants introduced into the reactor from the bottom often through a sparger. These reactors are becoming more competitive with and are replacing fixed bed reactors due to their inherent advantages ⁽²⁾:

- Higher reaction rate per unit volume;
- Better temperature control;
- Higher online factor;
- Higher effectiveness factor;
- Lower pressure drop; and
- Higher gas holdup and mass transfer rate.

Due to these advantages slurry bubble column reactors are used in numerous industrial applications. Air Products and Chemicals and Eastman Chemicals successfully commercialized Liquid-Phase Methanol Synthesis process (LPMeOH) with the sponsorship of the U.S. Department of Energy ⁽³⁾. Similarly, SASOL, South Africa commissioned the FT process in May 1993, on a commercial level in a 5 m diameter and 22 m high SBCR with a capacity of about 2500 bbl/day ^(1,4,5),6). Exxon's Advanced Gas Conversion technology (AGC-21) was introduced in 1990 on an R&D level in Baton Rouge, LA, using a slurry bubble column reactor of 1.2 m in diameter and 21 m high with a capacity of 200 bbl/day ⁽⁶⁾. In 1993, Rentech Inc. introduced its FT slurry reactor of 1.83 m (6 ft) in diameter and 16.76 m (55 ft) high in Pueblo, CO, capable of producing between 300 to 500 bbl/day ⁽⁷⁾. These new developments clearly indicate the increasing use of slurry technology for FT synthesis. Also the current trends in slurry FT process are outlined in Appendix A.

There are, however, some disadvantages associated with SBCRs which cannot be ignored such as ⁽²⁾:

- Important liquid backmixing caused by the flow of the gas bubbles;
- Catalyst deactivation and attrition;
- Important side products due to high liquid to solid ratio;
- Separation of fine solid particles from the viscous liquid; and
- Complexity of scaleup.

The design and scaleup of SBCRs require, among others, precise knowledge of the kinetics, hydrodynamics, and heat as well as mass transfer characteristics. More precisely, reaction orders with respect to reactants and products, reaction rate constant, liquid- and solid-

side mass transfer coefficients, phases holdup, flow regimes, pressure drop, and axial as well as radial solid distributions are fundamental parameters for modeling, design, and scaleup of such reactors. Furthermore, the hydrodynamic and mass/heat transfer coefficients should be available under actual industrial conditions since high pressure (10-80 bar), high gas throughput, large reactor diameter (5-8m)⁽⁸⁾, and high slurry concentration (30-40 vol.%) are needed in order to achieve high space-time yields⁽⁹⁾.

2.0 LITERATURE REVIEW AND BACKGROUND

In this section, studies on the hydrodynamic and mass transfer characteristics in the slurry bubble column reactors and industrial applications of these reactors are reviewed.

2.1 HYDRODYNAMICS

It has been reported that the operating conditions and design as well as the geometry of the column strongly affect the hydrodynamics of the SBCRs ^(10,11,12). In the following sections, the flow regimes and phase holdup characteristics of the SBCRs will be examined.

2.1.1 Flow Regimes

The hydrodynamics of bubble columns and slurry bubble column reactors depend strongly on the flow regime ⁽¹²⁾. There are three flow patterns that prevail in these reactors ⁽¹³⁾: 1) homogeneous flow (bubbly flow); 2) heterogeneous flow (churn-turbulent flow); and 3) slug flow regimes. In the bubbly flow regime, there is a homogeneous distribution of small and almost identical gas bubbles. The gas velocity is usually less than 0.05 m/s and the interaction among gas bubbles is weak. Under these conditions, the gas bubbles do not affect the liquid motion and almost no liquid mixing is observed. The gas bubble formation in this regime depends strongly on the injection point ^(14,15). As the gas velocity is increased, there is more interaction among gas bubbles and both coalescence and break up of bubbles are observed. This is the churn turbulent

flow or the heterogeneous regime, where the larger gas bubbles move in a plug flow, creating liquid recirculation as well as backmixing. The smaller gas bubbles, on the other hand, are entrained within the liquid re-circulation ⁽¹⁶⁾.

Letzel et al. ⁽¹⁷⁾, and Lin et al. ⁽¹⁸⁾ studied the effect of pressure on the flow regime transition from homogeneous to heterogeneous in bubble column reactors and reported that the transition was delayed with increasing system pressure. Their studies showed that both the gas holdup and gas velocity at the regime transition increase with increasing gas density, i.e., system pressure. This is important for the scaleup of commercial reactors, since the reactions often take place at high pressure and churn turbulent flow regime is desirable under such conditions. Furthermore, in small diameter columns, as the gas velocity increases, gas bubbles coalesce to form slugs whose diameters can be as large as the column diameter. This regime is called the slug flow regime. The effect of the column diameter is referred to as the wall effect and happens in columns with diameter up to 0.15 m ⁽¹⁰⁾. Anderson and Quinn ⁽¹⁹⁾ studied the flow regime of pure gas-liquid dispersion and found that when the length to diameter of the column ratio (H_C/D_C) was greater than $0.76(\epsilon_G^{-4/3})$ the slug flow regime would prevail. Further experiments carried out by these authors with different liquids, however, proved that such relationship does not always hold true and no slug formation was observed even though at 20% gas holdup, the H_C/D_C ratio was found to be greater than 40. The formation of the slugs is therefore dependent on the column diameter, and happens more frequently in columns of diameters less than 0.15m. ^(20,21). Nevertheless, the physical properties of the liquid, such as high viscosity, or a contamination of the liquid have been found to facilitate the formation of slugs even at very low superficial gas velocity ^(19,22).

Different flow maps for regime transition were proposed. Figure 1 shows a typical flow-map for bubble column that was initially proposed by Deckwer et al. ^(11,23) for air/water system based on the column diameter as a function of gas velocity. If the gas velocity is low (generally below 4 cm/s) the reactor tends to operate in bubbly flow regime and the column diameter seems to have small effect on the flow regime. On the other hand if the column diameter is too small, an increase in gas velocity will shift the flow regime and formation of slugs will be observed. Furthermore, the flow regime transition can also be dependent on the type of gas sparger used ⁽²³⁾. Since the flow regime transition depends on different parameters, the boundaries between the regimes in Figure 1 are not exact and there exist a transition regime where each flow regime can prevail depending the experimental setup and system used. A comprehensive study of the published works on the transition superficial gas velocity ($U_{G-trans}$) from homogeneous to heterogeneous flow regimes has been done by Sarrafi et al. ⁽¹⁵⁾, where it can be seen that $U_{G-trans}$ generally lies in the range of 0.044-0.067 m/s. Oshinowo and Charles ⁽²⁴⁾ carried out experiments at different operating conditions (pressure up to 1.7 bar and temperature between 283 and 300K) in a 0.254m diameter column and identified six different flow regimes in an upward liquid flow. These regimes are: 1) Bubble flow regime: dispersed gas as individual bubbles; 2) Quiet-slug flow regime: large bullet shaped bubbles; 3) Dispersed-slug flow: similar to the quiet-slug flow except an increase in size and rise of bubbles was observed accompanied by froth formation in the trailing part of the bubble. 4) Frothy slug flow regime: fast moving bubbles and froth formation over the entire boundary of large bubbles was observed; 5) Froth flow regime: highly turbulent mixture of degenerated bubbles and liquid; 6) Annular flow regime: similar to an annular liquid film on the wall with gas occupying the center of the column.

Nevertheless, regime transitions in bubble columns are still under investigation and several techniques such as computer-automated radioactive particle tracking (CARPT), particle image velocimetry (PIV), and laser Doppler velocimetry (LDV) are being employed to determine the flow behavior of the bubble column reactors^(25,26).

Chen et al.⁽²⁷⁾ using PIV technique in a 3-D bubble column identified 3 regimes: bubbly flow, turbulent flow and the vortical-spiral flow, which could be referred to as the transition regime shown in Figure 1.

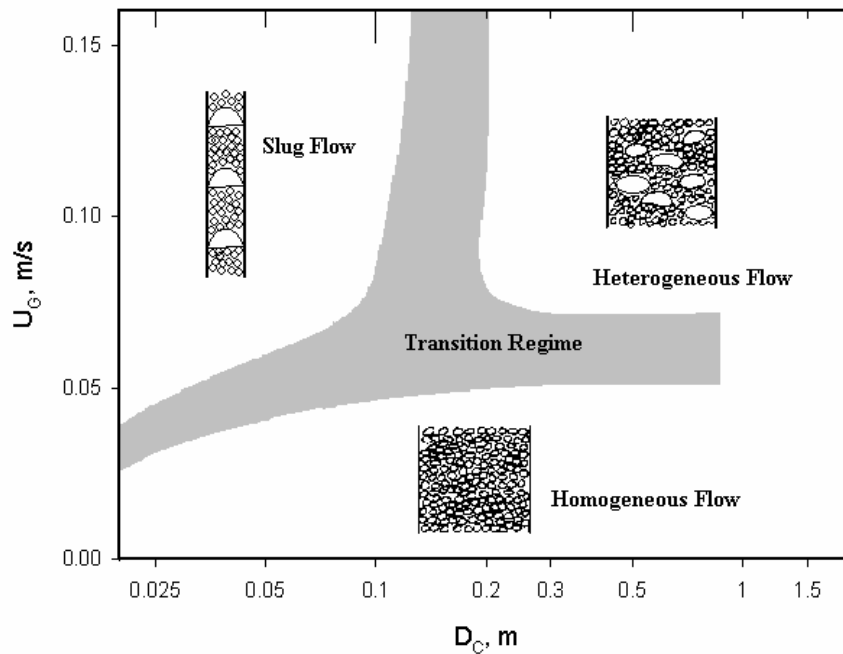


Figure 1 Flow-Regime Map for the Bubble Column Reactor^(2,11)

2.1.2 Gas Holdup, ϵ_G

In the SBCRs, the total volume, V_T , of the three-phase system is given by the following expression:

$$V_{\text{Total}} = V_{\text{Gas}} + V_{\text{Liquid}} + V_{\text{Solid}} \quad (2-1)$$

The holdup of any phase, i , is defined as the volume fraction occupied by this phase in the reactor:

$$\varepsilon_i = \frac{V_i}{V_G + V_L + V_S} \quad (2-2)$$

and accordingly,

$$\varepsilon_G + \varepsilon_L + \varepsilon_S = 1 \quad (2-3)$$

The gas holdup is one of the most important parameters used to describe the performance of the slurry bubble column reactors⁽²⁸⁾. The behavior of the gas holdup has been attributed to many different factors, including the physical properties of gas/liquid/solid phase, column geometry, gas distributor design, and the operating variables, i.e., pressure, gas velocity, temperature, and solid loading. Figure 2 illustrates the different parameters that affect the gas holdup, hence influencing the performance of SBCRs. Currently there are several techniques available to measure the gas holdup such as, pressure drop measurements, electroconductivity, X-ray transmission, γ radiation, mean residence time distribution, optical fiber probes, particle image velocimetry, and computer tomography^(29,30).

2.1.3 Effect of the Superficial Gas Velocity on ε_G

Most published studies have shown a positive effect of the superficial gas velocity on the gas holdup^(11,31,32,33,34) due to a direct influence on the regime transition in the reactor⁽²³⁾. The dependence of the gas holdup on the superficial gas velocity can best be defined by the following power-law expression⁽³⁵⁾:

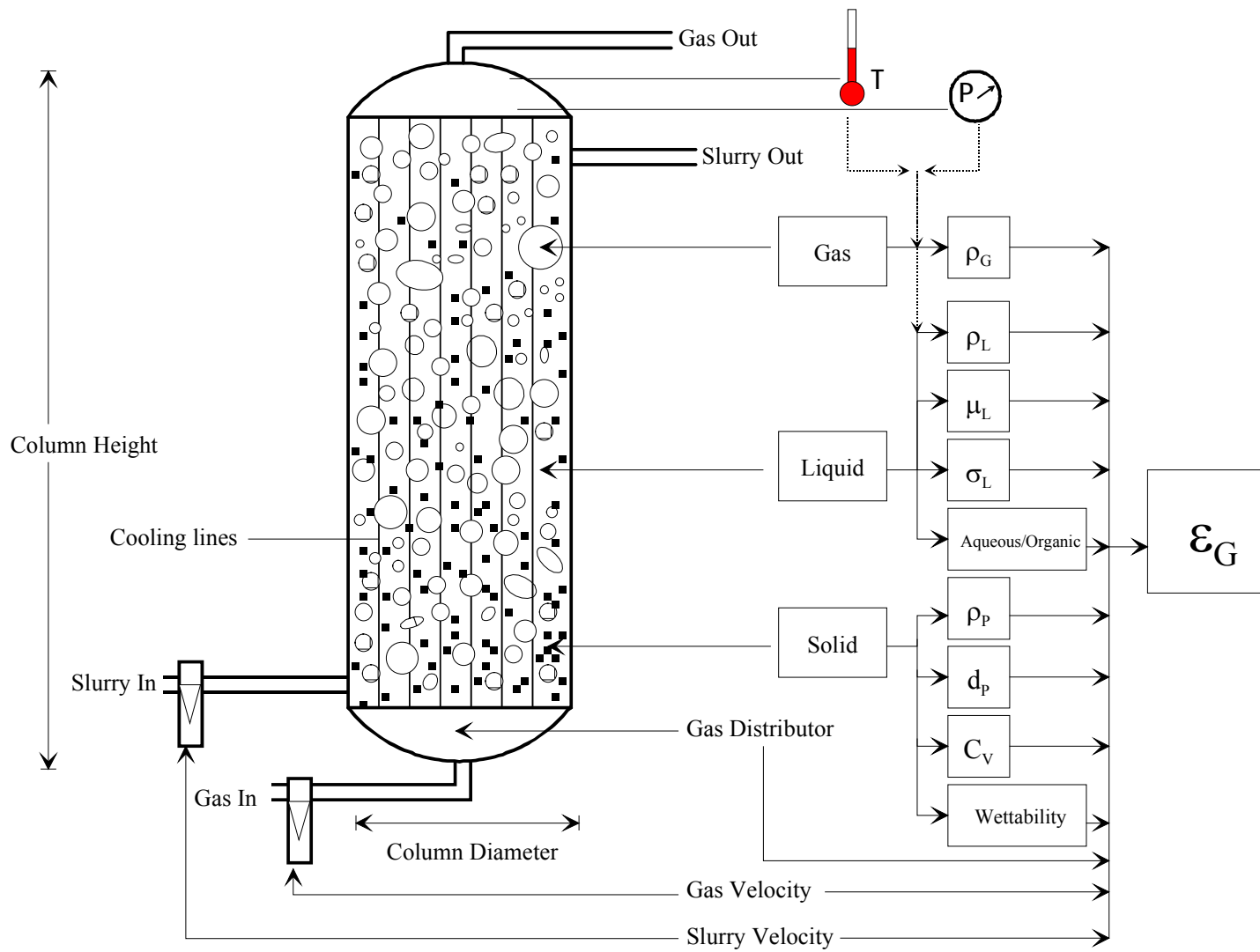


Figure 2 Parameters influencing the Performance of the Slurry Bubble Column Reactor

$$\varepsilon_G \propto U_G^n \quad (2-4)$$

Where n is dependent on the flow regime. Initially, the gas holdup seems to increase sharply and almost linearly with the superficial gas velocity in the homogeneous flow regime where the exponent n in Equation (2-4) is generally reported to be in the range of 0.7-1.2^(23,35). The gas holdup then reaches a maximum where the transition from homogeneous to heterogeneous flow regime occurs, and consequently a more non-linear increase with the superficial gas velocity beyond that point can be observed^(36,37). The exponent n in the heterogeneous flow regime is reported to be in the range of 0.4-0.7^(23,35). The range of the exponent n in Equation (2-4) suggests that the effect of the superficial gas velocity on the gas holdup in both the homogeneous and heterogeneous flow regime is strongly dependent on the operating variables, physical properties of the system, as well as the design characteristics of the column. The effects of these parameters are discussed in the following sections.

2.1.4 Effect of Pressure and Gas Density on ε_G

The effect of pressure on the gas holdup has been extensively carried out in the past few years and the majority of the studies have shown that the gas holdup of bubble and slurry bubble columns increased with increasing system pressure^(38,39,40,41,42,43,44,45). Numerous researches to determine the reasons of this increase with pressure have been previously reported. Several authors have directly attributed this increase to an increase of gas density^(46,47,48,49). Therefore, it can be concluded that gases with higher molecular weight will lead to higher gas holdup. Clark⁽⁵⁰⁾, however, found that at low gas velocity the gas holdup of H₂ was significantly higher than that of N₂. Only when the gas velocity was greater than 0.05 m/s, the trend was reversed and the

gas holdup of N₂ became greater than that of H₂. Clark ⁽⁵⁰⁾ proposed that in the velocity range below 0.05 m/s, the gas holdup was more influenced by the gas bubble surface tension than pressure. Pohorecki et al. ⁽⁵¹⁾ also observed no apparent effect of pressure on the gas holdup values of N₂-water system in the velocity range of 0.002-0.02 m/s. Kemoun et al. ⁽⁵²⁾ measured the radial gas holdup via computed tomography in a 0.162 ID bubble column up to 7 bar and found that the average gas holdup increased with pressure and the gas holdup was higher at the center of the column than near the walls. It is, however, widely accepted that an increase of pressure is mainly responsible for reducing the coalescence tendency of the gas bubbles and subsequently increases the volume fraction of the small gas bubbles ^(38,39,45). Jiang et al. ⁽⁵³⁾ observed gas bubbles photographically and found that the large bubbles that exist at low pressure gradually disappeared with pressure. Therning and Rasmuson ⁽⁵⁴⁾ studied the gas holdup in a 0.15 ID packed bubble column and found that in the range of 1 to 6.6 bar, both the gas holdup and the liquid dispersion coefficient increased. This increase was attributed to the formation of smaller gas bubbles in the bed.

2.1.5 Effect of the Physical Properties of the Liquid on ϵ_G

The influence of the liquid properties can have a major impact on the gas holdup, especially if the liquid has high viscosity and shows foaming tendencies. In the commercial SBCRs where a molten wax is usually the liquid phase, the hydrodynamic can vary from one wax to another despite comparable physical properties ⁽⁵⁵⁾. Öztürk et al. ⁽⁴⁹⁾ measured the gas holdup in 17 pure organic liquids, 5 inherently mixed liquids and 17 adjusted mixtures and found that gas holdup was higher in organic liquid mixture than in water. The gas holdup of a mixture of 2 pure organic liquids on the other hand, seemed to reach a maximum at intermediate mole fraction. Their

findings were comparable to those of Bhaga et al.⁽⁵⁶⁾ who studied the gas holdup in toluene/ethanol mixture. Oyevaar et al.⁽³⁸⁾ compared the gas holdup obtained in water and an aqueous solution of diethanolamine (DEA) with anti-foam and found that the effect of pressure on ε_G was higher in DEA than water. They attributed this effect to the coalescence behavior of the liquids. Stegeman et al.⁽⁴⁴⁾ found that pressure effect on gas holdup was more important for more viscous liquids. Consequently, among the physical properties of the liquid, viscosity can have a major effect on the gas holdup in bubble columns. It has been found that gas holdup decreases with increasing liquid viscosity^(57,58,59). Crabtree and Bridgwater⁽⁶⁰⁾ explained this behavior by suggesting that high liquid viscosity promotes bubble coalescence. It is therefore, expected that the gas holdup of a high viscous liquid will be due to larger gas bubbles. Wilkinson et al.⁽⁶¹⁾ studied the effect of liquid physical properties (i.e., viscosity and surface tension) on the gas holdup using *n*-heptane, mono-ethylene glycol and water. They found that the higher population of larger gas bubbles having faster rising velocity not only decreased the gas holdup but the transition from homogenous to churn turbulent flow regime occurred at lower gas velocity. Furthermore, it is believed that the effect of liquid viscosity obtained by adding solutions to an aqueous liquid does not produce the same results obtained with organic liquids⁽⁶¹⁾. Kantak et al.⁽⁶²⁾ measured the gas holdup for water-CMC solution and found that the gas phase dispersion decreased with increasing viscosity due to bubble coalescence. On the other hand, Guy et al.⁽¹²⁾ found no evident effect of viscosity while measuring the gas holdup in water and 7 other aqueous solutions (with different viscosity). They found that although there was no effect of viscosity on the gas holdup, the mixing efficiency decreased with increasing liquid viscosity.

The effect of surface tension on the gas holdup is also significant. In general, the amplitude of the cohesive forces that exists between the liquid molecules is responsible for the effect of the surface tension on the total gas holdup. Consequently, increasing the surface tension will help the formation of more gas bubbles within the liquid and hence prevent them from any further deformation under the operating variables. It has been reported that decreasing surface tension increased the gas holdup ^(61,63) due to the formation of smaller gas bubbles. Thus, it is believed that large population of small gas bubbles is responsible for the increase in gas holdup. Foaming occurs when the liquid phase is a mixture and in some commercial processes where selectivity could be low, the formation of side products creates significant foaming in the liquid phase which can influence the gas holdup. In fact, gas holdup was found to increase with foaming characteristics of the liquid ^(64,65). Yamashita ⁽⁶⁶⁾ observed an increase of the gas holdup in the foam layer and reported that this phenomenon was more pronounced at lower clear liquid height.

Changing the temperature can also alter the physical properties of the liquid. In fact, most industrial processes carried out in slurry bubble columns take place at temperatures greater than 180 °C ⁽²⁸⁾, and under such high temperatures, both the liquid viscosity and surface tension are low. Thus, the hydrodynamic of the reactor changes significantly and the data obtained at ambient condition should not depict the actual performance of these reactors. For instance, Clark ⁽⁵⁰⁾ compared his gas holdup values obtained at temperature as high as 180 °C with the available literature correlations and reported a very poor agreement between his data and those predicted by literature correlations. Few studies have also been conducted to determine the gas holdup in

bubble and slurry bubble column under elevated temperatures and Table 1 summarizes some of these studies available in the literature.

2.1.6 Effect of Solids on ϵ_G

In SBCRs, the volumetric solid concentration greatly affects the hydrodynamics. The solid particles in the bubble column reactors are typically in a micron size and are suspended in the liquid phase to form the slurry phase. Consequently, their concentration in the liquid phase changes the slurry physical properties, namely the density, and the viscosity. The effect of solid particles was reported by several investigators to decrease the total gas holdup^(67,68,69,70,71,72,73). The decrease of gas holdup with solid concentration was attributed to the increase of the pseudo-viscosity of the slurry phase, which enhanced the formation of large gas bubbles^(50,43,64). An increase of bubble size increases the bubble rise velocity and reduces the residence time of the bubbles in the reactor. de Swart et al⁽⁷⁴⁾ studied the gas holdup of air/paraffin oil in the presence of glass beads particles at atmospheric conditions. Their solid concentration was varied up to 20 vol.%. They found that the holdup of the large gas bubbles was independent of the slurry concentration. This finding was later confirmed by Krishna et al.⁽⁸⁾ who used the same three-phase system with solid concentration as high as 36 vol.% while using three different column diameters. Gandhi et al.⁽⁷³⁾ studied the effect of glass beads concentration in water up to 40 vol.% on the gas holdup. They found that at low solid concentration, the coalescence inhibitor increased the solids concentration gradient, whereas at higher concentration this effect was not observed. Yasunichi et al.⁽⁵⁸⁾ used glass beads up to 50 vol.% in water and glycerol, and reported that gas holdup decreased gradually with increasing slurry viscosity. They also found that at high solid concentration, there was no effect of gas velocity on the bubble size distribution and bubble

rise velocity. These studies clearly show that increasing solid concentration mainly affects the smaller gas bubbles by enhancing their coalescence upon early formation and disabling bubble break up later in the column. The larger gas bubbles are then not disturbed by the presence of solid particles and their higher rise velocity will contribute to a lower overall gas holdup.

The knowledge of the slurry viscosity is therefore important for estimating the gas holdup in SBCRs. Table 2 summaries some available correlations to predict the slurry viscosity. Nevertheless, the increase in pseudo-viscosity of the slurry phase has not always been the reason of the decrease of gas holdup. Banisi et al.⁽⁷⁵⁾ studied the gas holdup in a three-phase floatation device using Calcite particles (74% > 53 μm) and noticed a decrease in gas holdup with increasing solid concentration. They postulated four mechanisms to explain this behavior, where the change in density and viscosity of the slurry phase and coalescence of gas bubbles were not considered. Consequently, they explained the decrease of gas holdup by the increase of the bubble rise velocity caused by wake stabilization; and the change of the radial holdup and flow profiles. In contrast with the above studies, some investigators did not observe the same behavior of gas holdup with solid concentration. Bukur et al.⁽⁹¹⁾ measured the gas holdup for N_2 in molten wax at 265 °C in the presence of iron oxide and silica particles. On one hand they found that at batch mode and gas velocity greater than 0.04 m/s, gas holdup increased with solid concentration from 0 to 20 wt.%. When the reactor was operated in continuous mode with a slurry velocity of 0.005 m/s, however, the gas holdup was found to decrease with solid concentration. Bukur et al.⁽⁹¹⁾ attributed this behavior to the poor wettability of iron oxide and silica particles and their adhesion to the gas bubbles preventing them from coalescing.

The effect of solid particles, including magnesium hydroxide⁽⁷⁶⁾, calcium hydroxide⁽⁷⁶⁾, iron oxide⁽⁷⁷⁾, calcium carbonate⁽⁷⁸⁾, and carbon particles⁽⁶³⁾ at various concentrations in slurry reactors was reported to increase the gas holdup and gas-liquid interfacial area at low concentrations (< 5 vol. %). The increase of solid particle size, on the other hand, was found to decrease the gas holdup^(79,80). Furthermore, the effect of solid particles on the gas holdup should account not only for the solid concentration, but also for particle nature, size and density which might significantly affect the gas holdup and subsequently the gas-liquid interfacial area^(64, 81).

Also, foaming of the liquid could have formed at batch mode and could have been entrained with the liquid when the column was operated at continuous mode. Kluytmans et al.⁽⁶³⁾ measured the gas holdup in a 2-D slurry bubble column at ambient conditions using N₂ in distilled water and water with different solution of sodium gluconate as electrolyte. The solid phase consisted of carbon particles with 30 μm mean particle diameter. They found that the gas holdup increased with both the addition of the electrolyte, and presence of carbon particles. The increase of ϵ_G with the former is attributed to the decrease of water surface tension with the addition of the electrolyte solutions. To explain the increase of gas holdup with carbon particles, Kluytmans et al.⁽⁶³⁾ suggested that the wettability of the particles might have had a critical effect. Thus, the stabilization of gas bubbles with some particular solid particles can be explained by the formation of an additional layer of particles around the gas bubbles, which prevents them from coalescence.

Table 1 Available literature studies on high temperature bubble and slurry bubble column reactors

<i>Authors</i>	<i>System: gas/liquid/solid</i>	<i>Condition</i>	<i>Column IDxHeight</i>	<i>Mass Transfer</i>	<i>Remarks</i>
De Bruijn et al. ⁽⁸²⁾	H ₂ /Zerice Oil	P: 50 to 140 bar U _G up to 0.02 m/s T: 300°C	0.0508x2.4m	No	ϵ_G increased with pressure
Chabot and Lasa ⁽⁸³⁾	N ₂ /Paraffin oil	P _{atm} U _G : 0.022-0.147 m/s T: 100-175 °C	0.2x2.4m	No	Bubble chord length increased with decreasing T.
Grover et al. ⁽⁸⁴⁾	Air/H ₂ O, NaCl, CuCl ₂	P _{atm} , U _G : 0.001-0.045 m/s T: 30-80°C	0.1x1.5m	No	ϵ_G decreased with T for air/H ₂ O. but increased for air/electrolyte at low U _G)
Lin et al. ⁽¹⁸⁾	N ₂ /Paratherm NF	P up to 152 bar U _G up to 0.07 m/s T up to 78 °C	0.0508x0.8m	No	Regime transition delayed with P and T
Lin et al. ⁽⁸⁵⁾	N ₂ /Paratherm NF	P up to 152 bar U _G : 0.02-0.08 m/s T: up to 351 K	0.0508x0.8 m 0.1016x1.58m	No	Maximum stable bubble size decreased with P and T
Pohorecki et al. ⁽⁵¹⁾	N ₂ /H ₂ O	P: 1-11 bar U _G : up to 0.02 m/s T: 303-433 K	0.304x3.99m	No	ϵ_G and d ₃₂ are independent of P and T
Pohorecki et al. ⁽⁸⁶⁾	N ₂ /Cyclohexane	P: 2-11 bar U _G up to 0.06 m/s T: 30-160 °C	0.3x4m	No	ϵ_G increased with temperature.
Zou et al. ⁽⁸⁷⁾	Air/H ₂ O, Alcohol, 5% NaCl	P _{atm} , U _G : 0.01-0.16 m/s U _L : 0.007 m/s T: 25-96.56 °C	0.1x1.05m	No	ϵ_G increased with U _G and T.
Lau et al. ⁽⁸⁸⁾	N ₂ , air/Paratherm NF	P: up to 42.4 bar U _G : up to 0.4 m/s U _L : 0.08-0.89 cm/s T: up to 365 K	2 columns of 0.0508 and 0.1016 m ID	Yes	ϵ_G increased with P and T. Influence of column diameter. Influence of U _G and U _L on ϵ_G . Mass transfer was not measured at high T.

Table 1 (Continued)

<i>Authors</i>	<i>System: gas/liquid/solid</i>	<i>Condition</i>	<i>Column IDxHeight</i>	<i>Mass Transfer</i>	<i>Remarks</i>
Daly et al. ⁽⁸⁹⁾	N ₂ /FT-300 paraffin wax, Sasol wax	P _{atm} U _G : up to 0.12 m/s T: 538 K	0.05x3 0.21x3	No	Sauter-mean bubble diameters were higher in the smaller column for FT-300 wax
Soong et al. ⁽⁵⁵⁾	N ₂ /Drakeol-10 oil	P: 1, 13.6 bar U _G : up to 0.09 m/s T: 293, 538 K	0.1x2.44	No	d ₃₂ decreased with T
Ishibashi et al. ⁽⁹⁰⁾	H ₂ /Oil	P: 168 to 187 bar U _G : 0.07-0.08 m/s T: 49-458 °C	3 reactors of 1x11m	No	Coal properties had little effect on ε _G
Bukur et al. ⁽⁹¹⁾	N ₂ / FT-300 paraffin wax/ Iron oxide and silica	P _{atm} U _G : 0.02-0.12 m/s C _w : 10-30 wt.% T: 265°C	0.05x3m	No	Effect of slurry circulation and solid concentrations.
Clark ⁽⁵⁰⁾	N ₂ , H ₂ / H ₂ O, CH ₃ OH, Coal oil/Glass	P: atm-100 bar U _G up to 0.06 m/s T: 20-180°C	0.075x3m	No	Liquid vapor at high T increased ε _G . ε _G (H ₂)>ε _G (N ₂)
Deckwer et al. ⁽¹¹⁾	N ₂ /Paraffin wax/Al ₂ O ₃	P: up to 11 bar U _G : up to 0.04 m/s T: 416 and 543 K C _S : up to 16 wt.% P: 1-56.2 bar	2 Reactors of 0.04 and 0.1 m ID		ε _G decreased with T in small column, but independent in large column. No effect of P on ε _G
Luo et al. ⁽⁴³⁾	N ₂ /Paratherm NF/Alumina	U _G : up to 0.4 m/s T: 301, 351 K C _v : 8.1, 19.1 vol.%	0.102x1.37m	No	Maximum stable bubble size is independent of slurry concentration at high pressure
Saxena et al. ⁽⁷⁹⁾	Air/H ₂ O/Glass	P _{atm} U _G up to 0.3 m/s C _w :0-30 wt.% T: 25-90°C	0.305x3.25m	No	Effect of internal tubes on the gas holdup.
Yang et al. ⁽⁹²⁾	N ₂ /Paratherm NF/glass beads	P up to 42 bar U _G up to 0.2 m/s C _v up to 35 vol.% T up to 81 °C	0.1016x1.37 m	No	Heat transfer coefficient decreases with pressure.

Table 2 Available correlations for predicting slurry viscosity

<i>Authors</i>	<i>Correlation</i>	
Saxena and Chen ⁽¹⁰⁾	$\mu_{sl} = \mu_L (1 + 4.5C_V)$	(2-5)
Thomas ⁽⁹³⁾	$\mu_{sl} = \mu_L \left(1 + 2.5C_V + 10.05C_V^2 + 0.00273e^{16.6C_V} \right)$	(2-6)
Guth and Simba ⁽⁹⁴⁾	$\mu_{sl} = \mu_L (1 + 2.5C_V + 14.1C_V^2)$	(2-7)
Barnea and Mizrahi ⁽⁹⁵⁾	$\mu_{sl} = \mu_L \exp\left(\frac{5/3C_V}{1-C_V}\right)$	(2-8)
Roscoe ⁽⁹⁶⁾	$\mu_{sl} = \mu_L (1 - C_V)^{-2.5}$	(2-9)
Riquarts ⁽⁹⁷⁾	$\mu_{sl} = \mu_L \left(1 + \frac{\rho_P + \rho_L}{\rho_L} C_V \right) (1 - C_V)^{-2.59}$	(2-10)
Vand ⁽⁹⁸⁾	$\mu_{sl} = \mu_L \exp\left(\frac{2.5C_V}{1 - 0.609C_V}\right)$	(2-11)

2.1.7 Effect of Reactor Size on ϵ_G

It has been reported that the hydrodynamics of SBCRs are strongly dependent on the column geometry as well as the gas distribution technique ⁽³⁵⁾. In fact, based on the column geometry, the following three different regions with their respective gas holdup were identified ^(61,99,100): (1) sparger region (ϵ_G depends on the gas distributor design); (2) bulk region (ϵ_G is controlled by the liquid/slurry circulation); and (3) top region (ϵ_G is large due to the formation of a layer of froth above the liquid/slurry bed). In general, the gas holdup will then be the sum of the holdups in the three regions, however, if the column is long enough, the influence of the first and third regions on the gas holdup will be insignificant and thus the gas holdup will be close to the values measured in the bulk region ⁽⁶¹⁾. The ratio of height of the reactor to its diameter (H_C/D_C) would therefore affect the gas holdup. A number of investigators reported that typically no obvious change in the gas holdup was observed when H_C/D_C ratios were $> 5 - 6$ ^(61,65,101), as the effect of sparger on the total gas holdup within the top region of the reactor was insignificant.

Furthermore, the gas holdup was found to decrease with column diameter⁽¹⁵⁾ due to a reduction in the holdup of large gas bubbles^(6,102), a change in the liquid backmixing⁽³⁵⁾, and a reduction of the foaming ability of the liquid/slurry⁽⁶⁵⁾. A few investigators have also observed that with highly viscous liquid (i.e. ≥ 0.55 Pa s), the effect of column diameter on ε_G was more pronounced due to a weak wall effect on the rise velocity of the gas bubbles^(102,103). Koide et al.⁽⁶⁸⁾ measured the gas holdup of air/water system in the churn-turbulent flow regime and reported that ε_G values obtained in a 0.218 and 0.3 m ID columns were identical but systematically lower than those obtained in a 0.1 and 0.14m ID column. Similarly, many investigators have reported that the ε_G would level off when column diameters are ≥ 0.15 m^(23,31,61,101,104,105). More recently, to determine the effect of column diameter on the hydrodynamics, Eickenbusch et al.⁽¹⁰²⁾ compared 3 columns whose diameters were 0.19, 0.29 and 0.6 m with a height to diameter ratio of 10.2, 10.3 and 6.5, respectively. Using a viscous pseudoplastic polysaccharide solution, they found that churn turbulent flow regime was dominant and the column diameter had a minor effect on gas holdup. Moustiri et al.⁽¹⁰⁶⁾ measuring the gas holdup and liquid axial mixing in the continuous mode using two columns of 0.15 and 0.2 m ID, however, reported that at low superficial gas velocity, there was a pronounced effect of column diameter on the gas holdup. They conducted their experiments in the homogeneous flow regime and reported an increase of gas holdup with decreasing column diameter. They attributed this increase to the delay in gas bubble acceleration due to the prevailing wall effect. Moustiri et al.⁽¹⁰⁶⁾ also reported that the liquid axial mixing increased with column diameter due to the formation of large circulation cells. Koide et al.⁽¹⁰⁷⁾ measured the gas holdup and bubble sizes of air in water in a 5.5 m ID column and compared their data with those obtained in smaller columns (0.1 - 0.6 m ID) and

although they observed a small influence of the column diameters on the ϵ_G , they suggested that the difference was negligible ⁽¹⁰⁷⁾. They further reported, however, that the arithmetic mean bubble diameter measured in their column was higher than those calculated with correlations developed for smaller diameter columns, and attributed this behavior to the breakup and coalescence of gas bubbles along with gas dispersion which were affected by the design and geometry of their column ⁽¹⁰⁷⁾. In addition, they hinted that if larger gas bubbles were formed in larger columns, a relatively smaller total gas holdup would be expected. Thus, since most commercial SBCRs have inside diameters greater than 5 m ⁽⁶⁾, to conclude that the gas holdup will remain constant from a diameter of 0.15 to ≥ 5 m could be inaccurate. The careful approach would be to consider that the gas holdup continue to slightly decrease at column diameter > 0.15 m and slowly reach an asymptote depending on the operating variables, physicochemical properties of the gas-liquid system and the geometries of the column and gas sparger.

2.1.8 Effect of Gas Distributor on ϵ_G

Gas distributors are integral part of the design and scale-up of bubble columns and SBCRs. There are numerous types of gas distributor, which significantly differ in their size and number of orifices. Porous plates, perforated plates (sieve plate/sieve tray), multiple/single-orifice nozzle, bubble caps, perforated rings, annular shears, spider-type, injectors, and hollow fibers, among others account for the most commonly spargers employed in the bubble and slurry bubble column reactors ^(38,48,108,109,110). Figure 3 illustrates some of these gas distributors. The characteristics of a gas distributor include, among others, opening size, number of openings, sparger positioning, and nozzles position/orientation ⁽¹¹¹⁾. The porous plate usually consists of

micro size pores where the mean pore diameter could range from 1.7 to 100 μm ^(25,108). The perforated plate design, however, takes into account the number, the pitch and diameter of the holes. Each hole has the same diameter, which is usually in the mm range. Similarly, the diameter of the single orifice nozzle is also in the mm range and is often reported to maintain a heterogeneous flow regime in the bubble column for superficial gas velocity as low as 0.04 m/s ⁽²⁵⁾.

The initial bubble size and distribution at the orifice could be controlled by the sparger characteristics; nevertheless, Akita and Yoshida ⁽³¹⁾ reported that due to the balance between coalescence and breakup of gas bubbles, the initial bubble size created at the gas sparger would not describe the behavior of gas bubble size distribution in the entire bubble column. The effect of gas sparger on the gas holdup is considered complex ^(35,112), since its influence beyond the sparger zone is yet to be understood. Several investigators have reported that gas sparger had a minimal effect on the bubble sizes and gas holdup if the orifice diameters were $> 1\text{-}2$ mm ^(31,61,101). Jordan and Schumpe ⁽¹¹³⁾, however, took into account the effect of gas sparger on the gas holdup even though the orifice diameters of each of their 3 perforated plates were either equal or greater than 1 mm, and despite the fact that no considerable effect of the gas spargers on ε_G was observed ⁽¹¹³⁾. It should be mentioned that the quality of the gas holdup (small versus large) depends on the breakup and coalescence of the gas bubbles in the column. Porous plates, with relatively smaller pore diameters, have been found to generate smaller gas bubbles when compared to those by perforated plates ⁽⁶¹⁾. Also, single orifice nozzles, with diameters usually greater than 0.001- 0.002 m, generated large gas bubbles, even at very low superficial gas velocity ⁽³¹⁾ indicating a heterogeneous bubble size distribution ⁽¹¹⁴⁾. From these observations,

one can conclude the ε_G is inversely proportional to the orifice diameter, and when small gas bubbles are formed, the transition from homogeneous to heterogeneous flow regime is delayed, since the rate of bubble coalescence becomes smaller ⁽¹¹⁴⁾. An important effect of the gas distributors on ε_G was observed by Schügerl et al. ⁽¹¹⁵⁾ when they separately added 10 wt% sodium sulfate (Na_2SO_4) and 1% ethanol to water to obtain a non-coalescing system. The authors reported that under these conditions, the smallest gas holdup was measured with the perforated plate ($d_o = 5 \times 10^{-4}$ m), followed by the sintered plate ($d_o = 17.5 \times 10^{-6}$ m), the injector type ($d_o = 4 \times 10^{-3}$ m), and the ejector type ($d_o = 3 \times 10^{-3}$ m). It seems that the two jet-model spargers have systematically provided higher gas holdup values than those with the perforated and sintered plates, despite their larger orifice diameters. The reason for this behavior was attributed to the authors' unique mechanism of creating large gas-liquid interface by mixing the gas and the liquid prior to the injection into the column ⁽³⁵⁾. Furthermore, Schügerl et al. showed that in a coalescing system (i.e. H_2O) the effect of gas distributor on the ε_G values was not significant, confirming that in a non-coalescing system, the bubble size distribution is controlled by the gas distributor ^(112,115). Thus, if the gas/liquid system in a bubble column or SBCR is non-coalescing, one can expect that the bubble size distribution and subsequently the gas holdup would be strongly dependent on the gas distributor design.

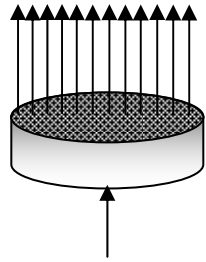
Typically, a minimum energy is required by the gas flow at the injection point in order to maintain solid suspension and mixing inside the columns ⁽⁵⁹⁾. The effect of hole number, hole size and orientation can be decisive if the concern is to lower the energy consumption ⁽¹¹¹⁾. Furthermore, due to a significant hydrostatic head pressure of the liquid over the gas sparger, important pressure drop will be expected which can consequently increase the power

consumption of the bubble and slurry bubble column reactors⁽⁹⁹⁾. An increase in gas flow rate increases the turbulences in the reactor; however, it can increase the pressure drop in the gas sparger. Using a porous or a multiple orifice nozzle, Vial et al.⁽²⁵⁾ reported that the bubble column could operate in the transition regime when the superficial gas velocity exceeds 0.04 m/s; and at 0.08 m/s only a heterogeneous regime could prevail if a wet porous plate is employed.

The presence of the liquid can considerably change the performance of some gas distributors. It has been reported that the pressure drop across perforated plates could indeed be influenced by the presence of liquid⁽¹¹⁶⁾ for which, the total pressure drop could be written as⁽⁹⁹⁾:

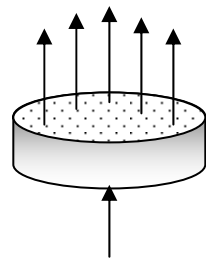
$$\Delta P_T = \Delta P_{\text{dry}} + \Delta P_{\text{residual}} + \Delta P_{\text{hydrostatic}} \quad (2-12)$$

Where ΔP_{dry} is the dry pressure drop, caused by a modified gas flow pattern due to absence of the liquid over the plate distributor. Similarly, ΔP_{wet} can be expressed as the sum of ΔP_{dry} , and $\Delta P_{\text{residual}}$, which is caused by the gas velocity at the orifice, plate geometry, and physical properties of the liquid. $\Delta P_{\text{hydrostatic}}$ is the pressure drop caused by the hydrostatic head pressure of the liquid⁽⁹⁹⁾. Thorat et al.⁽⁹⁹⁾ studied the wet and dry pressure drop caused by 32 different perforated plates with hole diameters ranging from 0.95 to 50 mm in two different bubble columns with $D_C \times H_C$ of 0.2x1.5 m, and 0.385x3 m. Their studies showed that there is a critical orifice Reynolds number where above this the ratio of $\Delta P_{\text{wet}}/\Delta P_{\text{dry}}$ increases with increasing orifice diameter, regardless of the clear liquid height. Thorat et al.⁽⁹⁹⁾ also reported that beyond this critical orifice Reynolds number the value of the wet pressure drop approached the one of the dry pressure drop and no more effect of the orifice diameter was found on the $\Delta P_{\text{wet}}/\Delta P_{\text{dry}}$ ratio.



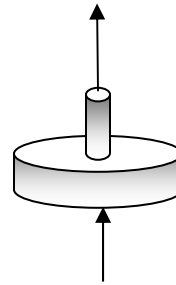
Gas Inlet

Porous plate



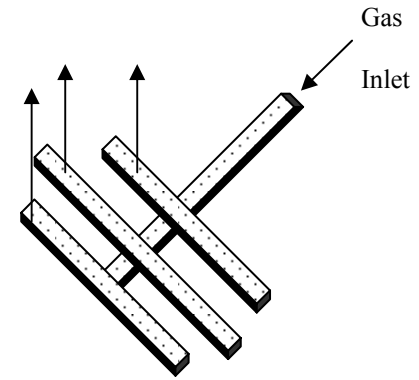
Gas Inlet

Perforated Plate

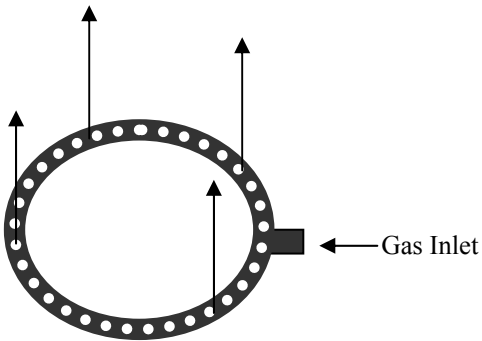


Gas Inlet

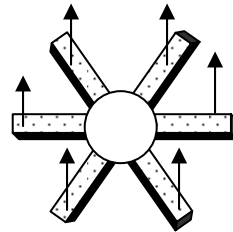
Single orifice nozzle



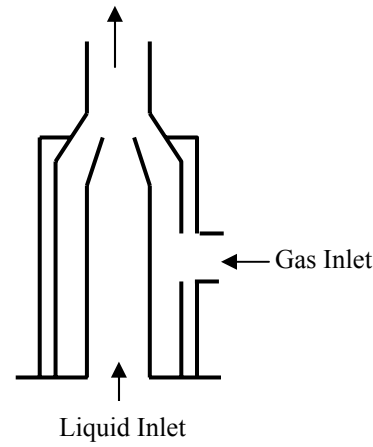
Multiple orifice nozzle



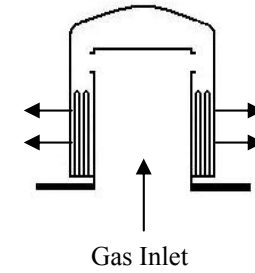
Perforated rings



Spider-type sparger



Injector type sparger



Bubble Cap

Figure 3 Different Types of Gas Distributors employed in Bubble and Slurry Bubble Column Reactors

For any given gas sparger size with a pre-determined number of openings or hole size, the gas initial force at the sparger orifice is related to the surface tension forces. This relationship is best described by Weber number (We), which is often used to design the gas sparger. According to Mersmann⁽¹¹⁷⁾ and Neubauer⁽¹¹⁸⁾, a $We > 2$ is necessary to assure bubble breakage and axial mixing in the liquid. The Weber number for gas is given as follow:

$$We = \frac{\rho_G U_{G,O}^2 d_o}{\sigma} = \frac{\rho_G U_G^2 D_C^4}{N_o^2 d_o^3 \sigma} \quad (2-13)$$

where N_o is the number of openings on the sparger.

Oyevaar et al.⁽³⁸⁾ reported that all studies using a porous plate always found a smaller effect of pressure on gas holdup when compared with perforated plates. Bouaifi et al.⁽¹¹¹⁾ found that an increase of the specific power consumption increased the bubble diameter when using a porous plate, and decreased the bubble diameter when using a perforated plate. Camarasa et al.⁽¹¹⁴⁾ used aqueous non-coalescing solutions and water to compare the effect of porous plate, multiple-orifice nozzle and perforated plate on the gas holdup. They found that bubble characteristics in water with porous plate and multiple-orifice nozzle were comparable, whereas the trend was different in non-coalescing solutions. The single-orifice nozzle, on the other hand, differed completely with the two other spargers. Contrary to the previous investigators, Pohorecki et al.⁽⁵¹⁾ found no significant effect of gas sparger on the gas holdup and Sauter-mean bubble diameter. They used several gas spargers of different geometry with a sparger diameter in the range of 22-108 mm, orifice diameter (1-5 mm), number of holes (1-27), with upward and downward positioning. Although Pohorecki et al.⁽⁵¹⁾ gave no further technical details of their spargers; it is believed that they used multiple orifice nozzles in their studies. Only superficial gas velocity was reported to have an effect on gas holdup and Sauter-mean bubble diameter,

however, the superficial gas velocity ranging from 0.002 to 0.02 m/s was responsible to maintain a homogeneous (bubbly) flow regime in the bubble column. Therefore, it can be assumed that at low superficial gas velocity (< 0.04 m/s) only a single orifice nozzle could provide a heterogeneous flow regime, while other spargers, i.e., perforated plates, porous plate and multiple orifice nozzles, would maintain a homogeneous flow regime and no effect of gas spargers would be observed.

2.1.9 Empirical Correlations for ϵ_G

Table 33 and 4 summarize some of the available correlations for predicting the gas holdup in bubble and slurry bubble column reactors, respectively. As can be seen in this table, a considerable number of these correlations were developed at ambient conditions and they do not take into account the effect of pressure nor the temperature. A number of correlations are only valid for air/aqueous solutions and do not consider the effect of gas/liquid nature. Consequently, the use of such correlations for predicting gas holdup in a typical industrial process can be risky.

2.2 DYNAMICS OF GAS BUBBLES

The bubble dynamics is controlled by the size and distribution of the gas bubbles present in the reactor. The bubble size controls the gas-liquid interfacial area and subsequently it influences the overall rate of reactions occurring in the reactor during commercial processes. The formation of gas bubble at the injection point is subject to the buoyancy forces due to the difference in density between the gas and liquid phases, and the surface tension forces that govern the stability of the gas bubble from the orifice and throughout the liquid/slurry phase. The behavior of the gas

Table 3 Correlations for gas holdup predictions in bubble column reactors

Authors	Gas/liquid	Conditions	Correlation
Akita and Yoshida ⁽³¹⁾	Air, O ₂ /H ₂ O, Glycol, Methanol	U _G : 0.003-0.4 m/s U _L : 0-0.044 m/s D _C : 0.152-0.6 m H _C : 1.26-3.5 m	$\frac{\varepsilon_G}{(1-\varepsilon_G)^4} = 0.2 \left(\frac{gD_C^2 \rho_L}{\sigma} \right)^{1/8} \left(\frac{gD_C^3}{\nu_L^2} \right)^{1/12} \left(\frac{U_G}{\sqrt{gD_C}} \right)$ (2-14)
Bach and Pilhofer ⁽³²⁾	Air/ Alcohol, Hydrocarbons	U _G : 0-0.2 m/s	$\frac{\varepsilon_G}{1-\varepsilon_G} = 0.115 \left(\frac{U_G^3}{\nu_L g (\rho_L - \rho_G) / \rho_L} \right)^{0.23}$ (2-15)
Chen and Leu ⁽¹¹⁹⁾	Air/H ₂ O/nickel Magnetized slurry bubble column	P _{atm} , U _G up to 0.04 m/s H up to 25000 A/m D _C x H _C : 0.05x0.5 m	$\varepsilon_G = 0.75 U_G^{0.78} \exp(8.12 \times 10^{-6} H)$ (2-16)
Hikita et al. ⁽³³⁾	Air, H ₂ , CO ₂ , CH ₄ , C ₃ H ₈ /H ₂ O, 30, 50wt% sucrose, methanol, n-butanol, aniline	P _{atm} , U _G : 0.042-0.38 m/s D _C : 0.1 m H _C : 1.5 m	$\varepsilon_G = 0.672 \left(\frac{U_G \mu_L}{\sigma} \right)^{0.578} \left(\frac{\mu_L^4 g}{\rho_L \sigma^3} \right)^{-0.131} \left(\frac{\rho_G}{\rho_L} \right)^{0.062} \left(\frac{\mu_G}{\mu_L} \right)^{0.107}$ (2-17)
Hughmark ⁽³⁴⁾	Air/H ₂ O, kerosene, oil	P _{atm} U _G : 0.004-0.45 m/s D _C >0.1m	$\varepsilon_G = \frac{1}{2 + \left(\frac{0.35}{U_G} \right) \left(\frac{\rho_L \sigma}{72} \right)^{1/3}}$ (2-18)
Idogawa et al. ⁽¹²⁰⁾	H ₂ , He, air/H ₂ O, CH ₃ OH, C ₂ H ₅ OH, acetone, aqueous alcohol solutions	P: 1-50 bar U _G : 0.005-0.05 m/s	$\frac{\varepsilon_G}{1-\varepsilon_G} = 0.059 U_G^{0.8} \rho_G^{0.17} \left(\frac{\sigma}{72} \right)^{-0.22 \exp(-P)} \quad \sigma \text{ [mN/m], } U_G \text{ [cm/s]}$ (2-19)
Jordan and Schumpe ⁽¹¹³⁾	N ₂ , He/Ethanol, 1-butanol, toluene, decalin	P: 1-40 bar U _G : 0.01-0.21 m/s D _C : 0.1 m H _C : 2.4 m	$\frac{\varepsilon_G}{1-\varepsilon_G} = b_1 Bo^{0.16} Ga^{0.04} Fr^{0.7} \left(1 + 27.0 Fr^{0.52} \left(\frac{\rho_G}{\rho_L} \right)^{0.58} \right)$ (2-20) Dimensionless numbers based on the bubble diameter b depends on the sparger: 19x1 mm PfP = 0.112, 1x1 mm PfP = 0.122, 1x4.3 mm PfP = 0.109, 3 mm S-ON = 0.135, 7x1 mm PfP = 0.153
Kang et al. ⁽⁴²⁾	Air/CMC	P: 1-6 bar U _G : 0.02-0.2 m/s μ _L : 1-38 mPa s D _C xH _C : 0.152x2 m	$\varepsilon_G = K \times 10^{-2.1} \left(\frac{D_C U_G \rho_G}{\mu_L} \right)^{0.201}$ (2-21) Where K is the correlation dimension

Table 3 (Continued)

Authors	Gas/liquid	Conditions	Correlation
Kojima et al. ⁽⁴⁰⁾	N ₂ , O ₂ /H ₂ O, Enzyme solutions (C _E)	P: 0.1-1.1 MPa U _G : 0.005-0.15 m/s C _E : 3-163 mg/dm ³ D _C : 0.055m H _C : 0.9-1.2 m	$\varepsilon_G = 1.18 U_G^{0.679} \left(\frac{\sigma}{\sigma_{H_2O, 20^\circ C}} \right)^{-0.546} \exp \left[A \left(\rho_L Q^2 d_o^{-3} \sigma^{-1} \right) (P/P_{atm})^B \right]$ (2-22)
Krishna and Ellenberger ⁽³⁶⁾	Air/H ₂ O, H ₂ O + Separan, Paraffin oil, Tetradecane	P atm. U _G : 0.001-0.866 m/s D _C : 0.1, 0.174, 0.19, 0.38, 0.63 m	A and B depend on C _E $\varepsilon_G = \varepsilon_{G-large} + \varepsilon_{df} (1 - \varepsilon_{G-large})$ (2-23)
			$\varepsilon_{df} = 0.59 \times (3.85)^{1.5} \sqrt{\frac{\rho_G^{0.96} \sigma_L^{0.12}}{\rho_L}}$ (2-24)
			$\varepsilon_{G-large} = 0.268 \times D_C^{-0.18} \frac{(U_G - U_{G-df})^{4/5}}{(U_G - U_{G-df})^{0.22}}$ (2-25)
			$U_{G-df} = U_{b-small} \varepsilon_{df} (1 - \varepsilon_{df}),$ (2-26)
			$U_{b-small} = \frac{\sigma_L^{0.12}}{2.84 \rho_G^{0.04}}$ (2-27)
Kumar et al. ⁽¹²¹⁾	Air/H ₂ O, glycerol, kerosene	P _{atm} , U _G : 0.0014-0.14 m/s	$\varepsilon_G = 0.728U - 0.485U^2 + 0.0975U^3$ (2-28)
			$U = U_G \left[\rho_L^2 / \sigma (\rho_L - \rho_G) g \right]^{1/4}$ (2-29)
Mersmann ⁽¹¹⁷⁾	Semitheoretical	(-)	$\frac{\varepsilon_G}{(1 - \varepsilon_G)^4} = 0.14 U_G \left[\frac{\rho_L^2}{\sigma (\rho_L - \rho_G) g} \right]^{1/4}$ (2-30)
Reilly et al. ⁽⁴⁸⁾	Air, N ₂ , He, Ar, CO ₂ /Isopar-G, Isopar-M, TCE, Varsol, H ₂ O	P: up to 11 bar U _G : 0.006-0.23 m/s D _C : 0.15 m H _C : 2.7 m	$\varepsilon_G = A \frac{\rho_G U_G}{\rho_L (1 - \varepsilon_G)}$ (2-31)
			$\varepsilon_G = B \left(\frac{\rho_G U_G}{\rho_L (1 - \varepsilon_G)} \right)^{1/3}$ (2-32)
			A and B depend on the liquid nature B = 3.8 (Isopar-G: ρ _L =740, μ _L =0.000861, σ _L =0.0235), 3.7 (Isopar-M: ρ _L =779, μ _L =0.002433, σ _L =0.0266), 3.6 (TCE: ρ _L =1462, μ _L =0.000572, σ _L =0.03), 4.6 (Varsol: ρ _L =773, μ _L =0.001012, σ _L =0.0283), 4 (H ₂ O: ρ _L =1000, μ _L =0.001, σ _L =0.0728)

Table 3 (Continued)

Authors	Gas/liquid	Conditions	Correlation
Sarrafi et al. ⁽¹⁵⁾	Air/H ₂ O	P _{atm} , U _G : 0-0.08 m/s Column base: 0.1 m width: 0.15 m height: 1.5 m	$\frac{U_G}{\varepsilon_G} - \frac{U_L}{1 - \varepsilon_G} = U_b F(\varepsilon_G) \quad (2-33)$
			Homogenous regime: $F(\varepsilon_G) = 0.71 - 9\varepsilon_G + 7.0 \left(\frac{U_G}{U_b} \right)^{3/4} \quad (2-34)$
			Heterogeneous regime: $F(\varepsilon_G) = 0.045 - 7.5\varepsilon_G + 5.5 \left(\frac{U_G}{U_b} \right)^{1/2} \quad (2-35)$
Sotelo et al. ⁽¹²²⁾	Air, CO ₂ /H ₂ O, C ₂ H ₅ OH, saccharose, glycerin	P _{atm} , U _G : 0-0.2 m/s d _{S.N.} = diameter of a single nozzle	$\varepsilon_G = 129 \left(\frac{U_G \mu_L}{\sigma} \right)^{0.99} \left(\frac{\mu_L g}{\rho_L \sigma^3} \right)^{-0.123} \left(\frac{\rho_G}{\rho_L} \right)^{0.187} \left(\frac{\mu_G}{\mu_L} \right)^{0.343} \left(\frac{d_{S.N.}}{D_C} \right)^{-0.089} \quad (2-36)$
Urseanu et al. ⁽¹⁰³⁾	N ₂ /Tellus oil, Glucose solutions	P: 1-10 bar U _G : up to 0.3 m/s D _C : 0.15, 0.23 m H _C : 1.22 m	$\varepsilon_G = 0.21 U_G^{0.58} \mu_L^{-0.12} \rho_G^{[0.3 \exp(-9\mu_L)]} \quad (2-37)$
Authors	System: gas/liquid/solid	Conditions	Correlation
Wilkinson et al. ⁽⁶¹⁾	N ₂ /n-heptane, mono- ethylene glycol, H ₂ O	P: 1-20 bar U _G : up to 0.2 m/s D _C : 0.158 m H _L : 1.5 m	$\varepsilon_G = \frac{U_{trans}}{U_{b-small}} + \frac{U_G - U_{trans}}{U_{b-large}} \quad (2-38)$
			$U_{b-small} = 2.25 \frac{\sigma_L}{\mu_L} \left(\frac{\sigma_L^3 \rho_L}{\mu_L^4 g} \right)^{-0.273} \left(\frac{\rho_L}{\rho_G} \right)^{0.03} \quad (2-39)$
			$U_{trans} = 0.5 \times U_{b-small} \exp(-193 \rho_G^{-0.61} \mu_L^{0.5} \sigma_L^{0.11}) \quad (2-40)$
			$U_{b-large} = U_{b-small} + 2.4 \frac{\sigma_L}{\mu_L} \left(\frac{\mu_L (U_G - U_{trans})}{\sigma_L} \right)^{0.757} \left(\frac{\sigma_L^3 \rho_L}{g \mu_L^4} \right)^{-0.077} \quad (2-41)$
Zou et al. ⁽⁸⁷⁾	Air/H ₂ O, Alcohol, 5% NaCl	P _{atm} , U _G : 0.01-0.16 m/s U _L : 0.007 m/s T: 25-96.56 °C D _C xH _C : 0.1x1.05 m	$\varepsilon_G = 0.17283 \left(\frac{\mu_L^4 g}{\rho_L \sigma^3} \right)^{-0.1544} \left(\frac{P + P_S}{P} \right)^{1.6105} \left(\frac{U_G \mu_L}{\sigma} \right)^{0.5897} \quad (2-42)$

Table 4 Correlations for gas holdup predictions in slurry bubble column reactors

Authors	Gas/liquid/solid	Conditions	Correlation
Fan et al. ⁽²⁸⁾	N ₂ /Paratherm NF/alumina	P: 1-56.2 bar	$\frac{\varepsilon_G}{1 - \varepsilon_G} = \frac{2.9(U_G^4 \rho_G / \sigma g)^\alpha (\rho_G / \rho_{SL})^\beta}{[\cosh(Mo_{SL}^{0.054})]^{4.1}}$ (2-43)
		U _G up to 0.45m/s	(2-44)
		C _V : 8.1, 19.1 vol.%	$Mo_{SL} = g(\rho_{SL} - \rho_G)(\xi \mu_L)^4 / \rho_{SL}^2 \sigma^3$ (2-45)
		T: 28 and 78 °C	$\alpha = 0.21 Mo_{SL}^{0.0079} \text{ and } \beta = 0.096 Mo_{SL}^{-0.011}$ (2-46)
		D _C : 0.102 m H _C : 1.37 m	$\ln \xi = 4.6 C_V \left\{ 5.7 C_V^{0.58} \sinh[-0.71 \exp(-5.8 C_V) \ln Mo^{0.22}] + 1 \right\}$
Kara et al. ⁽⁶⁷⁾	Air/H ₂ O/Coal, dried mineral ash	P _{atm}	$\varepsilon_G = \frac{Re_G}{A + B Re_G + C Re_{SL} + D \left(\frac{\varepsilon_S}{\varepsilon_S + \varepsilon_L} \right)}$ (2-47)
		U _G : 0.03-0.3 m/s U _{SL} : 0-0.1 m/s C _W : 0-40 wt.% D _C xH _C : N/A	A, B, C, and D depend on particle sizes
Koide et al. ⁽⁶⁸⁾	N ₂ /H ₂ O, glycerol, glycol, barium chloride, sodium sulphate/Glass and bronze	P _{atm}	$\frac{\varepsilon_G}{(1 - \varepsilon_G)^4} = \frac{A(U_G \mu_L / \sigma)^{0.918} (g \mu_L^4 / \rho_L \sigma^3)^{-0.252}}{1 + 4.35 \left(\frac{C_S}{\rho_P} \right)^{0.748} \left(\frac{\rho_P - \rho_L}{\rho_L} \right)^{0.881} \left(\frac{D_C U_G \rho_L}{\mu_L} \right)^{-0.168}}$ (2-48)
		U _G : 0.03-0.15 m/s C _S : 0-200 kg/m ³ D _C : 0.1-0.3 m H _C : 2.3-3 m	A = 0.227 H ₂ O, Glycerol, Glycol A = 0.364 Aqueous solution of inorganic electrolytes
Krishna and Sie ⁽⁶⁾	Air/Paraffin oil, Tellus oil/Silica	P atm.	$\varepsilon_G = \varepsilon_{G-large} + \varepsilon_{df} (1 - \varepsilon_{G-large})$ (2-49)
		U _G : up to 0.5 m/s	$\varepsilon_{G-large} = \frac{U_G - U_{G-df}}{U_{b-large}}$ (2-50)
		C _V : 0-36 vol.%	$U_{b-large} = 0.71 \sqrt{g d_b} (SF) (AF) (DF)$ (2-51)
		D _C : 0.1, 0.19, 0.38, 0.63 m	SF=1 for d _b /D _C < 0.125 (2-52) SF=1.13 exp(-d _b /D _C) for 0.125 < d _b /D _C < 0.6 SF=0.496(D _C /d _b) ^{0.5} for d _b /D _C > 0.6
			$AF = \alpha + \beta (U_G - U_{G-df})$ (2-53)
		$DF = \sqrt{1.29 / \rho_G}$ (2-54)	
		$d_b = \gamma (U_G - U_{G-df})^\delta$ (2-55)	

Table 4 (Continued)

Authors	Gas/liquid/solid	Conditions	Correlation
			for Tellus oil ($\rho_L = 862$, $\mu_L = 0.075$, $\sigma_L = 0.028$) $\alpha = 2.25$, $\beta = 4.09$, $\gamma = 0.069$, $\delta = 0.376$
			$U_{G-df} = U_{b-small} \varepsilon_{df}$ (2-56)
			$\varepsilon_{df} = \varepsilon_{df,0} \left(\frac{\rho_G}{\rho_{G,ref}} \right)^{0.48} \left(1 - \frac{0.7}{\varepsilon_{df,0}} C_V \right)$ (2-57)
Reilly et al. (123)	Air/H ₂ O, Solvent, TCE/ Glass beads	P atm. U _G : 0.02-0.2 m/s C _V : up to 10 vol.% H _C xD _C : 5x0.3 m	$\varepsilon_{df,0} = 0.27$ for paraffin oil ($\rho_L = 790$, $\mu_L = 0.029$, $\sigma_L = 0.028$) $\varepsilon_G = 296 U_G^{0.44} \rho_L^{-0.98} \sigma_L^{-0.16} \rho_G^{0.19} + 0.009$ (2-58)
Sauer and Hempel (124)	Air/H ₂ O/10 diff. Solids (1020 < ρ_p < 2780 kg/m ³)	P _{atm} , U _G : 0.01-0.08 m/s C _V : 0-20 vol.%	$\frac{\varepsilon_G}{1 - \varepsilon_G} = 0.0277 \left(\frac{U_G}{(U_G g v_{sl})^{0.25}} \right)^{0.844} \left(\frac{v_{sl}}{v_{eff,rad}} \right)^{-0.136} \left(\frac{C_s}{C_{S0}} \right)^{0.0392}$ (2-59)
			where C_{S0} is solid concentration at bottom of column, kg/m ³ $v_{sl} = \mu_L \left[1 + 2.5 C_V + 10.05 C_V^2 + 0.00273 \exp(16.6 C_V) \right] / \rho_{SL}$ (2-60)
			$v_{eff,rad} = 0.011 D_C \sqrt{g D_C} \left(\frac{U_G^3}{g v_L} \right)^{1/8}$ (2-61)
Schumpe et al. (64)	N ₂ , O ₂ /H ₂ O, 0.8M Na ₂ SO ₄ /Carbon, Kieselguhr, Aluminum oxide	P _{atm} , U _G : up to 0.07 m/s C _S : up to 300 kg/m ³ D _C : 0.095 m H _C : 0.85 m	$\varepsilon_G = F U_G^{0.87} \mu_{eff}^{-0.18}$ (2-62)
			F=0.81 (H ₂ O/salt solution) F=0.43 (H ₂ O, 0.8M Na ₂ SO ₄) $\mu_{eff} = k(2800 U_G)$ (2-63)
			where k is the fluid consistency index (Pa s ⁿ) k=1.97, n=0.951 and B = 0.81 or 0.43

bubbles depends, among others, on the hydrodynamic flow regime. If a bubbly flow regime governs in the reactor, the bubbles will be narrowly distributed and low bubble-bubble interactions could be expected. In fact a uniform bubble size distribution is generally characteristics of the homogeneous bubbly flow regime ⁽⁵¹⁾. As the superficial gas velocity is increased, the high frequency of gas bubble interactions leads to coalescence and breakup and the reactor is found to be operating in the churn turbulent flow regime, and a distinguishable bimodal bubble size distribution can be observed ⁽¹²⁵⁾. Consequently, bubbles in this regime can be arbitrary classified into “small”, and “large”. These bubbles appear to behave differently as the large gas bubbles rise rapidly in the reactor in a plug flow mode and create backmixing, and the small gas bubbles are entrained and re-circulate with the liquid/slurry ^(36,126,127). In the churn-turbulent flow regime, bubble breakup and coalescence can occur at any moment after the formation of the gas bubble at the orifice ⁽³⁵⁾, thus the bubble size distribution will depend on the balance between coalescence and breakup ⁽¹²⁸⁾.

2.2.1 Gas Bubble Formation

The initial bubble size at its formation (d_b^*) can be estimated using the theoretical Davidson and Schuler ⁽¹²⁹⁾ expression by:

$$d_b^* = \left[\frac{6d_o\sigma_L}{g(\rho_L - \rho_G)} \right]^{1/3} \quad (2-64)$$

This model is based on the assumption that bubble formation happens in two stages: in the first stage the expansion of the gas bubbles is assumed to be spherical and in the second stage the buoyancy forces acting on the gas bubble first pull the bubble away from the orifice before it completely detaches from the orifice ^(129,130). Other models, however, take into account the

contributions of local forces during the first stage and describe a non-spherical shape formation of the gas bubble at the orifice ^(131,132,133). According to Heijnen and Van't Riet ⁽¹¹²⁾ bubble formation at the sparger (d_b^*) can be classified into 3 regimes: separated bubbles, chain bubbling and jet regime, as illustrated in Figure 4. They reported that the height of the sparging zone depends on the difference between d_b^* and the equilibrium bubble size in the reactor after coalescence or breakup. In addition, they suggested that the reactor's optimum performance was achieved if the operation was carried in the chain bubbling regime ⁽¹¹²⁾. The initial bubble formation at the orifice, however, is subject to many different factors, especially the presence of liquid height over the distributor as explained in Section 2.1.8. The effect of pressure on the bubble formation has also been investigated and indicated that an increase of pressure increases the gas density which is responsible for forming smaller initial bubble size at the orifice ⁽⁴⁷⁾. This influence can be neglected, however, if the superficial gas velocity is low enough so it yields a Weber number for gas, in Equation (2-13) of 0.1 or less ⁽¹³³⁾. Furthermore, in the SBCRs, the presence of solid can greatly affect the formation of gas bubbles at the orifice. It has been reported that increasing solid concentration increases the initial bubble size at the orifice, and similarly bubbles are larger in a slurry system than in a liquid phase ⁽¹³⁴⁾. Fan et al. ⁽²⁸⁾ showed that the bubble formation at the orifice in the SBCRs occurred in two stages: the formation stage and detachment stage, where the interacting solid particles are often found in the liquid film that is formed around the gas bubbles during these stages. Fan et al. ⁽²⁸⁾ showed that the balance of all forces acting on the bubbles could be represented as the following:

$$\begin{aligned}
 (F_B)_{\text{Buoyancy}} + (F_M)_{\text{Gas momentum}} = (F_C)_{\text{Particle-bubble collision}} + (F_D)_{\text{Liquid drag}} + \\
 (F_{SI})_{\text{Suspension Inertia}} + (F_{\sigma L})_{\text{Surface tension}} + (F_{IB})_{\text{Bubble inertia}} + (F)_{\text{Basset}}
 \end{aligned}
 \tag{2-65}$$

Figure 5 shows the balance and expressions of all forces acting on the gas bubble during the expansion and detachment stages in SBCRs according to Fan et al.⁽²⁸⁾.

2.2.2 Gas Bubble Coalescence

Coalescence occurs when two gas bubbles first collide and trap a certain amount of liquid between them, which once drained may reduce the film thickness of the bubble to a critical value causing it to rupture and the gas bubbles to coalesce^(85,128,135). Prince and Blanch⁽¹²⁸⁾ identified three different forces responsible for bubble collisions: 1) turbulence from the random motion of gas bubbles, 2) buoyancy from the difference in the rise velocity of the gas bubbles, and, 3) laminar shear, which occurs when the gas bubbles in the central line liquid circulation interact with those in a relatively lower circulation zones. The knowledge of the collision efficiency hence, becomes important in order to assess which force (i.e., turbulence, buoyancy, and laminar shear) is the most determinant for the coalescence of the gas bubbles⁽¹²⁸⁾. The final rate of coalescence of a gas bubble of a certain diameter can therefore be expressed by the product of the total collision frequency and efficiency⁽¹²⁸⁾.

It should be noted, however, that coalescence will only happen if enough time is given for the trapped liquid to thin the film thickness of the gas bubbles, since the time it takes to rupture the film is generally faster^(85,128). Marrucci⁽¹³⁵⁾ reported that the thinning of the gas bubble film happens in two stages, where during the first stage the liquid film is thinned to a “quasi-equilibrium” thickness, and in the second stage the film is further reduced to its critical value before rupture⁽¹³⁵⁾. Marrucci also showed that the second stage determines the actual time for the coalescence as it is always slower than the first stage⁽¹³⁵⁾. The effect of operating variables and physical properties of the liquid also plays an important part in the mechanism of

the film thinning⁽¹³⁶⁾. Lin et al.⁽⁸⁵⁾ used the Sagert and Quinn expression for the rate of the liquid disk thinning⁽¹³⁶⁾, and showed that the rate of the film thinning significantly decreased with pressure until 150 bar, due to an increase of liquid viscosity and a decrease in surface tension, whereas it increased with temperature until 351 K mainly due to a decrease of liquid viscosity⁽⁸⁵⁾.

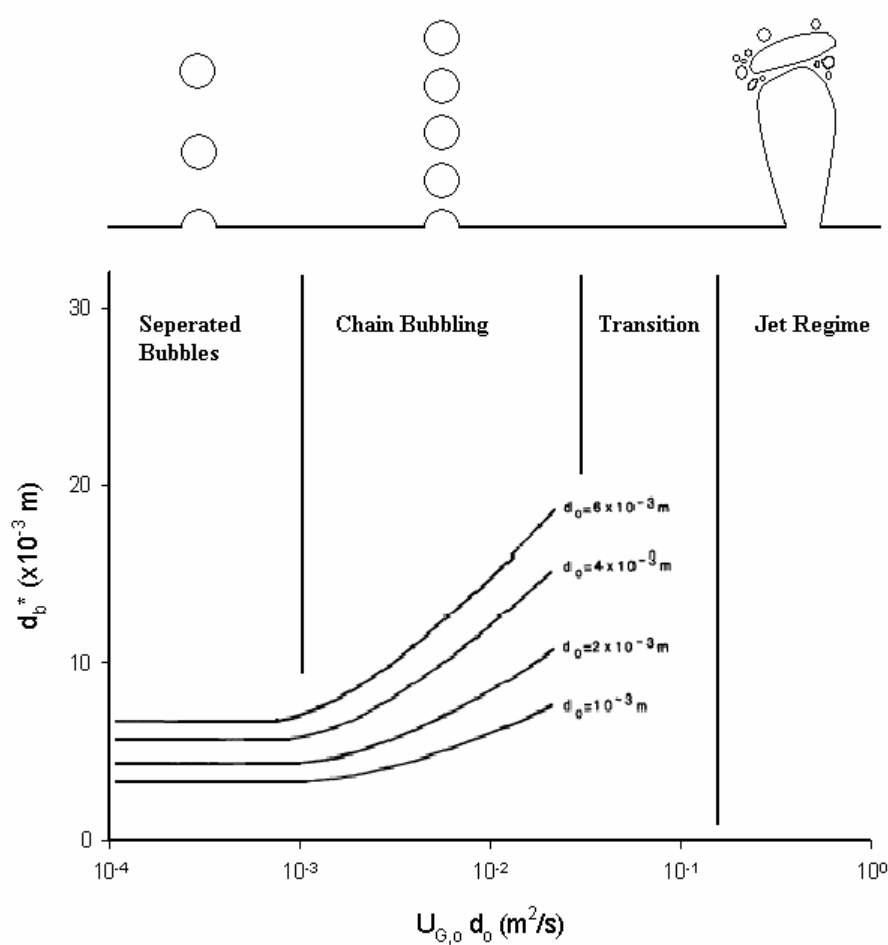


Figure 4 Air Bubble Formations at the Orifice in Water Based on the Experiments of Heijnen and Van't Riet⁽¹¹²⁾

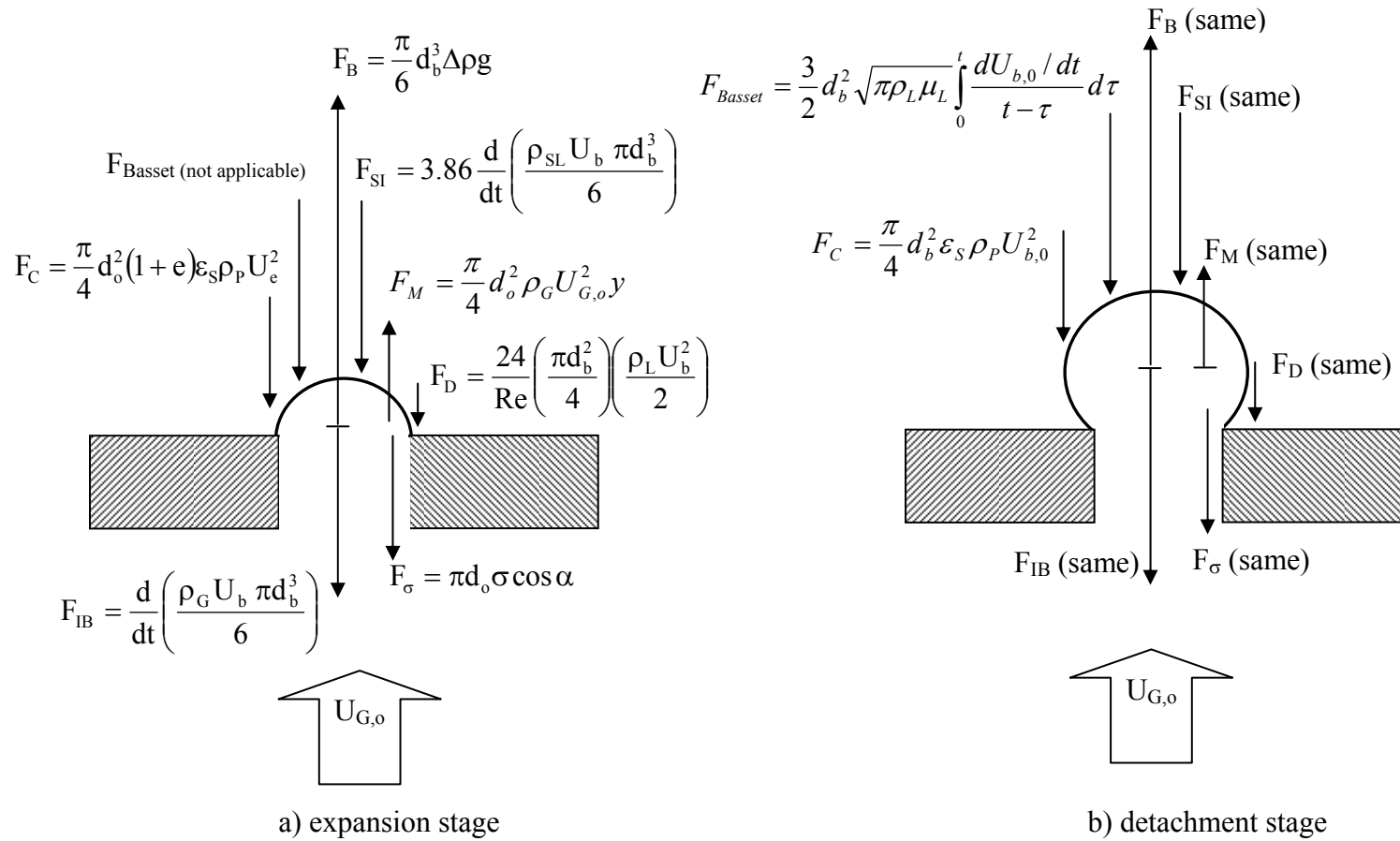


Figure 5 Balance and Expression of all Forces acting on the Gas Bubble at its Formation in SBCRs ⁽²⁸⁾

2.2.3 Gas Bubble Breakup

The knowledge of the stability of the bubble size in the reactor can be used to explain the mechanism of the gas bubble breakup⁽⁸⁵⁾. Most investigators who studied the behavior of the gas bubbles in the turbulent flows either used the Rayleigh-Taylor instability^(47,137,138) or the theory of the isotropic turbulence^(85,128,139,140,141) to estimate the maximum stable bubble size before breakup.

The Rayleigh-Taylor instability is basically the balance of the surface tension and gravity forces acting on a gas bubble. If the latter is greater than the former, the bubble will eventually breakup. According to Bellman and Pennington⁽¹³⁸⁾, if the diameter of a certain spherical cap bubble exceeds a critical wavelength, it would breakup. This in term can be referred to as the maximum stable bubble size and is generally expressed as:

$$\lambda_C = d_{b,\max} = 2\pi \sqrt{\frac{\sigma_L}{g(\rho_L - \rho_G)}} \quad (2-66)$$

Wilkinson and van Dierendonck⁽⁴⁷⁾ photographically monitored the breakup of large gas bubbles in the swarm due to the growth of disturbances on the top of the gas bubbles caused by the Rayleigh-Taylor instability. The difference between the experiments of Wilkinson and van Dierendonck⁽⁴⁷⁾ and those of Bellman and Pennington⁽¹³⁸⁾ lies in the fact that the disturbances on the gas bubbles in the swarm are not exactly those acting on a spherical cap bubble, because of the relative velocity between the gas and liquid phases. Similarly, to determine the maximum stable bubble size before breakup, Wilkinson and van Dierendonck⁽⁴⁷⁾ incorporated the Kelvin-Helmholz stability analysis into the Rayleigh-Taylor instability theory and obtained the following expression:

$$\lambda_c = d_{b,\max} = \frac{2\pi \sqrt{\frac{\sigma_L}{g(\rho_L - \rho_G)}}}{\frac{\rho_L}{\rho_L - \rho_G} \frac{\rho_G U_r^2 / 2}{\sqrt{\sigma_L g(\rho_L - \rho_G)}} + \left(1 + \frac{(\rho_L \rho_G U_r^2 / 2)^2}{(\rho_L + \rho_G)^2 \sigma_L g(\rho_L - \rho_G)}\right)^{0.5}} \quad (2-67)$$

Where U_r is the relative velocity between the gas and the liquid phase at the interface. The use of Equation (2-67) is challenging since the estimation of the relative velocity, U_r , can be difficult. Wilkinson and van Dierendonck ⁽⁴⁷⁾ suggested that if the velocity on the liquid side was equal to the slip velocity of the large gas bubbles, then the value of the relative velocity U_r in Equation (2-67) could be assumed to be in the range of 1-2 m/s. This assumption seemed to yield results that were in good agreement with their experimental observations ⁽⁴⁷⁾.

The other mechanism for bubble breakup considers a homogeneous isotropic turbulence, where the velocity fluctuations caused by the turbulent eddies exert different dynamic pressures on the gas bubbles, causing them to deform and eventually rupture ⁽¹⁴⁰⁾. This mechanism would work provided that the size of the eddies is smaller than those of the gas bubbles, since larger eddies tend to entrain the gas bubbles in the turbulent stream ^(128,141). Hinze showed that the forces acting on the gas bubbles could be represented by the Weber number for liquid, and consequently bubble breakup will occur when the Weber number exceeds a critical value defined as follow ⁽¹⁴¹⁾:

$$We_c = \frac{\rho_L \bar{U}_{rms}^2 d_{b,\max}}{\sigma_L} \quad (2-68)$$

Where \bar{U}_{rms}^2 is the average value of square of difference in turbulence velocity, which is a function of the specific power input, p and expressed as follow ⁽¹⁴¹⁾:

$$\bar{U}_{rms}^2 = 3 \sqrt{\left(\frac{p d_{b,max}}{\rho_L} \right)^2} \quad (2-69)$$

and p for bubble column reactors is defined as:

$$p = \frac{Q\Delta P_{Total}}{V_L} = \frac{Q(\rho_L gH + \Delta P_{sparger})}{V_L} = \frac{U_G}{H} (\rho_L gH + \Delta P_{sparger}) \cong \rho_L g U_G \quad (2-70)$$

Hinze experimentally determined the value of the We_C in Equation (2-68) and proposed the following expression for the maximum stable bubble size⁽¹⁴¹⁾:

$$d_{b,max} = 0.725 \frac{\sigma_L^{3/5}}{\rho_L^{1/5} p^{2/5}} \quad (2-71)$$

Both Levich⁽¹⁴⁰⁾ and Walter and Blanch⁽¹³⁹⁾ used this theory to study bubble breakup in turbulent flows. Levich emphasized on the effect of the liquid and gas density⁽¹⁴⁰⁾, whereas Walter and Blanch used the ratio of phase viscosities in their investigations⁽¹³⁹⁾. More recently, Lin et al.⁽⁸⁵⁾ experimentally measured the maximum stable bubble size at high pressure and temperature and proposed a combination of Levich⁽¹⁴⁰⁾ and Walter and Blanch⁽¹³⁹⁾ models to correlate their data as follow:

$$d_{b,max} = We_C^{3/5} \frac{\sigma_L^{3/5}}{\rho_G^{1/5} p^{2/5}} \left(\frac{\mu_L}{\mu_G} \right)^{0.1} \quad (2-72)$$

Where We_C , the critical Weber number accounts for the interaction between the surface tension and inertial forces, and is experimentally determined to be 0.7 and 1.36 at 351 and 300 K respectively⁽⁸⁵⁾. Lin et al. found that the maximum stable bubble size decreased with increasing temperature and pressure due to the decrease of surface tension⁽⁸⁵⁾. A general observation made by Lin et al.⁽⁸⁵⁾ was that the model proposed by Walter and Blanch⁽¹³⁹⁾ underestimated the effect

of pressure and therefore by incorporating the gas density in Equation (2-72), as proposed by Levich ⁽¹⁴⁰⁾, a better fit for the experimental data at high pressure could be obtained ⁽⁸⁵⁾.

In general the Rayleigh-Taylor and the isotropic turbulence theories seem to describe the mechanism of bubble breakup fairly well, but fail to take into account the internal circulation of the gas bubble. In fact when the gas bubble is rising through the liquid, it becomes subject to the drag forces exerted by the liquid around the gas bubble surface, which tend to create a dynamic or centrifugal force within the gas bubbles pointing outward ^(43,140). Consequently, the gas bubble breaks up when the centrifugal force exceeds the surface tension force. In his analysis, Levich assumed a complete entrainment of the gas at the interface by considering a relatively low gas density as compared to the liquid phase, and consequently proposed the following expression for the maximum bubble size when the internal circulation of the gas was hypothesized:

$$d_{b,\max} \approx 1.817 \frac{2\sigma_L}{U_b^2 \sqrt[3]{\rho_G \rho_L^2}} \quad (2-73)$$

where U_b is the rise velocity of the gas bubble.

Luo et al. ⁽⁴³⁾, on the other hand, considered the case where the gas density was relatively high and observed a poor prediction of their experimental data using Equation (2-73). Consequently, by considering the aspect ratio of a spherical cap bubble in both the liquid and slurry phase, Luo et al. proposed the following expression for the maximum stable bubble size ⁽⁴³⁾:

$$d_{b,\max} \approx k \sqrt{\frac{\sigma_L}{g\rho_G}} \quad (2-74)$$

where k was found to be 2.53 and 3.27 in liquid and slurry phase respectively ⁽⁴³⁾.

2.2.4 Gas Bubble Rise Velocity

Since the velocity of a given phase in the bubble column usually differs from the other phases, the volumetric flow rate fraction of that phase is not equal to its corresponding holdup, and hence the slip velocity, U_s , is introduced to account for this difference as follow:

$$U_s = \frac{U_G}{\varepsilon_G} - \frac{U_{SL}}{1 - \varepsilon_G} \quad (2-75)$$

If the operations run in the semi-batch mode and the linear superficial slurry velocity is zero, Equation (2-75) would become the mean bubble rise velocity in the swarm⁽²³⁾. In general, the bubble rise velocity determines the gas-liquid/slurry contact time in the reactor and is often expressed in terms of the terminal rise velocity of a single bubble in infinite medium, $U_{b,\infty}$ ⁽¹³⁾. The knowledge of the terminal rise velocity is important since, in conjunction with the interaction of neighboring bubbles, it can provide a better assessment of the slip velocity in the column as follow⁽¹⁴²⁾:

$$U_s = U_{b,\infty} F(\varepsilon_G) \quad (2-76)$$

Where $F(\varepsilon_G)$ represents the effect of the interaction of the neighboring gas bubbles. Due to different degree of interactions that exist in each class of bubbles, it becomes important to understand the mechanism of the terminal rise velocity in separate bubble size distribution. If the bubbles are small, the effect of surface tension tend to keep these bubbles in perfect spherical shape, thus Stokes Law could be applied:

$$U_{b,\infty} = \frac{d_b^2 g (\rho_L - \rho_G)}{18 \mu_L} \quad (2-77)$$

If the velocity gradients within the gas bubbles are considered while neglecting the gas density and viscosity, Stokes Law could be modified as follow ⁽¹⁴⁰⁾:

$$U_{b,\infty} = \frac{d_b^2 g \rho_L}{12 \mu_L} \quad (2-78)$$

Equation (2-78) is only valid when the Reynolds number for gas bubble is $\ll 1$ ⁽¹⁴⁰⁾.

For intermediate size bubbles, the effects of the physical properties, along with liquid inertial forces still remain important ⁽¹³⁾. Typically, if the Reynolds number for gas bubble is greater than 1 and less than 1600-2000, the Stokes Law in Equation (2-77) could still be applied ⁽¹⁴⁰⁾. If the bubbles are large, the effect of surface tension and viscosity becomes less significant and commonly the expression for the rise velocity can be expressed by the Davies-Taylor equation ^(13,143):

$$U_{b,\infty} = \frac{2}{3} \sqrt{g R_C} \quad (2-79)$$

where R_C is the radius of the curvature of the spherical cap bubble with a flat base. Equation (2-79) is only valid for Eötvös number (Eo) greater than 40 ^(143,144).

Most investigators who have studied the bubble rise in the bubble and slurry bubble columns, have based their results on the terminal rise velocity of the bubbles ^(145,146,147,148,149).

Table 5 presents some of the available models for the prediction of the bubble terminal rise velocity. Figure 6 illustrates the terminal rise velocity as a function of the bubble diameter obtained using the correlations in Table 5. This approach, however, does not take into consideration the liquid circulation created by the rise of gas bubbles in the swarm. When the bubble rise is measured in the swarm, the effect of the operating conditions and the physical properties of the gas-liquid-solid systems become important and hence the evaluation of U_b for

either small or large gas bubbles will become a function of all these variables. Table 6 lists some of the correlations in the literature for the prediction of the rise velocity of gas bubbles in the swarm.

Table 5 Correlation for the terminal rise velocity of a single bubble

<i>Authors</i>	<i>Correlation</i>	
Jamialahmadi et al. ⁽¹⁵⁰⁾	$U_b = \frac{U_{b,sph} U_{b,wav}}{\sqrt{(U_{b,sph})^2 + (U_{b,wav})^2}}$	(2-80)
	$U_{b,sph} = \frac{gd_b^2(\rho_L - \rho_G)}{18\mu_L} \left(\frac{3\mu_L + 3\mu_G}{2\mu_L + 3\mu_G} \right)$	(2-81)
	$U_{b,wav} = \sqrt{\frac{2\sigma}{d_b(\rho_L + \rho_G)} + \frac{gd_b}{2}}$	(2-82)
Fukuma et al. ⁽¹⁵¹⁾	$U_b = 1.3\sqrt{gd_b}$	(2-83)
de Swart and Krishna ⁽⁷⁰⁾	$U_b = 1.95D_C^{1/6}\sqrt{gd_b} \quad \text{for } d_b \geq 0.005 \text{ m}$	(2-84)
Fan and Tsuchiya ⁽¹⁵²⁾	$U_b \left(\frac{\rho_L}{\sigma_L g} \right)^{1/4} = \left\{ \left[\frac{Mo^{-1/4} \left(\frac{\rho_L - \rho_G}{\rho_L} \right)^{5/4}}{K_b} d_b^2 \frac{g\rho_L}{\sigma_L} \right]^{-n} + \left[\frac{2c \left(\frac{g\rho_L}{\sigma_L} \right)^{-1/2}}{d_b} + \frac{(\rho_L - \rho_G)d_b \left(\frac{g\rho_L}{\sigma_L} \right)^{1/2}}{2\rho_L} \right]^{-n/2} \right\}^{-1/n}$	(2-85)
	n= 0.8 (contaminated liq.), 1.6 (purified liq.) c=1.2 (monocomponent liq.), 1.4 (multicomponent liq.) K _b = max (K _{b,0} Mo ^{-0.038} , 12) K _{b,0} = 14.7 (aqueous sol.), 10.2 (organic solvent/mixture)	
Maneri ⁽¹⁵³⁾	$U_b = \sqrt{\frac{gd_b(\rho_L - \rho_G)}{2\rho_L} + \frac{2c\sigma_L}{d_b\rho_L}}$	(2-86)
	Where c depends on the liquid nature and was determined by linear regression from the Authors' work to be:	
	$c = 0.449 \frac{\rho_L^{0.128}}{\mu_L^{0.019} \sigma_L^{0.083}}$	(2-87)
	1301 ≤ ρ _L (kg/m ³) ≤ 2927 4.23 ≤ μ _L (Pa s x10 ⁴) ≤ 83.6 0.024 ≤ σ _L (N/m) ≤ 0.049	
Tomiyama et al. ⁽¹⁵⁴⁾	$C_D = \frac{4}{3} \frac{g(\rho_L - \rho_G)}{\rho_L} \frac{d_b}{U_b^2}$	(2-88)

Table 5 (Continued)

<i>Authors</i>	<i>Correlation</i>
	For purified system:
	$C_D = \max \left\{ \min \left[\frac{16}{\text{Re}} \left(1 + 0.15 \text{Re}^{0.687} \right), \frac{48}{\text{Re}} \right], \frac{8}{3} \frac{Eo}{Eo + 4} \right\} \quad (2-89)$
	For partially contaminated system:
	$C_D = \max \left\{ \min \left[\frac{24}{\text{Re}} \left(1 + 0.15 \text{Re}^{0.687} \right), \frac{72}{\text{Re}} \right], \frac{8}{3} \frac{Eo}{Eo + 4} \right\} \quad (2-90)$
	For sufficiently contaminated system:
	$C_D = \max \left[\frac{24}{\text{Re}} \left(1 + 0.15 \text{Re}^{0.687} \right), \frac{8}{3} \frac{Eo}{Eo + 4} \right] \quad (2-91)$
	Re is the Reynolds number for gas bubble, and Eo is the Eötvös number.
Krishna et al. ⁽¹⁵⁵⁾	$U_b = 0.71 \sqrt{gd_b} (SF) \quad \text{for } Eo > 40 \quad (2-92)$
	SF=1 for $d_b/D_C < 0.125$
	SF=1.13 exp(- d_b/D_C) for $0.125 < d_b/D_C < 0.6$
	SF=0.496(D_C/d_b) ^{0.5} for $d_b/D_C > 0.6$
Clift et al. ⁽¹⁴⁶⁾	$U_b = \frac{\mu_L}{\rho_L d_b} M^{-0.149} (J - 0.857) \quad (2-93)$
	$M = \frac{g \mu_L^4 (\rho_L - \rho_G)}{\rho_L^2 \sigma_L^3} \quad (2-94)$
	J=0.94 H ^{0.747} for $2 < H \leq 59.3$ (2-95)
	J=3.42 H ^{0.441} for $H > 59.3$ (2-96)
	$H = \frac{4}{3} Eo M^{-0.149} \left(\frac{\mu_L}{\mu_{\text{water}}} \right)^{-0.14} \quad (2-97)$
	For the range of $M < 10^{-3}$, $Eo < 40$, $(\text{Re})_{\text{bubble}} > 0.1$
Luo et al. ⁽¹⁵⁶⁾	$U_b \left(\frac{\rho_{SL}}{\sigma_L g} \right)^{1/4} = \left\{ \left[\frac{M o_{SL}^{1/4}}{K_b} \left(\frac{\rho_{SL} - \rho_G}{\rho_{SL}} \right)^{5/4} d_b^2 \frac{g \rho_{SL}}{\sigma_L} \right]^{-n} \right. \quad (2-98)$
	$\left. + \left[\frac{2c}{d_b} \left(\frac{g \rho_{SL}}{\sigma_L} \right)^{-1/2} + \frac{(\rho_{SL} - \rho_G) d_b}{2 \rho_{SL}} \left(\frac{g \rho_{SL}}{\sigma_L} \right)^{1/2} \right]^{-n/2} \right\}^{-1/n}$
	$M o_{SL} = g (\rho_{SL} - \rho_G) (\mu_{SL})^4 / \rho_{SL}^2 \sigma_L^3 \quad (2-99)$
	n= 0.8 (contaminated liq.), 1.6 (purified liq.)
	c=1.2 (monocomponent liq.), 1.4 (multicomponent liq.)
	$K_b = \max (K_{b,0} Mo^{-0.038}, 12)$
	$K_{b,0} = 14.7$ (aqueous sol.), 10.2 (organic solvent/mixture)

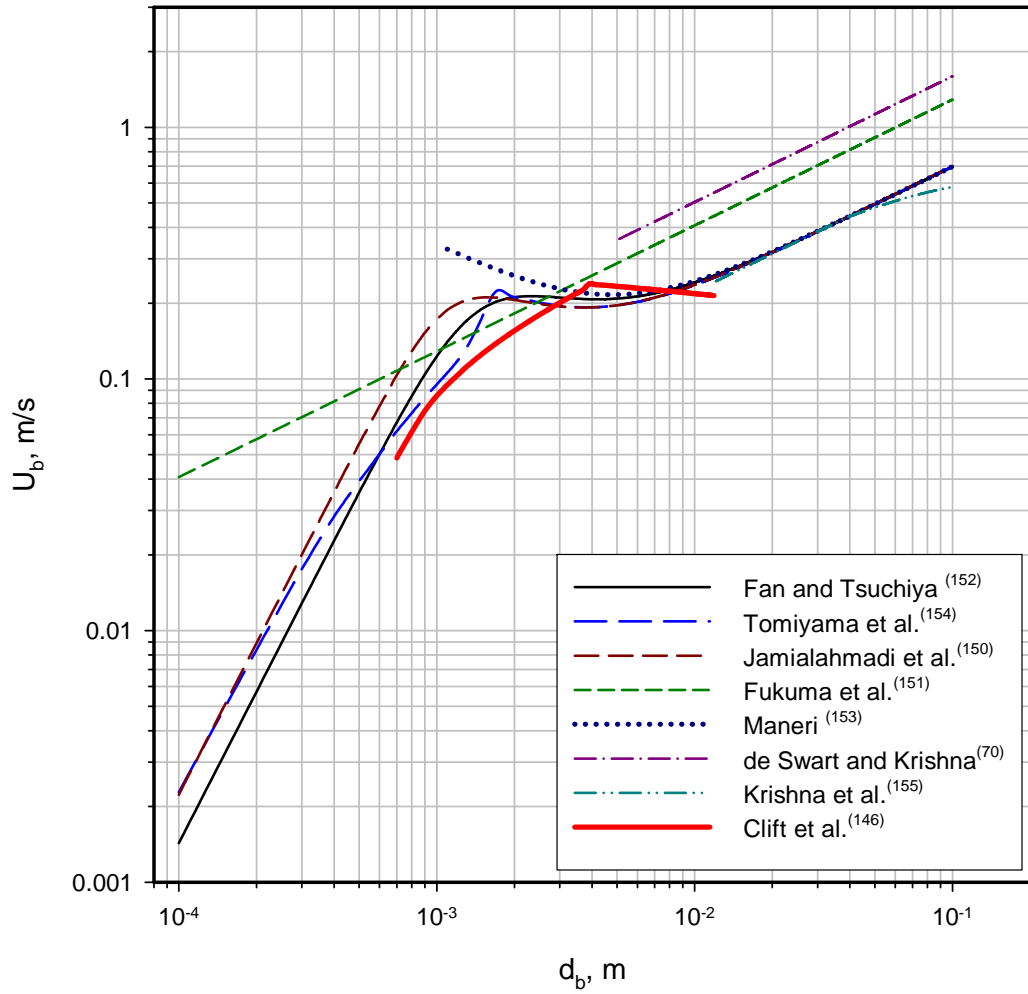


Figure 6 Prediction of the Terminal Rise Velocity of N₂ Gas Bubble in Isopar-M at 7 bar and 298 K Using the Correlation in Table 5

Table 6 Correlation for small and large bubble rise velocity in the swarm

<i>Authors</i>	<i>Correlation</i>	
Wilkinson et al. ⁽⁶¹⁾	$(U_b)_{small} = \frac{2.25\sigma_L}{\mu_L} \left(\frac{\sigma_L^3 \rho_L}{g\mu_L^4} \right)^{-0.273} \left(\frac{\rho_L}{\rho_G} \right)^{0.03}$	(2-100)
	$(U_b)_{large} \frac{\mu_L}{\sigma_L} = \frac{(U_b)_{small} \mu_L}{\sigma_L} +$	
	$2.4 \left(\frac{(U_G - U_{trans}) \mu_L}{\sigma_L} \right)^{0.757} \left(\frac{\sigma_L^3 \rho_L}{g\mu_L^4} \right)^{-0.077} \left(\frac{\rho_L}{\rho_G} \right)^{0.077}$	(2-101)
Reilly et al. ⁽⁴⁸⁾	$(U_b)_{small} = \frac{\sigma_L^{0.12}}{2.84 \rho_G^{0.04}}$	(2-102)
	$\varepsilon_{G-trans} = 0.59 B^{1.5} \sqrt{\frac{\rho_G^{0.96}}{\rho_L} \sigma_L^{0.12}}$	(2-103)
	$U_{G-trans} = (U_b)_{small} \varepsilon_{G-trans} (1 - \varepsilon_{G-trans})$	(2-104)
	B = 3.8 (Isopar-G: $\rho_L=740$, $\mu_L=0.000861$, $\sigma_L=0.0235$), 3.7 (Isopar-M: $\rho_L=779$, $\mu_L=0.002433$, $\sigma_L=0.0266$), 3.6 (TCE: $\rho_L=1462$, $\mu_L=0.000572$, $\sigma_L=0.03$), 4.6 (Varsol: $\rho_L=773$, $\mu_L=0.001012$, $\sigma_L=0.0283$), 4 (H ₂ O: $\rho_L=1000$, $\mu_L=0.001$, $\sigma_L=0.0728$)	
Krishna and Ellenberger ⁽³⁶⁾	$(U_b)_{large} = \frac{D_C^{0.18} (U_G - U_{G-trans})^{0.42}}{0.268}$	(2-105)
Krishna et al. ⁽¹⁵⁵⁾	$(U_b)_{large} = 0.71 \sqrt{g d_b} (SF)(AF) \quad \text{for } Eo > 40$	(2-106)
	$AF = 2.73 + 4.505(U_G - U_{G-trans})$	(2-107)
	SF=1 for $d_b/D_C < 0.125$	
	SF=1.13 exp(- d_b/D_C) for $0.125 < d_b/D_C < 0.6$	
	SF=0.496(D_C/d_b) ^{0.5} for $d_b/D_C > 0.6$	

For the prediction of $U_{G-trans}$ in Equations (2-105) and (2-107), Krishna and Ellenberger ⁽³⁶⁾ and Krishna et al. ⁽¹⁵⁵⁾ have suggested the use of Equation (2-104) proposed by Reilly et al. ⁽⁴⁸⁾.

2.3 DYNAMICS OF DISPERSED SOLIDS

The knowledge of the relation between the mixing of solids in the liquid is considered an important factor in the design and operation of slurry bubble column reactors. This is because the performance of the reactor is dependent on the concentration and distribution of the solids in the liquid. In commercial slurry bubble column, high solid concentration is preferred for high reactor productivity⁽⁷¹⁾. It is therefore expected that the axial solid dispersion could strongly affect the conversion of the reactants^(157,158).

In general, the majority of studies indicate that the axial solid concentration should decrease with column height^(73,157,158,159,160). O'Dowd et al.⁽¹⁶¹⁾ studied the axial solid dispersion in baffled and unbaffled slurry bubble column reactors operating in a continuous mode. They found that for the baffled column, the solid concentration at the top is the same as the bottom (feed), whereas for the unbaffled column the solid concentration was higher at the top than at the bottom. They also reported that gas velocity increased both the solid axial dispersion coefficient and particle settling velocity. Zhang⁽¹⁶²⁾ measured the axial solid concentration in a Tapered Slurry Bubble Column (TSBC) and a cylindrical slurry bubble column reactor under similar operating conditions. The tapered column had an angle of 1.91°. His studies showed that the axial solid concentration was more uniform in the TSBC. According to Zhang⁽¹⁶²⁾ the TSBC is more convenient to suspend heavy solid particles of different sizes at the bottom of the column where the superficial gas velocity is relatively high; similarly the entrainment of light solid particles at the top of the column, where the gas velocity would be lower, is prevented.

2.3.1 Particle Settling Velocity

The terminal settling velocity of a single particle in infinite medium, $U_{t,\infty}$ is obtained by the balance of the drag and buoyancy forces exerted by the liquid and the gravitational force accelerating the particles downward ⁽¹⁶³⁾.

For a spherical particle of a diameter d_p , three regimes for the terminal settling velocity have been identified ^(2,163):

Stokes regime ($Re_p < 0.4$),

$$U_{t,\infty} = \frac{gd_p^2(\rho_p - \rho_L)}{18\mu_L} \quad (2-108)$$

Intermediate regime ($0.4 < Re_p < 500$),

$$U_{t,\infty} = \frac{[1777.9g^2(\rho_p - \rho_L)]^{1/3} d_p}{\rho_L \mu_L} \quad (2-109)$$

and,

Newton's regime: ($500 < Re_p < 2.5 \times 10^5$),

$$U_{t,\infty} = \frac{\sqrt{3094g(\rho_p - \rho_L)d_p}}{\rho_L} \quad (2-110)$$

The Reynolds number for particle (Re_p) is defined as:

$$Re_p = \frac{\rho_L U_{t,\infty} d_p}{\mu_L} \quad (2-111)$$

When the slurry viscosity increases with an increase of solid concentration in the liquid, the interaction between solid particles becomes significant ⁽¹⁶³⁾. Consequently, the terminal settling velocity can no longer be applied, since the actual settling velocity of particles is reduced (or hindered) amid higher particle interactions, suspension viscosity, and wall effect ^(163,164). This

is referred to as the hindered settling velocity, U_p , where a generalized expression for its prediction as a function of the solid concentration is proposed by Maude and Whitmore⁽¹⁶⁵⁾ as follow:

$$U_p = U_{t,\infty} (1 - C_V)^\beta \quad (2-112)$$

The exponent β in Equation (2-112) is a function of the particle shape, size distribution and Reynolds number (Re_p)⁽¹⁶⁵⁾. Typically, the value of β is found to be 4.65, and 2.33 for Stokes and Newton's regime respectively^(163,165).

2.3.2 The Axial Dispersion-Sedimentation Model

The axial "dispersion-sedimentation model" is widely employed to describe the behavior of the solid in slurry reactors. Cova⁽¹⁶⁶⁾ and Suganuma and Yamanishi⁽¹⁶⁷⁾ described the concept as a solid dispersion flux, where a solid flux and a convective slurry flux are coupled to form a diffusion-type equation. As a result, the parameters required to solve the model are the axial solid dispersion coefficient (D_s) and the hindered settling velocity (U_p). In commercial SBCR where the gas, liquid and solid are moving co-currently from the bottom of the reactor, the flux of solid can be described as follows⁽¹⁶⁶⁾:

$$\frac{\partial C_s}{\partial t} + \nabla \cdot \bar{m}_p = 0 \quad (2-113)$$

Where \bar{m}_p is the mass flux obtained by modifying Fick's law to account for the effect of the gravitational force on the solid particles⁽¹⁶⁶⁾. The first step in solving the above equation is to assume that the solid concentration only varies along the axial position (z) of the column. Therefore, the following expression can be written:

$$-\frac{\partial^2 C_s}{\partial z^2} D_s + \frac{\partial C_s}{\partial z} \left(\frac{U_{SL}}{1 - \varepsilon_G} - U_P \right) = \frac{\partial C_s}{\partial t} \quad (2-114)$$

The second step is to assume that all operations are run at steady state. Therefore, upon integration the above expression is reduced to:

$$-D_s \frac{\partial C_s(z)}{\partial z} + C_s(z) \left(\frac{U_{SL}}{1 - \varepsilon_G} - U_P \right) = 0 \quad (2-115)$$

For a batch operation, the linear superficial slurry velocity, U_{SL} , becomes zero. Also, to simplify the above model the following assumptions should also be made ^(73,158): 1) ε_G , D_s and U_P are independent of the axial position, z ; 2) the solid particles are well suspended in the liquid due to a high gas velocity; 3) the particle terminal settling velocity $U_{t,\infty}$, is identical for all particles in the liquid. Hence, the general solution of Equation (2-115) upon integration is:

$$C_s(z) = C_1 + C_2 \exp\left(-\frac{U_P z}{D_s}\right) = C_1 + C_2 \exp(-Pe_z) \quad (2-116)$$

Where Pe_z is the Peclet number with the characteristic length, z corresponding to the axial position in the column.

Table 7 presents a number of available models for predicting the axial solid dispersion coefficient and the particle settling velocity in slurry reactors.

Table 7 Available models for predicting the axial solid dispersion coefficient and particle settling velocity

Authors	Solid system	Correlation	
Kato et al. ⁽¹⁵⁹⁾	Glass beads $\rho_p = 2520 \text{ kg/m}^3$ $75.5 < d_p < 163 \text{ }\mu\text{m}$ $C_S: 48\text{-}202 \text{ kgm}^{-3}$	$\frac{U_G D_C}{D_S} = 13 Fr_G \frac{1 + 0.009 Re_p Fr_G^{-0.8}}{1 + 8 Fr_G^{0.85}}$	(2-117)
		$U_P = 1.33 U_{t,\infty} \left(\frac{U_G}{U_{t,\infty}} \right)^{0.25} (1 - C_V)^{2.5}$	(2-118)
Kojima et al. ⁽⁶⁹⁾	Glass beads $105 < d_p < 125 \text{ }\mu\text{m}$ $C_S: 3.1\text{-}62 \text{ kgm}^{-3}$	$\frac{U_G D_C}{D_S} = 10 Fr_G^{0.76}$	(2-119)
Murray and Fan ⁽¹⁵⁷⁾	Glass beads $2450 < \rho_p < 2990 \text{ kg/m}^3$ $44 < d_p < 177 \text{ }\mu\text{m}$	$D_S = 0.022 U_G^{0.938} U_{t,\infty}^{-0.702}$	(2-120)
Reilly et al. ⁽¹⁶⁰⁾	Glass beads, coal $1510 < \rho_p < 4470 \text{ kg/m}^3$ $45 < d_p < 1190 \text{ }\mu\text{m}$ $C_S: 11.8\text{-}182 \text{ kg/m}^3$	$\frac{U_P}{D_S} = 573 \left(\frac{U_{t,\infty}}{\rho_L} \right)^{2/3} \left(\frac{\rho_P - \rho_L}{\rho_L} \right)^{1/3} U_G^{-0.1}$	(2-121)
O'Dowd et al. ⁽¹⁶¹⁾	Glass beads $\rho_p = 2420 \text{ kg/m}^3$ $88 < d_p < 105 \text{ }\mu\text{m}$ $C_S: \text{up to } 420 \text{ kgm}^{-3}$	$\frac{U_G D_C}{D_S} = 7.7 \left(\frac{Fr_G^6}{Re_G} \right)^{0.098} + 0.019 Re_p^{1.1}$	(2-122)
		$U_P = 1.69 U_G^{0.23} U_{t,\infty}^{0.80} (1 - C_V)^{1.28}$	(2-123)
Smith and Ruether ⁽¹⁵⁸⁾	Glass beads $\rho_p = 2420, 3990 \text{ kg/m}^3$ $48.5 < d_p < 164 \text{ }\mu\text{m}$ $C_S: \text{up to } 420 \text{ kgm}^{-3}$	$\frac{U_G D_C}{D_S} = 9.6 \left(\frac{Fr_G^6}{Re_G} \right)^{0.1114} + 0.019 Re_p^{1.1}$	(2-124)
		$U_P = 1.10 U_G^{0.026} U_{t,\infty}^{0.8} (1 - C_V)^{3.5}$	(2-125)
Zhang ⁽¹⁶²⁾	Quartz sand $\rho_p = 2636 \text{ kg/m}^3$ $50 < d_p < 200 \text{ }\mu\text{m}$	$\frac{U_G D_C}{D_S} = 0.0814 Fr_G^{-0.0526} Ar^{0.509} \left(1 - \frac{C_S}{\rho_{SL}} \right)^{0.954} S_b^{1.256}$	(2-126)

where S_b is the influence of taper angle and static slurry height defined as $S_b = h^2/h_B^2$ where h is the expanded slurry height based on conical base (m) and h_B is distance from distributor to conical base (m).

2.4 MASS TRANSFER CHARACTERISTICS

2.4.1 Gas/Liquid/Solid Transport

For a reaction to take place in a three-phase system, several steps must be followed by the reactants if both transport and kinetic resistances are important. The reaction may take place in the liquid, as it is the case for some hydrogenation processes ⁽¹⁶⁸⁾, or the liquid may serve as a solvent to improve heat and mass transfer between species, as in the case of Fischer Tropsch synthesis in SBCRs ⁽¹⁶⁹⁾. In the latter case, the reaction could take place on the surface, or in the pores of the solid catalyst where the reactants will have to diffuse and then chemically react; thus, the knowledge of the effectiveness factor of the solid catalyst should be evaluated ⁽¹⁶⁹⁾. Table 8 and Figure 7 show the steps for mass transfer accompanied by a chemical reaction in a gas/liquid system containing a solid catalyst, where the reaction takes place inside the pores of the catalyst. The mass transfer between phases can then be represented by Fick's Law with the following expression:

$$\frac{\partial C}{\partial t} = -D_{AB} \frac{\partial^2 C}{\partial x^2} \quad (2-127)$$

where D_{AB} is the diffusivity of phase A into B.

The products of the chemical reaction will follow the inverse direction back to the gas phase in the case of volatile gaseous products.

Table 8 Steps in three-phase reaction and parameters involved

<i>Step</i>	<i>Reactants activity</i>	<i>Site</i>	<i>Parameters</i>
1	Transport	gas film → gas-liquid interface	k_G
2	Transport	gas-liquid interface → liquid film	k_L
3	Transport	liquid film → liquid bulk	-
4	Transport	liquid bulk → liquid-solid interface	-
5	Transport	liquid-solid interface → surface of the catalyst	k_S
6	Diffusion	surface → inside of the pores of the catalyst	D_{eff}
7	Reaction	on the active sites of the catalyst particle	k_0

Using the two-film model based on a modified Fick's Law and initially developed by Lewis and Whitman ⁽¹⁷⁰⁾, step 1 through 5 can be described by a steady-state mass transfer flux, J_i , across a stagnant gas-liquid and liquid-solid interface by the following expressions:

$$J_G = k_G a (P_G - P^*) \quad (2-128)$$

$$J_L = k_L a (C^* - C_L) \quad (2-129)$$

$$J_S = k_S a_p (C_L - C_S) \quad (2-130)$$

In Equation (2-128), P_G is the partial pressure of the gas phase and P^* is the pressure at equilibrium defined as:

$$P^* = C^* H_e \quad (2-131)$$

Where C^* is the concentration at equilibrium (solubility) and H_e is Henry's Law constant.

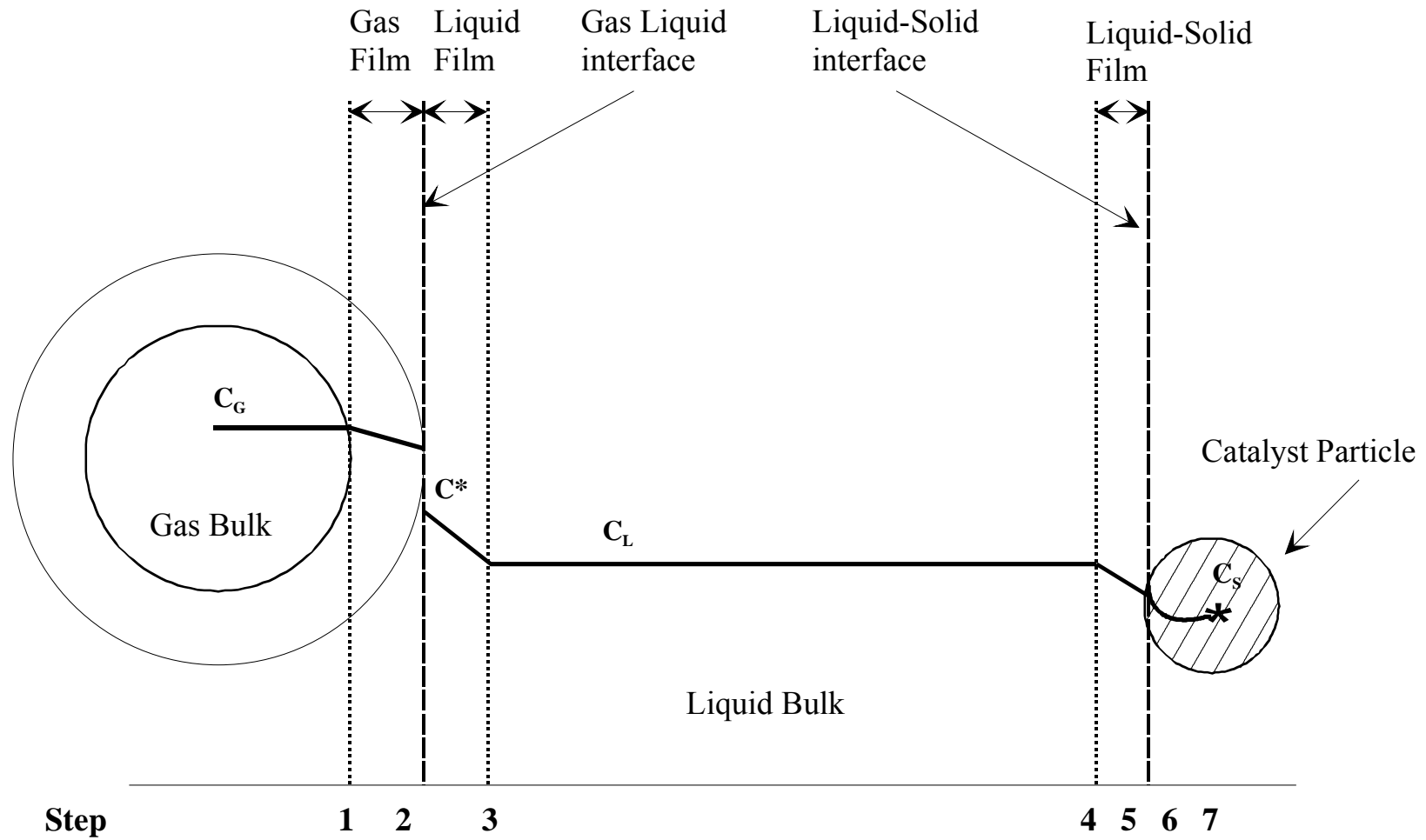


Figure 7 Concentration Profile for a Three-Phase System with Chemical Reaction inside the Pores of the Catalyst

In general, the reactant concentration in the gas film is high enough to prevent the partial pressure of the liquid in the gas phase from imposing any resistance to transport. Therefore, step 1, the resistance due to the transport of the reactant through the gas film can be neglected. Also, the catalyst particles are generally very small in size (micron size) so the resistance in step 5 could be ignored. Consequently, the main resistance occurs in step 2 from the gas-liquid interface to the liquid film. As a result, Equation (2-129) becomes the overall rate of mass flux, where k_L , the mass transfer coefficient is related to the gas-liquid diffusivity and the liquid film thickness, δ , as shown by the following equation:

$$k_L = \frac{D_{AB}}{\delta} \quad (2-132)$$

The above expression, however, is not always true, and generally when the penetration theory is considered the mass transfer coefficient is expressed as a function of the diffusivity as follow:

$$k_L \propto D_{AB}^{0.5} \quad (2-133)$$

Step 6 is the diffusion of the reactant from the surface to the inside of the pores of the catalyst. Usually, the pores of the catalyst pellet are not similar and totally straight, rather they are tortuous. This implies that the diffusion of the reactant is not happening to all area normal to the direction of the flux and the pores present different cross sectional area ⁽¹⁷¹⁾. This kind of diffusion is described by the effective diffusion as follow ⁽¹⁷²⁾:

$$D_{eff} = \varepsilon_{cat} \frac{D_{AB}}{\tau_{cat}} \quad (2-134)$$

Where ε_{cat} is the void fraction of the catalyst particle, and τ_{cat} is the tortuosity factor.

Step 7 is the chemical reaction. Depending on the catalyst used, this step can be either slow or fast. Typically, for a hydrogenation process such as the Fischer-Tropsch synthesis, the kinetic rate is expressed as a first-order type reaction. The kinetic rate depends strongly on the catalyst nature characterized by intraparticle diffusivity and represented by the effectiveness factor η . The kinetic rate is expressed as follow:

$$R_s = k_0 a_p C_s \eta \quad (2-135)$$

The overall rate of reaction should include the three transport rates of mass flux from the gas phase to the catalyst particle expressed by Equations (2-128) through (2-130) and the kinetic term, Equation (2-135) as:

$$R_s = \frac{C_G - C_S}{\frac{1}{k_G a_{He}} + \frac{1}{k_L a} + \frac{1}{k_S a_P} + \frac{1}{k_0 a_P \eta}} \quad (2-136)$$

Thus, proper design of slurry bubble column reactors for a specific commercial process, the knowledge of both the transport and kinetic parameters is essential in the determination of the rate-limiting step.

2.4.2 Volumetric Liquid-Side Mass Transfer Coefficient, $k_L a$

Since the overall rate of mass transport flux during the reaction process is reduced to Equation (2-129), it is therefore essential to determine the liquid-side mass transfer coefficient, k_L , and the gas-liquid interfacial area, a . The calculation of the liquid-side mass transfer coefficient, based on Equation (2-132) requires the knowledge of the gas-liquid diffusivity and the liquid film thickness. The diffusivity can be obtained using available literature correlations, however, the measurement of the liquid film thickness can be a challenging task.

One method is to measure the volumetric liquid-side mass transfer coefficient, $k_L a$ and the gas-liquid interfacial area separately, then couple them to calculate the mass transfer coefficient, k_L . Table 9 summarizes available literature studies to measure k_L and a separately and the method employed to carry out the experiments.

Most of these studies were conducted to investigate the mass transfer in parallel with the gas holdup. The multiscale modeling of Bauer and Eigenberger⁽¹⁷³⁾ takes into consideration the hydrodynamics, mass transfer, reaction kinetics, and bubble-bubble interaction. They showed that the change in local bubble size, due to mass transfer with reaction, and a change in local mass fluxes between the gas and liquid phases could significantly change the hydrodynamic of the bubble column. Furthermore, in most of these studies, the effects of a number of operating conditions, including system pressure, liquid viscosity, liquid surface tension, and solid concentration, on the gas holdup, ε_G and the volumetric liquid-side mass transfer coefficient, $k_L a$ were investigated.

Koide et al.⁽⁶⁸⁾ and Salvacion et al.⁽¹⁷⁴⁾ reported that increasing solid particles concentration appeared to decrease the ε_G by increasing the coalescence tendency of the gas bubbles and similarly decrease $k_L a$. Quicker et al.⁽⁸¹⁾ and Schumpe et al.⁽⁶⁴⁾ found that $k_L a$ values increase with fine solid particles at low concentrations, whereas the gas-liquid interfacial area decreases with increasing solid concentrations. Dewes et al.⁽¹⁷⁵⁾ observed an increase of $k_L a$ values with pressure (from 1 to 8 bar) due to the increase of the gas-liquid interfacial area. These authors reported that the gas holdup and the interfacial area slightly decrease with the addition of up to 2 vol.% glass particles and that k_L at 8 bar was greater in the slurry system than in the gas/liquid system. Fukuma et al.⁽¹⁵¹⁾ used up to 50 vol.% glass beads and observed that k_L values

are proportional to the volume-surface mean bubble diameter and decrease with liquid viscosity, μ_L . Muller and Davidson ⁽¹⁷⁶⁾ studied the effect of surfactants on the mass transfer in a viscous liquid and found an increase of k_{La} values with the addition of the surfactant. They attributed a 60-75% of this increase to the small gas bubbles created in the system. Koide et al. ⁽⁶⁸⁾ studied ϵ_G and k_{La} in the transition and heterogeneous flow regimes and reported that their values in both regimes decrease with increasing solid concentration. They also observed that this decrease was more pronounced in the transition regime than in the heterogeneous flow regime.

A number of correlations available in the literature for predicting k_{La} values under different conditions are listed in Table 10. As can be seen in this table the majority of these correlations were developed under ambient conditions, using air/water system in the absence of solid particles. These conditions, unfortunately, are not typical of those employed in various important industrial applications, where a high solid concentration is usually used to achieve high reaction rates. Thus, in order to understand the behavior of the industrial SBCRs, the hydrodynamic and the mass transfer characteristics should be obtained in a wide range of operating variables typical to industrial applications, using a large-scale reactor.

Table 9 Literature survey on a and k_L in bubble and slurry bubble columns.

<i>Authors</i>	<i>System</i>	<i>Parameter measured and Method</i>	<i>k_L correlation</i>
Akita and Yoshida ⁽³¹⁾	Air, O ₂ /H ₂ O, glycol, CCl ₃	d_b , photographic	$k_L = 0.5g^{5/8} D_{AB}^{1/2} \rho_L^{3/8} \sigma^{-3/8} d_{32}^{1/2}$ (2-137)
Bouaifi et al. ⁽¹¹¹⁾	Air/H ₂ O	d_b , photographic	$k_L = 1.13 \sqrt{\frac{D_{AB}}{d_{32}}} U_{SP}^{1/2}$ (2-138)
Godbole et al. ⁽⁵⁷⁾	N ₂ , air/CMC, sulfate solution	a , CMC oxidation	$k_{L(CMC)} = 1.12 \times 10^{-4} U_G^{-0.03} \mu_{eff}^{-1/2}$ (2-139) μ_{eff} is given in Equation (2-63)
Oyevaar et al. ⁽³⁸⁾	CO ₂ /DEA	a , absorption rate measurement	N/A
Stegeman et al. ⁽⁴⁴⁾	CO ₂ /DEA	a , absorption rate measurement.	N/A
Vázquez et al. ⁽¹⁷⁷⁾	CO ₂ /sodium carbonate, bicarbonate, surfactant and sodium arsenite	a , absorption rate measurement	$k_L = K \sigma^{1.35} U_G^{0.5}$ (2-140) K=0.17587 ($d_{pp}=150-200 \mu m$) ^(a) , K=0.18233 for $d_{pp}=90-150 \mu m$, K=0.18689 for $d_{pp}=40-90 \mu m$
Vázquez et al. ⁽¹⁷⁸⁾	CO ₂ , O ₂ /(Na) or (K) carbonate, bicarbonate + (Na) or (K) arsenite	a , by Danckwerts method and chemical method: sodium sulfite and sodium dithionite method	N/A
Miyahara et al. ⁽¹⁷⁹⁾	Air/H ₂ O, glycerol, ethanol solutions, CMC/polystyrene.	d_b , optical fiber two-phase flow system	$\frac{k_L d_{32}}{D_{AB}} = 2 \times 10^{-4} Sc^{0.5} (Re Mo^{0.15})^3$ (2-141)
Fukuma et al. ⁽¹⁸⁰⁾	Air/H ₂ O, glycerol/glass beads	d_b , electroresistivity probe	$\frac{k_L d_{32}}{D_{AB}} = 4.5 \times 10^{-4} Sc^{0.5} Ga^{0.8} Bo^{-0.2}$ (2-142)
Neme, et al. ⁽⁵⁹⁾	N ₂ /Fe(CN), NaOH, CMC, HNaCO ₃ , Na ₂ CO ₃ /glass, diatomite, silicon carbide, alumina	k_L , electrochemical reduction	$\frac{k_L}{U_G} = 0.105 (Re Fr Sc^2)^{-0.268}$ 2-phase (2-143)
			$\frac{k_L}{U_G} = 0.103 (Re Fr Sc^2)^{-0.265}$ 3-phase (2-144)
Schumpe et al. ⁽⁶⁴⁾	N ₂ , O ₂ /H ₂ O, 0.8M Na ₂ SO ₄ /Carbon, Kiselguhr, Aluminum oxide	a , sulphite oxidation	$k_L = K U_G^{-0.05} \mu_{eff}^{0.15}$ (2-145) K=9.7x10 ⁻⁵ (H ₂ O/salt solution), K=6.45x10 ⁻⁵ (H ₂ O, 0.8M Na ₂ SO ₄), μ_{eff} in Equation (2-63)
Yang et al. ⁽¹⁸¹⁾	H ₂ , CO/Paraffin oil/silica gel	a , optical fiber probe	H ₂ : $\frac{k_L d_{32}}{D_{AB}} = 1.546 \times 10^2 Eu^{0.052} Re^{0.076} Sc^{-0.231}$ (2-146)
			CO: $\frac{k_L d_{32}}{D_{AB}} = 8.748 \times 10^2 Eu^{-0.012} Re^{0.024} Sc^{-0.133}$ (2-147)

(a) d_{pp} = diameter of the pores of the gas distributor plate

Table 10 Correlations for volumetric mass transfer coefficients in bubble and slurry bubble columns

Authors	System: gas/liquid/solid	Conditions	Correlation
Akita and Yoshida ⁽³¹⁾	Air, O ₂ /H ₂ O, Glycol, Methanol	U _G : 0.003-0.4 m/s U _L : 0-0.044 m/s D _C : 0.152-0.6 m H _C : 1.26-3.5 m Quiscent regime	$\left(\frac{k_L a D_C^2}{D_{AB}}\right) = 0.6 \left(\frac{\mu_L}{\rho_L D_{AB}}\right)^{0.5} \left(\frac{g D_C^2 \rho_L}{\sigma}\right)^{0.62} \left(\frac{g D_C^3 \rho_L^2}{\mu_L^2}\right)^{0.31} \varepsilon_G^{1.1} \quad (2-148)$
Fair ⁽¹⁰⁾	Air/H ₂ O		$k_L a = 3.31 \left(\frac{D_L \varepsilon_G}{d_{32}^2}\right) \left(\frac{\mu_L}{\rho_L D_{AB}}\right)^{1/3} \left(\frac{d_{32} \rho_L U_G}{\mu_L \varepsilon_G}\right)^{1/2} \quad (2-149)$
Godbole et al. ⁽⁵⁷⁾	Air/H ₂ O, CMC, sodium sulfate	Patm, U _G up to 0.24 m/s D _C xH _C :0.305x3.4 m	$k_L a = 8.35 \times 10^{-4} U_G^{0.44} \mu_{eff}^{-1.01} \quad (2-150)$ μ _{eff} is given in Equation (2-63)
Hikita et al. ⁽¹⁸²⁾	Air, H ₂ , CO ₂ , CH ₄ , C ₃ H ₈ /H ₂ O, 30, 50wt% sucrose, methanol, n-butanol	P _{atm} , U _G : 0.042-0.38 m/s D _C : 0.1m H _C : 1.5 m	$\frac{k_L a U_G}{g} = 14.9 \left(\frac{U_G \mu_L}{\sigma}\right)^{1.76} \left(\frac{\mu_L^4 g}{\rho_L \sigma^3}\right)^{-0.248} \left(\frac{\mu_G}{\mu_L}\right)^{0.243} \left(\frac{\mu_L}{\rho_L D_{AB}}\right)^{-0.604} \quad (2-151)$
Kang et al. ⁽⁴²⁾	Air/CMC	P: 0.1-0.6 MPa U _G : 0.02-0.2 m/s μ _L : 1-38 mPa s D _C xH _C :0.152x2 m	$k_L a = K \times 10^{-3.08} \left(\frac{D_C U_G \rho_G}{\mu_L}\right)^{0.254} \quad (2-152)$ Where K is the correlation dimension
Kojima et al. ⁽⁴⁰⁾	N ₂ , O ₂ /H ₂ O, Enzyme solutions (C _E)	P: 0.1-1.1 MPa U _G : 0.005-0.15 m/s C _E : 3-163 mg/dm ³ D _C xH _C :0.055x0.9-1.2 m	$k_L a = C \varepsilon_G^D (\rho_L Q^2 d_0^{-3} \sigma^{-1})^E (P/P_{atm})^F \quad (2-153)$ C, D, E and F depend on C _E
Özturk et al. ⁽⁴⁹⁾	Air, N ₂ , He, CO ₂ , H ₂ /17 pure organic liq., 5 inherently mixed liq, 17 adj. Mixtures	P _{atm} , U _G : 0.008-0.1 m/s D _C xH _C :0.095x0.85 m	$\frac{k_L a d_B^2}{D_{AB}} = 0.62 Sc^{0.5} Bo^{0.33} Ga^{0.29} Fr^{0.68} \left(\frac{\rho_G}{\rho_L}\right)^{0.04} \quad (a) \quad (2-154)$
Gestrich et al. ⁽¹⁰⁾	135 measurements of 7 different groups	-	$k_L a = 0.0424 U_G^{0.21} \left(\frac{H_S}{D_C}\right)^{-0.561} \left(\frac{\rho_L \sigma^3}{g \mu_L^4}\right)^{0.116} \varepsilon_G \quad (b) \quad (2-155)$
Alvarez et al. ⁽¹⁸³⁾	CO ₂ /aqueous solution of sucrose and surfactants	Patm, U _G : up to 0.0016 m/s D _C : 0.06 m H _L : 0.6, 0.9 m	$k_L a = k_1 U_G^{2/3} \sigma^{3/4} \mu_L^{-3/4} \rho_L^{3/2} \quad (2-156)$ k ₁ depends on pore size of the plate distributor: plate 0: 150-200 μm, k ₁ = 1.924 x 10 ⁻⁷ plate1:90-150 μm, k ₁ = 1.969 x 10 ⁻⁷ plate 2: 40-90 μm, k ₁ = 2.079 x 10 ⁻⁷

Table 10 (Continued)

Authors	System: gas/liquid/solid	Conditions	Correlation
Jordan and Schumpe ⁽¹¹³⁾	N ₂ , He/Ethanol, 1-butaol, toluene, decalin	P: 1-40 bar U _G : 0.01-0.21 m/s D _C : 0.1 m H _C : 2.4 m	$\frac{k_L a d_b^2}{D_{AB}} = a_1 Sc^{0.5} Bo^{0.34} Ga^{0.27} Fr^{0.72} \left(1 + 13.2 Fr^{0.37} \left(\frac{\rho_G}{\rho_L} \right)^{0.49} \right)$ (2-157) a ₁ depends on the perforated plate: plate 1: 19x1 mm, a ₁ = 0.522, plate 2: 1x1 mm, a ₁ = 0.599, plate 3: 1x4.3 mm, a ₁ =0.488
Kawase et al. ⁽¹⁸⁴⁾	Air/H ₂ O, carbopol, CMC	Semitheoretical	$\frac{k_L a D_C^2}{D_{AB}} = 12 C_4 \frac{1}{\sqrt{\pi}} \sqrt{10.7 n^{1/3} Sc^{1/2} Re^{\frac{2+n}{2+2n}} Fr^{\frac{11n-4}{39(1+n)}} Bo^{3/5}}$ (2-158) $C_4 = 0.0645 n^{3/2}$ (2-159)
Schumpe at al. ⁽⁶⁴⁾	N ₂ , O ₂ /H ₂ O, 0.8M Na ₂ SO ₄ /Carbon, Kieselguhr, Aluminum oxide	P _{atm} , U _G : up to 0.07 m/s C _S : up to 300 kg/m ³ D _C xH _C :0.095x0.85 m	$k_L a = K U_G^{0.82} \mu_{eff}^{-0.39}$ (2-160) K=0.063 (H ₂ O/salt solution) K=0.042 (H ₂ O, 0.8M Na ₂ SO ₄) μ _{eff} is given in Equation (2-63)
Dewes and Schumpe ⁽¹⁸⁵⁾	He, N ₂ , air, sulfur hexafluoride/0.8 M sodium sulfate + Xantham gum / Kieselghur, alumina	P: 1 to 10 bar U _G : 0.01-0.08 m/s C _V : up to 18 vol.% D _C xH _C :0.115x1.37 m	$k_L a = U_G^{0.9} \mu_{eff}^{-0.55} \rho_G^{0.46}$ (2-161) μ _{eff} is given in Equation (2-63)
Chen and Leu ⁽¹¹⁹⁾	Air/H ₂ O/nickel	Magnetized SBCR P _{atm} , U _G up to 0.04 m/s H up to 25000 A/m D _C xH _C :0.05x0.5 m	$k_L a = 0.40 U_G^{0.625} U_L^{0.26} \exp(1.477 \times 10^{-5} H)$ (c) (2-162)
Koide et al. ⁽⁶⁸⁾	N ₂ /H ₂ O, glycerol, glycol, barium chloride, sodium sulphate/Glass and bronze	P _{atm} U _G : 0.03-0.15 m/s C _S : 0-200 kg/m ³ D _C : 0.1-0.3 m H _C : 2.3-3 m	$\frac{k_L a \sigma}{\rho_L D_{AB} g} = \frac{2.11 \left(\frac{\mu_L}{\rho_L D_{AB}} \right)^{0.5} \left(\frac{g \mu_L^4}{\rho_L \sigma_L^3} \right)^{-0.159} \varepsilon_G^{1.18}}{1 + 1.47 \times 10^4 C_V^{0.612} \left(\frac{U_{\infty}}{\sqrt{D_C g}} \right)^{0.486} \left(\frac{D_C^2 g \rho_L}{\sigma} \right)^{-0.477} \left(\frac{D_C U_G \rho_L}{\mu_L} \right)^{-0.345}}$ (2-163)
Salvacion et al. ⁽¹⁷⁴⁾	Air, N ₂ / H ₂ O, alcohol solutions/calcium alginate gel, polystyrene	P _{atm} , U _G up to: 0.15 m/s C _V : 20 vol.% D _C : 0.14, 0.218, 0.3 m H _L : 1.5 m	$\frac{k_L a \sigma}{\rho_L D_{AB} g} = 12.9 Sc^{0.5} Mo^{-0.159} Bo^{-0.184} \varepsilon_G^{1.3}$ (2-164) $\times \left[0.47 + 0.53 \exp \left(-41.4 \frac{\Pi_{\infty} k_1}{\mu_L U_P} Re_B^{-1/2} \right) \right] \times (1 + 0.62 C_V)^{-1}$

Table 10 (Continued)

Authors	System: gas/liquid/solid	Conditions	Correlation
			$\Pi_{\infty} = -C_B(d\sigma/dC_B)$ (2-165)
			$k_1 = -(d\sigma/dC_B)(3U_P r_B/2D_B)^{1/2}/r_B RT$ (d) (2-166)
Sauer and Hempel ⁽¹²⁴⁾	Air, H ₂ O, 10 different solid particles (1020 ≤ ρ _p ≤ 2780)	P _{atm} , U _G : 0.008-0.08 m/s C _V : 0-20 vol.% D _C : 0.14 m	$k_L a \left(\frac{\mu_{SL}}{g \rho_{SL} U_G} \right)^{0.5} = C \left(\frac{U_G}{(\mu_{SL} g U_G / \rho_{SL})^{0.25}} \right)^{B1} \left(\frac{\mu_{SL}}{\rho_{SL} v_{eff,rad}} \right)^{B2} \left(\frac{C_S}{C_{S,0}} \right)^{B3}$ (2-167)
			<i>C_{S0}</i> is solid concentration at bottom of column, kg/m ³ <i>v_{eff,rad}</i> is calculated from Equation (2-61) <i>μ_{SL}</i> is calculated from Equation (2-6) Sintered plate: C=2.31x10 ⁻⁵ , B1=0.305, B2=-0.0746, B3=-0.0127 Perforated plate: C=1.97x10 ⁻⁵ , B1=0.385, B2=-0.0715, B3=-0.0114
Behkish et al. ⁽⁷⁷⁾	H ₂ , CO, N ₂ , CH ₄ /Isopar-M, Hexanes/Glass Beads, Iron Oxide	P: 1.7-7.9 bar U _G : 0.05-0.25 m/s C _V : 0-36 vol.% D _C : 0.316 m	$k_L a = 0.18 Sc^{-0.6} \left(\frac{\rho_L v_A}{M_B} \right)^{-2.84} (\rho_G \times U_G)^{0.49} e^{-2.66 C_V}$ (2-168)

(a) All dimensionless numbers in terms of d_B (rather than D_C)(b) H_S : Slumped column height, m

(c) H: Applied magnetic field, A/m

(d) C_B=concentration of alcohol, mol/m³; D_B: Diffusivity of alcohol in the liquid, m²/s

3.0 OBJECTIVE

The overall objective of this study is to investigate the hydrodynamic and mass transfer parameters in a pilot-scale slurry bubble column reactor simulating the Fischer-Tropsch synthesis under typical industrial conditions. These parameters will be determined using syngas and methane, among others, and organic liquid mixture, in the presence and absence of alumina particles Fischer-Tropsch catalysts at high loading. Furthermore, the effect of pressure, superficial gas velocity and temperature on these parameters will be investigated.

In order to achieve this objective, the experimental work will be conducted in two SBCRs:

- 1) Cold Slurry Bubble Column Reactor: A large-scale slurry bubble column reactor operating at ambient temperature is used to investigate the effect of pressure, superficial gas velocity, and solid loading on the hydrodynamic and mass transfer parameters of H₂, CO, CH₄, He and N₂ in an organic liquid mixture (Isopar-M), in presence and absence of glass beads and alumina particles. From this work, the effect of gas nature and solid nature on the gas holdup, bubble size distribution, Sauter-mean bubble diameter and volumetric liquid-side mass transfer coefficient are determined.
- 2) Hot Slurry Bubble Column Reactor: A slurry bubble column reactor similar to the cold is used to investigate the effect of high temperature, high pressure, and high superficial gas velocity on the hydrodynamic and mass transfer parameters. The hot SBCR is equipped

with Jerguson sight windows to allow online photographic measurements of the gas bubble size.

- 3) The experimental data obtained in the cold and hot SBCRs are used to develop empirical and Neural Network models to predict the hydrodynamic and mass transfer of Low-Temperature Fischer Tropsch synthesis in a large scale slurry bubble column reactor operating under typical industrial conditions.

All experiments in the cold and hot SBCRs are statistically designed using the Central Composite Statistical Design approach.

4.0 EXPERIMENTAL

The following sections present the properties of the gas, liquid and solid phases used in this study.

4.1 THE GAS-PHASE

The gases used in this study were purchased from Valley National Gas, Pittsburgh, USA and Praxair, USA, with purity above 99%. Some thermodynamic parameters of these gases are given in Table 11.

Table 11 Thermodynamic properties of gases

<i>Component</i>	<i>Mol wt.</i> <i>(kg/kmol)</i>	<i>T_c</i> <i>(K)</i>	<i>P_c</i> <i>(bar)</i>	<i>ω</i> <i>(-)</i>	<i>V_c</i> <i>(m³/kmol)</i>	<i>Z_c</i> <i>(-)</i>
H ₂	2.016	33.20	13.0	-0.218	0.0651	0.306
N ₂	28.013	126.2	33.9	0.039	0.0898	0.290
CO	28.010	132.90	35.0	0.066	0.0932	0.295
CH ₄	16.043	190.4	46.0	0.011	0.0992	0.288
He	4.003	5.19	2.27	-0.365	0.0574	0.302

The viscosity of gases in kg m⁻¹ s⁻¹, was calculated using the following equation:

$$\mu_G = A + BT + CT^2 \quad (4-1)$$

The parameters used in Equation (4-1) are given in Table B-1 in Appendix B. It should be mentioned that the effect of pressure on the viscosity of the five gases is small. Figure 8 depicts the viscosity of all five gases as a function of temperature.

4.2 THE LIQUID PHASE

4.2.1 Composition

The liquid used was Isopar-M, which is an iso-paraffinic liquid mixture manufactured by Exxon Chemicals with physical properties, at ambient conditions close to Fischer-Tropsch wax as shown in Table 12. The FT wax was arbitrary classified into three groups: light (C₆-C₁₁), medium (C₁₁-C₂₂), and heavy wax (C₂₂ +)⁽¹⁸⁶⁾. Figure 9 a) and Table 13 show that the composition of Isopar-M is similar to FT medium wax. The physical properties of Isopar-M are given in the following sections.

4.2.2 Vapor Pressure

The vapor pressure values, P_S [bar], of Isopar-M as a function of temperature were obtained from Exxon Chemicals in the temperature range of 277 to 478 K. These values were correlated with Equation (4-2) as:

$$\text{Log}_{10}(P_S) = -\frac{2950.9}{T(K)} + 6.0719 \quad (4-2)$$

Figure 9 b) shows the experimental and predicted vapor pressure of Isopar-M.

Table 12 Physical properties of Isopar-M

Density, kg/m ³	15.6 °C	789.0
	30.0 °C	780.0
	55.0 °C	768.0
	200.0 °C	697.4
Viscosity, Pa s	25.0 °C	0.0027
	40.0 °C	0.0023
Vapor Pressure, bar	38.0 °C	4x10 ⁻⁴
	204.6°C	0.6469
Surface Tension, N/m	25.0 °C	0.0266
Molecular Weight, kg/kmol		192
Initial boiling point, °C		223.0
Flash point, °C		91.0

Table 13 Composition of Isopar-M

Component	Mol. %
<i>i</i> -C ₁₁	0.565
<i>n</i> -C ₁₁	0.120
<i>i</i> -C ₁₂	26.542
<i>n</i> -C ₁₂	1.147
<i>i</i> -C ₁₃	28.323
<i>n</i> -C ₁₃	1.009
<i>i</i> -C ₁₄	31.357
<i>n</i> -C ₁₄	0.511
<i>i</i> -C ₁₅	9.249
<i>n</i> -C ₁₅	0.248
<i>i</i> -C ₁₆	0.929

4.2.3 Density

The density values of Isopar-M were obtained from Exxon Chemicals in the range of 288 to 473 K. The density data were then correlated as a function of temperature with Equation (4-3) and presented in Figure 9 c).

$$\rho_L = 929.81 - 0.4915 T \quad (4-3)$$

4.2.4 Viscosity

Exxon Chemicals provided the viscosity of Isopar-M at 25 and 40 °C. Reid et al. ⁽¹⁸⁷⁾ proposed the following expression for the viscosity calculation for a temperature range from freezing to the normal boiling point:

$$\ln(\mu_L) = A + \frac{B}{T} \quad (4-4)$$

Using the two viscosity data provided by Exxon Chemicals at 25 and 40 °C the constant in Equation (4-4) were determined and the following correlation was obtained for the viscosity of Isopar-M:

$$\ln(\mu_L) = \frac{1274.7}{T} - 10.19 \quad (4-5)$$

The effect of pressure on the viscosity of the liquid mixture was correlated using the method described by Reid et al. ⁽¹⁸⁷⁾ and details of the calculation can be found in Appendix B.

Figure 9 d) presents the effect of temperature and pressure on the viscosity of the Isopar-M mixture. From this figure it can be seen that the viscosity decreases with temperature. This decrease was about 80% at a given pressure from 298 to 473 K. The increase of pressure over the liquid mixture seems to increase the viscosity of the ungasged liquid mixture by almost 5% from 7 to 35 bar at 298 K and by 8.5% at 473 K.

4.2.5 Surface Tension

The method used to estimate the surface tension of Isopar-M was adopted from Reid et al. ⁽¹⁸⁷⁾ using the Parachor contribution group technique. The details of the calculation procedures are

given in Appendix B. Using this method, the surface tension of Isopar-M as a function of temperature was calculated and correlated with the following expression:

$$\sigma_L = 58.5 \times 10^{-9} T^2 - 10.39 \times 10^{-5} T + 5.35 \times 10^{-2} \quad (4-6)$$

Figure 9 e) shows the effect of temperature on the surface tension of Isopar-M. The effect of pressure on the surface tension was found to be negligible.

4.2.6 Gas-Liquid Diffusivity

The diffusivity of the five gases in Isopar-M was obtained using the Wilke and Chang⁽¹⁸⁸⁾ Correlation as shown below:

$$D_{AB} = 1.173 \times 10^{-16} \frac{(\lambda M_B)^{0.5} T}{\mu_L \upsilon_A^{0.6}} \quad (4-7)$$

Where the value of λ is 1 and M_B is the molecular weight of the liquid and υ_A is the solute molar volume. Figure 9 f) shows the effect of temperature on the diffusivity of the gases in Isopar-M.

4.3 THE SOLID PHASE

Glass beads and alumina powder are used in the cold SBCR, and alumina powder is employed as solid particles in the hot SBCR.

4.3.1 Particle Size Analysis

Scanning Electron Microscope (SEM) was used to analyze the glass beads and alumina powder particles, as shown in Figure 10 a) and b), respectively. A particle size distribution for both particles was obtained, as illustrated in Figure 11. The mean particle size was found to be 15.7

and 32.33 μm for glass beads and alumina powder, respectively. Also, the Sauter-mean particle diameter about 19 and 42.37 μm for glass beads and alumina powder, respectively.

4.3.2 Particle Density

The densities of the particles were measured using the displacement method with water and a graduated pycnometer. The densities obtained were 2500 and 3218.3 kg/m^3 for glass beads and alumina, respectively.

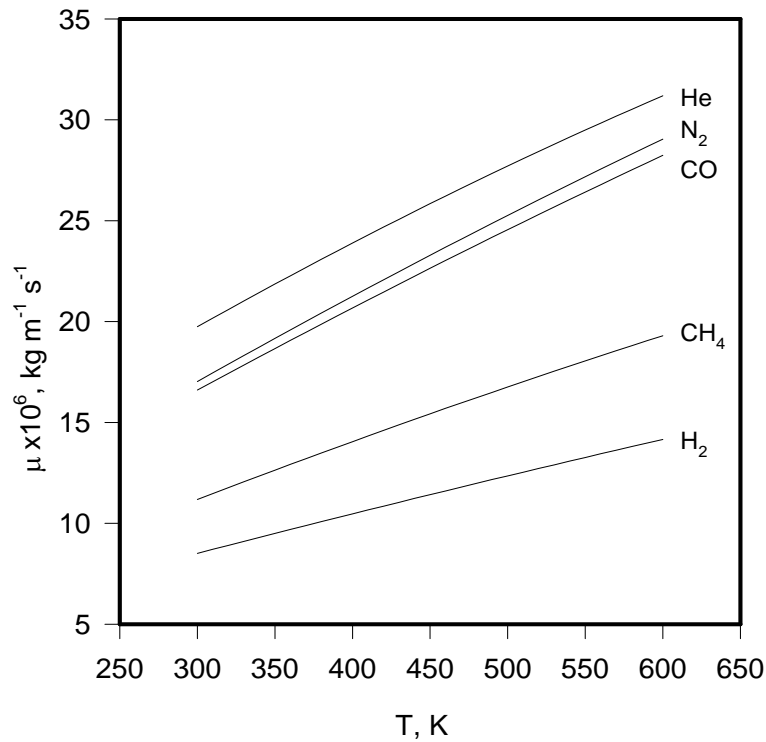


Figure 8 Viscosities of the Gases used

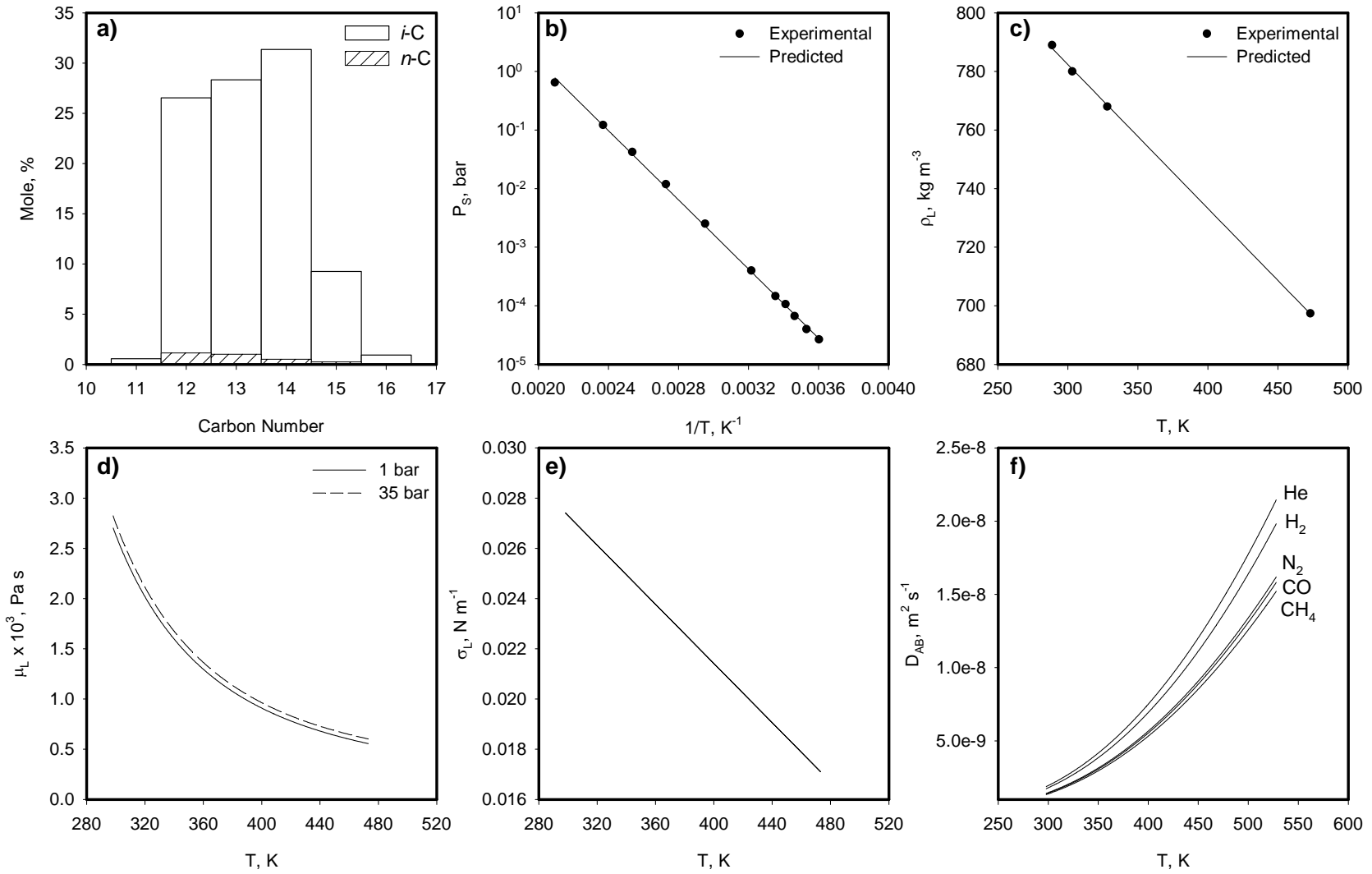


Figure 9 Properties of Isopar-M

a) Composition; b) Vapor pressure; c) Density; d) Viscosity; e) Surface tension; f) Diffusivity

4.3.3 Slurry Density

The density of the slurry was calculated at each solid concentration with the following equation:

$$\rho_{SL} = C_V \rho_P + (1 - C_V) \rho_L \quad (4-8)$$

4.3.4 Slurry Viscosity

There are several equations proposed in the literature to calculate the slurry viscosity as shown in Table 2. Figure 12 shows the slurry viscosity obtained from Equations (2-5) to (2-11) as a function of solid volumetric concentration. In this figure it can be seen that most correlations are independent of the nature of the solid particles. The correlation proposed by Riquarts ⁽⁹⁷⁾, however, takes into account the density of the particles, and subsequently, a higher slurry viscosity is obtained with the alumina/Isopar-M slurry than the glass beads/Isopar-M slurry.

4.4 EXPERIMENTAL SETUP

Two slurry bubble column reactors have been used in this work. The first reactor operates at ambient temperature, and the second operates at high temperature; and throughout this study they are referred to as the Cold and Hot SBCR respectively. The characteristics of the pipes used for the construction of these two columns are given in Table 14. The mechanical specifications of the cold column are given in Figure 13, and for the hot column in Figure 14 and Figure 15.

Table 14 Characteristics of the pipes

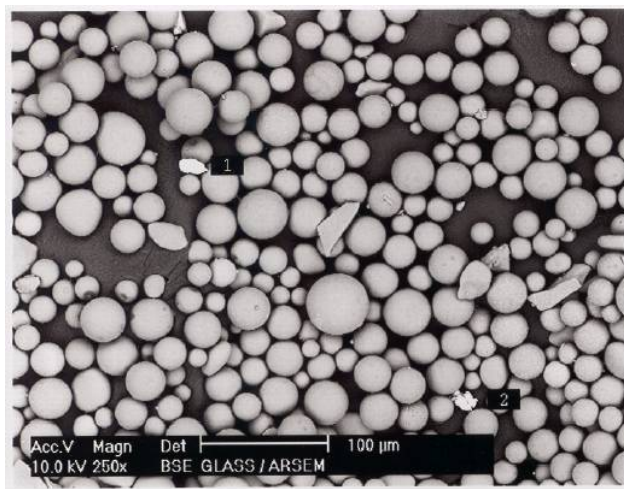
	<i>Cold SBCR</i>	<i>Hot SBCR</i>
Nominal Diameter	12 in	12 in
Schedule	5S	80
Material	Stainless Steel	Stainless Steel
Outside diameter, m	0.324	0.324
Inside diameter, m	0.316	0.289
Wall thickness, m	0.004	0.017
Inside C.S. area, m ²	0.078	0.066
Transverse metal area, m ²	0.004	0.017
Section modulus, m ³	3.15x10 ⁻⁴	12.23x10 ⁻⁴
Outside surface area, m ² /m	1.017	1.017
Inside surface area, m ² /m	0.993	0.908
Weight, kg/m	31.226	131.895
Height, m	2.823 (2x1.411)	3.00
Height/Diameter ratio	8.93	10.38

The details of the two setups are given in the following sections.

4.4.1 Cold SBCR

The schematic of the cold SBCR setup is illustrated in Figure 16. The setup is identical to that used by Inga⁽¹⁸⁹⁾. The column is constructed from SS 304L, SCH 5 with a maximum pressure rating of 10.3 bar (150 psig). The reactor inside diameter is 0.316 m and its height is 2.82 m as shown in Table 14. The column consists of two identical pipes provided with flanges. There are two thermocouples and one pressure transducer on the reactor column. The hydrostatic pressure can be measured through ten lines connected to two ultra-sensitive dP cells. Four ports are found on these lines to withdraw slurry samples when needed. All thermocouples are type J and pressure transducers are from Setra model 205-2. The gas before entering the column goes through the damper. This unit has a 0.101 m diameter and a length of 0.305 m constructed from

a) Glass Beads



b) Alumina

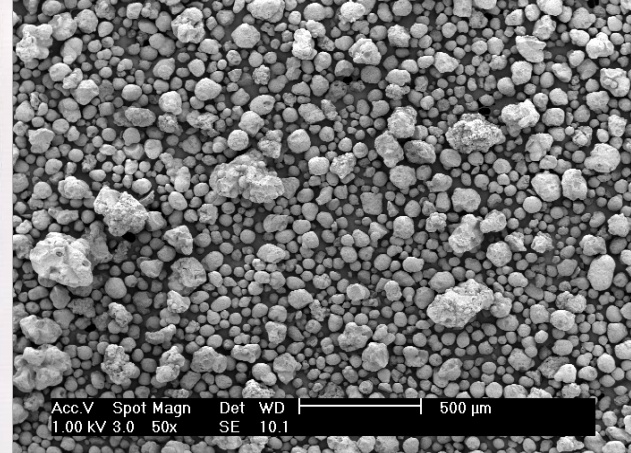
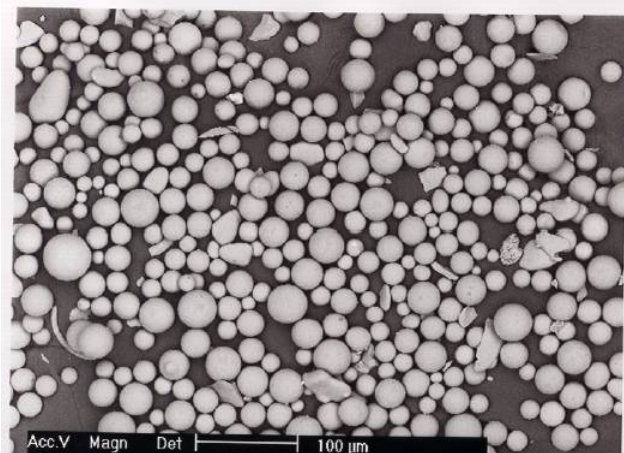
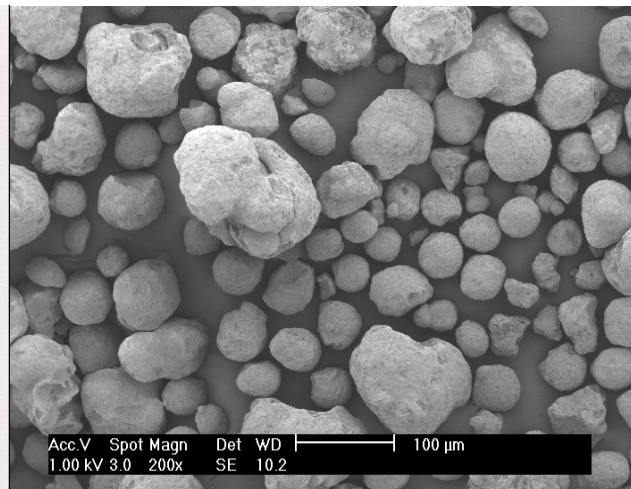


Figure 10 SEM of Glass Beads and Alumina Particles

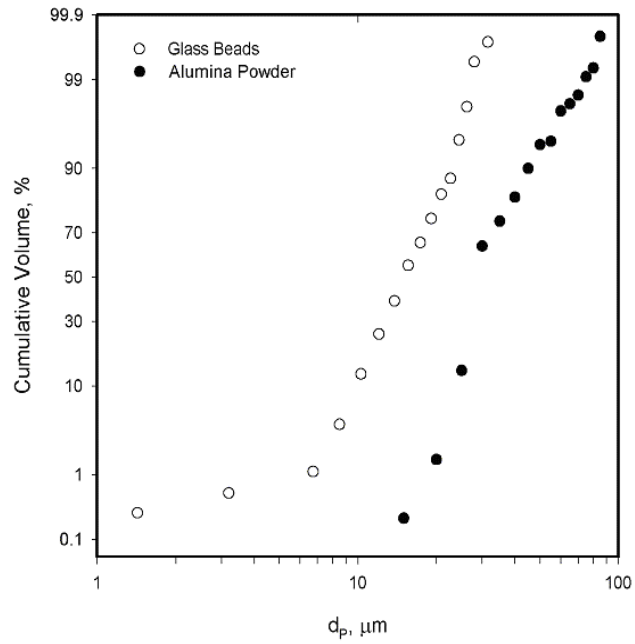


Figure 11 Glass Beads and Alumina Powder Particle Size Distribution

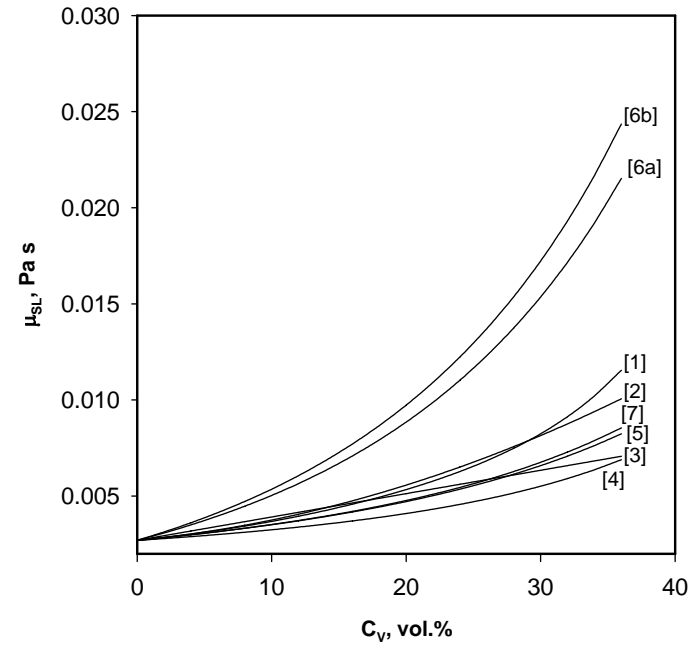


Figure 12 Correlations for Predicting Slurry Viscosity in Isopar-M

[1] Thomas⁽⁹³⁾, [2] Guth and Simba⁽⁹⁴⁾, [3] Saxena and Chen⁽¹⁰⁾, [4] Barnea and Mizrahi⁽⁹⁵⁾, [5] Roscoe⁽⁹⁶⁾, [6a] Riquarts⁽⁹⁷⁾ (glass beads), [6b] Riquarts⁽⁹⁷⁾ (alumina), [7] Vand⁽⁹⁸⁾

SS 316 SCH 40. It is used to absorb the pressure fluctuations created by the compressor and reduce the noises in the pressure readings. A demister, with the same dimensions as the damper, is placed at the outlet of the column to trap any liquid droplets or solid particles carried with the exit gas stream from entering the compressor. This compressor is a model 8 AGD-1 and is manufactured by Haskel Inc., USA. It is a double acting single stage gas booster operating with house air at 6.2 bar (90 psig). The maximum output pressure is at 20.7 bar and is suitable for the five gases used in this study.

The gas is first charged to a vessel before being charged to the system. This unit is the supply vessel and is a high-pressure unit made of 4" SCH 80 SS 304 L with an inside diameter of 0.0984 m and a height of 0.965 m. One pressure transducer and one thermocouple are connected to this unit in order to calculate the number of moles of gas before and after charging the reactor. Two vacuum pumps are used. These are model Cit-Alcatel type 2012A, which are an oil-sealed mechanical vacuum pump with a 560 W (0.75 HP) electric motor and can reach a pressure down to 0.1 Pa in the reactor. The gas is introduced at the bottom of the column.

The two dP cells used in the reactor for measurement of the pressure drop across the slurry bed are manufactured by Foxboro Co. and have ratings of 0.037 (15) and 0.046 (18.5) bar (in H₂O). They are connected to the column through the ten lines as illustrated in Figure 16. The pressure within the lines of the dP cells are measured with two pressure transducers which allow the adjustment of the pressure required for the dP cells lines before the respective valves are opened. This prevents the slurry in the reactor to not fill the dP cells lines.

All the pressure transducers, dP cells, and thermocouples are connected to a personal computer through a Keithley Data Acquisition Interface, model KDAC 500. This unit allows

storing the data at 20 Hz frequency. The gas superficial velocity is measured using two different calibrated orifice meters. The orifice diameter used for H₂ and He is 8mm, and that used for N₂, CO and CH₄ gases, has a 16mm diameter.

4.4.2 Hot SBCR

The schematic of the hot SBCR setup is shown in Figure 17. The reactor is 3-m high and 0.29-m diameter SCH 80, 304 Stainless steel pipe with 600 lb flanges at both ends. The reactor is provided with two Jerguson site-windows located near the bottom and the middle of the reactor in order to enable recording the bubbles size/behavior under a given operating condition. The reactor's hydro-pressure is 85.5 bar at 295 K and its maximum allowable working pressure is 57 bar at a maximum temperature of 590 K. The reactor is equipped with 12 heating elements and an internal cooling coil of 0.306 m² total contact area. The heating elements, covered with a heavy-duty insulation jacket, operate with 460V and are controlled by a Solid State Contactors rated up to 50 amps.

The gas is introduced from a supply vessel through the bottom of the column via a six-arm spider-type gas distributor, similar to that used in the cold SBCR. The gas is recycled through the reactor using a single-stage compressor built by Fluitron Inc., Ivy land, USA. The compressor has a nominal displacement of 4.8×10^{-3} m³/rev. using 30 HP, 1160 RPM electric motor. The gas flow rate is measured using a Coriolis mass and density meter model CMF100M330NU that transmits a current output signal through a transmitter model RFT9739E4SUJ, manufactured by Micro Motion, USA. The gas velocity can be adjusted with a needle valve through a bypass line around the compressor inlet and outlet. There is a damper

vessel placed at the compressor's outlet in order to reduce the vibrations and fluctuations created by the movements of the piston.

A demister is placed at the outlet of the column to prevent the liquid and solid particles from entering the compressor. In addition, a filter manufactured by Parker Hannifin Corp., USA is placed between the demister and the compressor as second stage device to prevent any solid particles or oil mist from entering the compressor. There are two differential pressure cells (dP), model IDP10-V20A11F manufactured by Foxboro, USA rated at 7.5 kPa connected at different locations on the reactor, which allow the measurement of the hydrostatic pressure head between any two levels in the reactor. The pressure and the temperature of the entire system are recorded with 5 pressure transducers manufactured by Wika, Germany, and 7 thermocouples type J manufactured by Omega Engineering Inc., USA. The design of this unit allows the gas to flow through or bypass the liquid using the two pneumatically actuated valves (AV-1 and AV-2), and permits up to 60% of the gas in the reactor to be sent back to the supply vessel without venting to the hood.

An online data acquisition from the thermocouples, pressure transducers, dP cells and the Coriolis mass flow meter was performed using the National Instrument FieldPoint modules FP-TC-120 and FP-AI-110, which are connected to a serial bus module (FP-1000) with RS-232 interface to a host PC. The output signals from the host PC are received by the FieldPoint module FP-AO-V10 for controlling the pneumatically activated valves and the heating elements of the reactor. The LabView software is used to monitor the process and perform the appropriate programs for I/O applications.

This setup has also two distinctive new operating features over the cold SBCR:

1. Gas circulation: The gas can circulate in the system by two different ways: first, through the liquid from the bottom of the column, and second, through the top of the reactor avoiding the gas passage through the liquid. Two pneumatically actuated valves (AV-1 and AV-2) working in opposite pattern direct the gas in one direction at a time.
2. Gas recycle: the gas can be recycled back to the supply vessel, so that venting the gas is prevented. Up to 60% of the total gas can be recycled back to the supply vessel using the compressor in some experimental conditions.

The data acquisitions from the thermocouples, pressure transducers, dP cells and the Coriolis mass flow meter is performed using the National Instrument FieldPoint modules FP-TC-120 and FP-AI-110, which are connected to a serial bus module (FP-1000) with RS-232 interface to a host PC. The output signals from the host PC are received by the FieldPoint module FP-AO-V10 for the control of the pneumatically activated valves and the heating elements of the reactor. The LabView software is used to monitor the process and perform the appropriate programs for I/O applications.

Figure 18 shows a picture of the cold SBCR. Figure 19 shows three different views of the hot SBCR, where the compressor, Jerguson sight-windows and the Coriolis mass flow meter can be seen.

4.4.3 Gas Sparger

The gas spargers used in the cold and hot SBCRs were identical in design so that the gas bubbles at formation in both columns could be identical. To design the gas sparger so that the reactor would operate in the fully developed hydrodynamic regime, Weber number in Equation (2-13) was used to guarantee a minimum value of 2 at the lowest operating conditions. Consequently, a spider-type gas sparger with six legs was designed. Each leg has 6 openings of 0.005 m ID on each side and on the bottom, totaling 18 holes. There are no openings on the top of the legs so that no solid particles could block the orifice. There are a total of 108 openings on the gas sparger. A schematic of the spider-type gas sparger is given in Figure 20. The gas sparger is screwed to a 0.0254 m ID pipe and its maximum height from the bottom of the column is about 0.152 m (6in). The picture of the spider-type gas sparger is given in Figure 21.

4.4.4 High-Speed Camera

The hot SBCR is equipped with two Jerguson sight-windows which allow simultaneous monitoring of the gas bubbles and the bed height. A high-speed Phantom camera version 3.3.294-R0 with a recording rate of 1000 picture per second (pps) and an exposure time of 50 μ s is used to monitor and record through the site-windows the size/behavior of the gas bubbles at any operating condition. On the average, 300 frames are recorded and saved to obtain a fully animated file for each experimental run. The images are selected from each of the mini-movie recorded for the gas bubbles rising through the solid-free liquid. Analyzing a single frame obtained under a specific operating condition allows the determination of the bubble size distribution. Figure 22 shows the setup for the high-speed camera.

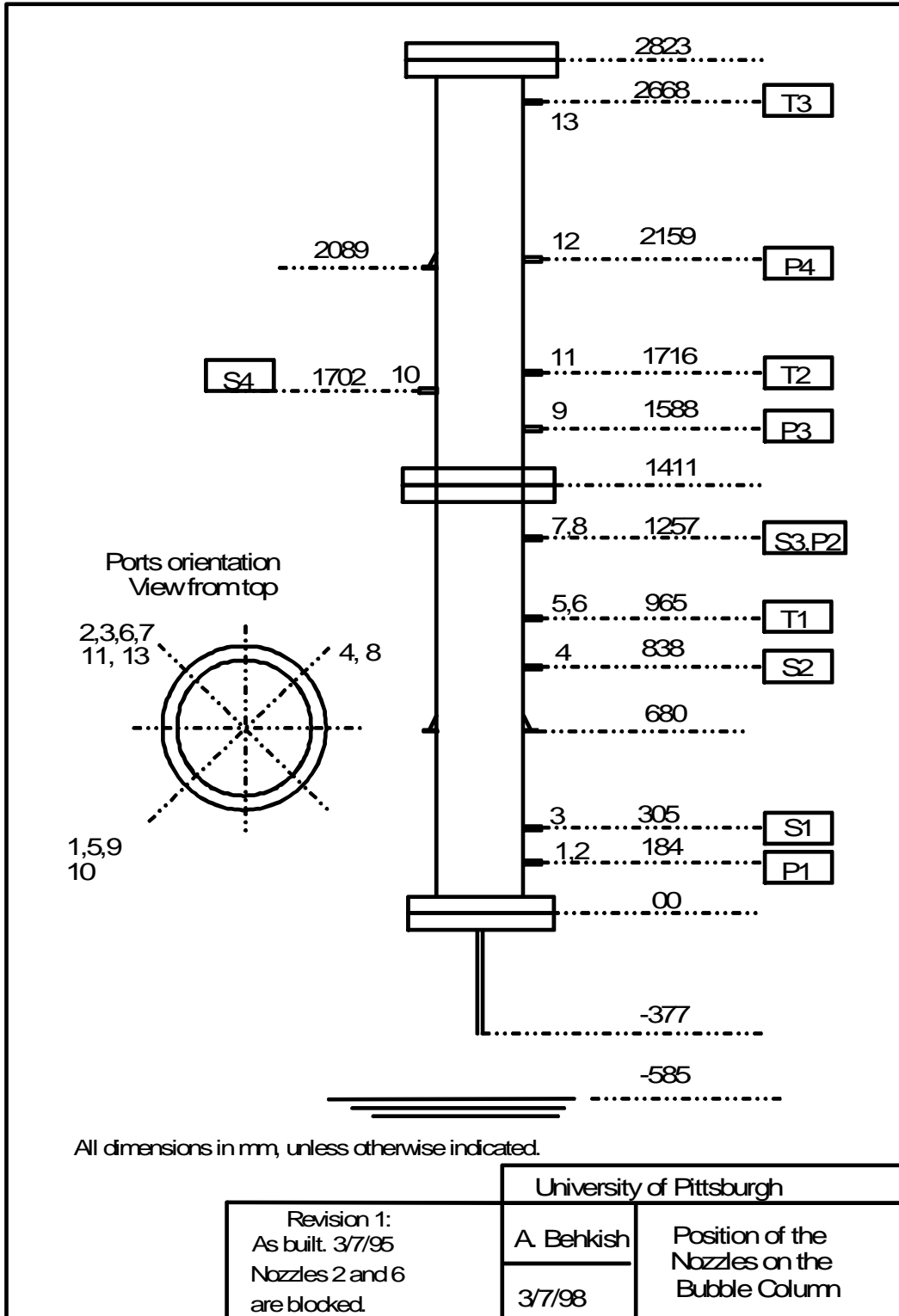


Figure 13 Mechanical Specifications of the Cold SBCR

Slurry Bubble Column:
Front View

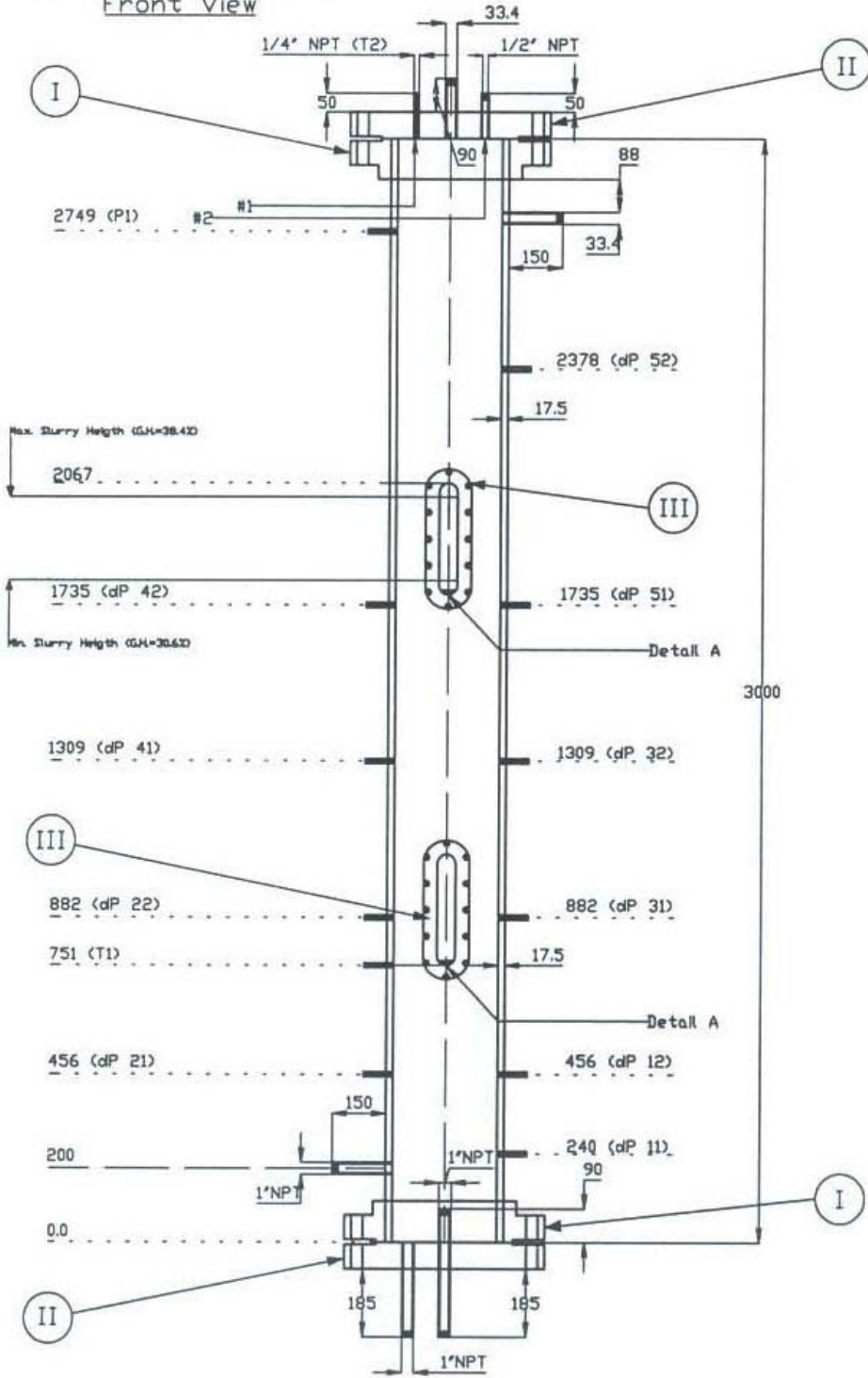


Figure 14 Part 1 of Mechanical Specifications of the Hot SBCR

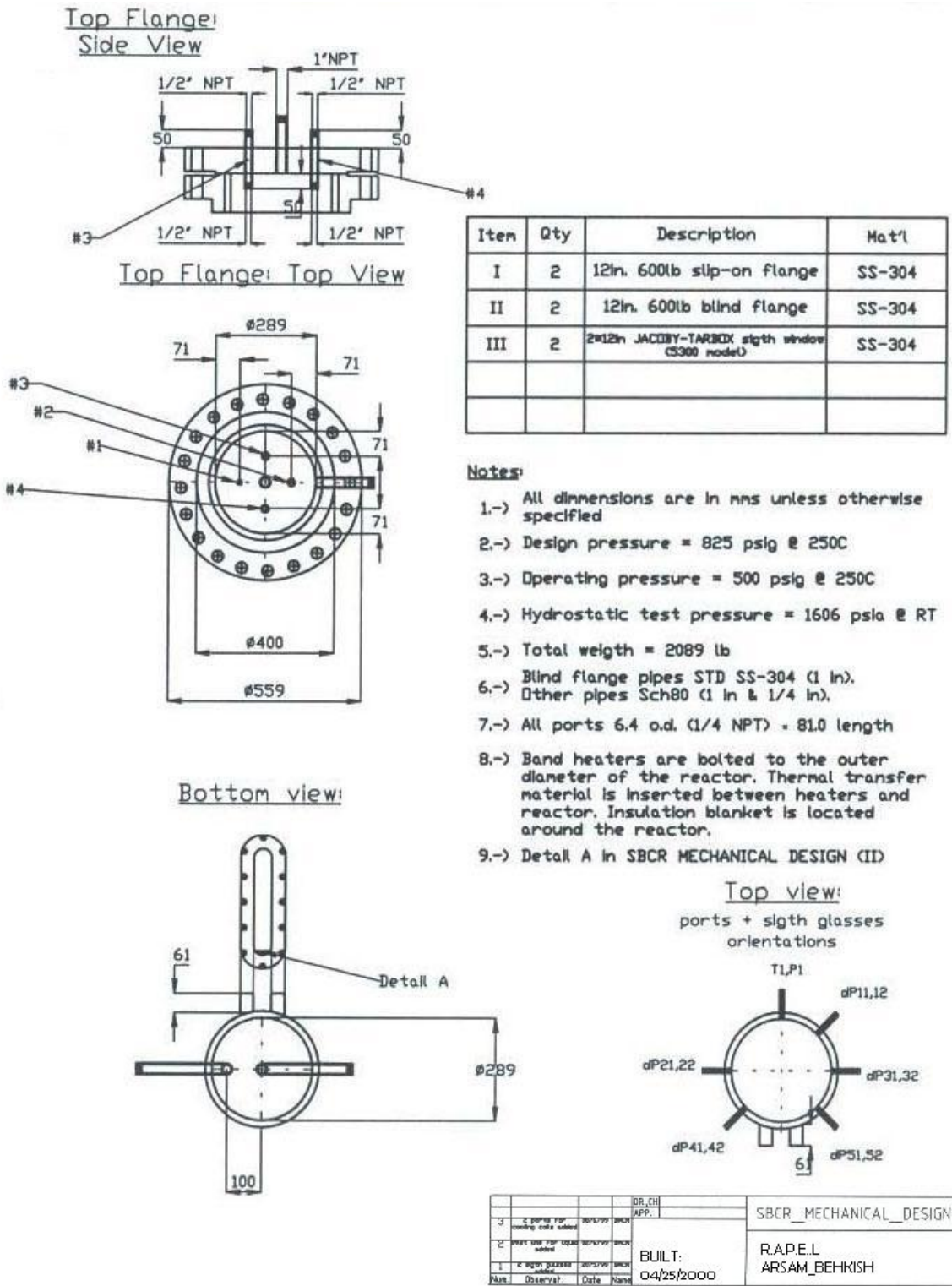


Figure 15 Part 2 of the Mechanical Specifications of the Hot SBCR

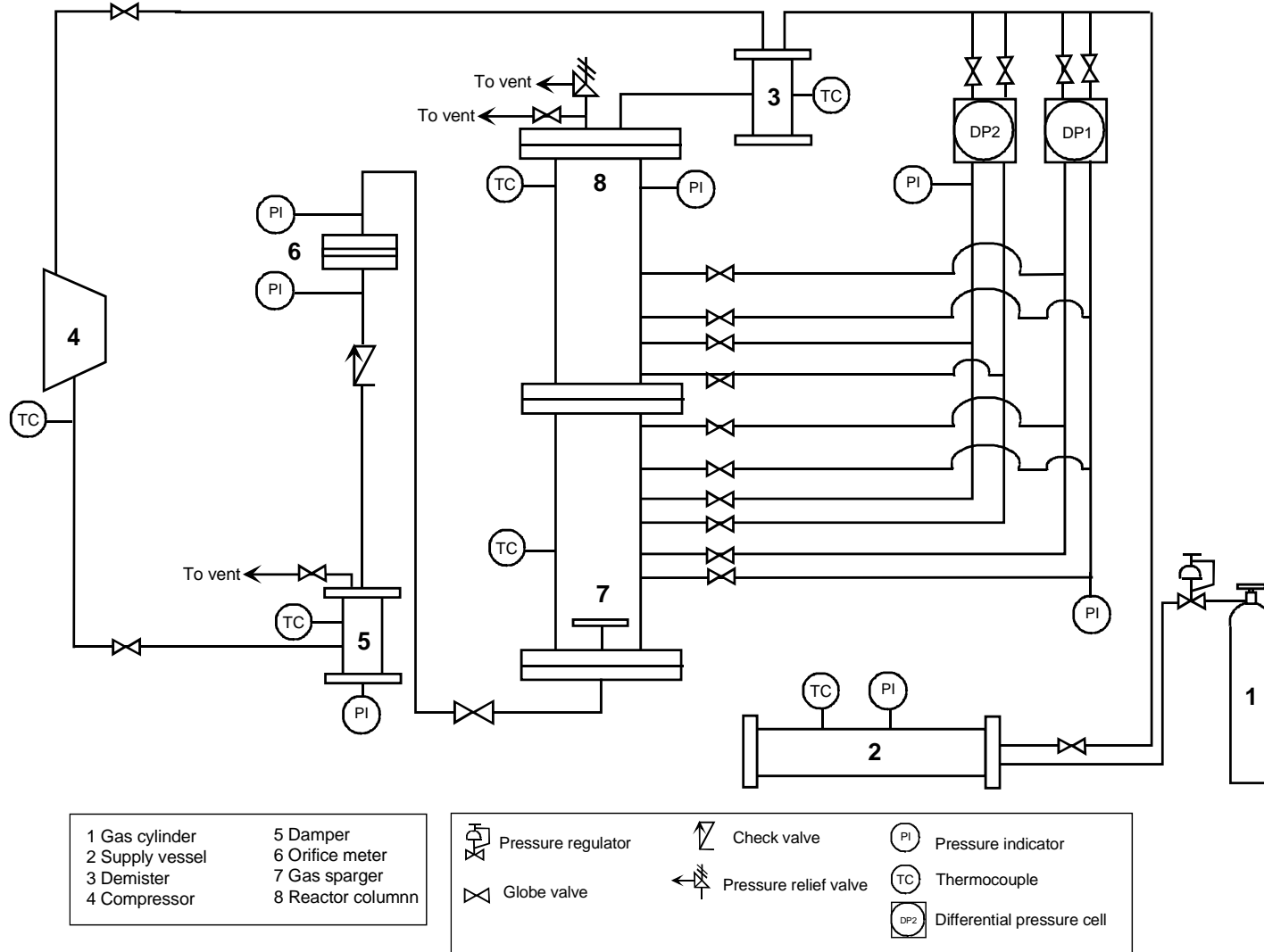


Figure 16 Schematic of the Cold Slurry Bubble Column Reactor Setup

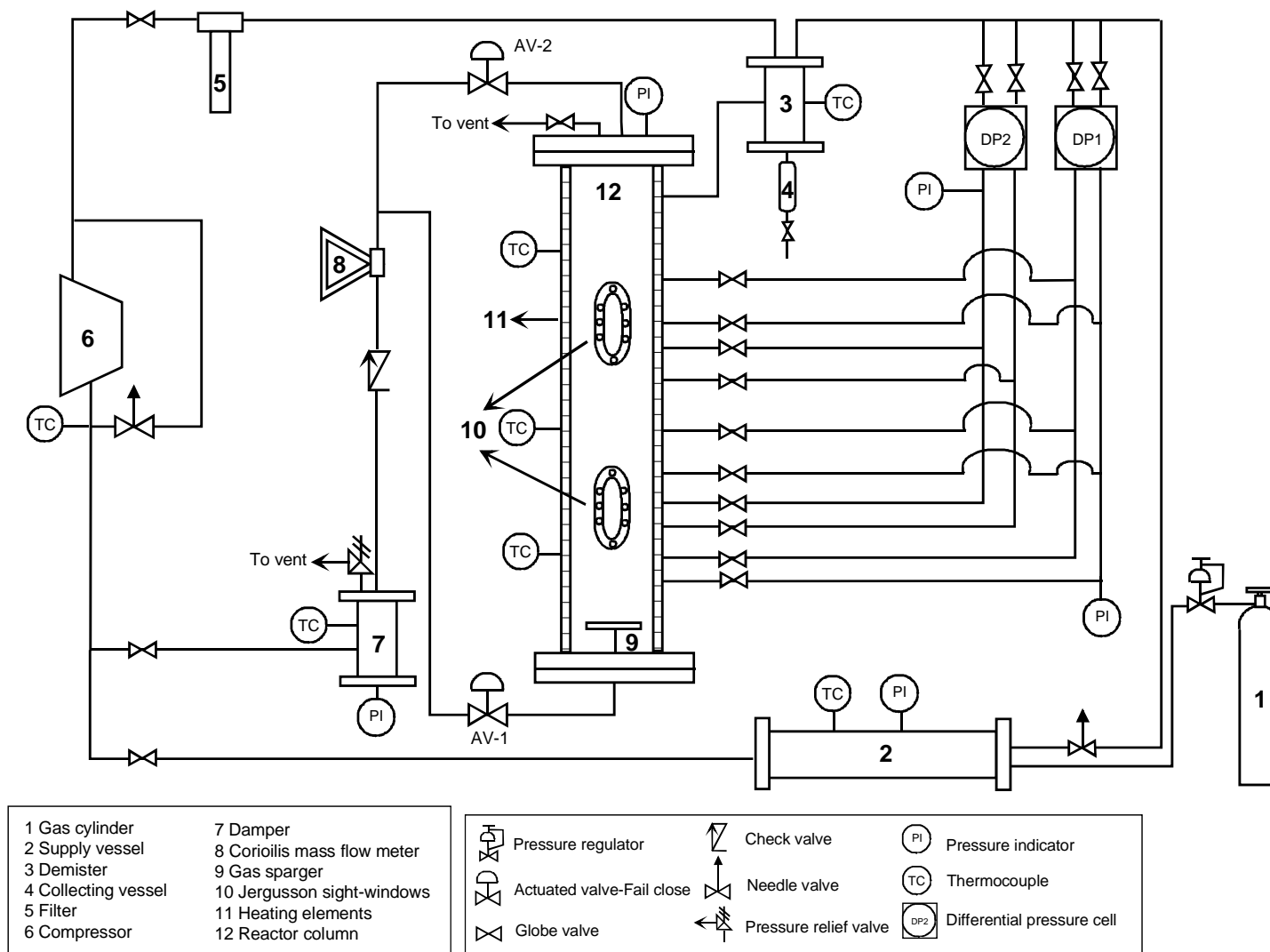


Figure 17 Schematic of the Hot Slurry Bubble Column Reactor Setup

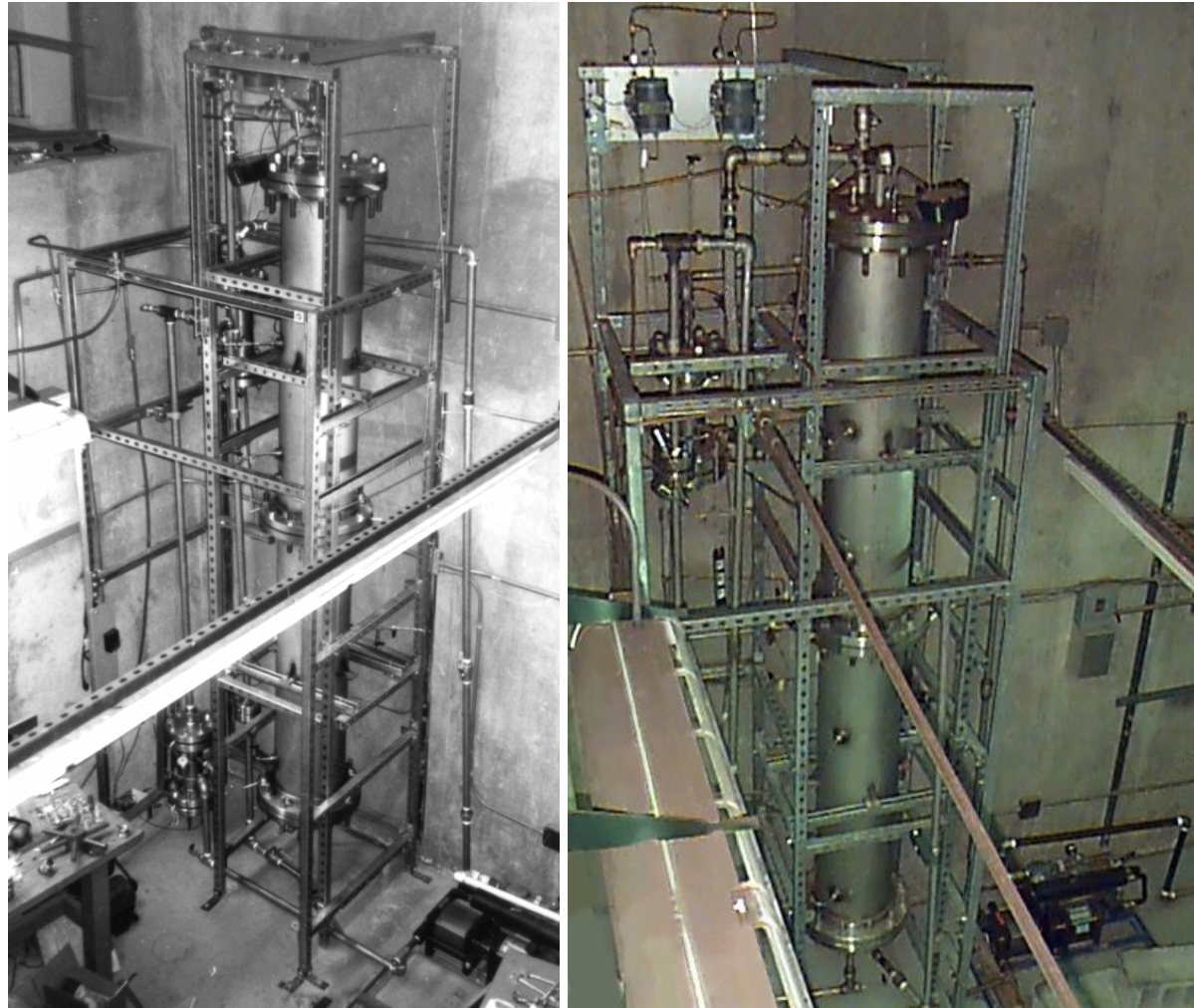


Figure 18 Pictures of the Cold Slurry Bubble Column Reactor

Right View



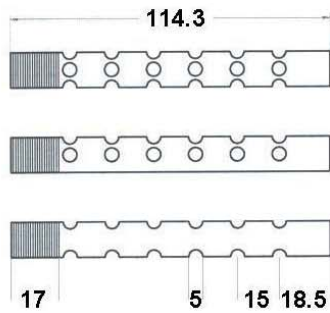
Front View



Left View



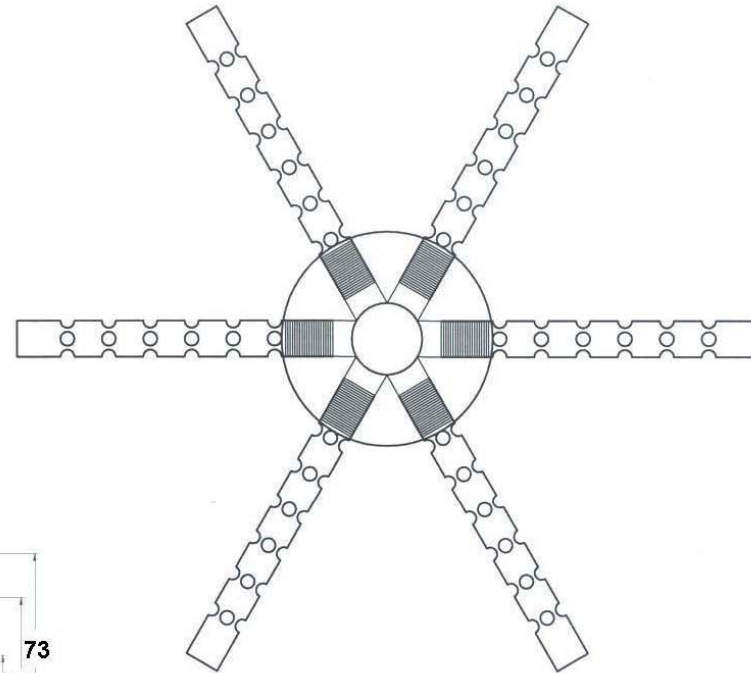
Figure 19 Pictures of the Hot Slurry Bubble Column Reactor



Bottom View

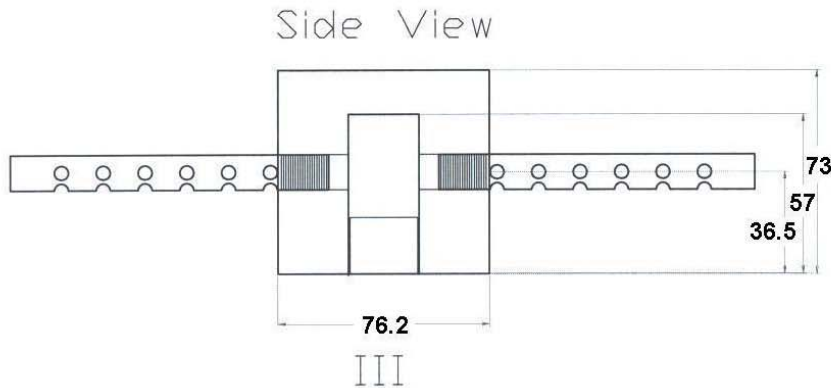
Side View I, II

Top View



Bottom View

All dimensions in mm unless otherwise mentioned



- I. 1/2" NPT Pipe. 6 holes on sides and bottoms, no holes on top. (Total 18 holes)
- II. 90° Angle between holes on each side.
- III. 1" F-NPT threads

(Verwendungsbereich)	(Zul. Abw.)	(Oberfl.)	Maßstab: MABSTAB	(Gewicht)
			(Werkstoff, Halbzeug) (Rohteil-Nr) (Modell- oder Gesenk-Nr)	
		Datum	Name	
		Bearb. BEARBEIT	NAME	
		Gegr. GEPRÜFT	NAME	
		Norm		
				GAS_SPARGER
				ARSAM.BEHKISH
				Blatt
Zust.	Änderung	Datum	Name	Ursprung
				Ersatz für
				Ersatz durch

Figure 20 The Mechanical Specifications of The Spider-Type Gas Sparger

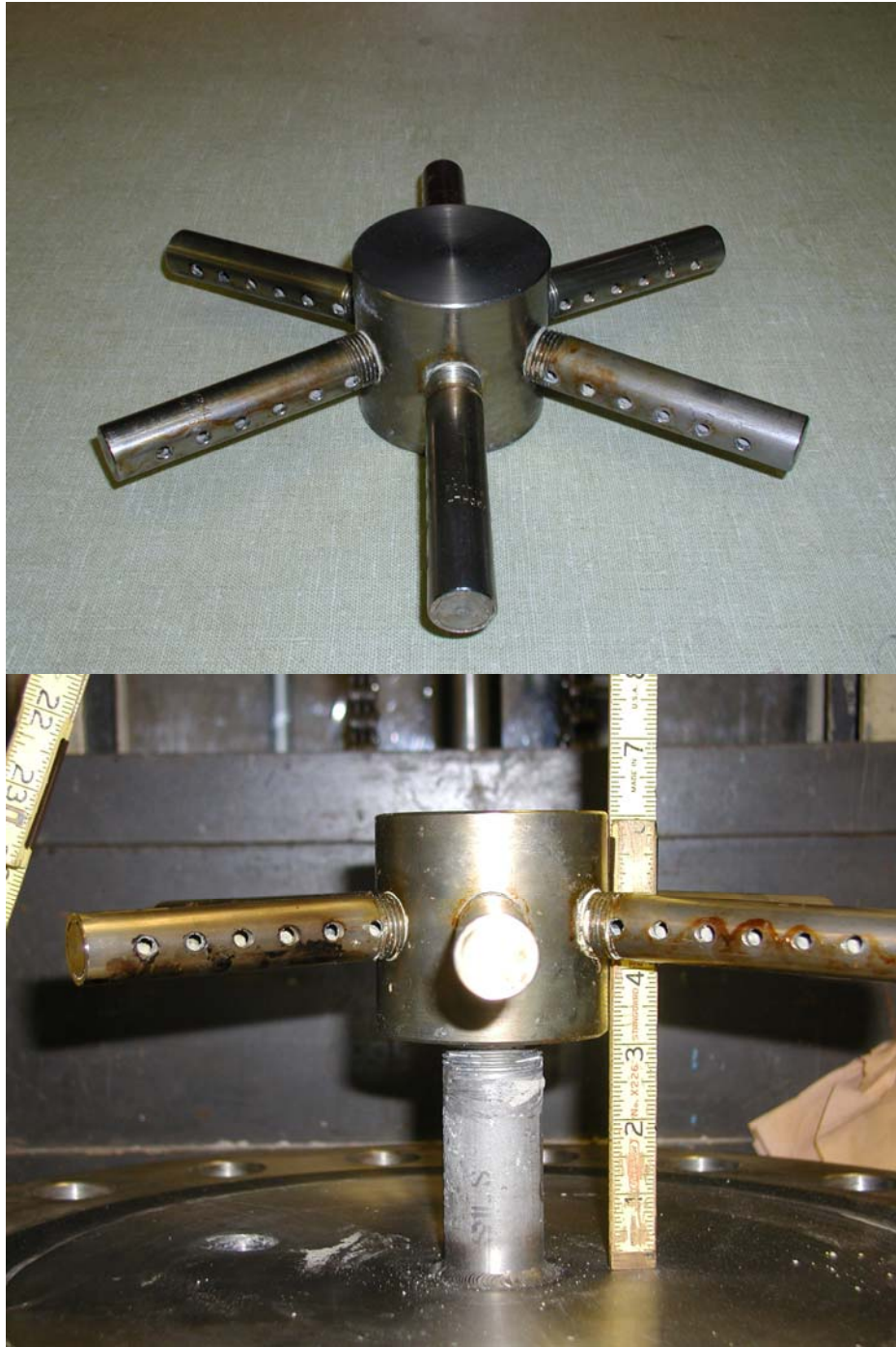


Figure 21 Pictures of the Spider-Type Gas Sparger and its Distance from the Bottom of the Column



Figure 22 Picture of the Setup for the High-Speed Phantom Camera used with the Hot SBCR

4.5 STATISTICAL EXPERIMENTAL DESIGN

The experimental approach was based on the Central Composite Statistical Design (CCSD) similar to that employed by Kim ⁽¹⁹⁰⁾, Li et al. ⁽¹⁹¹⁾, Tekie et al. ⁽¹⁹²⁾, Inga and Morsi ⁽¹⁹³⁾, and Fillion and Morsi ⁽¹⁶⁸⁾. This approach determines the effect of the variables at five levels on the gas holdup and mass transfer characteristics. This statistical design has a 2^k form where k defines the number of variables. For the hot SBCR the variables are pressure (P), superficial gas velocity (U_G), solid concentration (C_V), and temperature (T). In this design, all experiments should be equally distant from the center of a hypersphere have a radius of \sqrt{k} . The response surface can be expressed by:

$$\sum_{i=1}^k x_i^2 = \sqrt{k} \quad (4-9)$$

where x_i represents the coded value of each variable and is defined by:

$$x_i = 2 \left[\frac{2X_i - (X_{i,L} + X_{i,H})}{X_{i,H} - X_{i,L}} \right] \quad (4-10)$$

Where X_i is the i th variable and $X_{i,L}$ and $X_{i,H}$ are the lowest and highest levels of X_i . Equation (4-10) is only valid for 4-variable design.

To analyze the effect of these variables on the gas holdup and the volumetric liquid-side mass transfer coefficient, the results obtained according to this matrix are correlated in terms of these parameters. The statistical correlation is generally in the form of:

$$Ln(\Omega) = a_0 + \sum_{i=1}^k a_i X_i + \sum_{\substack{i=1 \\ j \geq i}}^{\Psi} b_{i,j} X_i X_j \quad (4-11)$$

Where Ω is the response parameters to be correlated and in this study it is either ε_G or $k_L a$. The parameters X_i are the coded variables corresponding to the operating variables, a_0 , a_i and b_{ij} are coefficients.

The term Ψ in Equation (4-11) depends on the number of variables k and is given as:

$$\Psi = \sum_{n=1}^k n \quad (4-12)$$

4.5.1 CCSD for the Cold SBCR

The operating variables for the cold SBCR are pressure (P), superficial gas velocity (U_G), and volumetric solid concentration (C_V). The gases used in the first unit are H_2 , He, CO, N_2 and CH_4 . The coded values are normalized and the coordinates of the experiments with the coded variables are: (0, 0, 0) for the central point, $(\pm 1, \pm 1, \pm 1)$ for the factorial points and $(\pm\sqrt{3}, 0, 0)$, $(0, \pm\sqrt{3}, 0)$ and $(0, 0, \pm\sqrt{3})$ for the axial points. Table 15 lists the value of the coded variables. Figure 23 a) shows the distribution of experiments according to the statistical composite design matrix for the cold SBCR.

4.5.2 CCSD for the Hot SBCR

The operating variables in the second unit SBCR are the same as in the first unit plus the temperature (T). Due to safety consideration, the gases to be used in the hot unit are N_2 and He as a substitute for CO and H_2 respectively. The coded values are normalized and the coordinates of the experiments with the coded variables are: (0, 0, 0, 0) for the central point, $(\pm 1, \pm 1, \pm 1, \pm 1)$ for

the factorial points and $(\pm 2, 0, 0, 0)$, $(0, \pm 2, 0, 0)$ and $(0, 0, \pm 2, 0)$, $(0, 0, 0, \pm 2)$ for the axial points. Table 16 list the value of the coded variables used in this study. Figure 23 b) shows the distribution of experiments according to the statistical composite design matrix.

Table 15 Values of the coded variables for the experimental design in the cold SBCR

<i>Variable</i>	<i>Coded variable</i>	<i>Values of the coded Variables</i>				
		$-\sqrt{3}$	-1	0	$+1$	$+\sqrt{3}$
P, (bar)	X ₁	1.72	2.84	4.45	6.02	7.17
U _G , (m/s)						
H ₂		0.080	0.100	0.138	0.172	0.197
CH ₄	X ₂	0.080	0.097	0.120	0.140	0.160
He		0.080	0.095	0.115	0.135	0.150
CO/N ₂		0.080	0.093	0.110	0.127	0.140
C _V , (vol.%)	X ₃					
Glass beads		0	7.60	18	28.40	36
Alumina		0	4.62	10	15.77	20

Table 16 Value of the coded variables for the experimental design in the hot SBCR

<i>Variable</i>	<i>Coded variable</i>	<i>Values of the coded Variables</i>				
		-2	-1	0	$+1$	$+2$
P, (bar)	X ₁	6.89	12.07	17.24	22.41	27.58
U _G , (m/s)	X ₂	0.180	0.1975	0.215	0.2375	0.250
T (K)	X ₃	323	355.5	388	420.5	453
C _V , (vol.%)	X ₄	0	5	10	15	20

a) Cold SBCR

		C1	C2	C3	C4	C5
U1	P1					
	P2					
	P3			■		
	P4					
	P5					
U2	P1					
	P2		■		■	
	P3					
	P4		■		■	
	P5					
U3	P1					
	P2					
	P3	■		■		■
	P4					
	P5			■		
U4	P1					
	P2		■		■	
	P3					
	P4		■		■	
	P5					
U5	P1					
	P2					
	P3			■		
	P4					
	P5					

b) Hot SBCR

		C1					C2					C3					C4					C5				
		P1	P2	P3	P4	P5	P1	P2	P3	P4	P5	P1	P2	P3	P4	P5	P1	P2	P3	P4	P5	P1	P2	P3	P4	P5
T1	U1																									
	U2																									
	U3														■											
	U4																									
	U5																									
T2	U1																									
	U2																									
	U3																									
	U4																									
	U5																									
T3	U1																									
	U2																									
	U3																									
	U4																									
	U5																									
T4	U1																									
	U2																									
	U3																									
	U4																									
	U5																									
T5	U1																									
	U2																									
	U3																									
	U4																									
	U5																									

Figure 23 Central Composite Statistical Design Matrixes

a) 3 Variables at 5 Levels in the Cold SBCR

b) 4 Variables at 5 Level in the Hot SBCR

4.6 EXPERIMENTAL PROCEDURES

The experimental procedures to obtain the volumetric mass transfer coefficients ($k_L a$), gas holdup (ϵ_G), and the bubble size distribution, Sauter-mean bubble diameter (d_{32}), and the axial solid distribution, $C_S(z)$, are given below.

4.6.1 $k_L a$ Measurement

The physical gas absorption technique was employed to obtain $k_L a$ for the gases in Isopar-M under the operating conditions listed in Table 15 and Table 16. The experimental procedure to obtain $k_L a$ in both the cold and hot SBCRs is described below:

1. A predetermined amount of slurry is charged to the reactor, (98 liters to cold and 95.1 to the hot SBCR, respectively).
2. The entire system is vacuumed to remove any dissolved gases in the liquid. Once the pressure in the reactor reaches the vapor pressure of Isopar-M, the vacuum is stopped.
3. The hot SBCR reactor is then heated to the desired temperature.
4. The gas is charged to the supply vessel and an initial mass balance is built.
5. The gas is then charged to the reactor until the desired pressure is reached.
6. The compressor is started to a preset gas velocity and the gas enters the bottom of the reactor (through the slurry). The reactor pressure is recorded as a function of time during the gas absorption in the slurry until thermodynamic equilibrium is reached.
7. Once the system reaches thermodynamic equilibrium, data collection is stopped. $k_L a$ is then calculated from the transient part of the pressure-time data and the gas solubility is

obtained from the equilibrium part. In order to obtain different k_{La} at various pressures, Steps 3-5 are repeated.

4.6.2 ϵ_G Measurement

Once the system has reached thermodynamic equilibrium, the following procedure is followed to obtain the gas holdup:

1. The dP cells legs are purged of liquid or slurry and pressurized with the gas.
2. At the predetermined gas velocity, the hydrostatic pressure is measured at different positions along the height of the reactor by opening and closing the corresponding valves.
3. The computer collects the dP cell readings and calculates the gas holdup at any given position.

4.6.3 Bubble Size Distribution Measurement

The Dynamic Gas Disengagement (DGD) technique was used to obtain the bubble size and the bubble size distribution. In this procedure, the dP cell legs at a given position are opened. The compressor and the inlet valve for the gas flow at the bottom of the reactor are then shut off, and as a result the gas within the liquid disengages. The dP readings are then recorded until all the gas bubbles are completely disengaged and the pressure is leveled off.

In the hot SBCR, this procedure was performed without shutting off the compressor by redirecting the gas flow from the bottom to the top of the reactor using the pneumatically actuated valves.

4.6.4 Sampling of the Solid Particles

Solids are collected from the sampling ports located on the legs of the dP cells. Three and four sampling ports are used in the cold and hot SBCRs respectively. The distance of the sampling ports from the bottom of the columns are 0.299, 0.832, and 1.252 m for the cold SBCR and 0.241, 0.457, 0.883, and 1.310 m for the hot SBCR.

To collect solid particles at a given concentration, the reactor is pressurized, and for the hot SBCR, heated to a pre-determined pressure and temperature. The compressor is then turned on at a specific superficial gas velocity and the gas is sparged in the slurry until a good mixing is achieved. A certain amount of slurry (~0.25 L) is then collected from each sampling ports. The samples are first weighted before the liquid is filtered. The wet solids are dried in an oven until all liquids are evaporated. The dry samples are then weighted and the concentration of the solids in the slurry for every axial position is measured. These steps are repeated for other pressures, gas velocities, temperatures and solid concentrations.

5.0 CALCULATIONS

The calculation of the gas solubility was carried out using the Peng-Robinson Equation of State and the ideal gas law. C^* was measured using a 4-liter stirred reactor and the physical gas absorption technique was used to obtain $k_L a^{(189)}$. The details of the calculation of C^* and $k_L a$ and the general assumptions are described below.

In both reactors the binary mixture behaviors was assumed to be ideal and the operating conditions used justify such an assumption. Thus, the use of an Equation-of-State, which requires the knowledge of the binary interaction parameters, was unnecessary.

In the feed tank, a non-ideal gas was assumed and the Peng-Robinson Equation-of-State (PR-EOS) was used, since the pressure in this unit was high.

The gas and liquid were assumed well mixed, i.e., the concentration of the gas phase in the liquid phase was assumed to be homogeneous.

5.1 PENG-ROBINSON EQUATION OF STATE

The Peng and Robinson Equation-of-State (PR-EOS) was used to calculate the number of moles of the gas in the feed tank before and after charging the reactor. The equation can be written as:

$$P = \frac{RT}{v-b} - \frac{a(T)}{v(v+b)+b(v-b)} \quad (5-1)$$

This equation can be expressed in terms of the compressibility factor, Z as:

$$Z^3 - (1 - B)Z^2 + (A - 3B^2 - 2B)Z - (AB - B^2 - B^3) = 0 \quad (5-2)$$

where

$$A = \frac{aP}{R^2T^2} \quad (5-3)$$

$$B = \frac{bP}{RT} \quad (5-4)$$

$$z = \frac{Pv}{RT} \quad (5-5)$$

For a single-component, one-phase system the solution of the Equation (5-2) results in three real roots or one real and two imaginary roots. The real root is referred to the gas phase. At the critical point:

$$a(T_C) = 0.45724 \frac{R^2 T_C^2}{P_C} \quad (5-6)$$

$$b(T_C) = 0.07780 \frac{RT_C}{P_C} \quad (5-7)$$

At any temperature:

$$a(T) = a(T_C) \alpha(T, \omega) \quad (5-8)$$

$$b(T) = b(T_C) \quad (5-9)$$

where

$$\alpha^{1/2} = 1 + \kappa(1 - T_R^{1/2}) \quad (5-10)$$

$$\kappa = 0.37464 + 1.5422 \omega - 0.26992 \omega^2 \quad (5-11)$$

Equation (5-2) was used to calculate the molar volume of the gas in the feed tank at given pressure. The number of gas moles is obtained from the molar volume and the preheater volume.

$$N_{1,FT} = \frac{V_{FT}}{v} \quad (5-12)$$

5.2 CALCULATION OF EQUILIBRIUM SOLUBILITY, C*

The solubility of the gas in Isopar-M was calculated using a material balance built on the gas and liquid phases. The number of mole of the gas in the liquid was equated to the difference between the total amount of gas charged in the reactor before mixing, $N_{1,T}$ and the amount of remaining gas in the reactor after reaching thermodynamic equilibrium, $N_{G,T}$.

$$N_{1,T} = \left(\frac{1}{v_{I,FT}} - \frac{1}{v_{F,FT}} \right) V_{FT} \quad (5-13)$$

$$N_{G,T} = \frac{P_{1,F} V_G}{RT} \quad (5-14)$$

The solubility C^* was expressed as:

$$C^* = \left[N_{1,T} - \frac{P_{1,F} V_G}{RT} \right] \frac{1}{V_L} \quad (5-15)$$

The C^* values obtained at various pressures were correlated as a function of the equilibrium pressure $P_{1,F}$ with a linear or a quadratic equation as follows:

- The linear correlation, known as Henry's Law, is:

$$C^* = \frac{P_{1,F}}{He} \quad (5-16)$$

where He is Henry's Law constant.

- The quadratic correlation is:

$$C^* = E_o P_{1,F} + E_1 P_{1,F}^2 \quad (5-17)$$

The selection of Equation (5-16) or (5-17) for $k_L a$ calculation is based on the best fit of the solubility data.

5.3 CALCULATION OF $k_L a$

The transient physical gas absorption technique, where the decline of the total pressure of the system with time is recorded, in conjunction with total moles and volume balances was used to calculate $k_L a$ values. The rate of mass transfer from the solute gas to the liquid phase was calculated using the two-film model as:

$$\frac{dn_{1L}}{dt} = k_L a (C^* - C_L) V_L \quad (5-18)$$

where n_{1L} is the number of moles of component 1 absorbed in the liquid phase, C^* is the concentration of the solute 1 at the gas-liquid interface, C_L is the concentration of solute 1 in liquid bulk, and V_L is the volume of the liquid phase.

Three methods were developed by Inga ⁽¹⁸⁹⁾ for the calculation of the gas/liquid volumetric mass transfer coefficient in the SBCR, namely: the integral method, the differential method, and the multiple linear regression method. These three methods gave similar results, however, the selection of one of them should be based upon the mathematical stability of the final function. In the following, a summary of these methods is given.

5.3.1 The Integral Method

The calculated solubility values can be modeled by Henry's Law as:

$$C^* = \frac{P_T - P_S}{He} \quad (5-19)$$

The total number of moles, N_0 can be written as:

$$N_0 = N_G + N_L = \frac{(P_T - P_S)V_G}{RT} + C_L V_L \quad (5-20)$$

Using Equations(5-19) and (5-20), the rate of mass transfer between phases, (5-18), can be written as:

$$\frac{V_G}{RT} \frac{dP_T}{dt} = -(V_L k_L a) \times \left[\frac{P_T - P_S}{He} - \frac{N_0 - (P_T - P_S)V_G/RT}{V_L} \right] \quad (5-21)$$

Separating the variables for integration gives:

$$\frac{\theta}{(P_T - P_S) \left[\frac{1}{He} + \theta \right] - \frac{N_0}{V_L}} dP_T = -k_L a dt \quad (5-22)$$

Integrating both sides, one will obtain the following relation:

$$\frac{\theta}{\frac{1}{He} + \theta} \ln \left[(P_T - P_S) \left(\frac{1}{He} + \theta \right) - \frac{N_0}{V_L} \right] = -k_L a \cdot t + C \quad (5-23)$$

where

$$\theta = \frac{V_G}{V_L RT} \quad (5-24)$$

If the left-hand side of the Equation (5-23) is plotted vs. time t and gives a straight line during the transient part, the slope of this line will be the value of $k_L a$.

It should be mentioned that this method was used to obtain $k_L a$ in the present study.

5.3.2 The Differential Method

Equation (5-22) was solved by approximating dP as ΔP and dt as Δt .

Since the readings were taken at $\Delta t < 0.05$ s, this assumption seems reasonable. Equation (5-22) can be expressed as:

$$A_L \Delta P = -V_L k_L a \Delta t \quad (5-25)$$

If the ratio between $(A_L \Delta P)$ and $(-V_L \Delta t)$ is constant, the resulting value will correspond to $k_L a$.

5.3.3 The Multiple Linear Regression Method

This method was based on the linearization of Equation (5-22):

$$-\frac{\theta}{k_L a} dP_T = \left[(P_T - P_S) \left[\frac{1}{He} + \theta \right] - \frac{N_0}{V_L} \right] dt \quad (5-26)$$

This function can be rewritten as a linear expression:

$$A_1 \Delta P = A_2 P_T \Delta t + A_3 \Delta t + A_4 \quad (5-27)$$

where

$$A_1 = -\frac{\theta}{k_L a} \quad (5-28)$$

$$A_2 = \frac{1}{He} + \theta \quad (5-29)$$

$$A_3 = \left[-\frac{N_0}{V_L} - P_s \left(\frac{1}{He} + \theta \right) \right] \quad (5-30)$$

$$A_4 = \text{constant} \quad (5-31)$$

Using multiple linear regression, the coefficients A_1 , A_2 , A_3 and A_4 can be found. The accuracy of this method was tested by the value of residuals and the constant obtained from the regression, (A_4). A_4 should be zero without forcing the data to go through the origin.

$$C^* = A_2 P - \theta \quad (5-32)$$

5.4 CALCULATION OF THE GAS HOLDUP, ϵ_G

The passage of gas bubbles throughout the slurry phase alters the pressure drop along the column and can be expressed by the following expression:

$$\frac{dP}{dh} = -\rho_F g \quad (5-33)$$

where ρ_F is the density of the three-phase system. The above expression can be integrated as follow:

$$\int_{P_B}^{P_T} dP = - \int_{L_B}^{L_T} \rho_F g dh \quad (5-34)$$

where the lower and higher limits are defined by the position of the dP cell legs on the column as shown in Figure 24, and hence gives:

$$(P_B - P_T) = \rho_F g (L_T - L_B) \quad (5-35)$$

The pressure difference between the lower and the higher legs is directly measured by the dP cell and since the distance between the legs is known, the above expression can be written as:

$$\Delta P_{cell} = \rho_F g \Delta L_{cell} \quad (5-36)$$

The density of the three-phase system can be expressed in terms of the gas holdup as follow:

$$\rho_F = \varepsilon_G \rho_G + (1 - \varepsilon_G) \rho_{SL} \quad (5-37)$$

By substituting Equation (5-37) into Equation (5-36) and solving for ε_G , the following expression for the gas holdup can be obtained:

$$\varepsilon_G = \left(\frac{\rho_{SL}}{\rho_{SL} - \rho_G} \right) \times \left(1 - \frac{\Delta P_{cell}}{\rho_{SL} g \Delta L_{cell}} \right) \quad (5-38)$$

If $\rho_{SL} \gg \rho_G$ the above expression is reduced to:

$$\varepsilon_G = 1 - \frac{\Delta P_{cell}}{\rho_{SL} g \Delta L_{cell}} \quad (5-39)$$

5.5 CALCULATION OF THE SAUTER-MEAN BUBBLE DIAMETER USING DGD TECHNIQUE

The total value of the gas holdup can be split into a gas holdup fraction corresponding to large and small gas bubbles. The separation of these two fractions is possible using the Dynamic Gas Disengagement (DGD) technique. The DGD technique relies on the assumption that large gas bubbles have greater rise velocity and therefore disengage first, whereas small gas bubbles retained within the slurry or entrained in the wakes created by the flow of large gas bubbles have smaller rise velocity and therefore disengage in later stage ⁽¹²⁶⁾. Numerous investigators (8,89,125,126,194,195,196,197,198,199,200) reported that the use of the DGD allowed to classify gas bubbles into two categories, large and small bubbles. The classification was generally performed by

analyzing the rate of gas bubbles disengagement recorded when the gas flow into the reactor was suddenly interrupted. Several investigators, however, argued that the disengagements of the large and small gas bubbles occur simultaneously whether the bubbles are interacting or independent of each others^(197,199). Another argument was made concerning the consideration of a constant slip velocity between the gas bubbles and the liquid during bubbles disengagement and liquid down-flow,^(194,197). Also, Jordan et al.⁽²⁰⁰⁾ pointed out that the “sequential” disengagement of large and then small gas bubbles could lead to underestimation of the gas holdup of small gas bubbles and showed that considering the effect of a constant gas slip velocity on the gas holdup of small gas bubbles could be neglected within an acceptable error.

In this study, the DGD technique was used to obtain the bubble size distribution and the Sauter mean bubble diameter, classify gas bubbles into small and large, and calculate the corresponding gas holdup of the small and large gas bubbles in the SBCR. The technique, introduced by Inga and Morsi⁽¹²⁶⁾ assuming that the total volume of small and large gas bubbles entering and leaving the dP zone delineated by the two legs remains unchanged, was adopted in this study. This assumption overcomes the problem of underestimating the gas holdup of small gas bubbles as suggested by Jordan et al.⁽²⁰⁰⁾. The DGD responses were analyzed to determine the bubble sizes as well as the corresponding gas holdup of small ($\epsilon_{G\text{-small}}$) and large ($\epsilon_{G\text{-large}}$) gas bubbles and in this study, gas bubbles having a diameter ≤ 0.0015 m ($d_B^* = 1.5$ mm) were arbitrarily considered small bubbles.

There are two approaches, which are based on the DGD method. The first approach uses the actual drop of the bed level and the second one is based on the measurement of the hydrostatic pressure with time. The limitation of the first approach is related to the method of

monitoring the change of the bed level, which may be carried out by visual observations (restricted to clear systems or gas/liquid systems) or by floating devices (restricted to a gas/liquid system due to the attachment of solid particles to the floating device). The second approach is based on the use of a dP cell and is only limited by the cell specifications. The assessment of ε_G with time using Equation (5-38) or (5-39) can lead to the estimation of the rate of disengagement of each “size” of bubbles.

An example of the behavior of ε_G with time is shown in Figure 24. Using the second approach, the two volume fractions corresponding to small and large bubbles as they leave the zone covered by the dP cell can be identified. From $t=0$ to t_1 , the dP cell shows no decline in ε_G , however, the signal from the orifice meter indicates no gas flow. This means that the amount of gas that is leaving the dP cell section (from L_B to L_T) is the same as that leaves the lower section (from L_0 to L_B). From t_1 to t_2 , the large gas bubbles having a bubble rise velocity (U_b) from L_T/t_1 to L_T/t_2 disengage from the cell region and during this period, the small gas bubbles present in the lower section (L_0 to L_B) do not affect the dP cell reading. From t_2 to t_3 , the small gas bubbles are disengaging from the cell region (L_B to L_T) and the dP cell reflects the small gas bubbles with U_b from L_T/t_2 to L_T/t_3 . The amount of the gas bubbles that leaves the dP cell region can therefore be represented by the decrease of the total gas holdup as follow:

$$\Delta\varepsilon_{G,i} = \int_{t_{i-1}}^{t_i} \frac{d\varepsilon_G}{dt} dt \quad (5-40)$$

And consequently the total gas holdup is defined as:

$$\varepsilon_G = \sum_{i=1}^n \Delta\varepsilon_{G,i} \quad (5-41)$$

The rise velocity of each size of the bubbles is then calculated at any time t .

This method is valid when dealing with gas/liquid system, however, the presence of solids should be accounted for, due to the settling velocity of the solid particles.

In this study, the correlation proposed by Fukuma et al. ⁽¹⁵¹⁾, Equation (2-83) who used up to 50 vol.% glass beads, was used to calculate the bubble size $d_{b,i}$. The Sauter mean bubble diameter (d_{32}) was calculated using the following expression:

$$d_{32} = \frac{\sum_{i=1}^k n_i d_{b,i}^3}{\sum_{i=1}^k n_i d_{b,i}^2} \quad (5-42)$$

Furthermore, the total gas holdup is expressed in terms of the holdup of small and large gas bubbles as:

$$\varepsilon_G = \varepsilon_{G\text{-Small}} + \varepsilon_{G\text{-Large}} \quad (5-43)$$

5.6 CALCULATION OF THE BUBBLE SIZE DISTRIBUTION USING PHOTOGRAPHIC METHOD

The hot SBCR was equipped with two Jerguson sight-windows which allowed simultaneous monitoring of the gas bubbles and the bed height. Using the phantom high-speed camera, a mini-movie of the gas bubbles rising through the solid-free liquid was recorded. The images were selected from each of the mini-movie recorded for the gas bubbles rising through the solid-free liquid. Analyzing a single frame obtained under a specific operating condition allowed the determination of the bubble size distribution. All bubble sizes visible in the frame of reference were carefully selected, and using Adobe Photoshop, the picture was digitalized so it

could be statistically analyzed. Figure 25 a) Snap shot using Phantom High-Speed Camera through the Jerguson Site- windows of the bubble column reactor, b) The digitalized image of the same shot using Adobe Photoshop software. shows a sample image shot using the Phantom camera and the digitalized image of the same shot. Once every gas bubble has been identified and the image digitalized, the Bios can Optima's version 4.1 Software package was used to determine the area of each gas bubble from which the individual bubble diameter was calculated. The bubble size distribution, statistically obtained, is then expressed in terms of the number frequency as a function of the bubble diameter. On the average about 200 bubbles were systematically analyzed for each photograph. It should be mentioned, however, that the photographic method was only used when the column was operating in the bubble column mode because the addition of the solid particles to the liquid made imaging of the gas bubbles difficult and proper video sampling of the gas bubbles was not feasible.

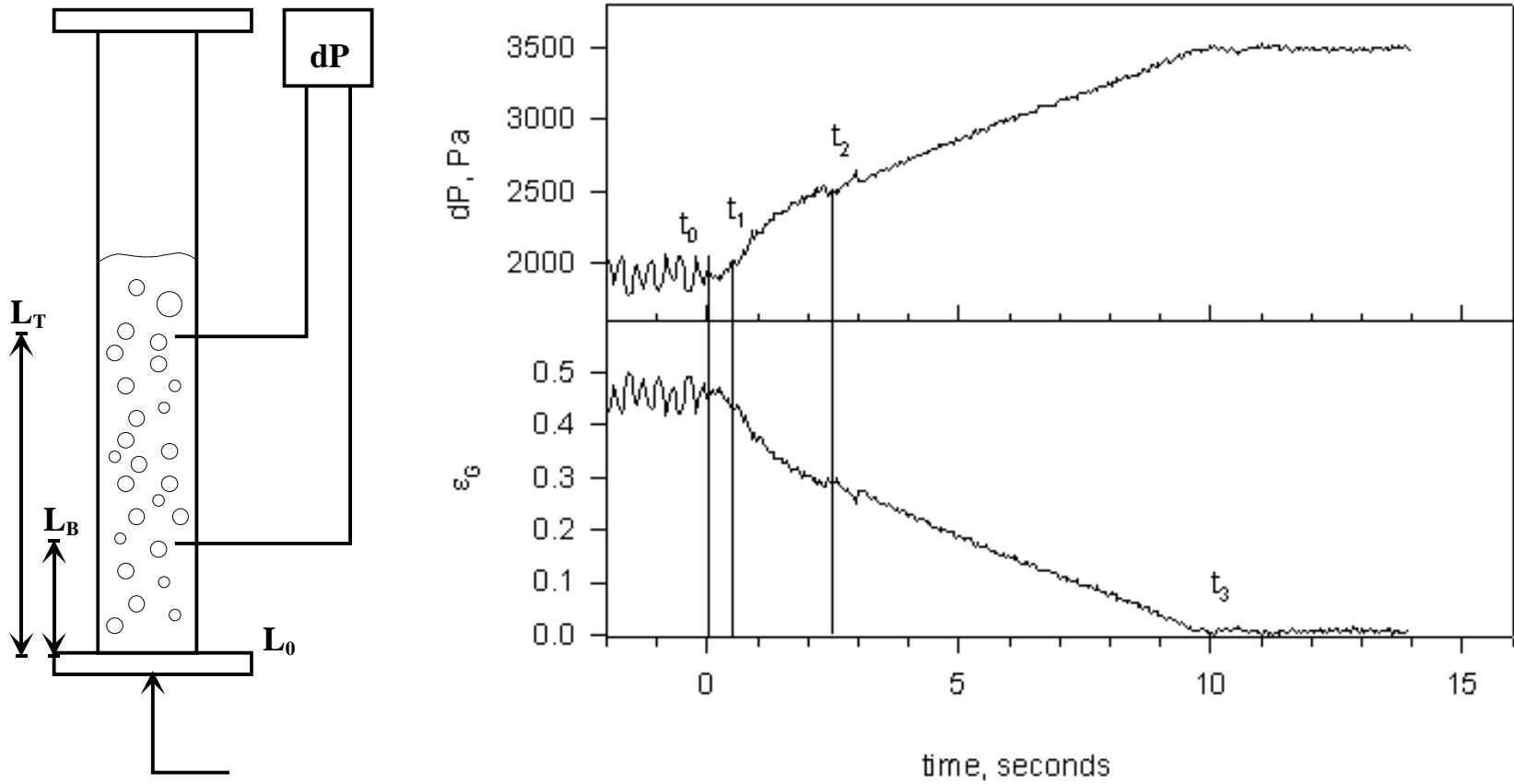


Figure 24 Dynamic Gas Disengagement in the Slurry Bubble Column Reactor

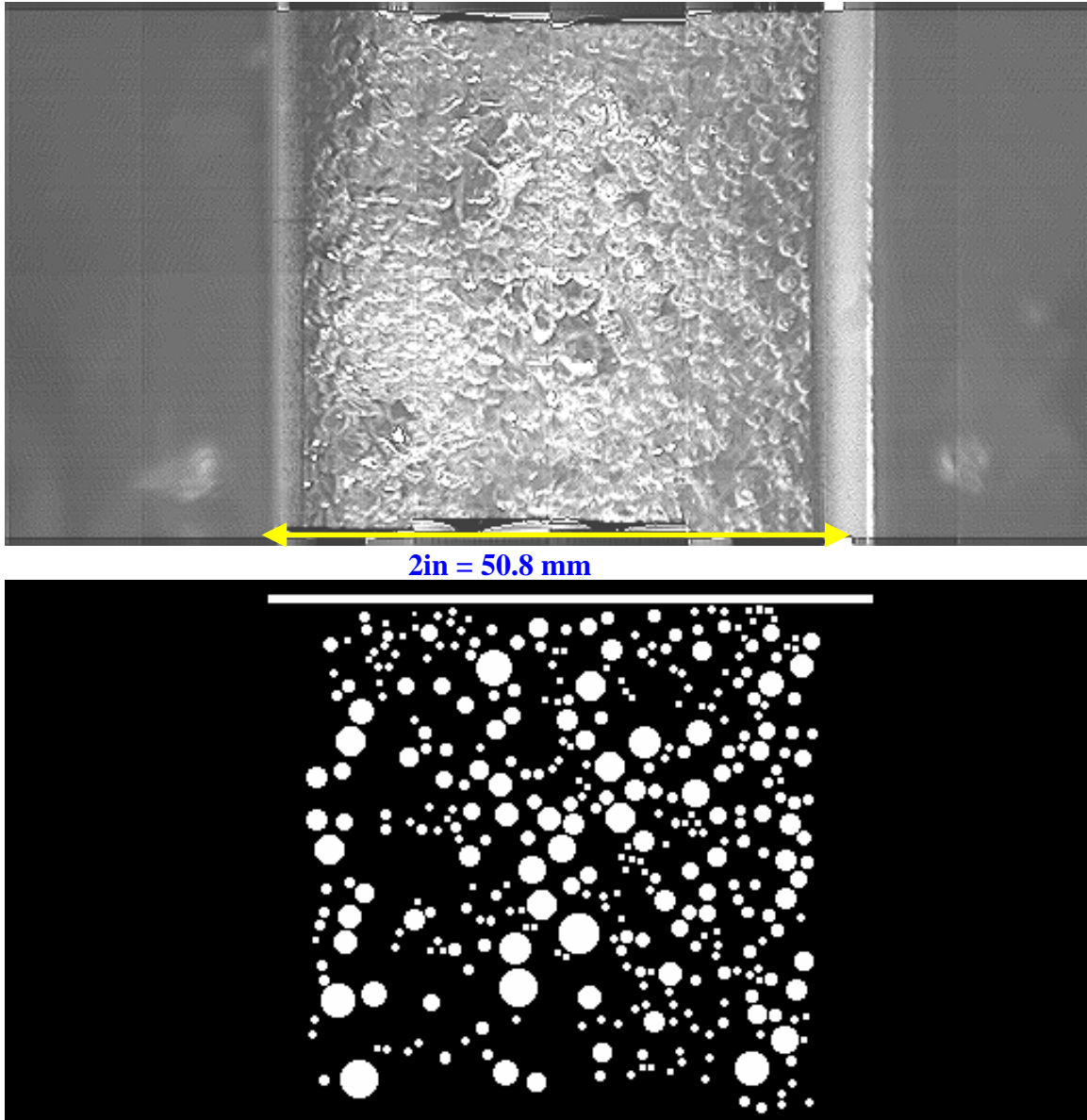


Figure 25 a) Snap shot using Phantom High-Speed Camera through the Jerguson Site-windows of the bubble column reactor, b) The digitalized image of the same shot using Adobe Photoshop software.

6.0 RESULTS AND DISCUSSION

The following sections present the experimental hydrodynamic and mass transfer data obtained in this study.

6.1 SOLUBILITY OF GASES IN ISOPAR-M

The solubilities of H₂, N₂, CO, CH₄ and He in Isopar-M were calculated using the material balance and the equilibrium thermodynamic conditions after the absorption had been completed. In this study, these values were obtained in the absence of solids particles under room temperature in a stirred reactor to insure better temperature and pressure control and more accurate liquid volume. Figure 26 presents the solubility of the gases in Isopar-M as a function of pressure. A comparison between the solubility values obtained in the stirred reactor and SBCR is illustrated in Figure 27, and as can be seen the data in both reactors are in good agreement.

The C* values were found to vary linearly with the gas partial pressure and Henry's law, Equation (5-16), was used to model the data with a correlation coefficient (R²) of 99%. The Henry's law constants, H_e, obtained for the five gases are given in Table 17. Also, in the pressure range studied, the solubility values obtained for the five gases in Isopar-M follow the trend:

$$C_{CH_4}^* > C_{CO}^* > C_{N_2}^* > C_{H_2}^* > C_{He}^*$$

Chang and Morsi ^(201, 202), Li et al. ⁽¹⁹¹⁾, and Inga ⁽¹⁸⁹⁾ previously reported the solubility of the same gases in different hydrocarbon liquid mixtures. They found that the solubility values for these gases followed the same trend as that obtained in this study.

Table 17 Henry's Law constants for gases in Isopar-M at 298 K

<i>Gas</i>	<i>He, bar m³/kmol</i>
H ₂	312.50
CO	140.85
N ₂	191.31
CH ₄	45.05
He	649.35

In the hot SBCR unit, the equilibrium solubility values of the two gases used (N₂ and He) were calculated using the same technique as mentioned above. Figure 28 a) and b) present the solubility of N₂, and He in Isopar-M as a function of pressure at different temperature, respectively. The Henry's law constant (He)_C was then calculated for each gas at different temperature as given in Table 18. From Figure 28 it can be noticed that the solubility of He in Isopar-M is dependent on temperature whereas in the case of N₂, the effect of temperature on the solubility values is less pronounced.

Figure 29 shows the Henry's Law constant as a function of 1/T and as can be observed Henry's law constants for N₂ are significantly lower than those of helium indicating that helium is notably less soluble in Isopar-M than N₂. Also, the Henry's law constants seem to first increase with temperature then decrease for both gases used. Although these changes in the trend of Henry's law constant with temperature is not very significant, such a behavior has been previously noticed by Alghamdi ⁽²⁰³⁾ using a N₂, He, H₂ and CO in Isopar-M.

Table 18 Values of the Henry's Law constant for the gases

Temperature (K)	$H_e, \text{bar m}^3 \text{ kmol}^{-1}$	
	N ₂	He
298	191.31	649.35
323	194.48	657.89
348	196.31	649.35
373	193.24	602.41
398	190.55	526.32
423	182.95	446.43
448	179.37	421.94
473	177.84	404.86

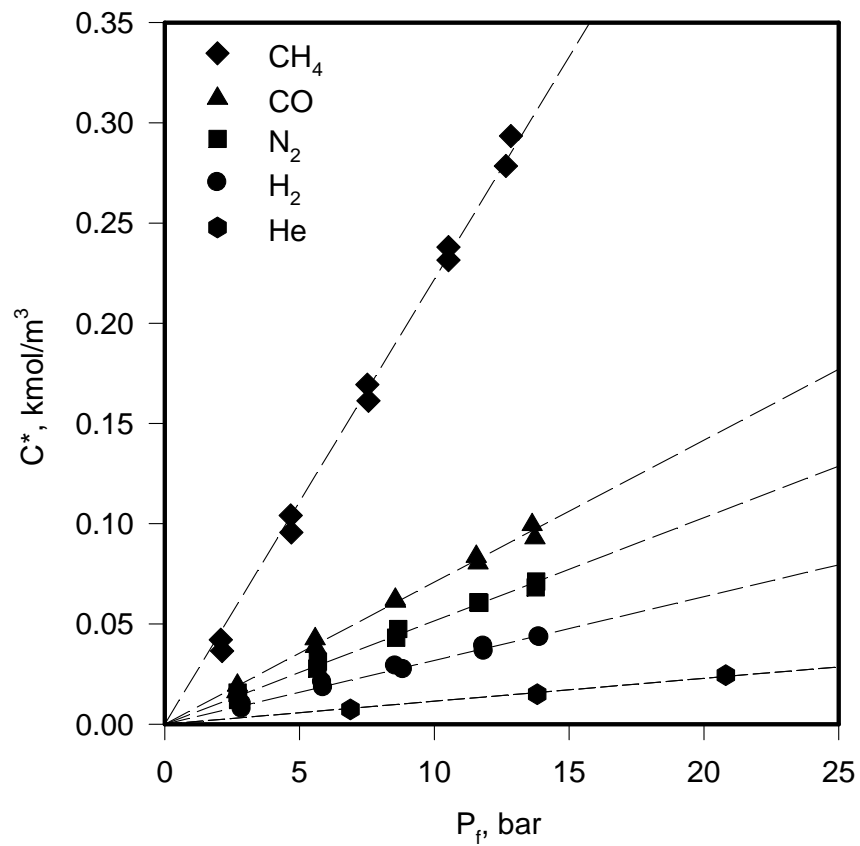


Figure 26 Solubility of Gases in Isopar-M at 298K

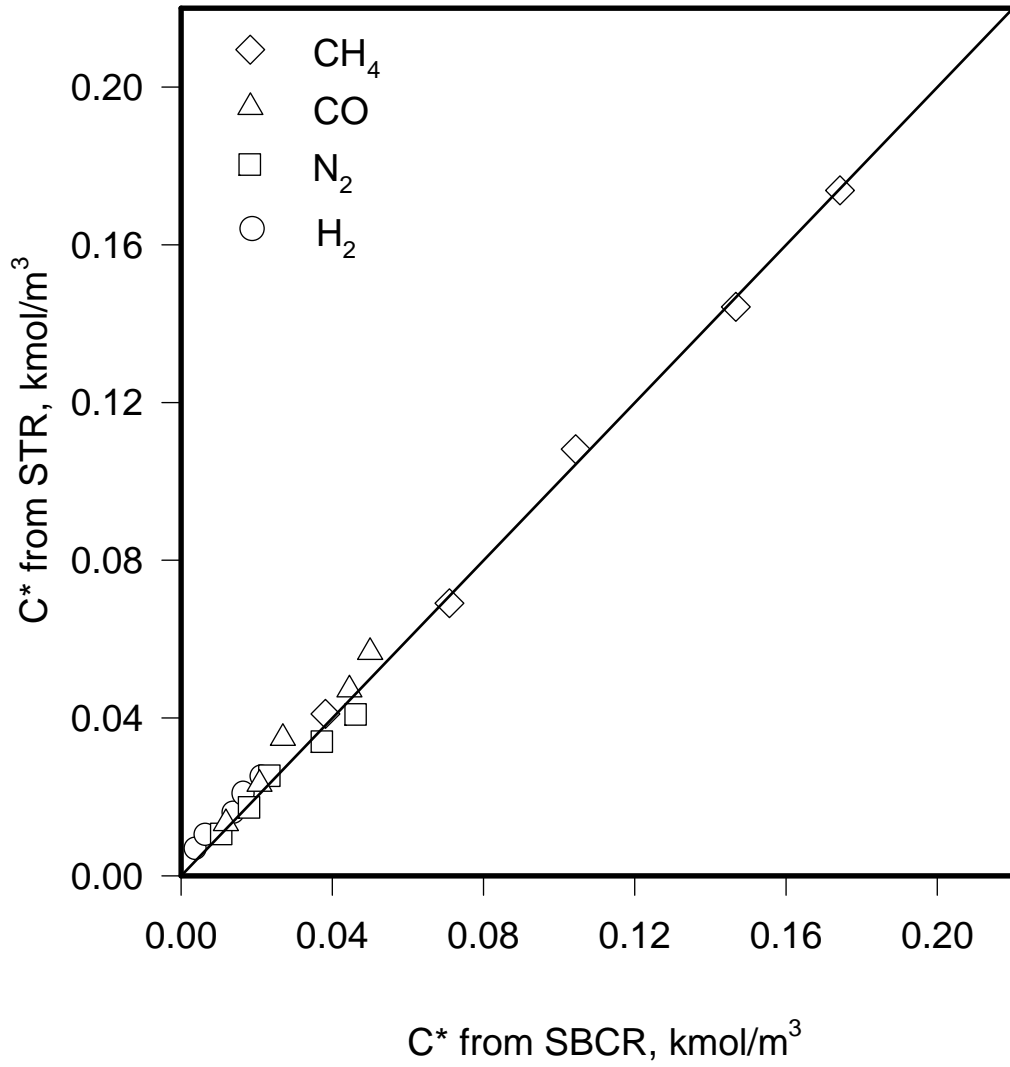


Figure 27 Comparison of C^* Values obtained in Cold SBCR and STR

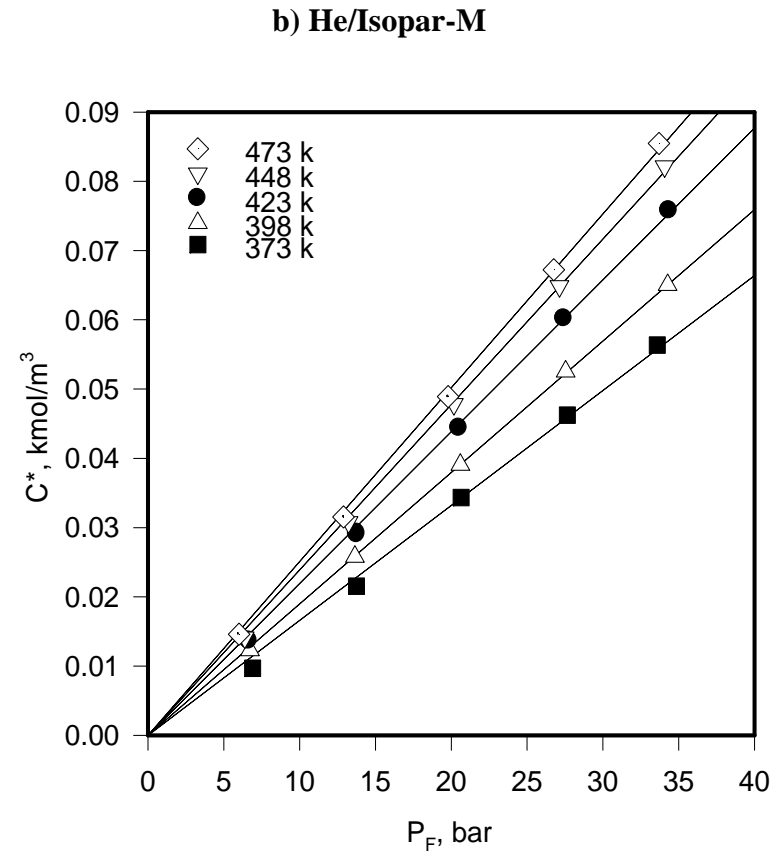
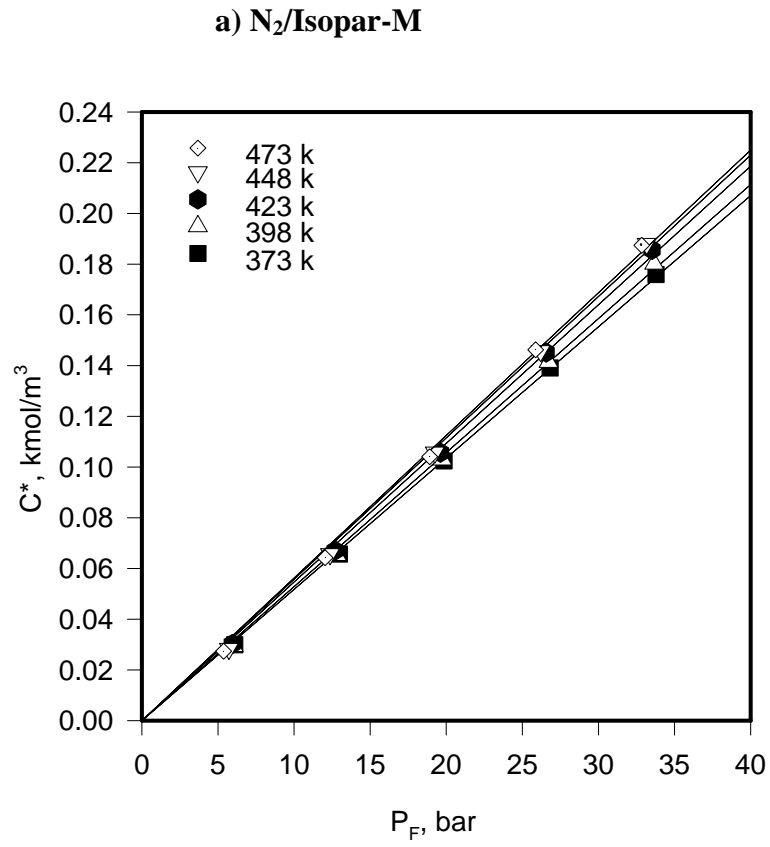


Figure 28 Solubility of N₂ and He in Isopar-M as a Function of Temperature

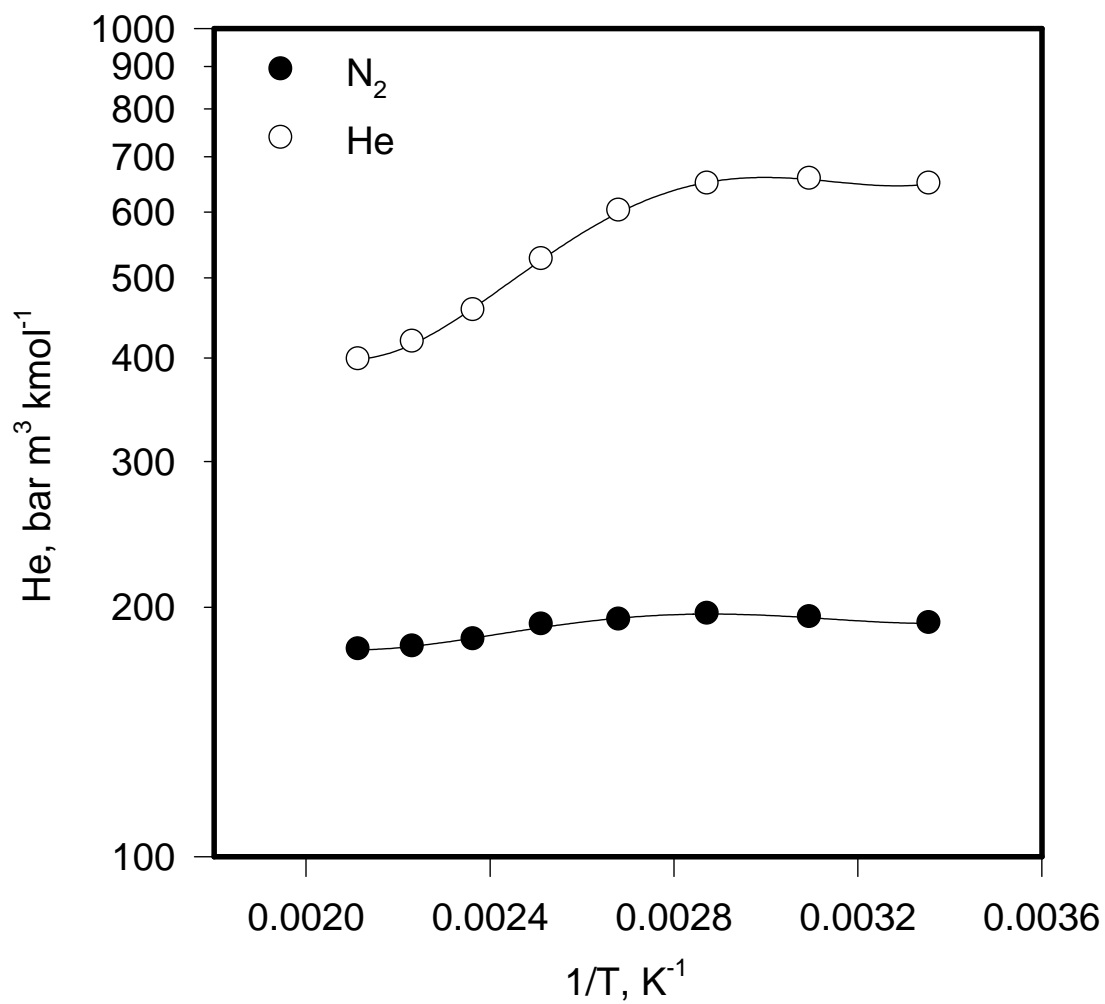


Figure 29 Henry's Law Constant for N_2 and He in Isopar-M

6.2 GAS HOLDUP IN THE COLD AND HOT SBCRS

As mentioned in Section 4.5.1, the gas holdup experiments in the cold and hot SBCRs were selected according to the central composite statistical design (CCSD) method. Equation (4-11) was modified to obtain the best fit by adding non-linear terms to correlate the total ε_G , $\varepsilon_{G\text{-Small}}$ and $\varepsilon_{G\text{-Large}}$ values. For the cold SBCR Equation (4-11) becomes:

$$\ln(\Phi)_{\text{COLD}} = a_0 + \sum_{i=1}^3 a_i X_i + \sum_{\substack{i=1 \\ j \geq i}}^6 b_{i,j} X_i X_j + \sum_{i=1}^3 c_i \sqrt{1 + \exp(X_i^2)} + d_1 \exp(-1 - X_3) \quad (6-1)$$

Where Φ can be ε_G , $\varepsilon_{G\text{-Small}}$ or $\varepsilon_{G\text{-Large}}$. The coefficients of Equation (6-1) for ε_G can be found in Table 19 and for $\varepsilon_{G\text{-Small}}$ and $\varepsilon_{G\text{-Large}}$ in Table 20.

Table 19 Coefficients for the ε_G correlation using Equation (6-1)

	<i>Glass beads system</i>				<i>Alumina system</i>	
	H ₂	CO	N ₂	CH ₄	He	N ₂
a ₀	-1.457	-2.444	-2.307	-1.997	-1.874	-1.584
a ₁	0.061	0.066	0.109	0.122	0.057	0.090
a ₂	0.109	0.078	0.082	0.101	0.101	0.065
a ₃	-	-0.287	-0.256	-0.184	-0.420	-0.264
b ₁₂	-	-0.007	-	-	-	-0.015
b ₁₃	0.009	-	0.020	-	-	-
b ₂₃	-	0.008	-	-	-	-
b ₁₁	-0.010	-0.057	-0.021	-0.023	-	-0.010
b ₂₂	-	-	-	-	-0.021	-0.051
b ₃₃	0.184	-0.468	-0.403	-0.177	0.112	0.193
c ₁	-	0.040	-	-	-	-
c ₂	-	-	-	-	-	0.020
c ₃	-0.235	0.402	0.341	0.148	-	-0.164
d ₁	-0.288	0.787	0.709	0.304	-0.433	-
AARE, %	1.5	2.0	2.1	2.3	3.6	4.2

Table 20 Coefficients for the $\varepsilon_{G\text{-Small}}$ and $\varepsilon_{G\text{-Large}}$ correlation using Equation (6-1)

	<i>Glass Beads System</i>								<i>Alumina System</i>			
	H_2		CO		N_2		CH_4		He		N_2	
	Small	Large	Small	Large	Small	Large	Small	Large	Small	Large	Small	Large
a_0	-3.812	-2.031	-2.983	-1.751	-4.046	-1.699	-3.835	-1.744	-4.215	-2.266	-3.657	-1.721
a_1	0.290	0.047	0.211	0.091	0.277	0.088	0.371	0.090	0.042	0.044	0.226	0.134
a_2	-	0.121	-	0.124	0.067	0.094	0.164	0.101	0.074	0.326	0.348	0.174
a_3	-0.931	0.302	-0.350	-0.305	-1.205	-0.287	-4.774	-0.139	-3.385	0.203	-0.679	-0.126
b_{12}	-	-	-0.043	-	-0.026	-	-0.091	-	0.061	0.024	0.079	0.045
b_{13}	0.130	-	-	0.025	0.039	0.019	0.096	0.020	-	-	-	-
b_{23}	-	-	-0.054	0.024	-	-	0.083	-	-	0.115	0.120	0.074
b_{11}	-	0.056	-	-	-0.057	-0.020	-	-	-	-	-0.198	-
b_{22}	-	-	0.153	-0.119	0.077	-0.015	-	-0.039	-	-0.093	0.137	0.063
b_{33}	-	-0.105	-	-	-0.729	-0.058	-	-	-	0.093	-	0.349
c_1	-	-0.062	-0.070	-0.026	-	-	-	-0.027	-	-	0.169	-
c_2	-0.080	-	-0.178	0.127	-	-	-	0.031	-	0.021	-	-
c_3	-	-0.090	-	0.073	0.402	0.101	2.522	0.009	1.037	-0.172	-0.080	-0.328
d_1	-0.388	0.694	0.244	-0.407	-	-0.358	-9.000	-0.132	-4.767	0.613	-	-
AARE,%	15	4	11	4	8	3	20	4	24	23	18	15

For the hot SBCR, Equation (4-11) was modified as follow:

$$Ln(\Phi)_{HOT} = a_0 + \sum_{i=1}^4 a_i X_i + \sum_{\substack{i=1 \\ j \geq i}}^{10} b_{i,j} X_i X_j + c_1 \exp(-1 - X_4) \quad (6-2)$$

The coefficients of Equation (6-2) for ε_G , and $\varepsilon_{G\text{-Large}}$ can be found in Table 21.

Figure 30 a) shows a comparison between the experimental and predicted values for all five gases in Isopar-M/glass beads, alumina slurry using Equation (6-1). Similarly, Figure 30 b) shows a comparison between the experimental and predicted values for N_2 and He in Isopar-M/alumina using Equation (6-2). As can be seen in these figures, all the predicted data are in good agreement with the experimental values.

Table 21 Coefficients for the ε_G , $\varepsilon_{G\text{-Small}}$ and $\varepsilon_{G\text{-Large}}$ correlation using Equation(6-2)

Coefficients	ε_G		$\varepsilon_{G\text{-Large}}$		$\varepsilon_{G\text{-Small}}$	
	N ₂	He	N ₂	He	N ₂	He
a ₀	-0.773	-1.071	-1.102	-0.990	-1.776	0.126
a ₁	0.058	0.079	0.054	0.055	0.082	0.012
a ₂	0.066	0.140	0.072	0.143	0.137	0.023
a ₃	0.036	0.016	-	-	0.074	0.007
a ₄	-0.316	-0.235	0.057	-0.264	-2.262	-0.115
b ₁₂	-0.017	-0.024	-	-	-	-
b ₁₃	-	-0.015	-	-	-	0.010
b ₁₄	-	0.015	0.011	0.016	-	-0.007
b ₂₃	-	-0.045	-0.043	-0.074	-	-0.014
b ₂₄	0.029	0.044	0.026	0.078	-	-
b ₃₄	-	-0.023	0.042	-	-0.080	-0.010
b ₁₁	-0.006	-0.012	-	-	-0.043	-0.004
b ₂₂	-	-0.065	-	-0.048	-0.059	-
b ₃₃	-0.006	-1.071	0.028	-	-0.097	-
b ₄₄	0.047	0.079	-0.098	-	0.678	0.033
c ₁	-0.227	-	-	-0.347	-2.376	-0.103
AARE, %	3	7	12	14	18	29

6.2.1 Effect of Pressure and Solid Concentration on ε_G

Figures 31 and 32 illustrate the effect of pressure on the total gas holdup (ε_G) and the holdup of large gas bubbles ($\varepsilon_{G\text{-large}}$) for CO, H₂, CH₄ and He in Isopar-M obtained in the cold SBCR; and for N₂ and He in Isopar-M obtained in the hot SBCR in the absence of solid particles, respectively. As can be seen in these figures the total gas holdups for all gases increase with pressure, whereas the gas holdup of large bubbles ($\varepsilon_{G\text{-large}}$) is almost independent of pressure. This means that the increase of ε_G with pressure (or gas density) is due mainly to the increase of the gas holdup of small gas bubbles ($\varepsilon_{G\text{-small}}$), which is in agreement with the finding reported in the literature⁽²⁰⁰⁾. Figure 32 also shows at low pressures the fast increase of the gas holdup for He in the hot SBCR suggests that its bubbles are larger than those of N₂, however, under high pressures from 17 to 30 bar the increase of ε_G for He and N₂ seems to lie within the same order

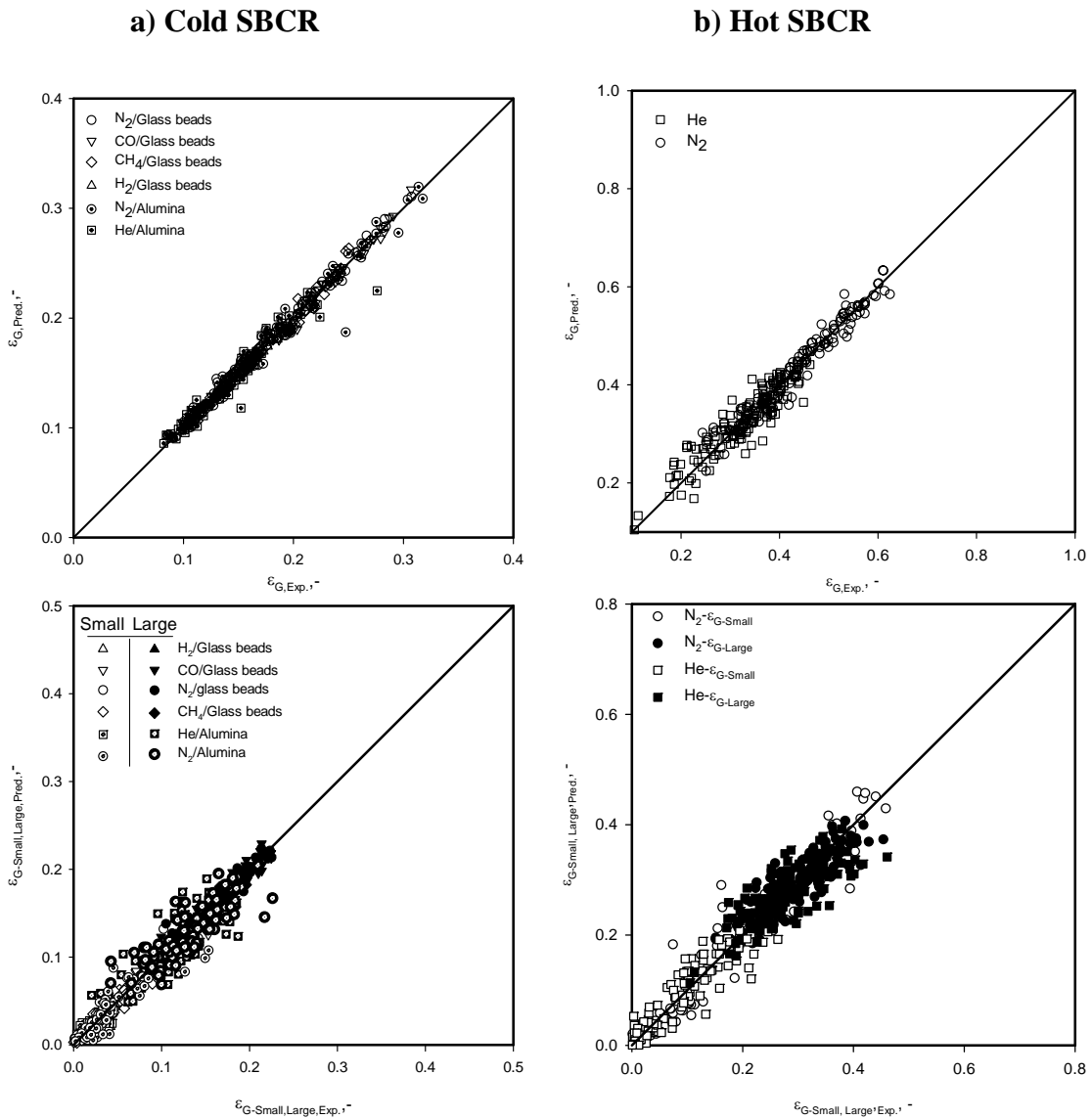


Figure 30 Comparison between the Experimental and predicted Holdup Values of the Gases in Isopar-M using Equation (6-1) and (6-2)

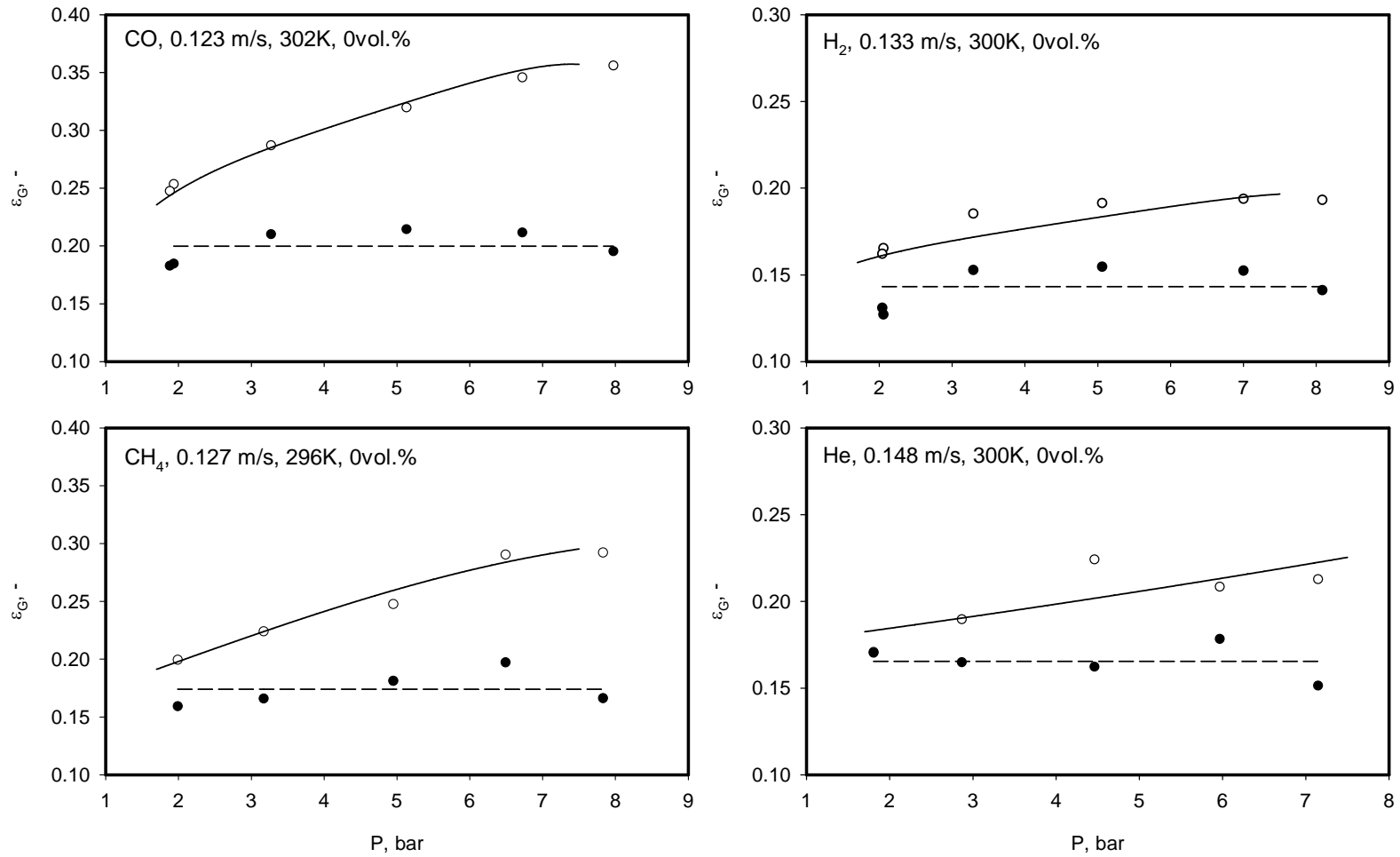


Figure 31 Effect of pressure on the ϵ_G and $\epsilon_{G-large}$ in the Cold SBCR

(Symbols: Plain: ϵ_G , Solid: $\epsilon_{G-large}$) Solid lines: Equation (6-1)

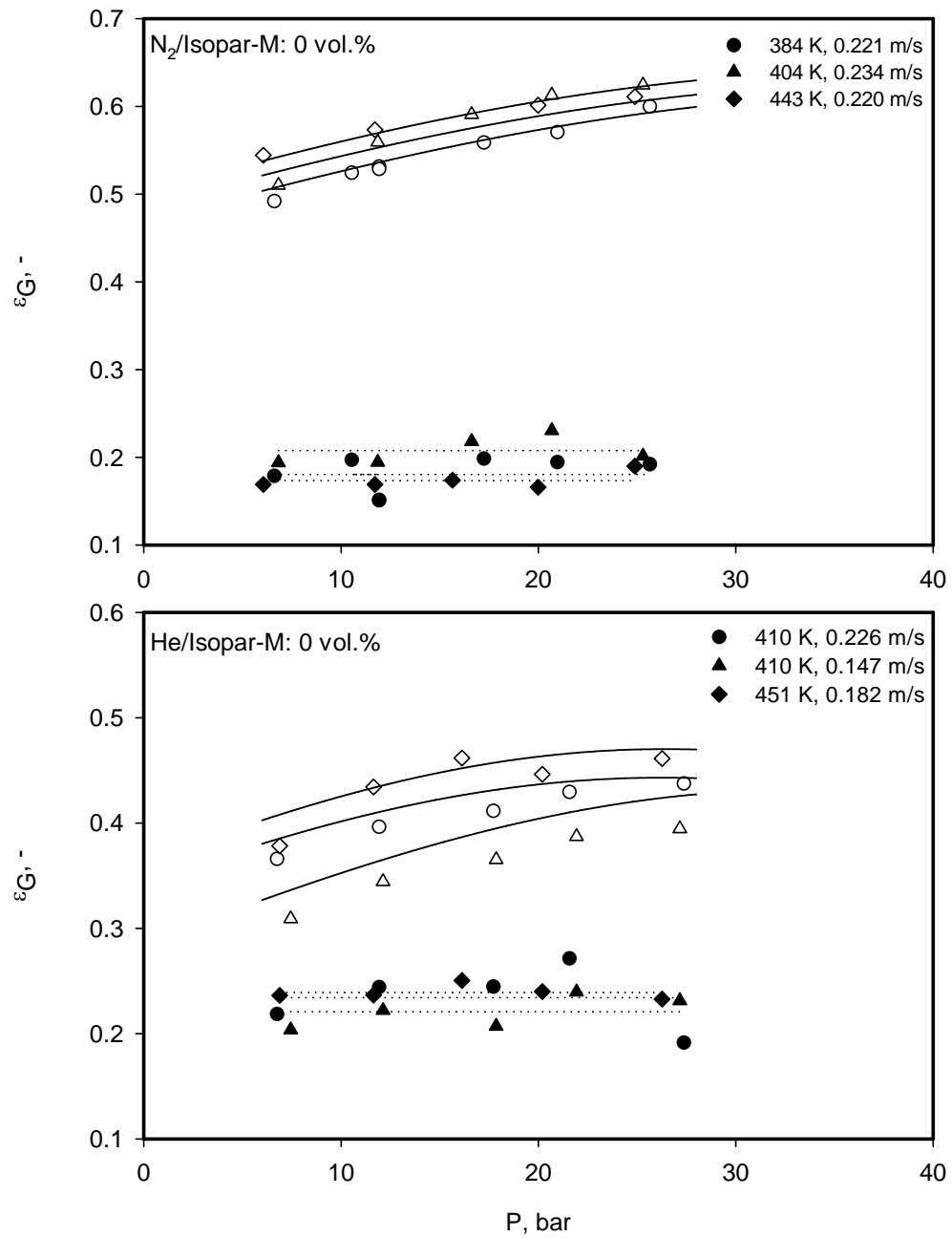


Figure 32 Effect of pressure on the ϵ_G and $\epsilon_{G-large}$ in the Hot SBCR

(Symbols. Plain: ϵ_G , Solid: $\epsilon_{G-large}$) Solid lines: Equation (6-2)

of magnitude. This behavior is because under low pressure, large and less-dense gas bubbles are formed and increasing the gas momentum under such conditions increases the rate of bubbles rupture and gas holdup of small gas bubbles, whereas under high pressures, small and dense gas bubbles are formed and increasing the gas momentum under such conditions would not be enough to rupture them and therefore the increase of ϵ_G becomes insignificant. Similar observations were made by Inga and Morsi ⁽¹²⁶⁾ who reported that ϵ_G increases under low pressures and then levels off under high pressures due to a balance between the gas bubbles rupture and coalescence. Under high pressure, it was reported that the coalescence rate of gas bubbles after their formation at the gas sparger would not be affected, and subsequently the gas holdup of large gas bubbles would remain constant ⁽⁴⁷⁾.

The gas holdup values of the five gases obtained also shows an increasing trend with pressure at any given solid concentration as shown in Figures 33 through 37 for the cold SBCR and in Figure 38 for the hot SBCR. The rate of ϵ_G increase, however, appears to gradually diminish with increasing pressure. For instance, the CH₄ data depicted in Figure 36 at a gas velocity of 0.099 m/s and zero solid concentration, show the increase of ϵ_G values from 1.9 to 5 bar is about 37%, whereas the difference from 5 to 7.8 bar is only 20%. Similar behavior can be observed at solid concentration of 28.4 vol.% where the increase of ϵ_G values from 1.7 to 4.4 bar is about 34% when compared to 12% from 4.4 to 7.2 bar. This means that the effect of the relative change in pressure (2.7 times from 1.7 to 4.4 bar) on ϵ_G is more important than the absolute change of 2.7 bar, indicating that ϵ_G values are strongly affected by the gas pressure, or the gas density, which is directly related to the gas momentum.

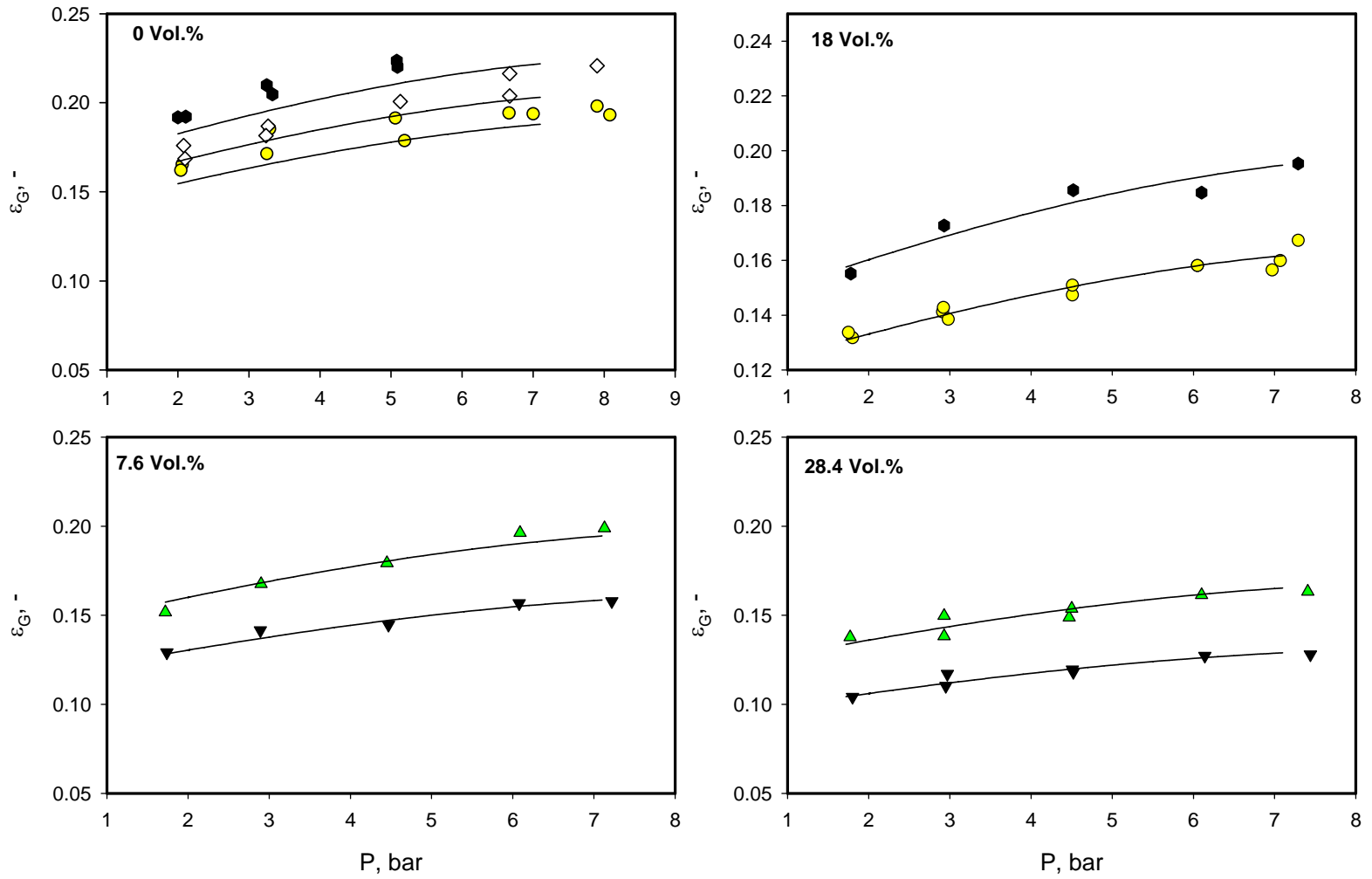


Figure 33 Effect of Operating Variables on ϵ_G of H_2 /Isopar-M/Glass Beads in the Cold SBCR

● 0.135 m/s
 ◇ 0.164 m/s
 ● 0.200 m/s
 ▼ 0.100 m/s
 ▲ 0.170 m/s
 Lines: Equation (6-1)

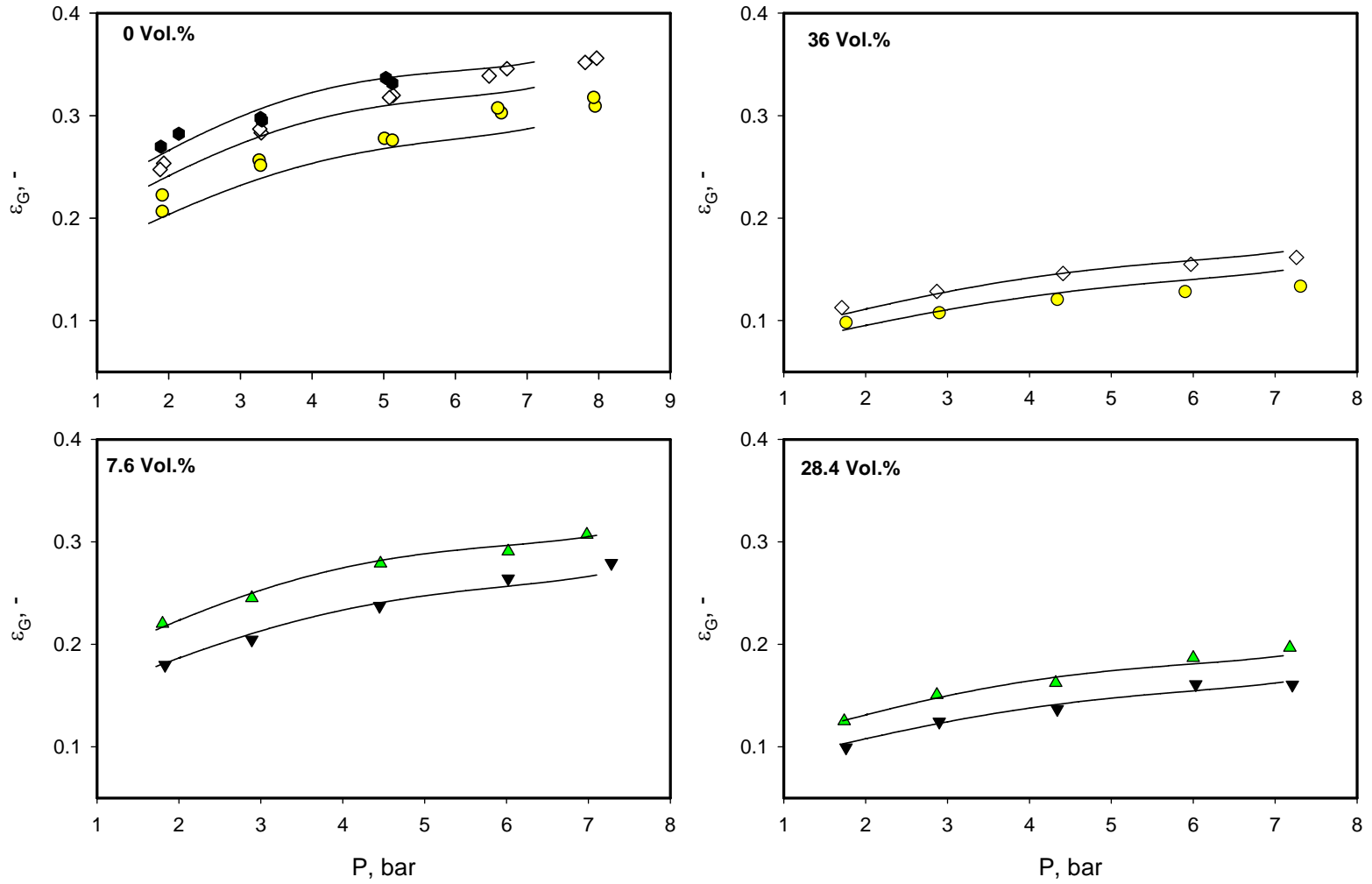


Figure 34 Effect of Operating Variables on ϵ_G of CO/ Isopar-M/Glass Beads in the Cold SBCR

● 0.085 m/s ▼ 0.093 m/s ▲ 0.103 m/s

◇ 0.122 m/s ● 0.141 m/s

Lines: Equation (6-1)

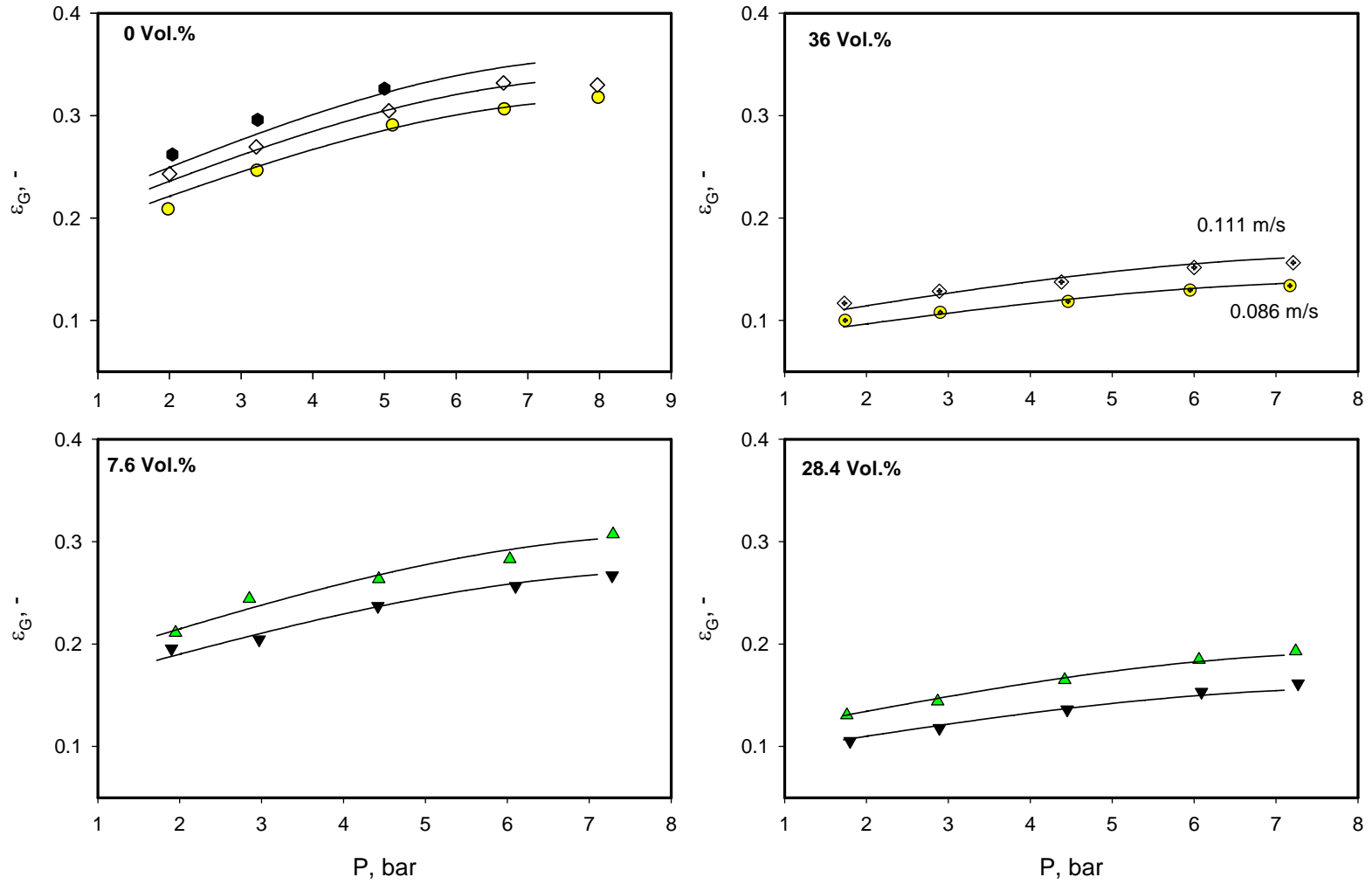


Figure 35 Effect of Operating Variables on ϵ_G of N_2 / Isopar-M/Glass Beads in the Cold SBCR

- 0.097 m/s
- ▼ 0.093 m/s
- ▲ 0.130 m/s
- 0.121 m/s
- 0.141 m/s

Lines: Equation (6-1)

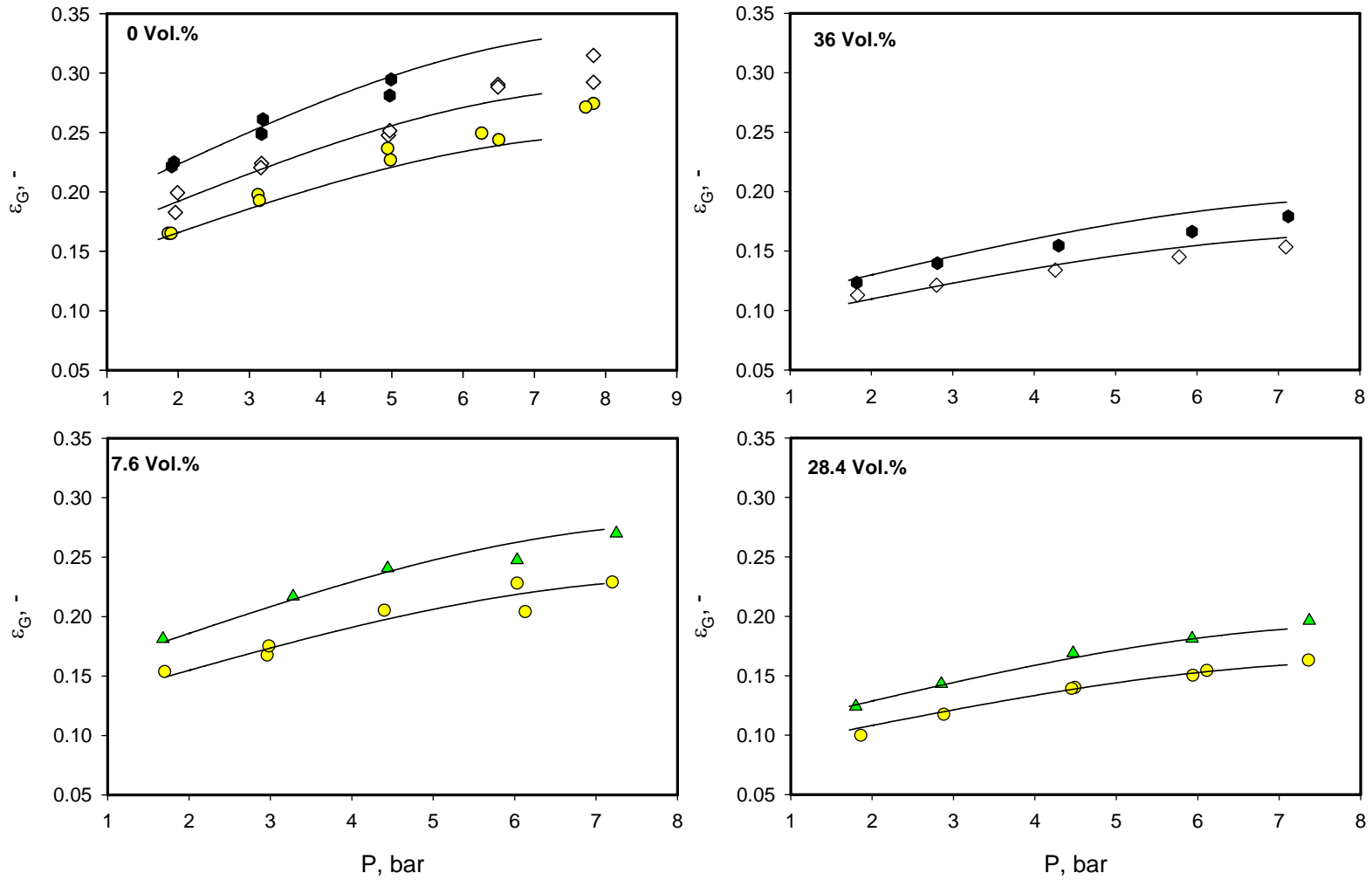


Figure 36 Effect of Operating variables on ϵ_G of CH_4 / Isopar-M/Glass Beads in the Cold SBCR

- 0.099 m/s
- 0.122 m/s
- ▲ 0.140 m/s
- 0.160 m/s

Lines: Equation (6-1)

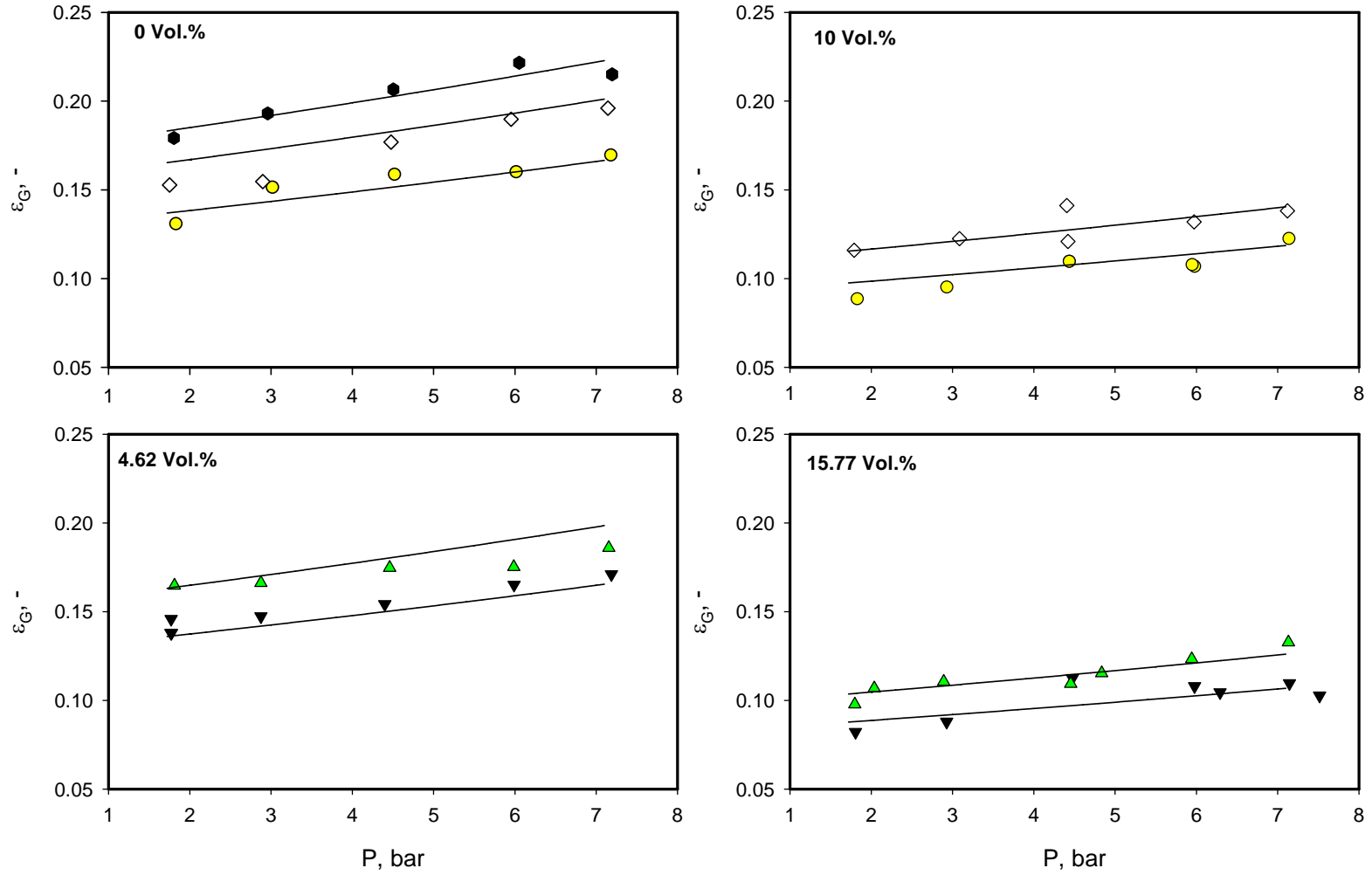


Figure 37 Effect of Operating variables on ϵ_G of He/ Isopar-M/Alumina in the Cold SBCR

● 0.086 m/s
 ◇ 0.114 m/s
 ● 0.150 m/s
 ▼ 0.098 m/s
 ▲ 0.134 m/s
 Lines: Equation (6-1)

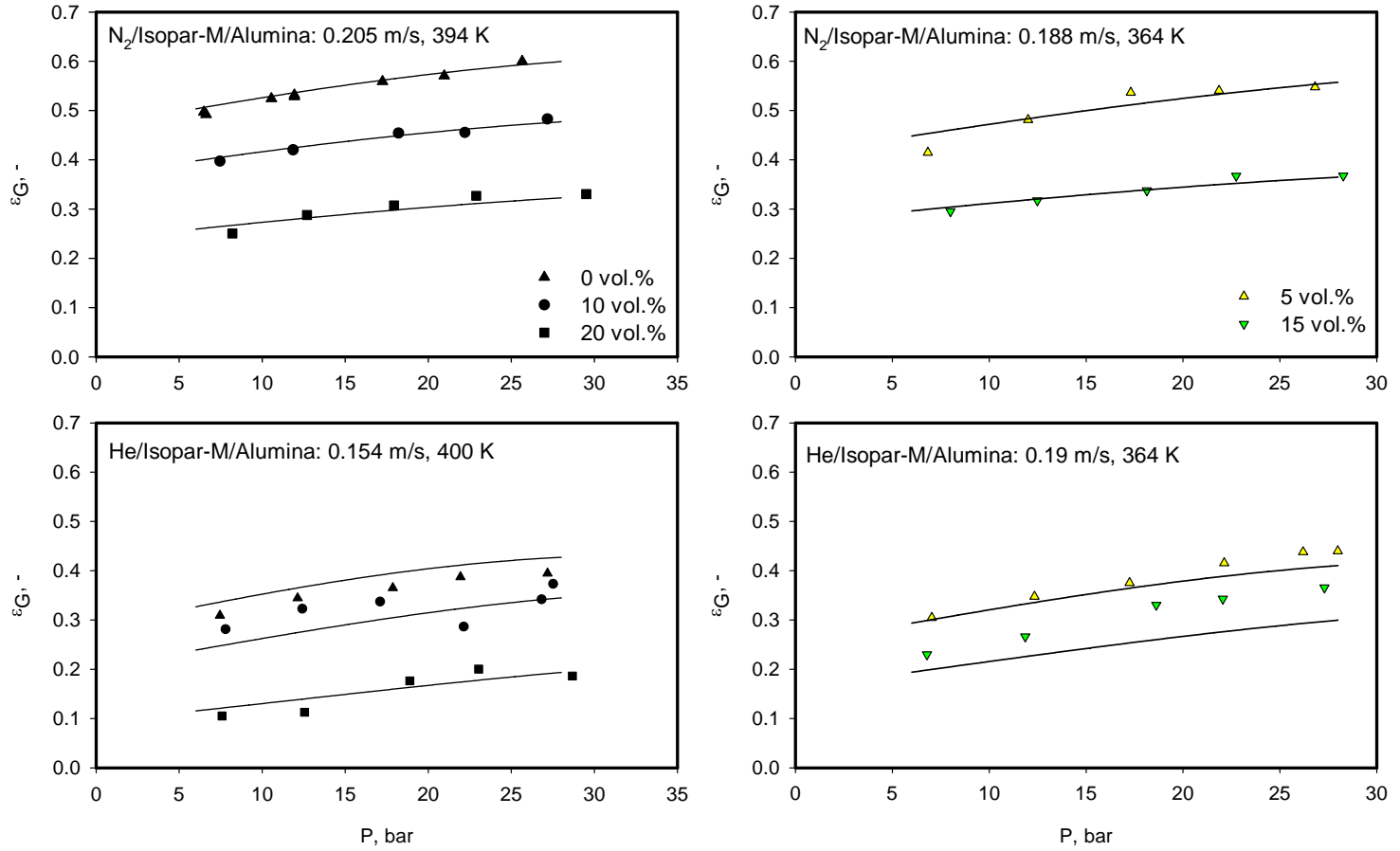


Figure 38 Effect of Operating variables on εG_3 of N_2 and He/ Isopar-M/Alumina in the Hot SBCR

Lines: Equation (6-2)

Figure 38 shows that in the case of N_2 in the hot SBCR, when the pressure increases from 6.7 to 17 bar, ϵ_G increases by 12, 14 and 22 % at 0, 10 and 20 vol.% solid concentration, respectively; and above 17 bar, the increase of ϵ_G for these three solid concentrations is about 7%. In the case of He, on the other hand, the increase of ϵ_G with pressure appears to be greater than that of N_2 as 18, 20 and 67% gas holdup increase can be observed with increasing pressure from 7 to 17 bar under the same solid concentrations used.

These figures also show the effect of solid concentration on the total gas holdup; and as can be observed increasing solid concentration dramatically decreases the total gas holdup of all of the gases used in the range of pressure investigated which agrees with available literature findings^(6,8,28,35,126). For instance, in the case of N_2 in the cold SBCR, ϵ_G in the absence of solid particles, increases by 52% from 2 to 8 bar at 0.098 m/s while at solid concentration of 36 vol.% it only increases by 34% at similar superficial gas velocity. In the case of H_2 , however, no significant effect of pressure can be observed. For example, at solid concentration of 18 vol.% ϵ_G increases by 25% from 1.75 to 7.3 bar at 0.135 m/s, and at solid concentration of 36 vol.% ϵ_G increases by almost the same magnitude under similar conditions. In the hot SBCR, when solid concentration is increased from 0 to 10 vol.%, the gas holdup of N_2 and He decreases by about 20% and 10%, respectively and when the solid concentration reaches 20 vol.%, the gas holdup values of N_2 and He decrease by about 50% and 65%, respectively. These behaviors can be related to the fact that increasing solid concentration leads to the increase of slurry viscosity which promotes the formation of larger gas bubbles. Furthermore, if the pressure and gas velocity are maintained constant, the gas momentum per unit mass of slurry would decrease with solid concentration, and consequently, the total gas holdup is expected to decrease⁽¹²⁶⁾.

Therefore, the slurry viscosity seems to have a strong impact on the gas holdup which is in agreement with literature data ^(6,126). It should be mentioned that the relatively small increase of gas holdup with pressure at high solid concentration indicates that the gas bubbles coalescence (forming large bubbles) is stronger than their shrinkage (forming small bubbles) under high pressures which is in agreement with the finding by Inga and Morsi ⁽¹²⁶⁾.

Figures 39 through 42 illustrate the effect of C_V on $\epsilon_{G-Small}$ and $\epsilon_{G-Large}$ of H_2 , CO , N_2 , CH_4 and He in the cold and hot SBCRs; and as can be observed $\epsilon_{G-Small}$ values of all five gases decrease with solid concentration. In the case of glass beads, it appears that a low pressure, both $\epsilon_{G-Small}$ and $\epsilon_{G-Large}$ decrease with increasing of solid concentration. When the pressure approaches 7.5 bar, however, $\epsilon_{G-Large}$ of the gases becomes less dependent of C_V . In the hot SBCR, $\epsilon_{G-Small}$ values for N_2 and He decrease at all solid concentrations used, whereas those of $\epsilon_{G-Large}$ first increase up to a solid concentration of 10 vol.% and then decrease with increasing solid concentration within the range of pressure investigated. In the case of N_2 , at solid concentrations from 0 to 10 vol.% the decrease of $\epsilon_{G-Small}$ is accompanied by an increase of $\epsilon_{G-Large}$, leading to a slight decrease of the total gas holdup. At solid concentrations from 10 to ~ 20 vol.%, however, only $\epsilon_{G-Small}$ is strongly affected, resulting in a significant decrease of the total gas holdup. Also, at solid concentration ≥ 20 vol.%, the population of small gas bubbles seems to completely disappear and the total gas holdup equals the $\epsilon_{G-Large}$. These findings prove that the decrease of the total gas holdup for N_2 with increasing solid loading can be mainly attributed to the decrease of $\epsilon_{G-Small}$. Krishna et al. ⁽⁸⁾ observed that in the churn-turbulent flow regime, $\epsilon_{G-Large}$ was independent, while $\epsilon_{G-Small}$ significantly decreased with increasing solid concentration. In the

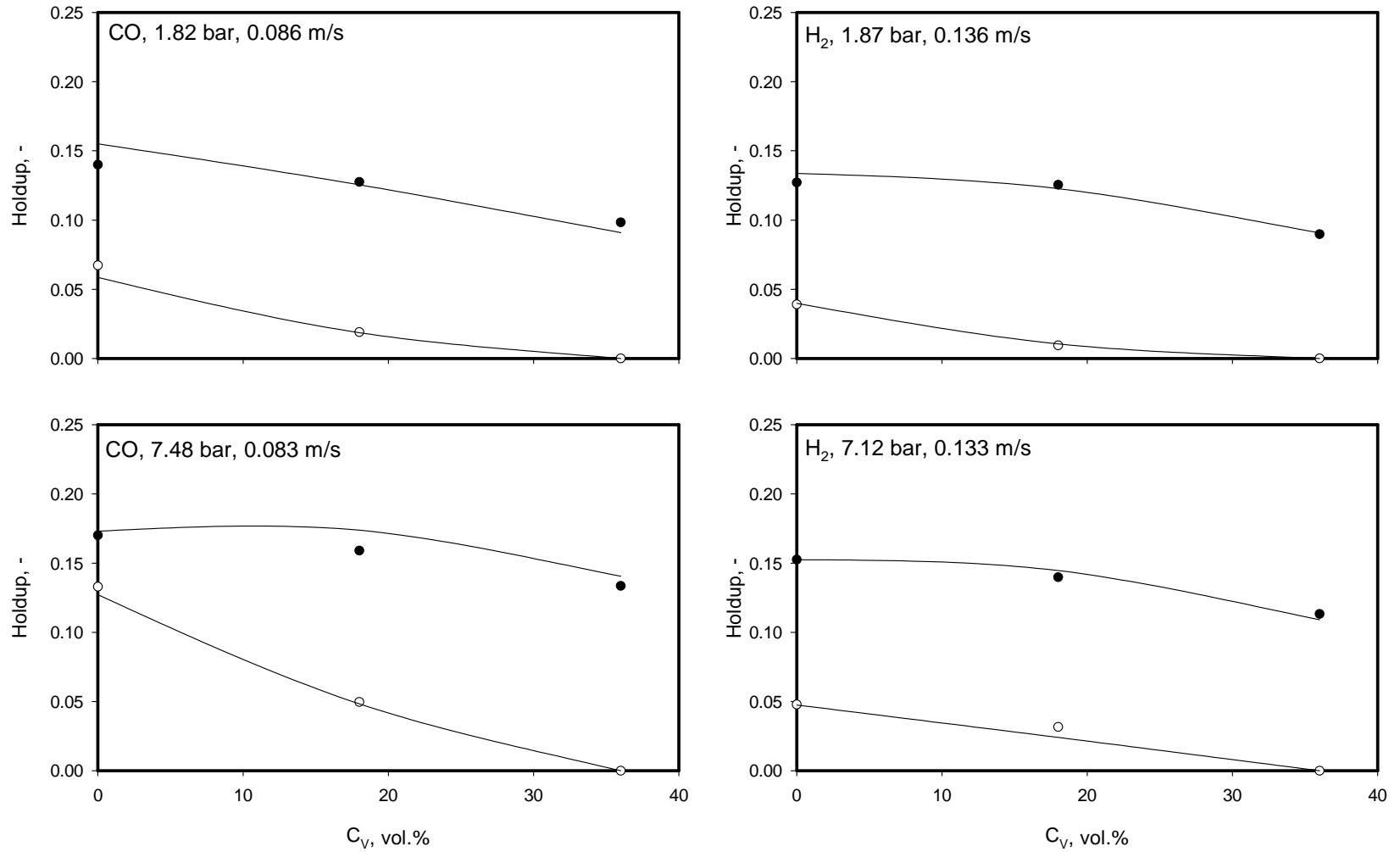


Figure 39 Effect of Glass Beads Particles on the $\epsilon_{G-Small}$ and $\epsilon_{G-Large}$ of CO and H₂ in the Cold SBCR

(Symbols. Plain: $\epsilon_{G-Small}$, Solid: $\epsilon_{G-Large}$) Solid lines: Equation (6-1)

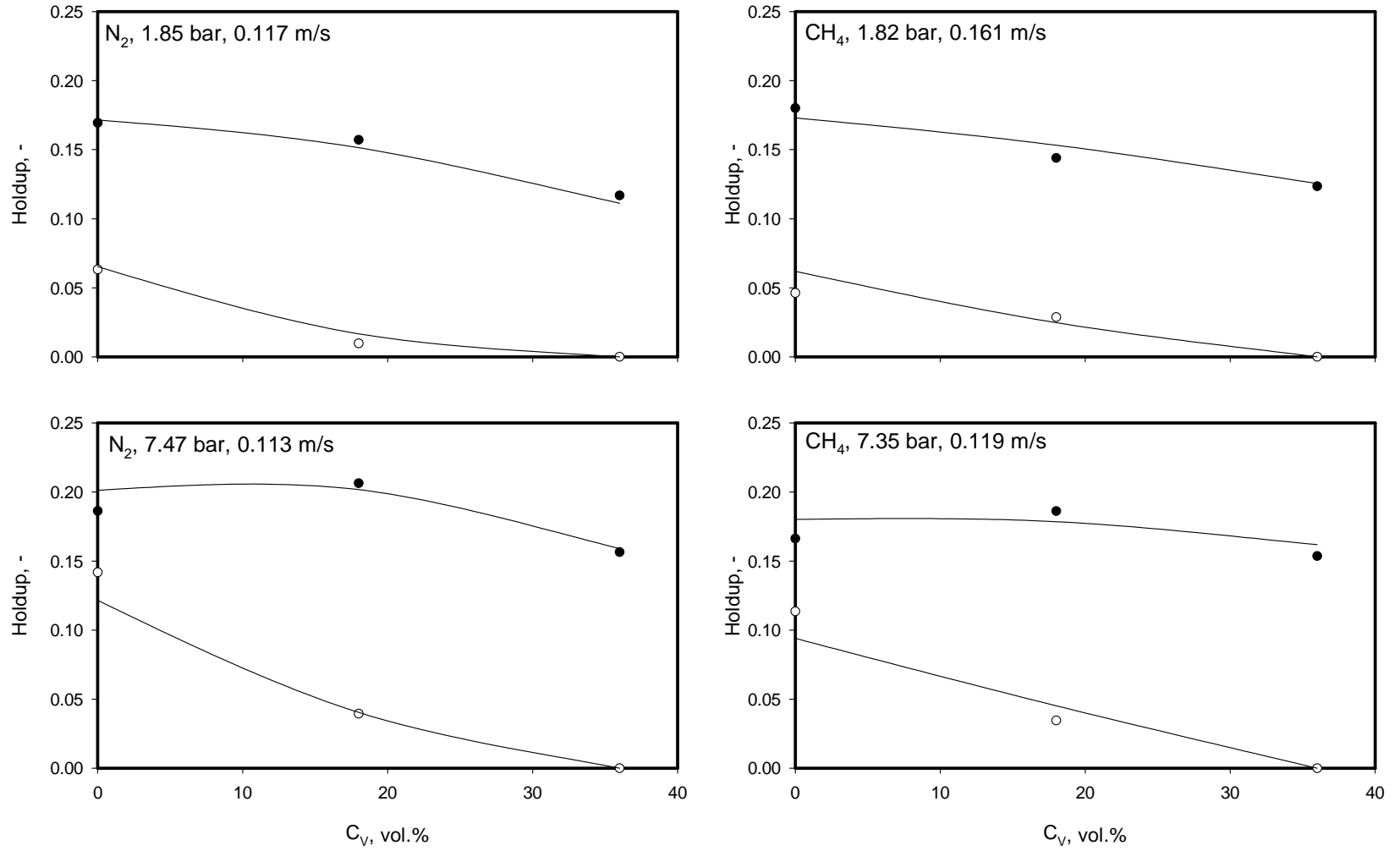


Figure 40 Effect of Glass Beads Particles on the $\epsilon_{G-Small}$ and $\epsilon_{G-Large}$ of N_2 and CH_4 in the Cold SBCR

(Symbols. Plain: $\epsilon_{G-Small}$, Solid: $\epsilon_{G-Large}$) Solid lines: Equation (6-1)

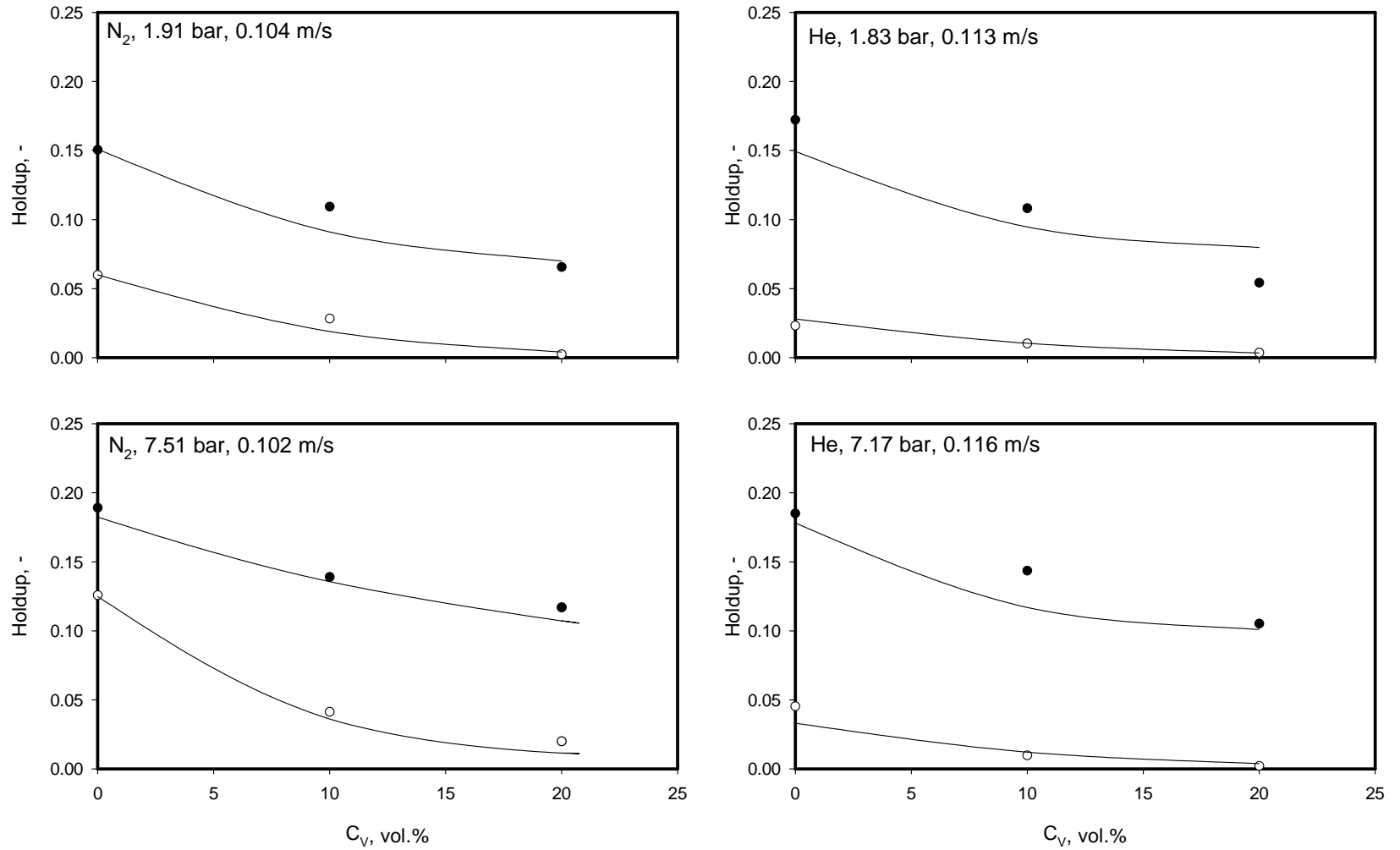


Figure 41 Effect of Alumina Particles on the $\epsilon_{G-Small}$ and $\epsilon_{G-Large}$ of N_2 and He in the Cold SBCR

(Symbols. Plain: $\epsilon_{G-Small}$, Solid: $\epsilon_{G-Large}$) Solid lines: Equation (6-1)

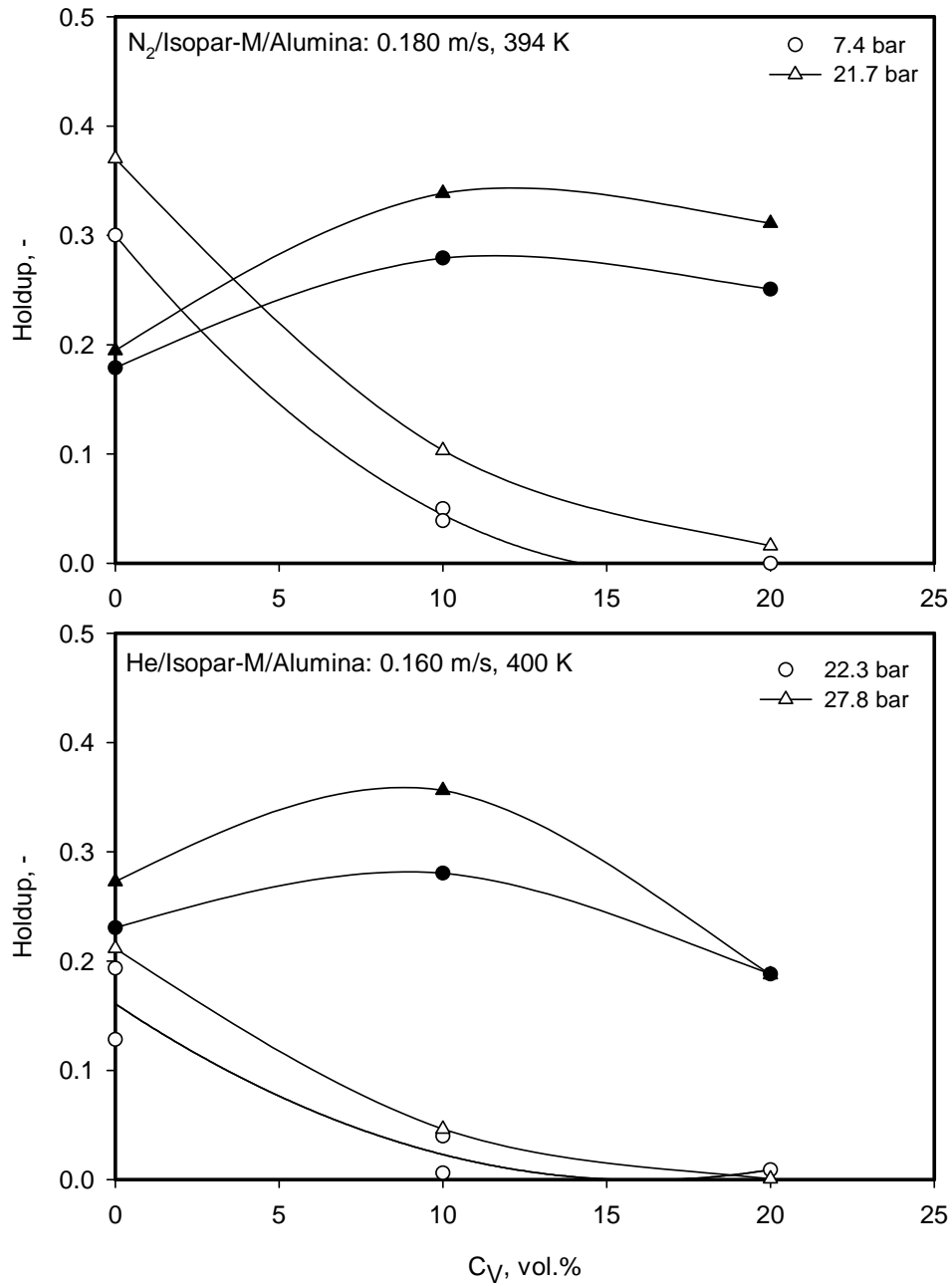


Figure 42 Effect of Alumina Particles on the $\epsilon_{G\text{-Small}}$ and $\epsilon_{G\text{-Large}}$ of N₂ and He in the Hot SBCR

(Symbols. Plain: $\epsilon_{G\text{-Small}}$, Solid: $\epsilon_{G\text{-Large}}$)

case of He, $\epsilon_{G-Large}$ appears to behave similarly as that of N_2 and the decrease of the total gas holdup in the solid concentration range from 0 to 10 vol.% can be correlated with the decrease of $\epsilon_{G-Small}$. At solid concentrations > 10 vol.%, however, the relatively stronger decrease of total ϵ_G for He can be attributed to its strong bubbles coalescence tendency due to their lower momentum when compared with that of N_2 bubbles under the same conditions. Thus, when $\epsilon_{G-Small}$ disappears, the He bubbles become large which is in agreement with the findings by de Swart et al. ⁽⁷⁴⁾. It seems also that in the presence of high solid concentration, the diameter of gas bubbles cannot decrease below a certain value due to coalescence, which was reported to be ≤ 10 mm for 38.6 vol.% of silica in paraffin oil by de Swart et al ⁽⁷⁴⁾.

6.2.2 Effect Gas Velocity on ϵ_G

The effect of the superficial gas velocity on the holdup values of the five gases in the cold SBCR can be seen in Figures 33 through 37, where increasing U_G increases ϵ_G for all gases; and, the increase of ϵ_G with gas velocity at low solid concentration seems to be more significant than at high solid concentration. For instance in the case of H_2 , from 0 to 18 vol.%, ϵ_G decreases by 14.7% at 0.135 m/s and 2 bar, whereas it decreases by 19.1% at 0.2 m/s and 2 bar. This observation agrees with the literature findings ⁽⁷²⁾. Furthermore, the decrease of ϵ_G values with solid concentration is greater than the increase of ϵ_G values with gas velocity. For example, the ϵ_G values of CH_4 decreased by 32% from 7.6 to 28.4 vol.% at 0.098 m/s and 4.5 bar, while the values only increase by 17% from 0.098 to 0.140 m/s at 7.6 vol.% and 4.5 bar. Since increasing the gas velocity increases both the gas holdup of small and large gas bubbles, at high solid concentration, the volume fraction of small gas holdup becomes so small that it can be neglected.

Under these conditions, the increase of ε_G is due mainly to the increase of gas holdup of the large gas bubbles as can be seen in Figures 43 and 44 where the effect of U_G on $\varepsilon_{G\text{-Small}}$ and $\varepsilon_{G\text{-Large}}$ at different solid concentrations is depicted. These Figures clearly show that increasing U_G tends to increase bubble-bubble collisions which results in increasing the rate of gas bubble coalescence.

The effect of superficial gas velocity on the holdup of N_2 and He in Isopar-M/alumina system in the hot SBCR is shown in Figure 45; and as can be observed the total ε_G for both gases increases with the superficial gas velocity in the presence of alumina powder. An average increase of about 6-15% can be observed for the gas holdup with increasing U_G , although the strongest increase is generally observed at the lowest system pressure (7 bar). This was expected since in the prevailing churn-turbulent flow regime, the gas bubbles interaction is strong, and bubble breakup is promoted as reported by Wilkinson et al. ⁽⁴⁵⁾. Also, increasing gas momentum, i.e., superficial gas velocity and/or pressure (gas density), is expected to rupture the large gas bubbles into smaller ones, increasing the holdup of small gas bubbles ($\varepsilon_{G\text{-Small}}$). If the gas bubbles were already dense and small, however, any further increase of the gas momentum might lead to a slight or negligible effect on the bubble size distribution and subsequently the total gas holdup. This could explain the behavior of the total gas holdup with increasing pressure for the two gases used. The slight increase of the total gas holdup at the highest pressure (~27 bar) indicates that the reactor is operating in the fully developed churn-turbulent flow regime. It can therefore be concluded that in the presence of solid particles and in the churn-turbulent flow regime, an increase of U_G has little effect on the gas holdup. Similar findings have been reported by Elgozali et al. ⁽¹¹⁰⁾ who reported no evident effect of U_G on the total gas holdup in the churn-turbulent and transition flow regimes. The results obtained in this study and those by Inga and Morsi ⁽¹²⁶⁾

indicate that the relative increase of ϵ_G values with increasing gas velocity was not high enough to compensate for the decrease of ϵ_G values due to presence of high catalyst concentrations. Therefore, it should be inferred that for SBCRs operating in the churn-turbulent flow regime, there is no incentive to use very high superficial gas velocity since the short gas residence time and high power consumption would not be economical. These findings are useful for the design of Fischer-Tropsch synthesis, since the SBCR is designed to operate at high gas velocities and high catalyst concentrations ⁽²⁰⁴⁾ in order to achieve large mass and heat transfer coefficients, high degree of mixing, complete suspension of the catalyst particles and high reactor productivity ⁽²⁰⁵⁾.

6.2.3 Effect of Temperature on ϵ_G

Figure 46 depicts the effect of temperature on the total gas holdup for N₂ and He in the Isopar-M/alumina slurry in the hot SBCR; and as can be seen increasing temperature increases the gas holdup for both gases in the experimental ranges investigated. The increase of gas holdup with temperature was more pronounced in the absence of solids, where the ϵ_G values increased by an average of 15-20% and 15-25% for N₂ and He, respectively. Figure 46, however, shows that the increase of ϵ_G with temperature in the presence of 10 vol.% of alumina particles decreases to an average of 9% for N₂ and remains almost unchanged for He. Figure 47 illustrates the effect of temperature on $\epsilon_{G\text{-Small}}$ and $\epsilon_{G\text{-Large}}$ of N₂ and He in Isopar-M in the absence of solid particles; and as can be seen in the case of N₂, when the temperature is increased, the $\epsilon_{G\text{-Small}}$ continues to increase while $\epsilon_{G\text{-Large}}$ tends to level off to the point that $\epsilon_{G\text{-Small}}$ becomes $> \epsilon_{G\text{-Large}}$. In the case of He, however, as the temperature increases, $\epsilon_{G\text{-Small}}$ increases and $\epsilon_{G\text{-Large}}$ first decreases and then

levels off, and in general $\epsilon_{G\text{-Large}}$ is $>$ $\epsilon_{G\text{-Small}}$. Thus, it can be concluded that the total holdup of He is composed mostly of large bubbles due to their lower momentum when compared with that of N₂ bubbles under same pressure and temperature. These findings can be related to the decrease of the surface tension and viscosity of the liquid-phase with increasing temperature. When the liquid surface tension is decreased, the cohesive forces which tend to maintain gas bubbles in a spherical shape are reduced and subsequently any increase of the gas momentum leads to the rupture of large gas bubbles into smaller ones, increasing the total gas holdup⁽²⁸⁾.

Also, when the viscosity is decreased, the bubbles coalescence is decreased resulting in the formation of large number of small gas bubbles⁽⁶¹⁾. The addition of solids, however, increases the slurry viscosity and enhances bubbles coalescence as large bubbles are formed. Figure 48 shows the effect of temperature on $\epsilon_{G\text{-Small}}$ and $\epsilon_{G\text{-Large}}$ of N₂ and He in Isopar-M at 10 vol.% of alumina; and as can be seen $\epsilon_{G\text{-Large}}$ of N₂ is systematically greater than $\epsilon_{G\text{-Small}}$. In the case of He, on the other hand, $\epsilon_{G\text{-Small}}$ completely disappears at pressure of 7.6 bar, but is present at 27 bar due to the high gas density. Figure 49 shows that at solid concentration of 15 vol. %, when the temperature is increased from 370 to 421 K for N₂ and from 361 to 432 K for He, the total gas holdup of both gases decrease. As the pressure increases, however, the effect of temperature on gas holdup seems to diminish as the difference between the ϵ_G values obtained at these two temperatures becomes smaller. This behavior of gas holdup with temperature at high solid concentration (i.e. \geq 15 vol.%) can be explained by the destruction of the froth formed in the reactor at high solid loading. Therefore, the effect of solid particles on gas holdup is related to the increase of coalescence of gas bubbles coupled with the destruction of froth, representing the small gas bubbles.

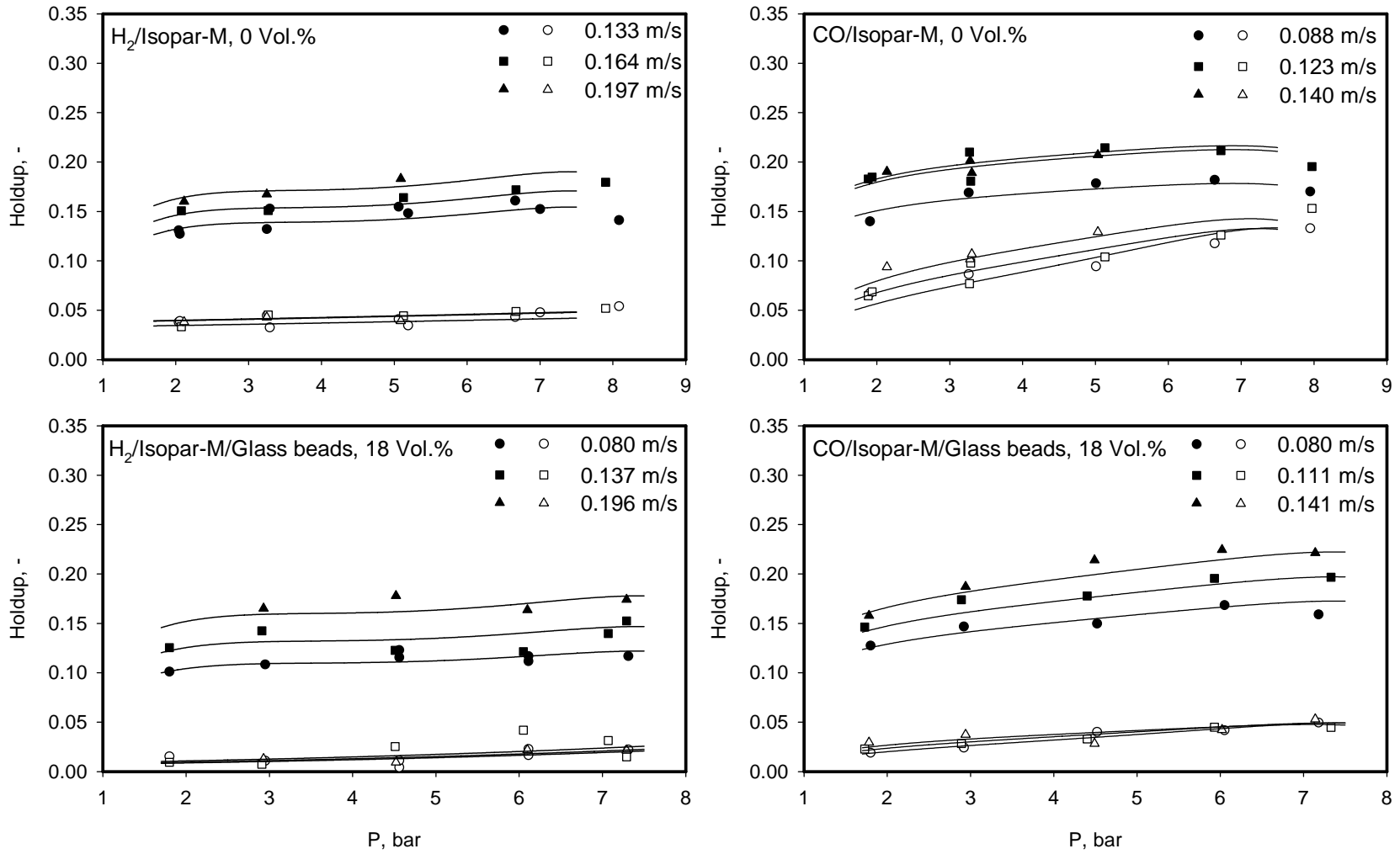


Figure 43 Effect of U_G on the $\epsilon_{G-Small}$ and $\epsilon_{G-Large}$ of H₂ and CO in the Cold SBCR

(Symbols. Plain: $\epsilon_{G-Small}$, Solid: $\epsilon_{G-Large}$) Lines: Equation (6-1)

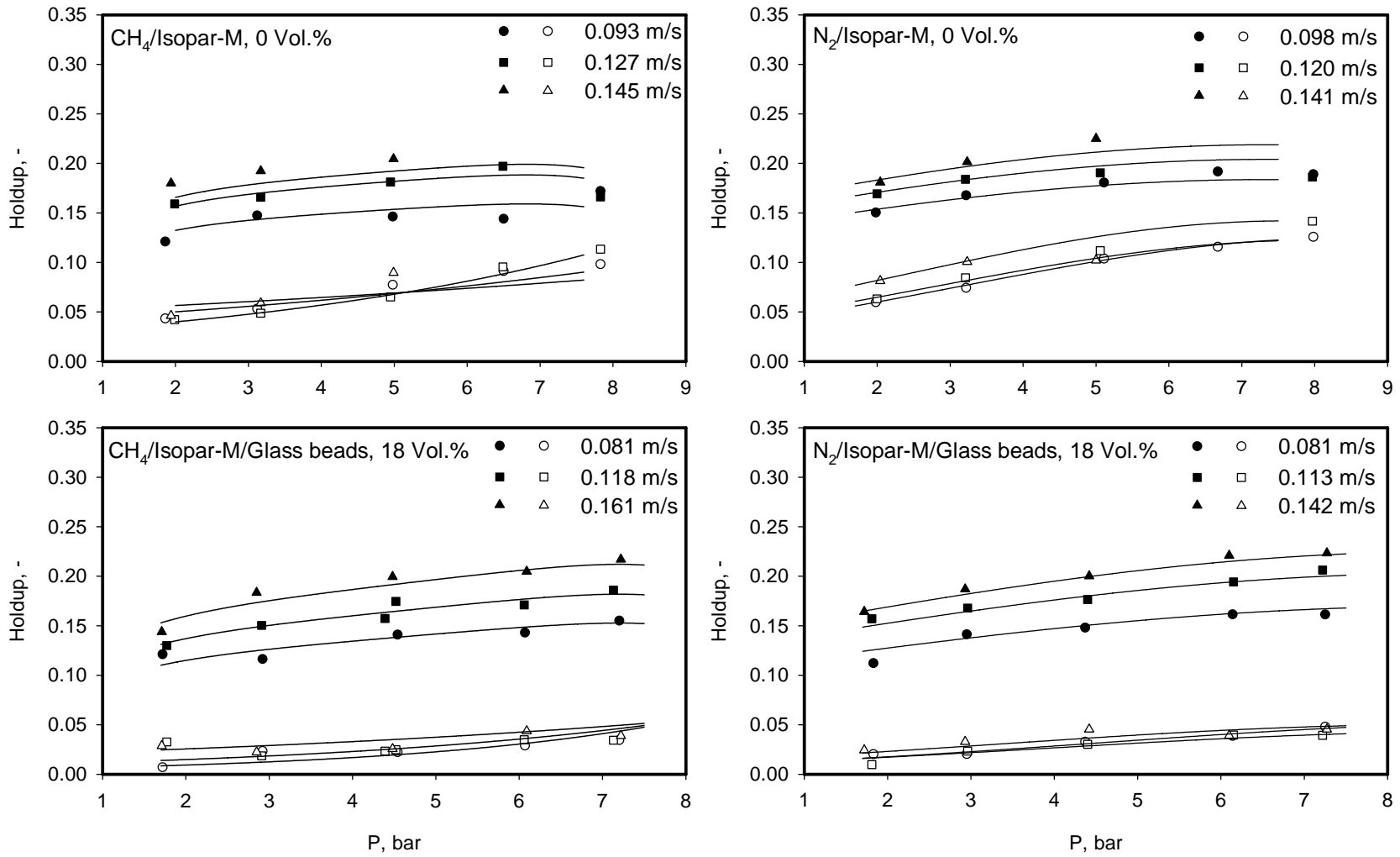


Figure 44 Effect of U_G on the $\epsilon_{G\text{-Small}}$ and $\epsilon_{G\text{-Large}}$ of CH_4 and N_2 in the Cold SBCR

(Symbols. Plain: $\epsilon_{G\text{-Small}}$, Solid: $\epsilon_{G\text{-Large}}$) Lines: Equation (6-1)

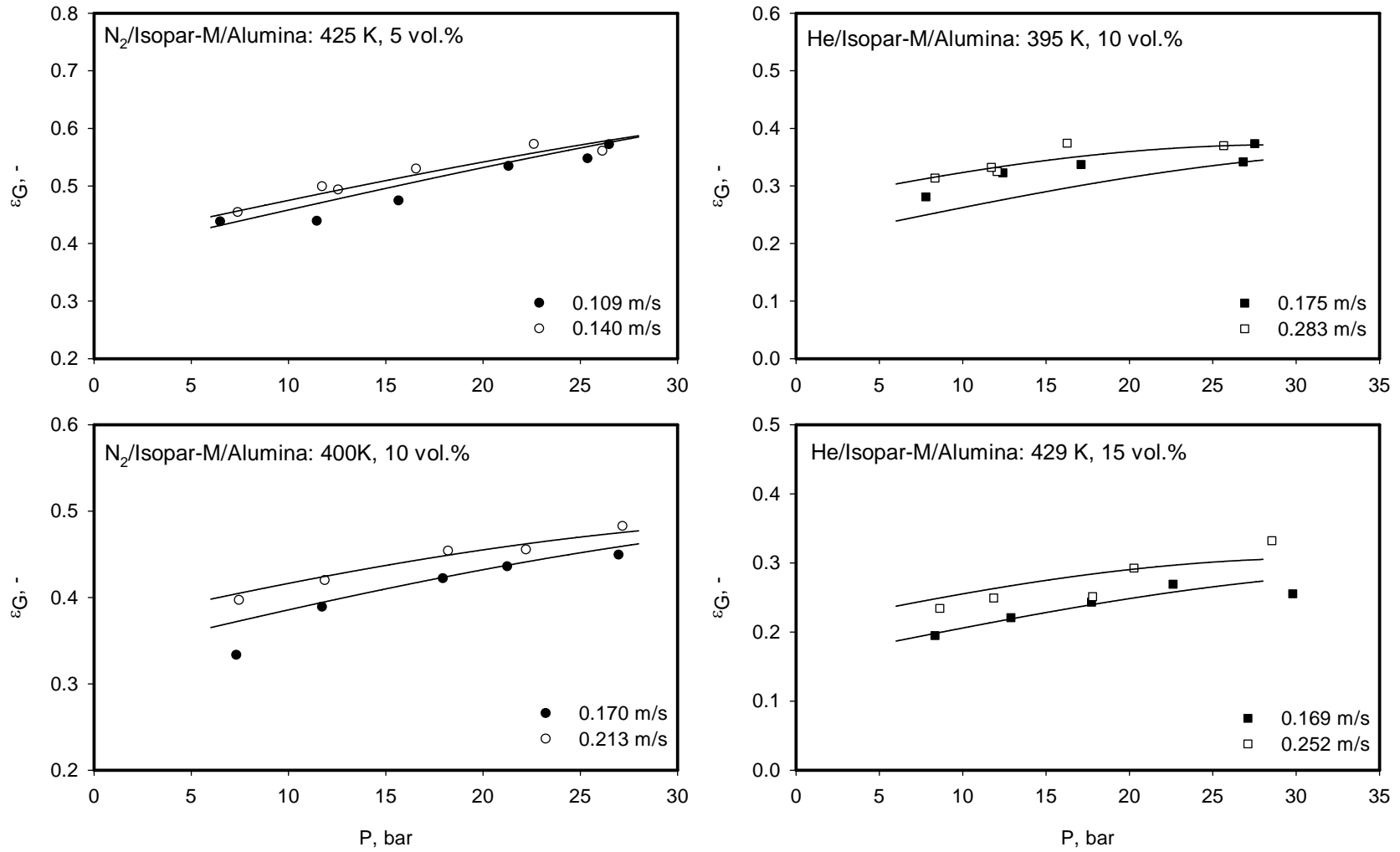


Figure 45 Effect of U_G on the ϵ_G of N₂ and He/Isopar-M/Alumina in the Hot SBCR

Lines: Equation (6-2)

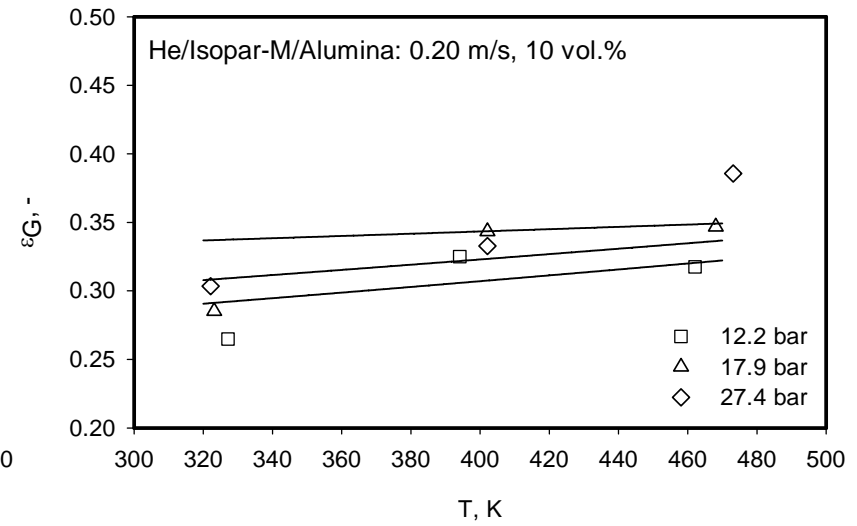
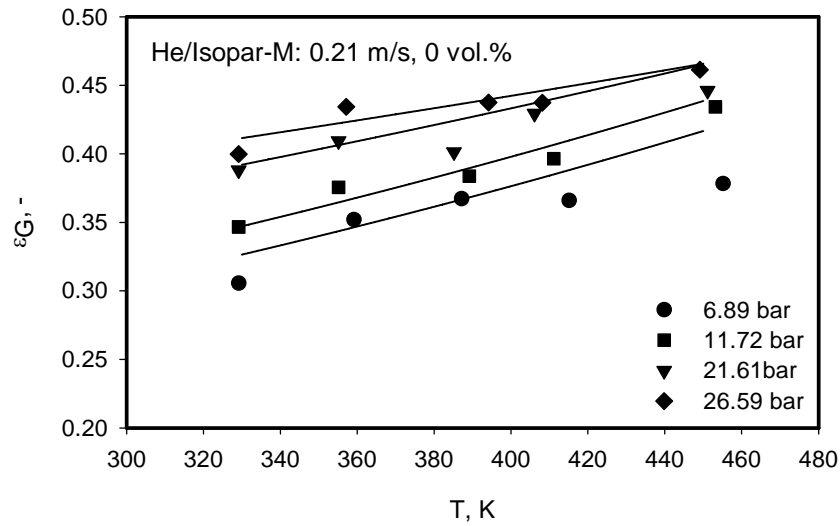
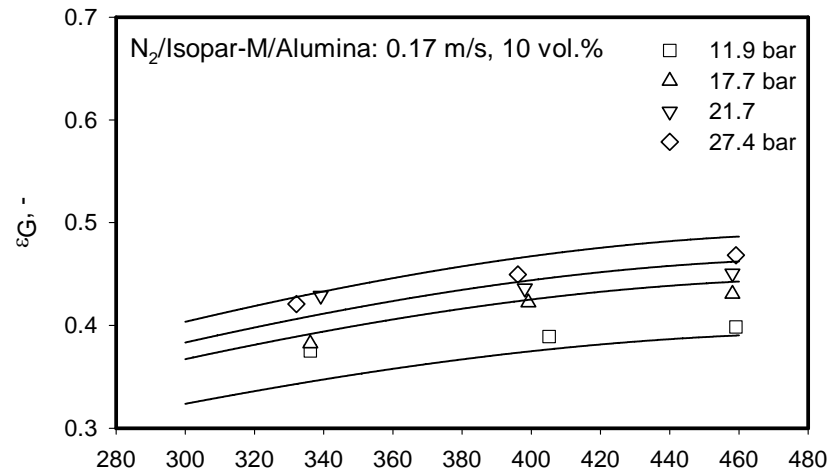
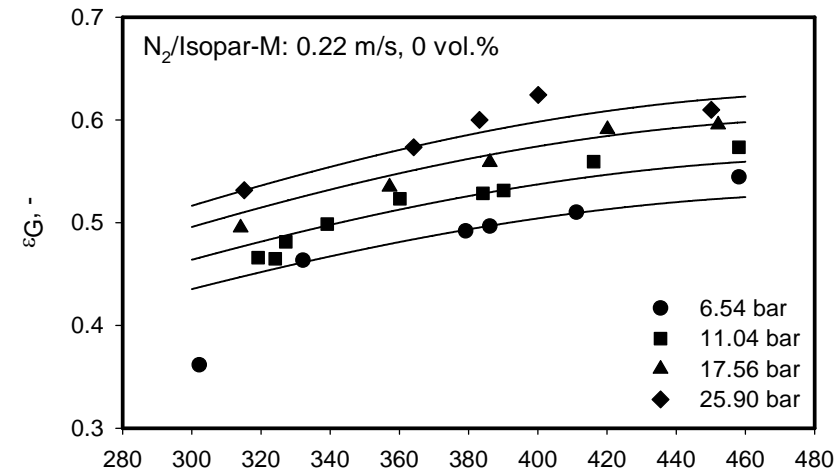


Figure 46 Effect of T on the ϵ_G of N_2 and He/Isopar-M/Alumina in the Hot SBCR

Lines: Equation (6-2)

6.2.4 Effect of Gas Nature on ϵ_G

The five gases used in this study showed different gas holdup values as can be observed in Figure 50, which illustrates the gas holdup as a function of gas superficial velocity obtained in the cold SBCR. It can be seen in this figure that the trend of ϵ_G behavior is:

$$\epsilon_{G,N_2} \approx \epsilon_{G,CO} > \epsilon_{G,CH_4} > \epsilon_{G,He} \approx \epsilon_{G,H_2}$$

This indicates that the gas holdup behavior follows that of the molecular weight, or the momentum carried by the gas jets, hence it is directly related to the gas density. Inga ⁽¹⁸⁹⁾ reported that H₂, having the lowest molecular weight, was responsible of creating local circulations around the gas sparger. This was due to the fact that the H₂ bubbles created at the sparger did not have enough momentum to induce liquid circulation, whereas N₂, CO and CH₄, showed a liquid circulation along the column. In this respect, the axial profile of the gas holdup has an increasing trend for the heavier gases and the gas holdup of H₂ would be larger at the lower part of the column. Inga ⁽¹⁸⁹⁾ explained this behavior in terms of the expansion and circulation of some gas bubbles with the liquid. Thus, the axial profile of the gas holdup can reflect the bubble size distribution at each portion of the column. A uniform axial profile of the gas holdup would indicate that the recirculation of the gas bubbles with the liquid is uniform and hence the same class of bubble sizes exists throughout the column.

Figure 51 shows the effect of the gas molecular weight on ϵ_G , $\epsilon_{G-Small}$, and $\epsilon_{G-Large}$ at 7 bar, 0.126 m/s and 0 vol.% in the cold SBCR; and as can be seen, the total gas holdup and the holdup of small gas bubbles increase with gas molecular weight, whereas $\epsilon_{G-Large}$ appears to be constant for the heavier gases.

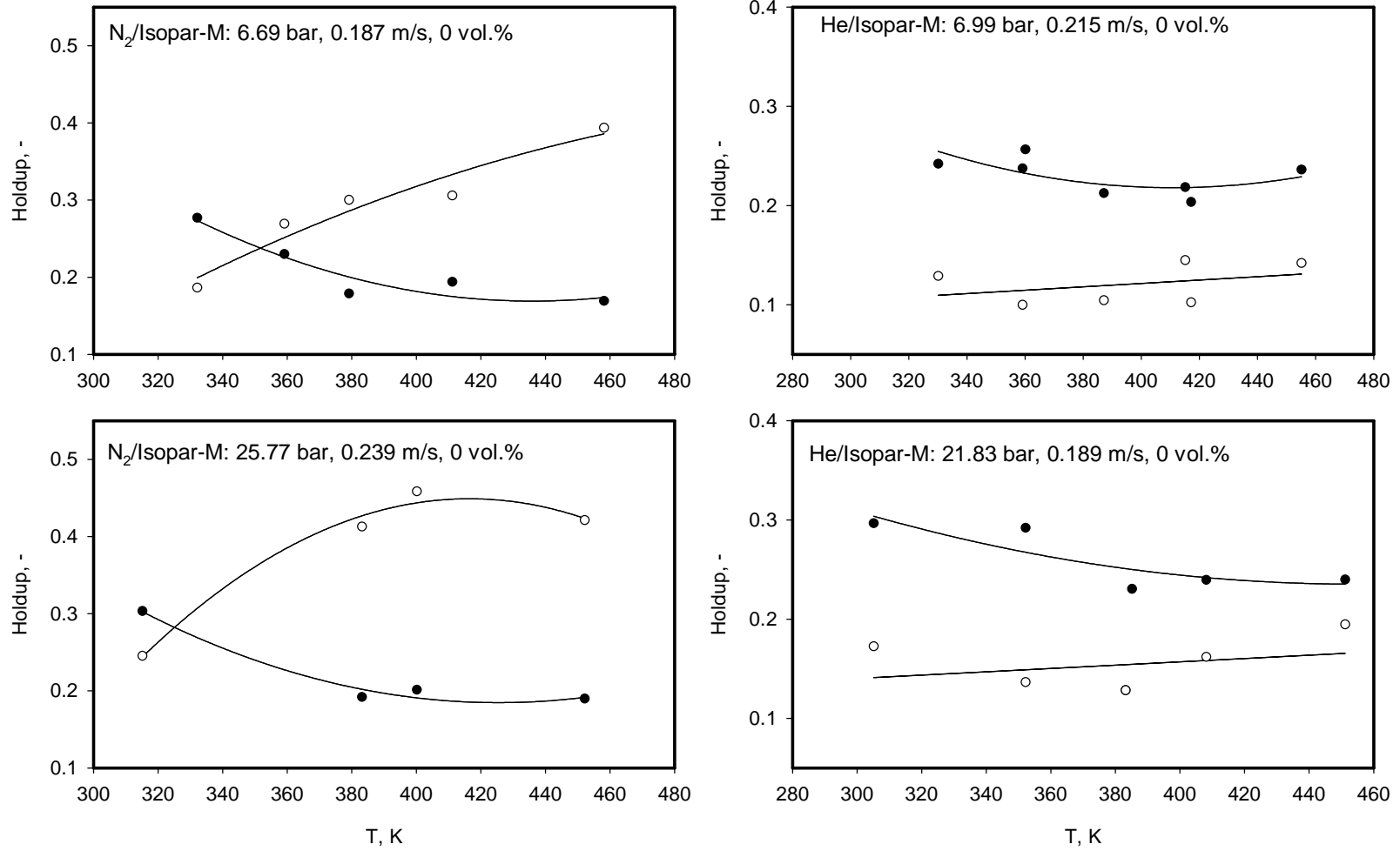


Figure 47 Effect of T on the $\epsilon_{G-Small}$ and $\epsilon_{G-Large}$ of N₂ and He in Isopar-M in the Hot SBCR

(Symbols. Plain: $\epsilon_{G-Small}$, Solid: $\epsilon_{G-Large}$)

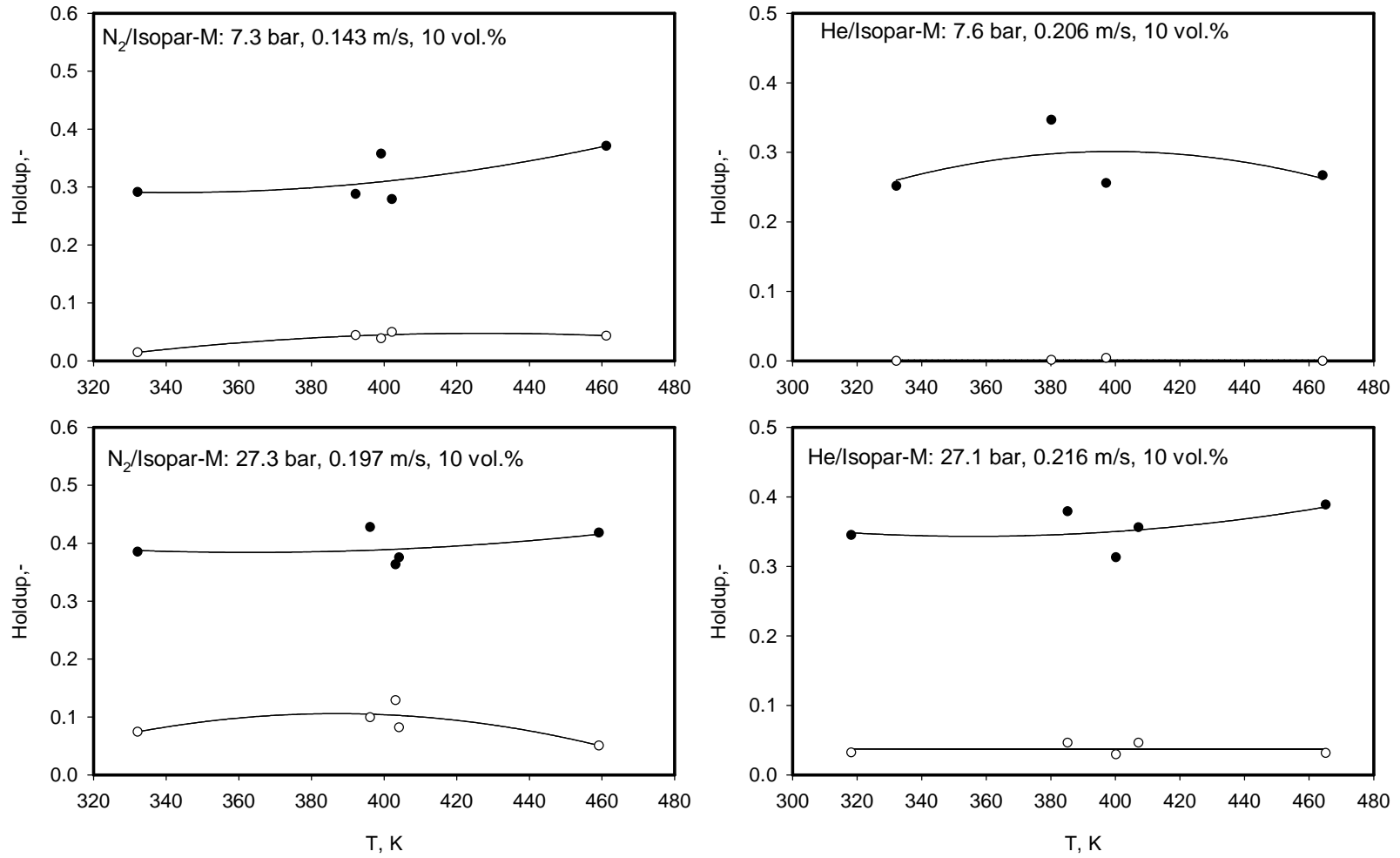


Figure 48 Effect of T on the $\epsilon_{G-Small}$ and $\epsilon_{G-Large}$ of N₂ and He at 10 vol.% Alumina in the Hot SBCR

(Symbols. Plain: $\epsilon_{G-Small}$, Solid: $\epsilon_{G-Large}$)

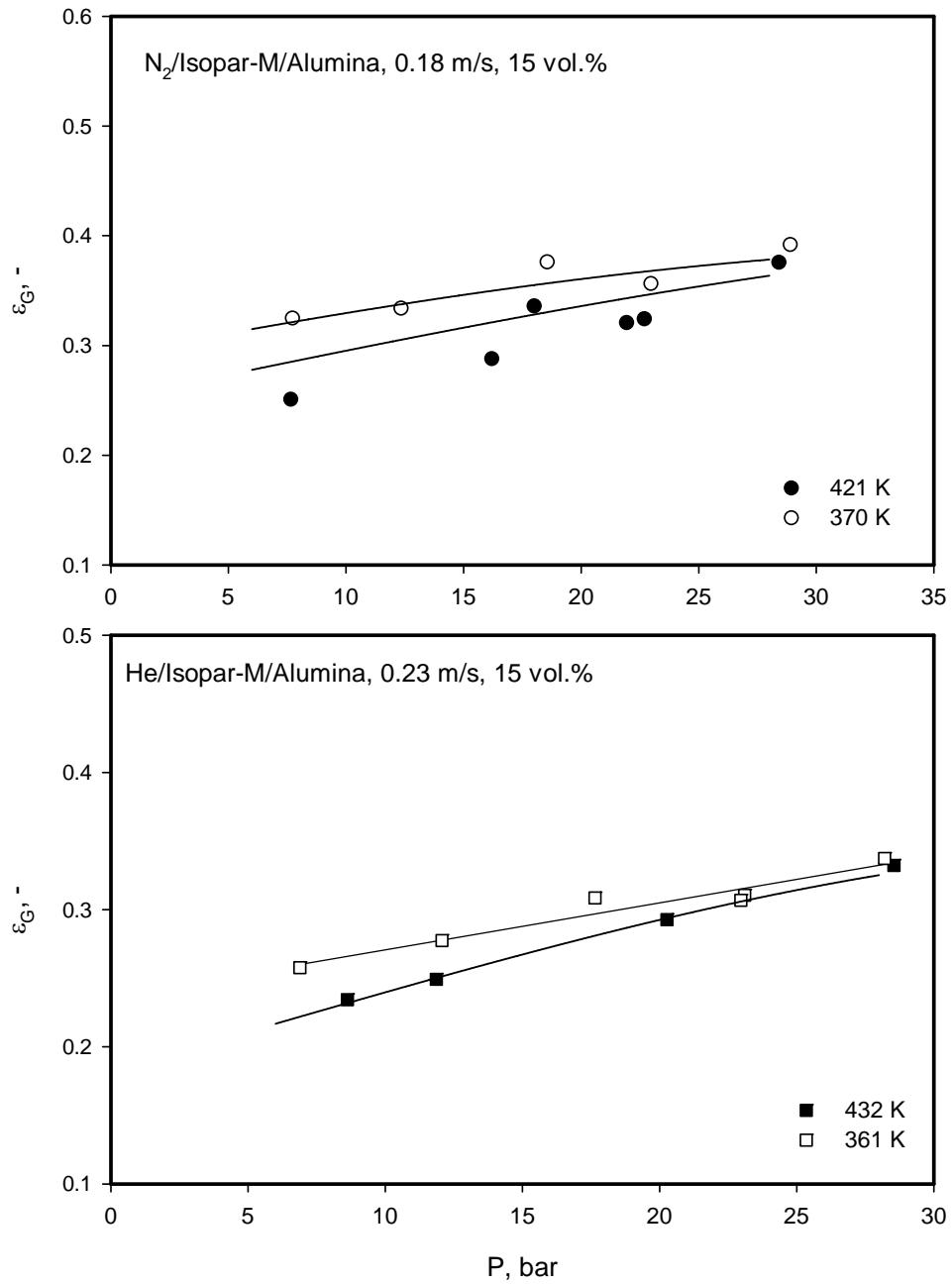


Figure 49 Effect of T on the ϵ_G of N₂ and He at 15 vol.% Alumina in the Hot SBCR

Lines: Equation (6-2)

The effect of gas nature on ε_G can also be explained in terms of the gas momentum per unit mass of slurry defined as:

$$M_G = \frac{m_G U_{G-swarm}}{m_{SL}} = \frac{m_G U_G / \varepsilon_G}{m_{SL}} \quad (6-3)$$

By incorporating Equation (2-2) for ε_G , and the gas and slurry densities into Equation (6-3), the following expression can be obtained:

$$M_G = \frac{\rho_G U_G}{\rho_{SL}(1 - \varepsilon_G)} \quad (6-4)$$

Reilly et al. ⁽⁴⁸⁾ reported that in the churn-turbulent flow regime, the gas holdup in bubble column reactors can be directly correlated with the gas momentum per unit mass of liquid to power 1/3. Thus, increasing gas momentum, or molecular weight, is expected to increase the gas holdup.

6.2.5 Comparison of ε_G with Literature Data

Inga and Morsi ⁽¹²⁶⁾ found that the increase of ε_G values with pressure was more noticeable at higher superficial gas velocity, and related this behavior to the formation of large number of small rigid gas bubbles under high pressures. Their total gas holdup values for the same five gases used were significantly higher than those obtained in this study. It should be mentioned that they used a mixture of liquid hexanes, which has a viscosity (0.3×10^{-3} Pa.s) that is much lower than that of Isopar-M (2.7×10^{-3} Pa s) used in this study. Consequently, the ε_G behavior could be attributed to the effect of viscosity on ε_G as illustrated in Figure 52 where, a comparison with other investigators is presented. This figure shows that the gas holdup values obtained by Wilkinson et al. ⁽⁶¹⁾ and Tarmy et al. ⁽⁴⁶⁾ in *n*-heptane and by Inga and Morsi ⁽¹²⁶⁾ in hexanes

mixture are in good agreement, since the physical properties of their liquids, i.e. viscosity and surface tension are close under the same conditions, however, the gas holdup values obtained in this study with Isopar-M are significantly lower.

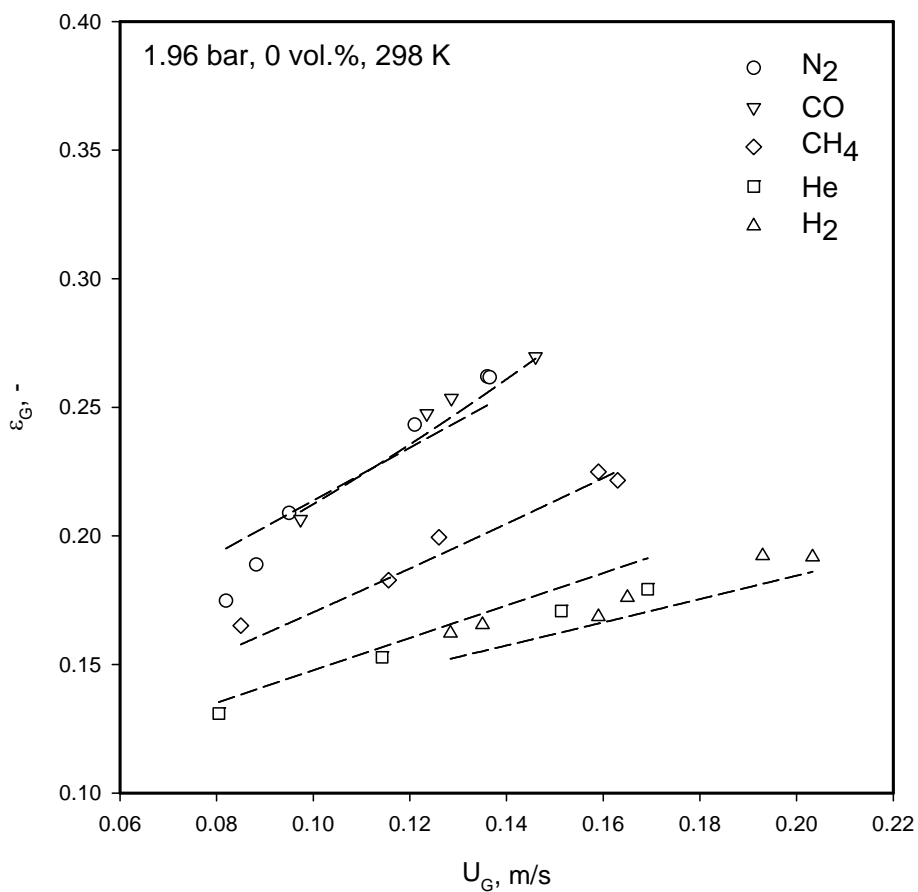


Figure 50 Effect of Gas Nature on the Gas Holdup in the Cold SBCR

Lines: Equation (6-1)

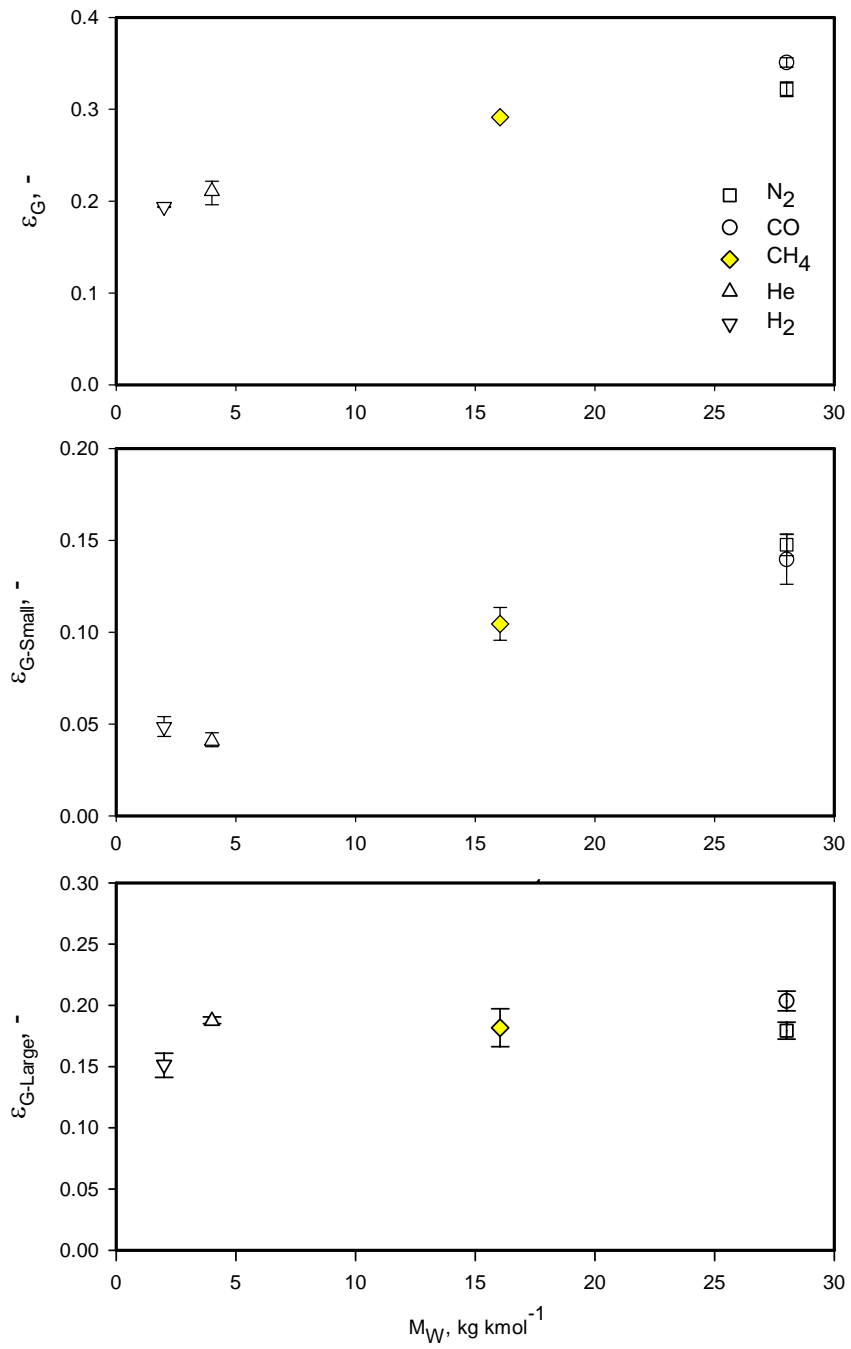


Figure 51 Effect of Gas Nature on ϵ_G , $\epsilon_{G\text{-Small}}$, and $\epsilon_{G\text{-Large}}$ in the Cold SBCR

(7 bar, 0.126 m/s, 0 vol.%)

Krishna et al. ⁽⁸⁾ studied the effects of gas velocity and solid concentration on the gas holdup using N₂ in Paraffin oil, with properties ($\rho_L=790 \text{ kgm}^{-3}$, $\mu_L = 0.029 \text{ Pas}$, $\sigma_L = 0.028 \text{ Nm}^{-1}$, at 298K) which are close to those of Isopar-M, using Silica particles ($\rho_P = 2100 \text{ kgm}^{-3}$). A comparison between their data and those obtained in this study can be seen in Figure 53, which shows a fair agreement. Since both columns have almost the same dimensions, the difference between the ε_G values could be explained by the difference in the pressure, slurry density, and gas distribution scheme. In fact Krishna et al. ⁽⁸⁾ employed a sintered plate ($d_O = 5 \times 10^{-5} \text{ m ID}$), whereas a spider-type gas sparger ($d_O = 0.005 \text{ m ID}$) was used in this study.

6.3 BUBBLES SIZE DISTRIBUTION IN THE COLD AND HOT SBCRS

The size of gas bubbles in SBCRs operating in churn-turbulent flow regime has been classified into small and large. The large gas bubbles rise quickly through the slurry and create backmixing, whereas the small ones are slower and re-circulate with the slurry. The rupture and coalescence of the bubbles may take place at any point inside the reactor, and could be explained by two competing forces, namely the surface tension and the inertial force. The former tends to maintain the gas bubbles in a spherical shape, whereas the latter tends to elongate them. The inertial force depends on the gas velocity at the sparger and the gas density. The ratio of these two forces is the Webber number defined by Equation (2-13). The bubbles are more likely to rupture as the gas velocity relative to the liquid velocity increases, due to the increase of the shear on the bubble surface. Thus, an increase of We could result in an increase of the rate of gas bubble ruptures.

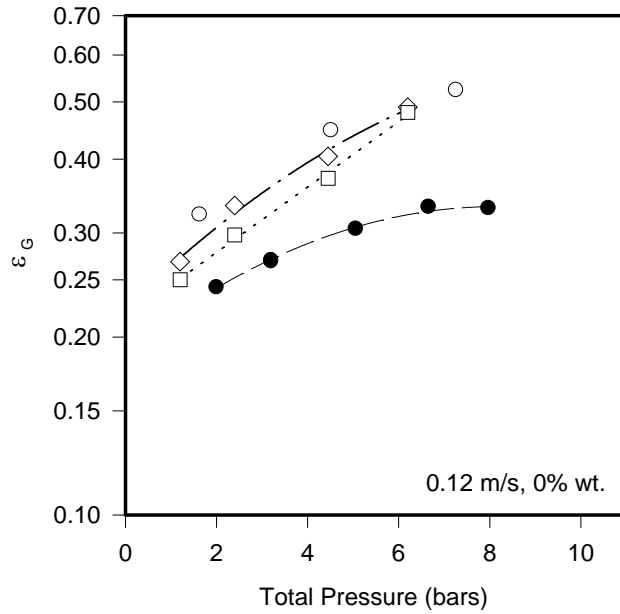


Figure 52 Comparison with the Literature Data on Gas

Holdup obtained with low Viscosity Liquid

- Inga and Morsi ⁽¹²⁶⁾, N₂/C₆ mixtures
- Tarmy et al. ⁽⁴⁶⁾, N₂/C₇ ◇ Wilkinson ⁽⁶¹⁾, N₂/C₇
- This study, N₂/Isopar-M

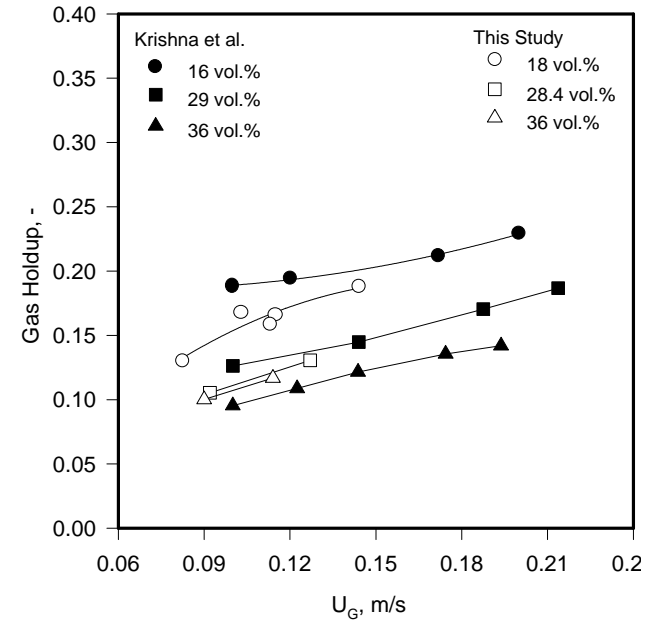


Figure 53 Comparison of ϵ_G Data with the Literature

Values obtained with comparable Liquids

Krishna et al. ⁽⁸⁾, Air/Paraffin oil/Silica, P = 1 bar, $D_C = 0.380$ m

This study, N₂/Isopar-M/Glass beads, P = 1.75 bar, $D_C = 0.316$ m

In this study, the Dynamic Gas Disengagement (DGD) technique was used to determine the bubbles size distribution in the cold and hot SBCRs. Also, the photographic method was employed in the hot SBCR in the absence of solid particles to determine the bubble size distribution. The effects of the main process variables, pressure, superficial gas velocity, temperature and solid concentration on bubble size distribution were studied.

The Sauter-mean bubble diameter, d_{32} , defined by Equation (5-42), was determined from the bubble size distribution obtained from the DGD and the photographic techniques based on average number distribution and average volume distribution, respectively. Figure 54 shows values of d_{32} for N_2 and He in Isopar-M obtained with the photographic and DGD methods in the hot column and in the absence of solid particles; and as can be observed the d_{32} values obtained with both methods are generally in a reasonable agreement with an average difference of less than 14 %. The reason for such a difference can be attributed to the visual limitations of the camera and the presence of froth which is under-emphasized in the photographic method than in the DGD technique. Such a behavior has already been reported in the literature by Daly et al. ⁽⁸⁹⁾ who used both the photographic and DGD methods to obtain the Sauter-mean bubble diameter for FT-300 and Sasol wax in two columns of 0.05 and 0.21 m ID at 538 K and atmospheric pressure. They reported that although the d_{32} values obtained using the two techniques were in a good agreement, in the presence of froth, however, d_{32} values obtained photographically became consistently lower than those measured with the DGD technique ⁽⁸⁹⁾. Thus, it can be concluded that the DGD technique is an adequate method for the estimation of the bubble size distribution even in the presence of froth. This also validates the correlation by Fukuma et al. ⁽¹⁵¹⁾ employed in this study to estimate the bubble rise velocity.

All the DGD experiments conducted in the cold and hot SBCRs were selected based on the CCSD approach, and therefore the d_{32} for all gases, along with $d_{32\text{-Small}}$, and $d_{32\text{-Large}}$ were correlated using Equation (4-11). For the cold SBCR, Equation (4-11) was modified to obtain the best fit for all the data as follow:

$$\begin{aligned} \text{Ln}(\Phi)_{\text{COLD}} = & a_0 + \sum_{i=1}^3 a_i X_i + \sum_{\substack{i=1 \\ j \geq i}}^6 b_{i,j} X_i X_j + \sum_{i=1}^3 c_i \sqrt{1 + \exp(X_i^2)} + d_1 \exp(-1 - X_3) \\ & + \sum_{i=1}^3 e_i \exp(\alpha_i X_i) + f_1 \exp\left(\sum_{i=1}^3 \beta_i X_i\right) \end{aligned} \quad (6-5)$$

Where Φ can represent d_{32} , $d_{32\text{-Small}}$ or $d_{32\text{-Large}}$. The coefficients of Equation (6-5) for d_{32} can be found in Table 22 and for $d_{32\text{-Small}}$ and $d_{32\text{-Large}}$ in Table 23.

For the hot SCBR, Equation (4-11) was modified as:

$$\text{Ln}(\Phi)_{\text{HOT}} = a_0 + \sum_{i=1}^4 a_i X_i + \sum_{\substack{i=1 \\ j \geq i}}^{10} b_{i,j} X_i X_j + c_1 \exp(-1 - X_4) \quad (6-6)$$

The coefficients of Equation (6-6) for d_{32} , $d_{32\text{-Small}}$ and $d_{32\text{-Large}}$ can be found in Table 24.

Figure 55 a) shows a comparison between the experimental and predicted d_{32} values for all five gases in Isopar-M/glass beads, alumina slurry using Equation (6-5). Similarly, Figure 55 b) shows a comparison between the experimental and predicted values of d_{32} for N_2 and He in Isopar-M/alumina using Equation (6-6). As can be seen in these figures all the predicted data are in good agreement with the experimental values.

Table 22 Coefficients for the d_{32} correlation using Equation (6-5)

	<i>Glass beads system</i>				<i>Alumina system</i>	
	H ₂	CO	N ₂	CH ₄	He	N ₂
a ₀	-4.750	-5.390	-5.201	-5.331	129.4546	-5.6093
a ₁	0.013	-0.030	-0.092	-0.061	-0.0956	-0.0676
a ₂	0.071	-	-	0.056	19.768	-0.0827
a ₃	0.560	0.553	0.507	0.400	12.4602	-0.7262
b ₁₂	-	-	0.050	-	0.0224	-0.0705
b ₁₃	0.060	0.044	-	0.053	-	-
b ₂₃	-0.039	0.040	-	0.067	1.57	-
b ₁₁	-	-	0.307	-	0.0396	-0.0296
b ₂₂	-	0.123	-0.070	-0.471	1.2386	-0.1794
b ₃₃	0.505	0.141	0.116	0.691	-	-
c ₁	-	-	-0.293	-	-	-
c ₂	-	-0.153	-	0.457	0.018	0.0697
c ₃	-0.402	-	-	-0.554	-	0.5406
d ₁	-	-	-	-	1.579	-2.0661
e ₁	-	-	-	-	-	-
e ₂	-	-	-	-	-	-
e ₃	-	-	-	-	-	-
f ₁	-	-	-	-	-134.963	-
α ₁	-	-	-	-	-	-
α ₂	-	-	-	-	-	-
α ₃	-	-	-	-	-	-
β ₁	-	-	-	-	-	-
β ₂	-	-	-	-	0.1439	-
β ₃	-	-	-	-	0.0832	-
AARE,%	14	12	15	15	12	11

Table 23 Coefficients for the d_{32} -Small and d_{32} -Large correlation using Equation (6-5)

	<i>Glass Beads System</i>								<i>Alumina System</i>			
	H ₂		CO		N ₂		CH ₄		He		N ₂	
	Small	Large	Small	Large	Small	Large	Small	Large	Small	Large	Small	Large
a ₀	-7.171	-4.522	-7.154	-4.909	-7.336	-4.737	-6.758	-4.958	-7.456	-4.857	-0.335	-0.181
a ₁	0.011	0.036	-	-	-0.050	-0.033	-0.059	-	-0.054	-0.031	-	0.017
a ₂	-0.061	0.119	-0.063	0.085	-0.051	0.079	-0.044	0.074	0.301	0.073	-0.046	-
a ₃	0.147	0.188	-0.061	0.244	0.120	0.308	0.117	0.226	-0.198	0.711	-	-0.037
b ₁₂	0.039	-	0.038	-0.073	-	0.063	-	-	0.028	-0.016	-0.122	0.118
b ₁₃	0.014	0.076	0.011	0.072	-0.031	-	-0.038	0.030	0.006	-0.034	-	0.045
b ₂₃	-	-0.048	0.028	0.080	-0.032	0.036	-	-	-0.049	0.031	0.229	-0.218
b ₁₁	0.010	-	0.022	-	0.035	-	0.142	-0.188	-	0.015	0.094	-0.065

Table 23 (Continued)

	<i>Glass Beads System</i>								<i>Alumina System</i>			
	H ₂		CO		N ₂		CH ₄		He		N ₂	
	Small	Large	Small	Large	Small	Large	Small	Large	Small	Large	Small	Large
b ₂₂	-	-0.026	-	-0.065	-	-	-	-0.216	-	-	-	-0.045
b ₃₃	-	-	-	-0.043	-	0.051	0.248	-	-	-0.381	-	0.380
c ₁	-	-	-	0.066	-	-0.050	-0.149	0.175	-0.004	-	-0.766	-0.792
c ₂	0.032	-	-	-	-	-	-	0.174	0.176	0.006	-	-
c ₃	-	-	-	-	0.051	-	-0.154	-0.047	0.180	-	-	-
d ₁	-	-	-0.071	-	-	-	-	-	-0.421	1.060	-	-
e ₁	-	-	-	-	-	-	-	-	-	-	-	-
e ₂	-	-	-	-	-	-	-	-	-0.036	-	-	-
e ₃	-	-	-	-	-	-	-	-	-	-	-	-
f ₁	-	-	-	-	-	-	-	-	-	-	-	-
α ₁	-	-	-	-	-	-	-	-	-	-	-	-
α ₂	-	-	-	-	-	-	-	-	1.971	-	-	-
AARE, %	10	18	7	27	9	13	7	13	17	12	12	12

Table 24 Coefficients for the d_{32-Small} and d_{32-Large} correlation using Equation (6-6)

	<i>d</i> ₃₂		<i>d</i> _{32-Large}		<i>d</i> _{32-Small}	
	He	N ₂	He	N ₂	He	N ₂
a ₀	-5.298	-5.339	-4.924	-5.323	-6.826	-6.596
a ₁	-0.043	-0.055	0.022	-0.035	-0.109	-0.021
a ₂	-0.018	0.028	0.040	0.042	-0.054	-0.085
a ₃	-	-0.033	-	0.042	-0.058	-0.036
a ₄	0.483	0.575	0.390	0.714	-0.174	-0.194
b ₁₂	0.021	-	-	-	-	0.026
b ₁₃	-	-	-	-0.022	0.038	0.018
b ₁₄	-	-	-	-	-0.047	-0.013
b ₂₃	-	-0.038	-0.091	-	-	-
b ₂₄	0.047	-0.035	-	-	-	-0.078
b ₃₄	0.107	0.061	-	-	0.029	0.044
b ₁₁	0.047	0.016	0.030	0.019	0.014	-
b ₂₂	-0.033	-	-0.112	-	-	-
b ₃₃	-	0.052	-	-0.039	-	-
b ₄₄	0.020	-0.085	-	-0.137	0.204	0.093
c ₁	-	-	0.304	0.842	-0.569	-0.579
AARE, %	14	12	16	12	20	12

6.3.1 Effect of Gas Nature on the d_{32} .

The five gases used showed different Sauter-mean bubble diameter. Figure 56 shows the effect of the gas density on the d_{32} , $d_{32\text{-Small}}$, and $d_{32\text{-Large}}$ at 7 bar and 0.126 m/s and in the absence of solid particles. As can be seen in this figure, d_{32} values for the heavier gases (i.e., CH₄, CO and N₂) decrease, whereas $d_{32\text{-Large}}$ always decrease with increasing the gas molecular weight. In Section 6.2.4, it was shown that H₂ had the lowest gas holdup, and d_{32} values indicates that ϵ_G of H₂ is mostly composed of large gas bubbles. CO and N₂ with $M_W = 28$ appear to behave similarly, and their variations are in the same range and magnitude. This figure clearly shows that d_{32} decreases with the gas molecular weight, which also confirms the behavior of the gas holdup with gas molecular weight. Figure 57 shows the effect of gas nature on d_{32} of N₂ and He in Isopar-M/alumina slurry obtained in the hot SBCR at 0 and 5 vol.%; and as can be seen, in the absence and presence of solid particles, d_{32} values of He are always greater than those of N₂ under similar operating conditions. The difference between the d_{32} values of the two gases is about 30% under the solid concentrations studied. This behavior can be attributed to the fact that the density of He is lower than that of N₂ under the same operating conditions, and accordingly He is expected to form larger gas bubbles when compared with those of N₂.

6.3.2 Effect of P, U_G , T and C_V on the Bubble Size Distribution

Figures 58 through 60 illustrate the effect of pressure, superficial gas velocity and solid concentration on the bubble size distribution of the five gases in the cold SBCR; and Figure 61 shows the effect of pressure, temperature and solid concentration on the bubble size distribution of N₂ and He in the hot SBCRs, respectively.

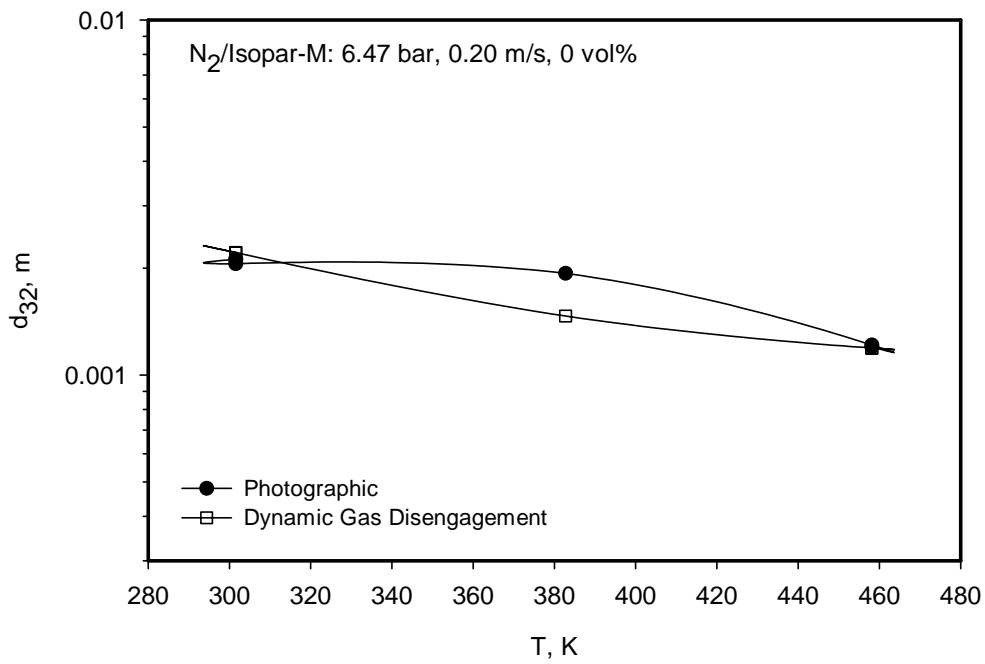
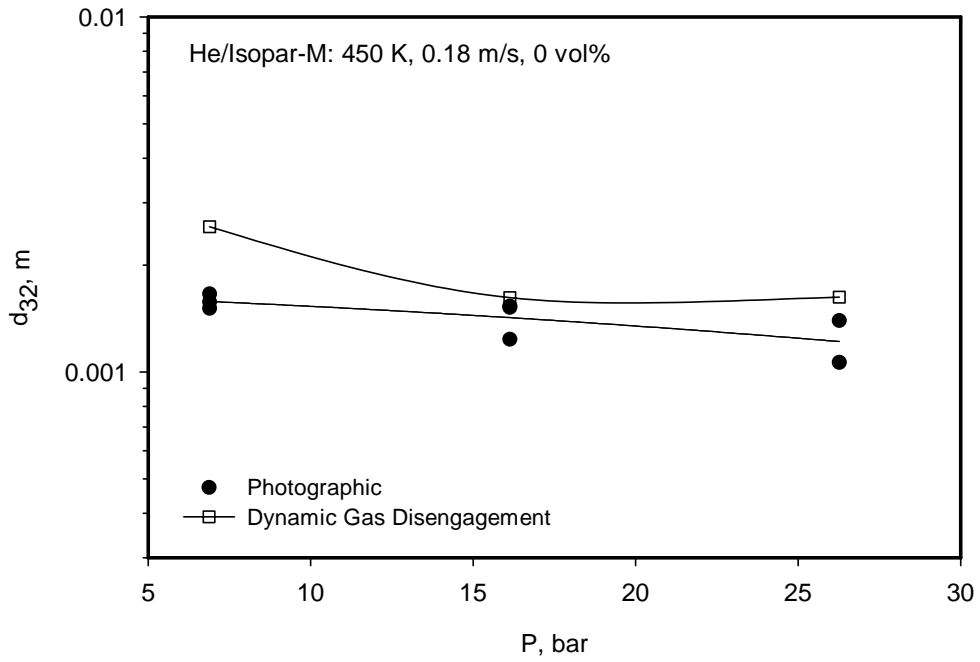


Figure 54 Comparison between Photographic Method and the DGD Technique

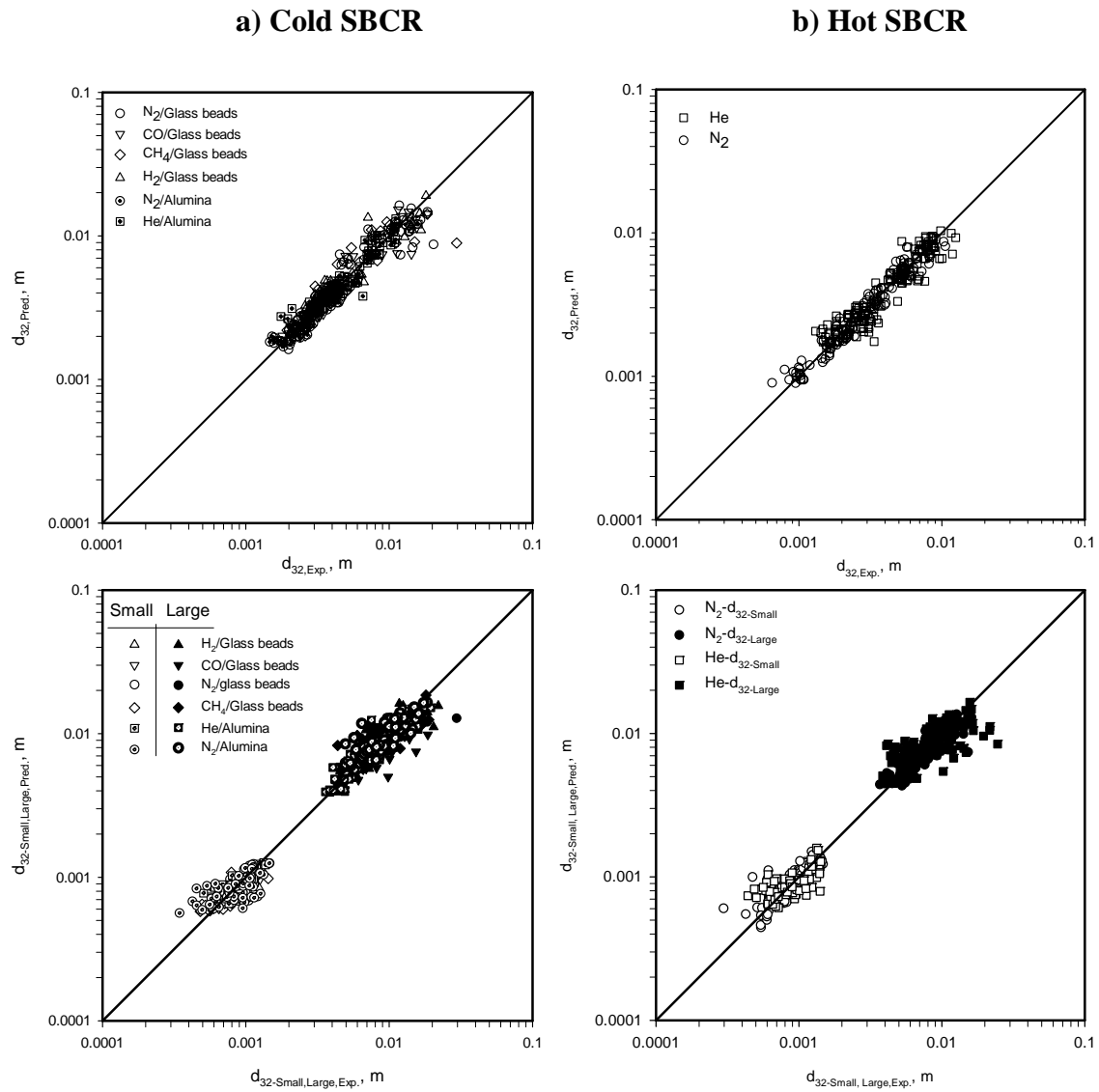


Figure 55 Comparison between the Experimental and predicted d_{32} Values of the Gases in Isopar-M using Equation (6-5) and (6-6)

As can be observed in these figures, the increase of pressure and temperature shifts the bubble size to the left by decreasing the volume fraction of the large gas bubbles, leading to the formation of small gas bubbles. Thus, increasing pressure is mainly responsible for the increase of the population of small gas bubbles, where the volume of the large gas bubbles is nearly unaffected or in some cases could decrease. This behavior supports the earlier findings in Section 6.2.1 concerning the increase of gas holdup with pressure, wherein it was demonstrated that $\varepsilon_{G-Large}$ did not change with pressure. One possible reason for this behavior is the increase of the gas density with pressure, which could be responsible for forming many dense and rigid gas bubbles that become less likely to coalesce when they collide with each other.

Figures 58 through 60 also show that increasing the gas superficial velocity has a slight effect on the bubble size distribution. In fact, a slight increase of the volume fraction of the large gas bubbles could be observed in some cases, indicating an increase of gas bubble coalescence at higher U_G . Therefore, increasing U_G or the gas flow rate through the reactor results in the formation of large gas bubbles, and consequently $\varepsilon_{G-Large}$ tends to increase, as it was shown in Section 6.2.2.

The increase of the gas velocity is responsible of increasing the probability of gas bubbles collisions and coalescence due to high turbulence. This tendency, however, is more pronounced with lighter gases such as H_2 , where an increase in their velocity leads to more coalescence, and sub consequently the increase of the total gas holdup with increasing U_G becomes less significant than that with the heavier gases. For instance, a 0.068 m/s increase in U_G of H_2 increases the total gas holdup by only 15%, whereas in the case of N_2 and CO , a 0.05 m/s increase in their U_G increases their gas holdup by 25 and 30%, respectively.

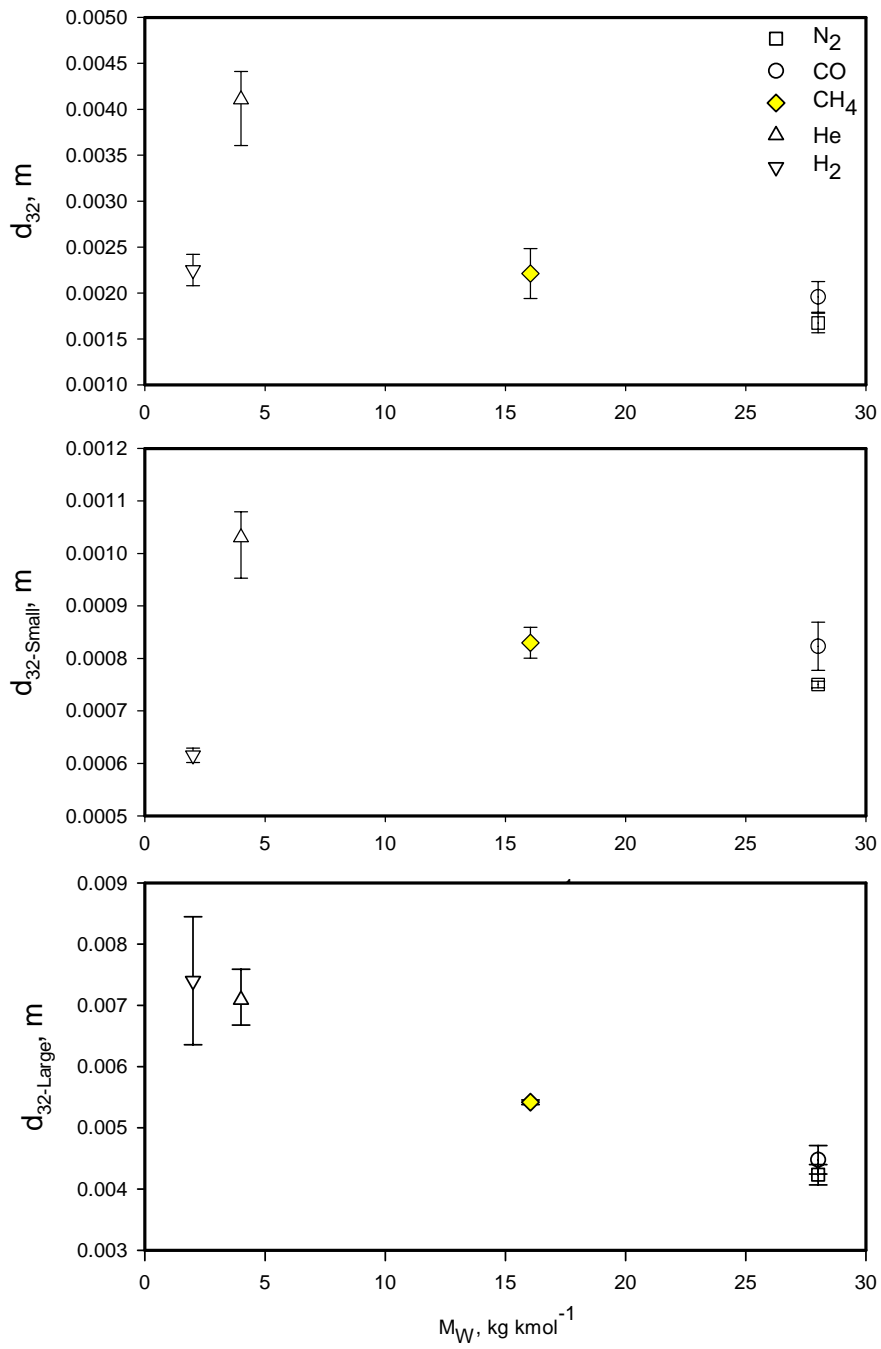


Figure 56 Effect of the Gas Nature on d_{32} , $d_{32-Small}$, $d_{32-Large}$ in the Cold SBCR
(7 bar, 0.126 m/s, 0 vol.%)

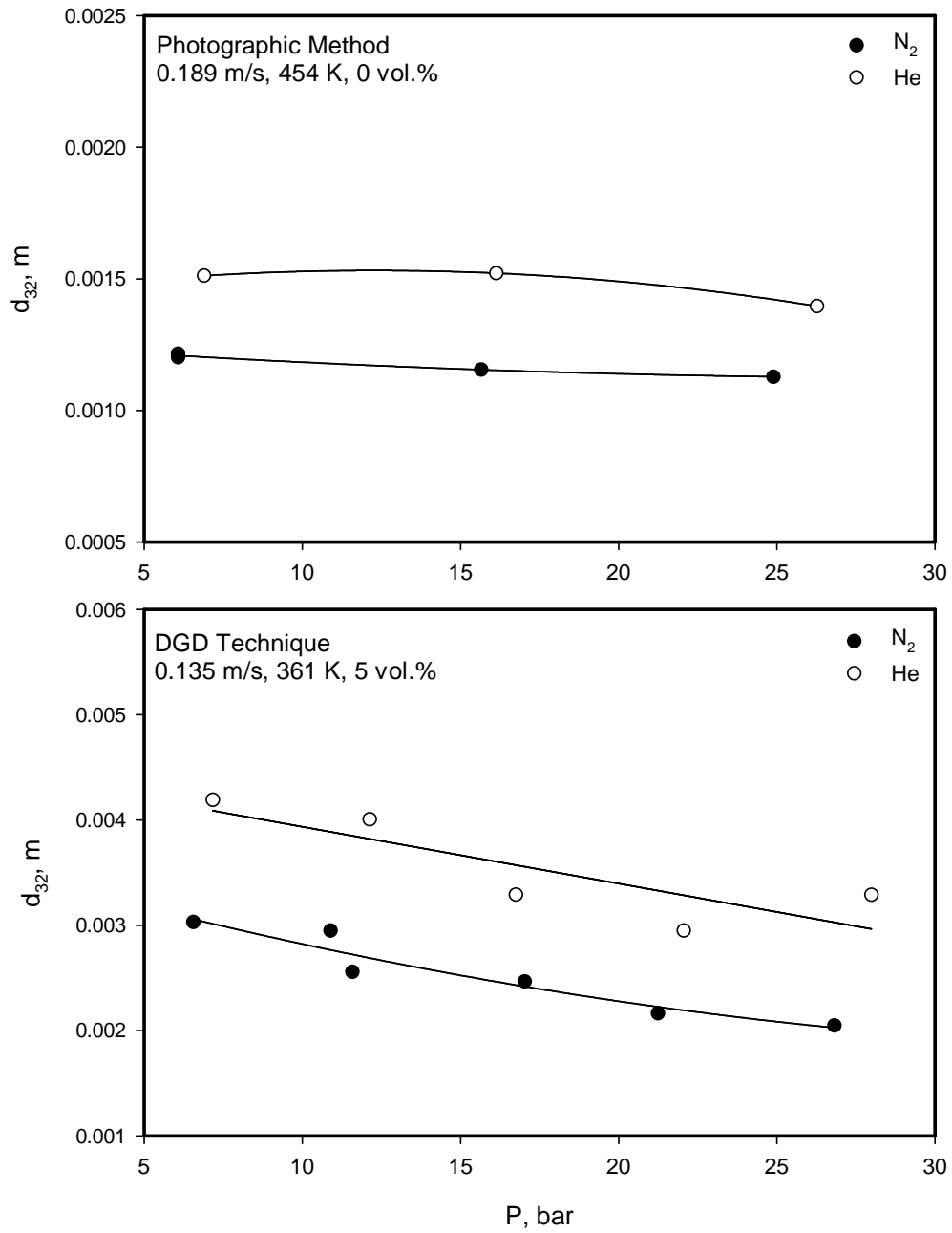


Figure 57 Effect of Gas Nature on d_{32} of N_2 and He obtained using the DGD and the Photographic Techniques in the Hot SBCR

Figures 58 through 61 show that the bubble size distributions of gases are strongly affected by the presence of the solid particles. In most cases, the volume fraction corresponding to bubble sizes less than 2 mm have either disappeared or considerably reduced. This happens as a result of the increase of slurry viscosity with solid concentration which is responsible for promoting coalescence of the gas bubbles and therefore reducing ϵ_G of small gas bubbles. As the bubbles become large, their rise velocity increases and the disengagement time is reduced. This high rise velocity of large bubble swarms creates a strong drag along their path entraining the small gas bubbles and increasing their rise velocities. In this situation, the large gas bubbles residence time within the slurry is reduced and the disengagement time is about 5 to 6 seconds for the highest solid concentration. In the case of the five gases used in the cold SBCR, the volume fraction of bubbles ranging from 0.005 to 0.03 m appeared to increase the most, whereas that of bubbles greater than 0.03 m was not strongly affected by the presence of solid particles. At any given slurry concentration, ϵ_G of large gas bubbles remains almost unchanged, which agrees with previous findings by other investigators ^(70,72,126,189).

6.3.3 Effect of P, T, U_G , and C_V on d_{32}

Figure 62 shows the effect of pressure and superficial gas velocity on the d_{32} of the gases in the cold SBCR, and Figure 63 depicts the effect of pressure and the solid concentration on the d_{32} of N_2 and He in Isopar-M/alumina system in the hot SBCR; and as can be observed in these figures at any given superficial gas velocity and solid concentration, increasing pressure decreases d_{32} of the gases. This indicates that increasing pressure shifts the bubble size distribution towards small gas bubbles which results in an increase of $\epsilon_{G-Small}$ and subsequently the total gas

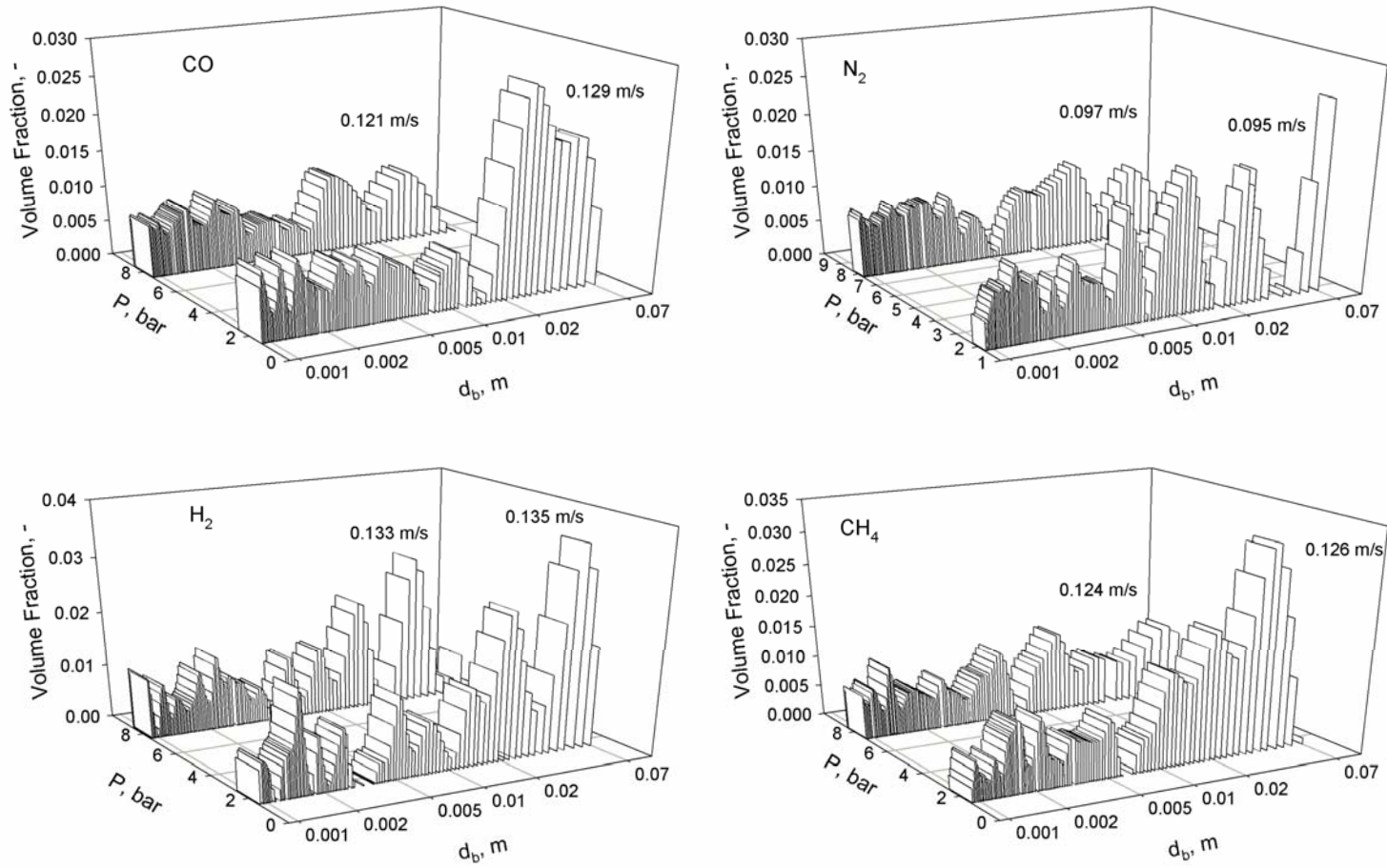


Figure 58 Effect of pressure on the Bubbles Size Distribution of the Gases in Isopar-M in the Cold SBCR

($C_V=0$ vol.%)

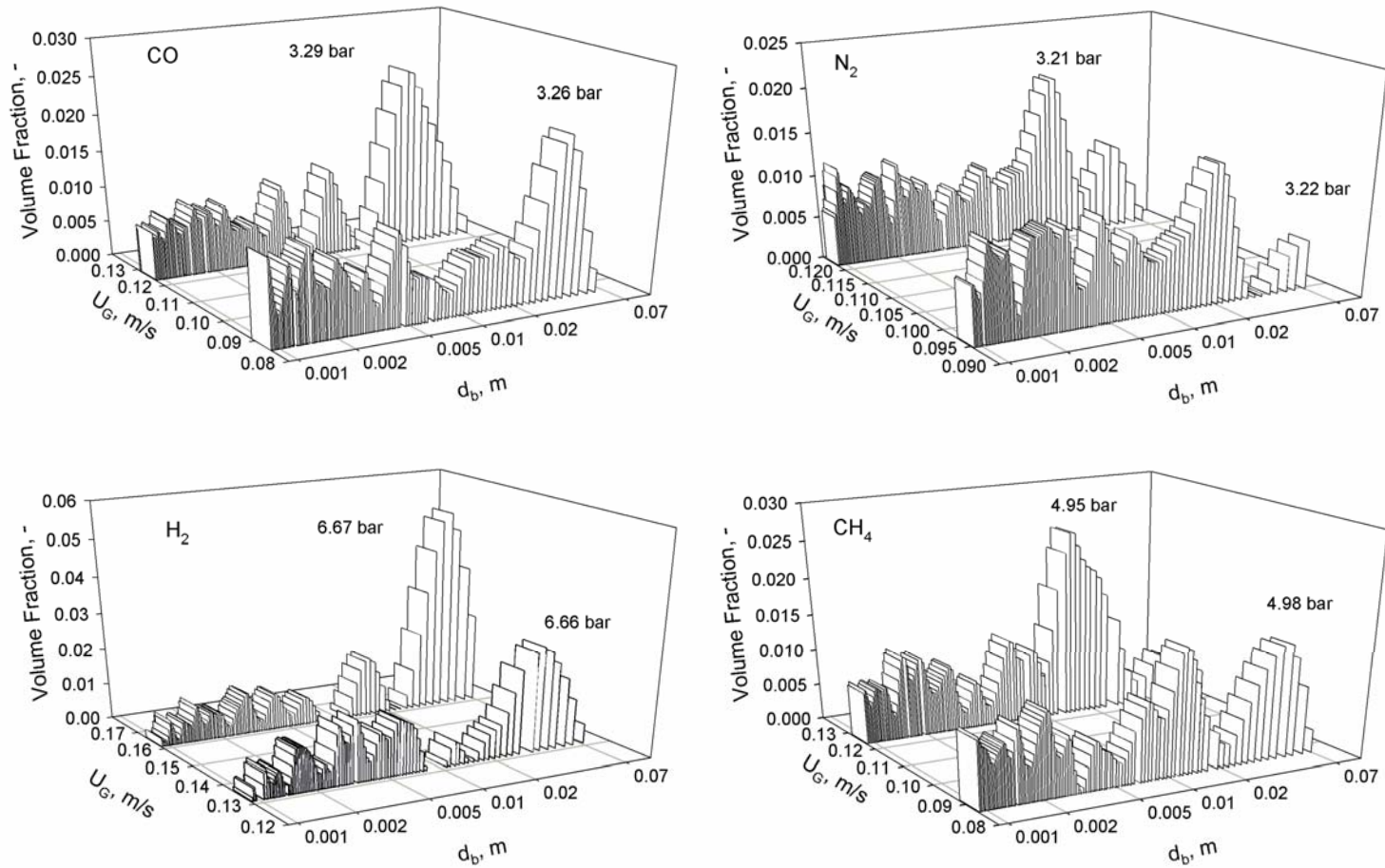


Figure 59 Effect of Gas Velocity on Bubbles Size Distribution of the Gases in Isopar-M in the Cold SBCR

(C_V=0 vol.%)

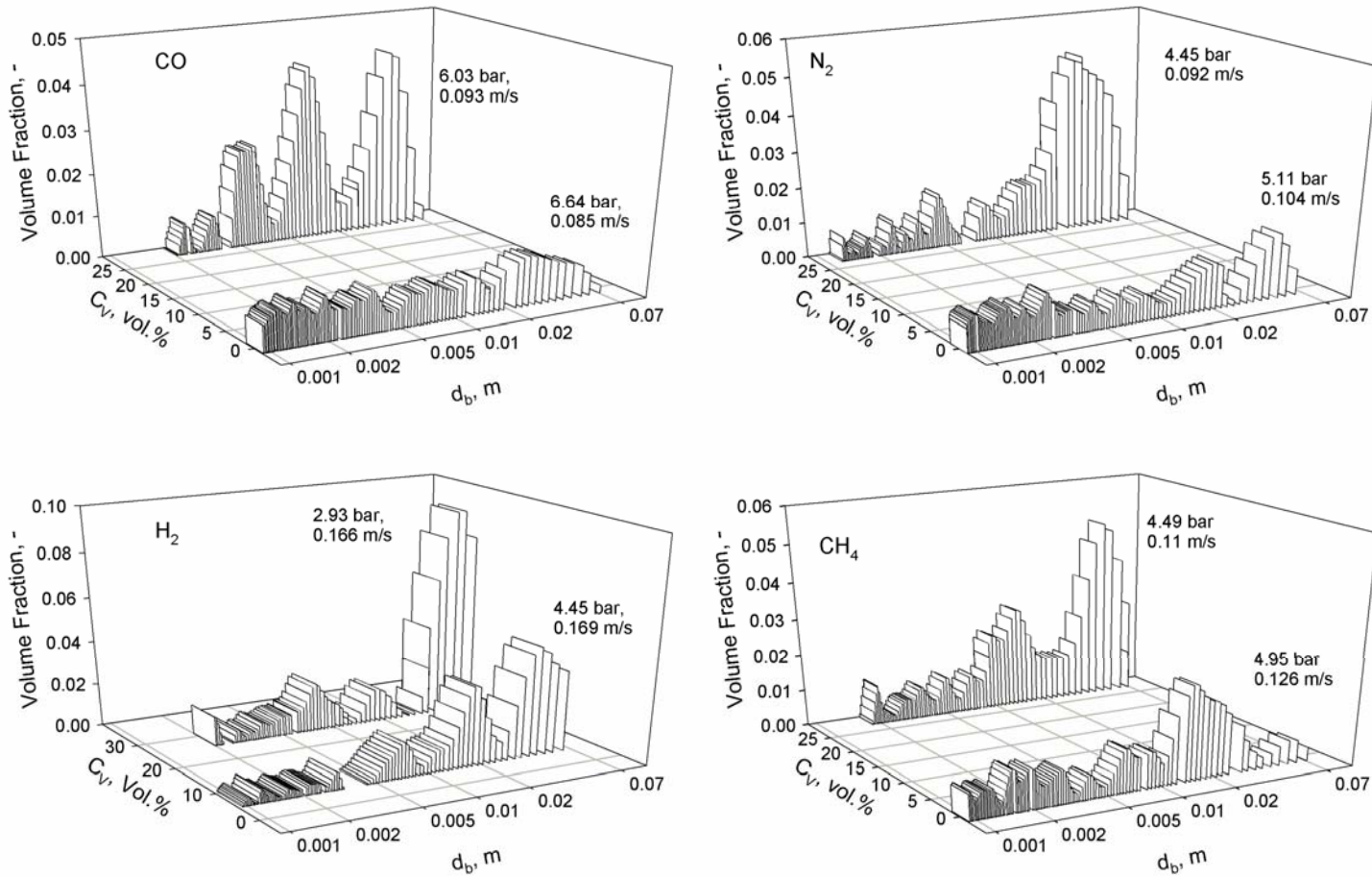


Figure 60 Effect of Solid Concentration on the Bubbles Size Distribution of the Gases in Isopar-M in the Cold SBCR

a) N₂/Isopar-M/Alumina

b) He/Isopar-M/Alumina

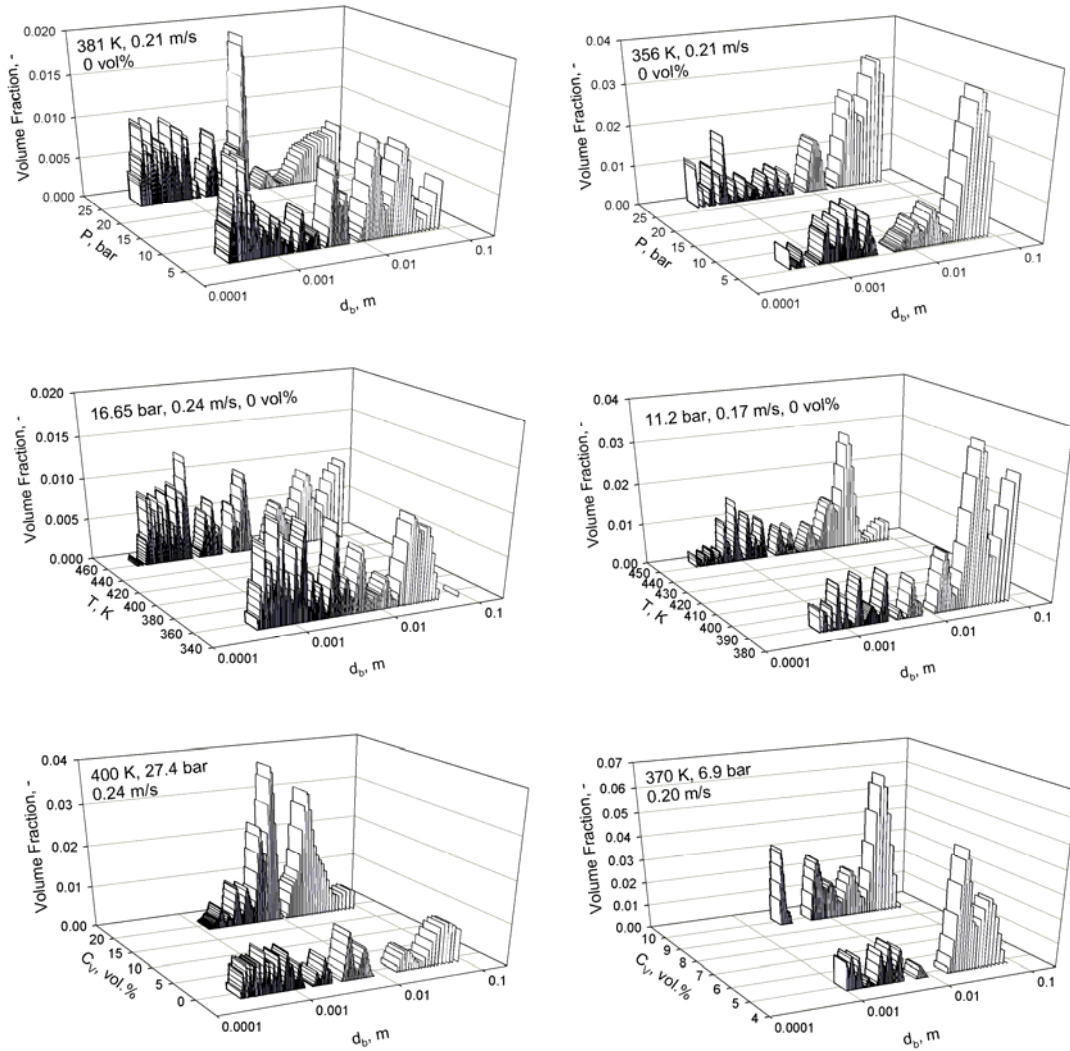


Figure 61 Effect of P, T and C_v on the Bubble Size Distribution of N₂ and He in the Hot

SBCR

holdup as mentioned in Section 6.2.1. This observation is also in accordance with the bubble size distribution of the gases, where increasing pressure shifted the distribution towards smaller gas bubbles. The decrease of d_{32} with pressure in the cold SBCR is about 32% for N_2 and only about 19% for H_2 at their lowest respective gas velocities. It can also be seen that the decrease of d_{32} with pressure is more significant until 5 bars. For instance in the case of CH_4 , d_{32} decreased by 29% from 1.86 to 4.98 bar, whereas it only decreased by 5.3% from 4.98 to 7.83 bar at 0.093 m/s. This behavior was observed for all the gases and suggests that the effect of pressure, although responsible for shrinking the gas bubbles, becomes negligible above a certain value, hence the bubbles were believed to approach their equilibrium size. Similarly, this behavior can also explain the weaker increase of the gas holdup at higher pressure, as it was presented in Section 6.2.1.

The analysis of the d_{32} of N_2 in the hot SBCR indicates that increasing pressure from 7.5 bar to around 15 bar at 5 vol.% solid concentration results in a decrease of d_{32} by more than 40%, accounting for more than 67% of the total decrease of d_{32} over the entire range of the pressure studied. This behavior can partly be related to the fact that at high pressure, the maximum stable bubble size becomes relatively small⁽⁸⁵⁾. Wilkinson and van Dierendonck⁽⁴⁵⁾ used the Kelvin-Helmholz stability analysis to show that in the churn-turbulent flow regime, high gas density (i.e., high pressure) reduces the stability of large gas bubbles due to the decrease of the maximum stable wave length of these large gas bubbles and the increase of the growth rate of the wave-like disturbances on their surfaces⁽⁴⁷⁾. At high solid concentrations (>10 vol. %), however, the effect of gas density (pressure) on d_{32} is hindered. These findings are important in the scale-up of SBCRs, since both high pressure and high solid concentration are used in order to increase

the productivity of the reactor⁽³⁵⁾ because high pressure insures high gas solubility and high solid loading increases the reactants conversion.

Figure 62 shows the effect of gas velocity on the d_{32} of the gases in the cold SBCR; and as can be observed, even though the increase of the gas velocity results in an increase of d_{32} , the gas velocity effect seems to be less significant than that of pressure. In the case of CO for instance, the average increase of d_{32} with U_G is not higher than 6% over the whole range of pressure studied, whereas in the case of H_2 , this increase is about 20%. The increase of d_{32} with gas velocity can be explained by the enhancement of coalescence of gas bubbles as U_G increases. This observation confirms the effect of the gas velocity on the gas holdup reported in Section 6.2.2, where it was shown that an increase of ϵ_G with U_G was mainly due to an increase of ϵ_G .

Large.

Figure 63 shows the effect of temperature on the d_{32} for N_2 and He in Isopar-M/alumina system in the hot SBCR; and as expected increasing temperature leads to a decrease of d_{32} for both gases which is in agreement with literature findings⁽⁵⁵⁾. Figure 64 illustrates that the effect of temperature on d_{32} becomes more important as the solid concentration is increased. For instance increasing solid concentration from 0 to about 5 vol.%, d_{32} values for both gases decrease with temperature, however, increasing solid concentration from 5 to 10 vol.%, the d_{32} values for both gases increase with temperature. This behavior can be attributed to the decrease of the froth stability of the Isopar-M at high temperature and solid concentration. Increasing temperature decreases the liquid surface tension and viscosity leading to the formation of small gas bubbles, whereas increasing solid concentration increases the slurry viscosity as well as bubble coalescence (i.e., bubble size) and decreases the froth stability, leading to formation of

large gas bubbles. Thus, the resultant effect of increasing temperature and solid concentration should be considered in the design and scaleup of SBCRs. Figure 65 shows two snapshots of the bed height with a solid concentration of 10 and 15 vol.% for N₂/Isopar-M/alumina system at 27.6 bar and 453 K; and as can be observed, froth as a cluster of cellular structure gas bubbles is formed at the top of the bed at a solid concentration of 10 vol.%. As the solid concentration is increased to 15 vol.%, however, the froth at the top of the bed is reduced significantly.

Figures 66 through 69 illustrate that d_{32} , $d_{32\text{-Small}}$ and $d_{32\text{-Large}}$ are strongly affected by solid concentration, and the effect of increasing solid concentration on d_{32} appears to be more important than that of increasing pressure. For instance in the case of N₂ in the hot SBCR at the maximum pressure studied (~ 27 bar), increasing alumina powder concentration from 5 to 15 vol.% in Isopar-M, increases d_{32} by a factor > 3.5 which means that the coalescence of gas bubbles is increased with increasing solid concentration. In the cold SBCR, the increase of C_V from 0 to 36 vol.% resulted in an increase of the mean bubble diameter by a factor of 8 to 10 independently of the gas type, and in all cases, $d_{32\text{-Small}}$ disappeared after 20 vol.% of solids. Actually, for H₂ the maximum d_{32} measured was about 1.6 cm at 36 vol.% solid. This behavior indicates once again that the effect of solid concentration on d_{32} is more important than that of pressure.

6.4 MASS TRANSFER IN THE COLD AND HOT SBCRS

The volumetric liquid-side mass transfer coefficient, $k_L a$, was determined using the transient physical gas absorption technique in the cold and hot SBCRs. In general, the behavior of $k_L a$ values is dependent on the effect of operating variables on the liquid-side mass transfer

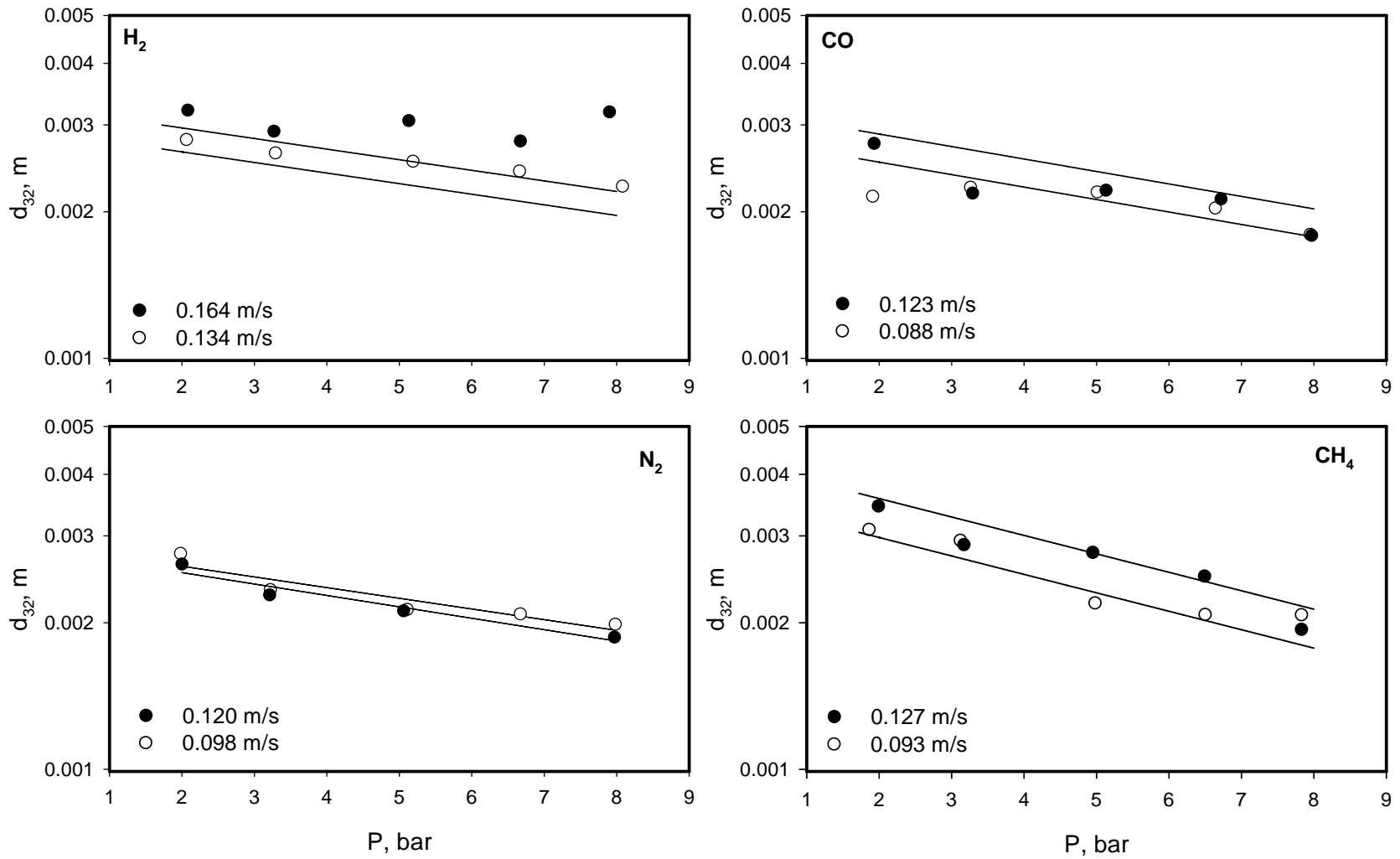


Figure 62 Effect of P and U_G on d₃₂ of the Gases in the Cold SBCR

Line: Equation (6-5)

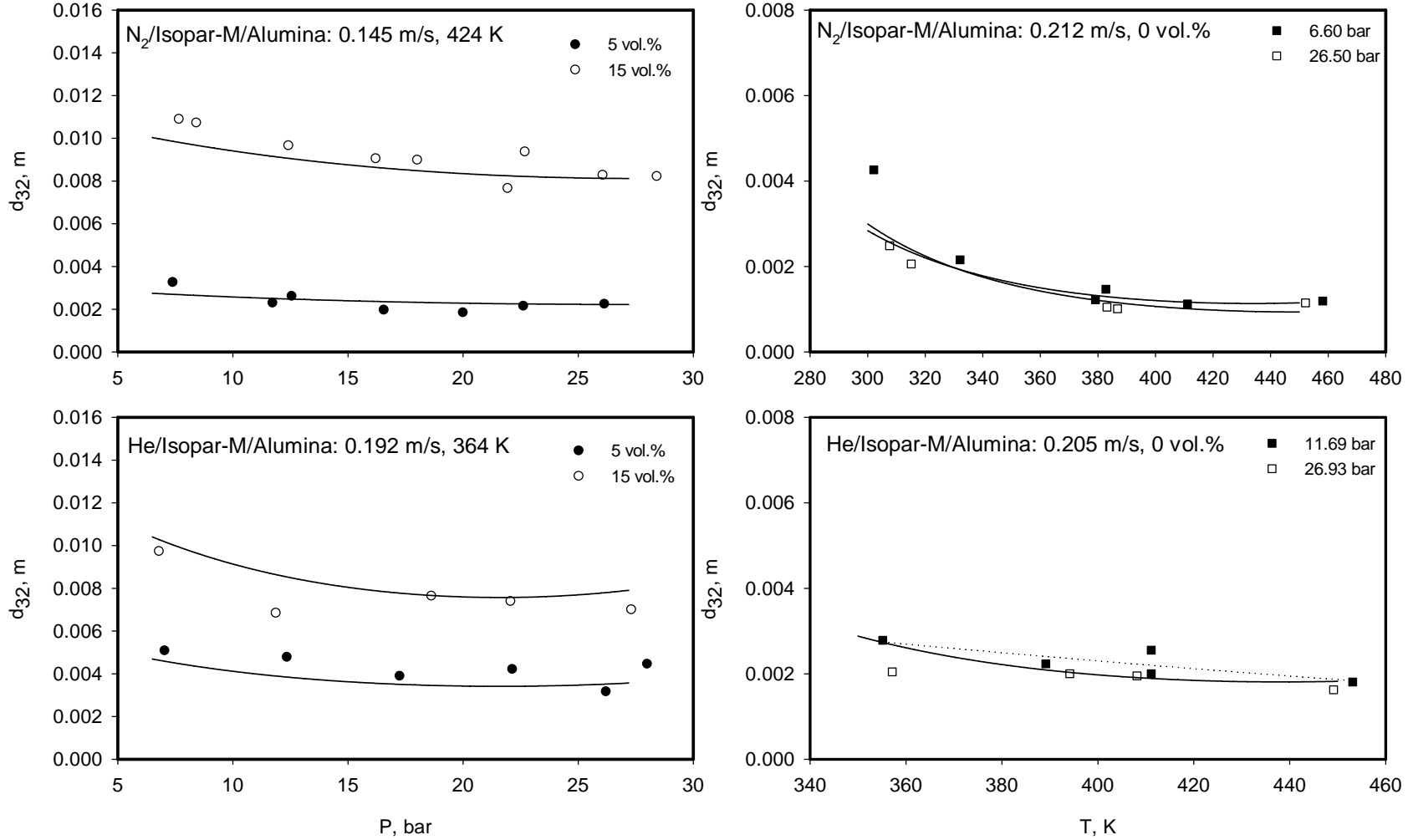


Figure 63 Effect of P , C_V and T on d_{32} of the N_2 and He in the Hot SBCR

Lines: Equation (6-6)

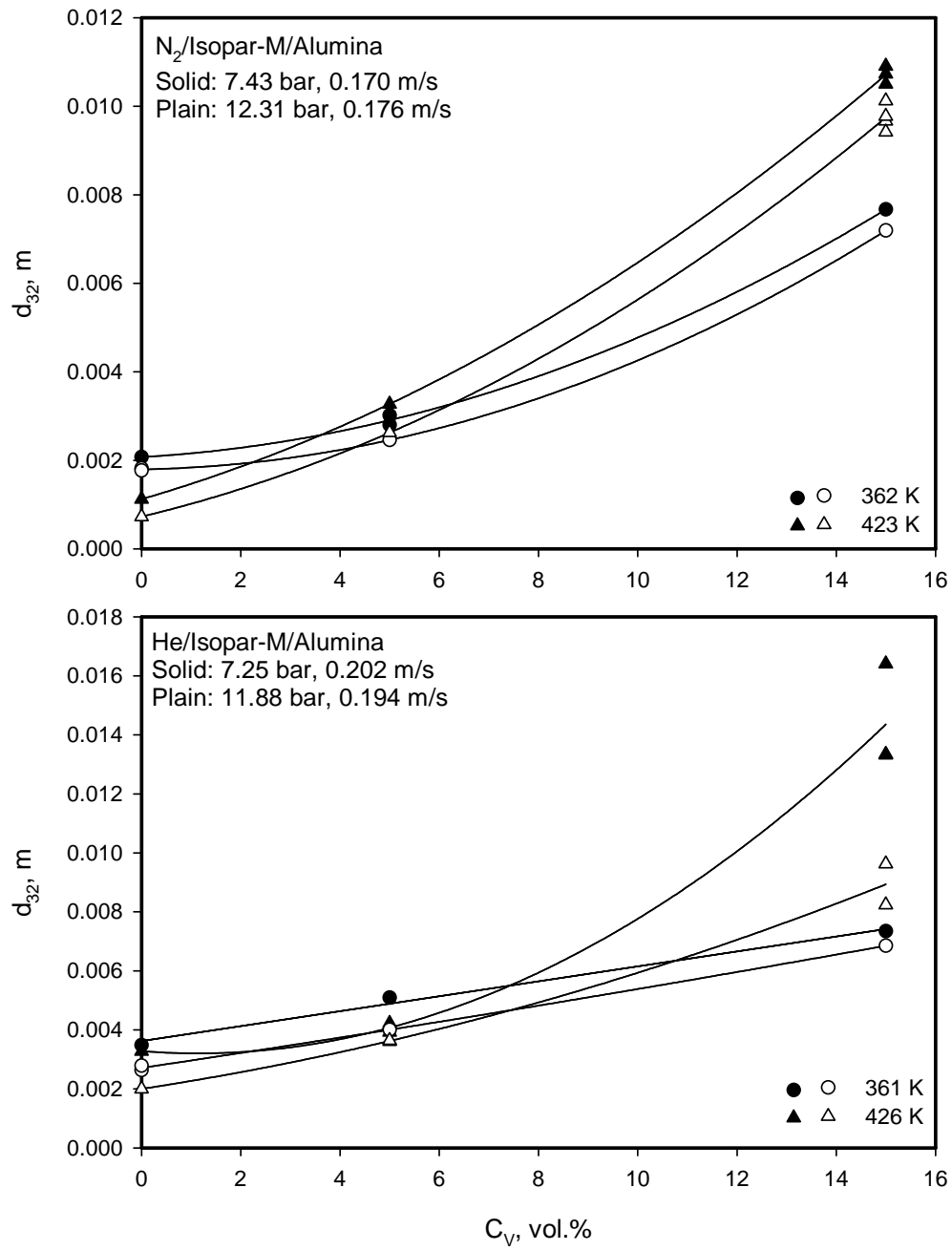


Figure 64 Effect of Temperature on the foaming of the Isopar-M/Alumina slurry in the Hot SBCR

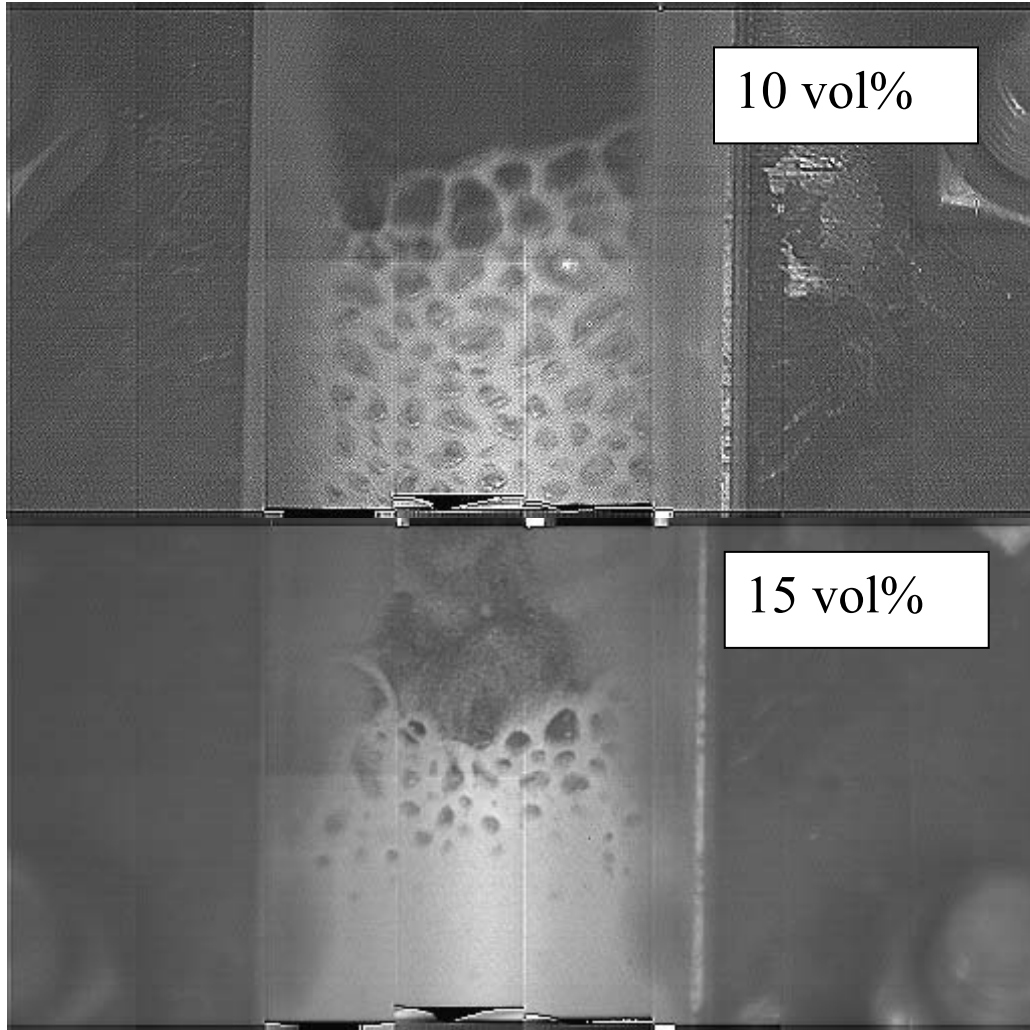


Figure 65 Effect of Solid Concentration on the Froth Characteristics of Isopar-M/Alumina Slurry Observed in the Hot SBCR

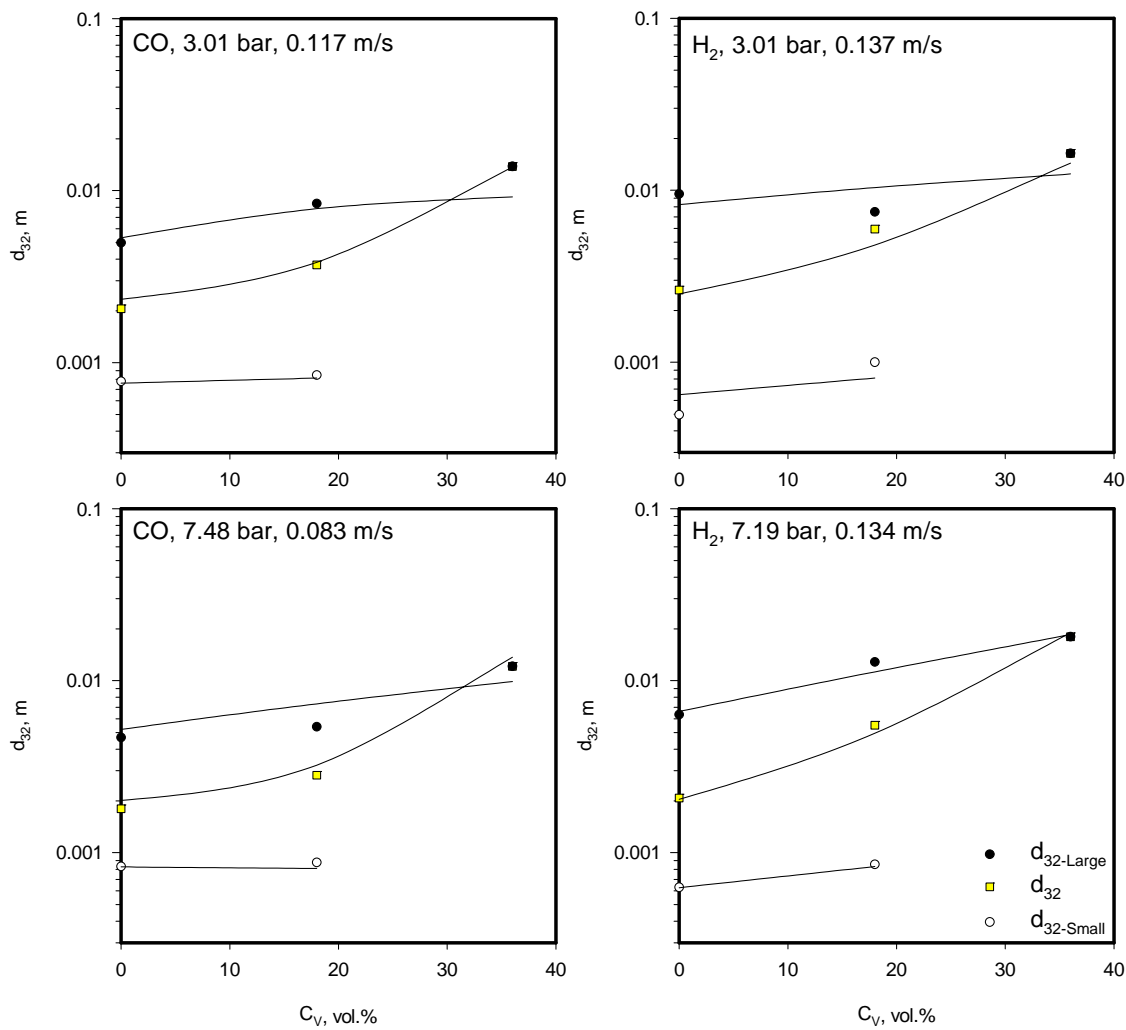


Figure 66 Effect of Glass Beads Concentration on d_{32} , d_{32} -Small, and d_{32} -Large of H₂ and CO in

the Cold SBCR

Lines: Equation (6-5)

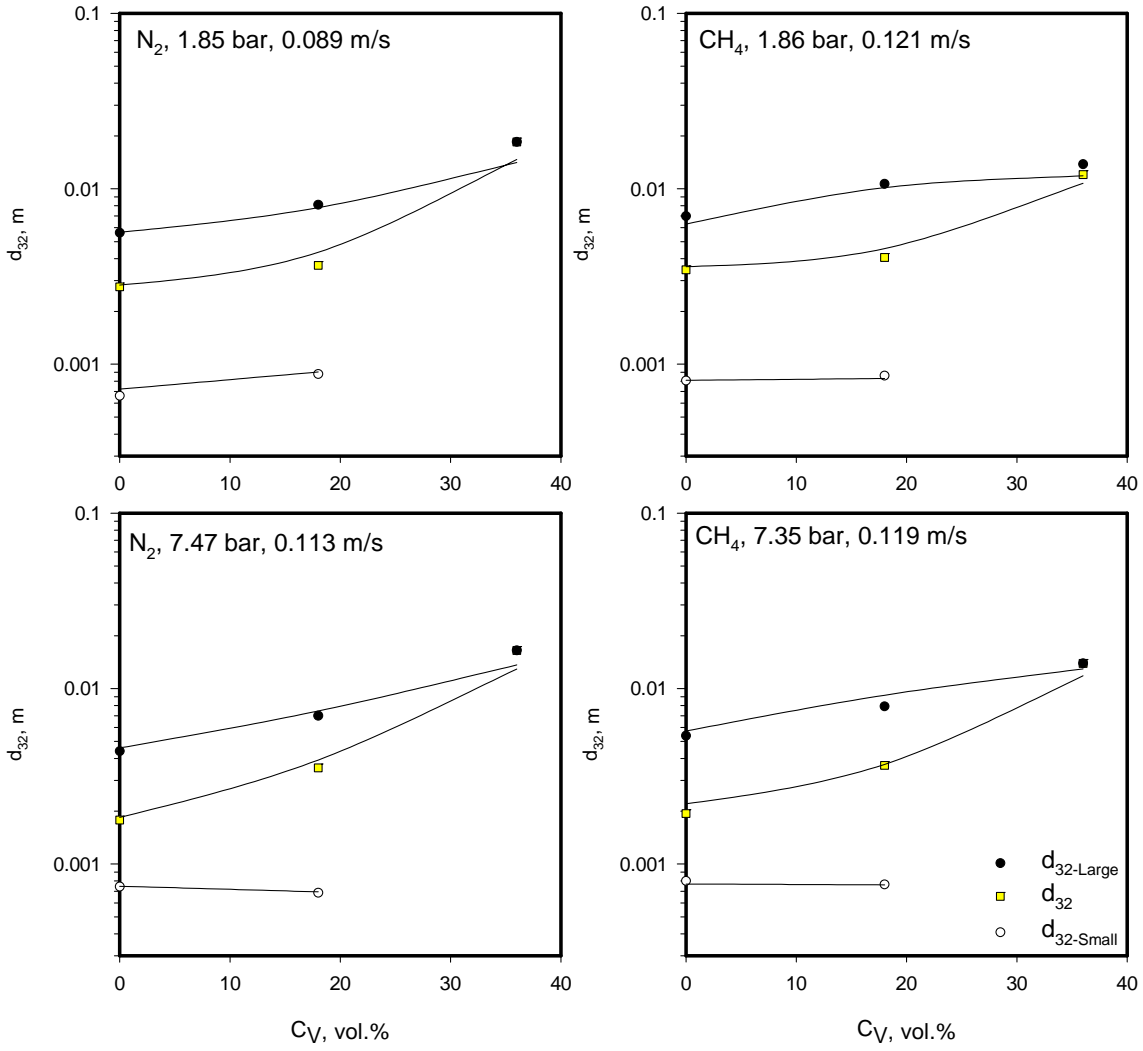


Figure 67 Effect of Glass Beads Concentration on d_{32} , d_{32} -Small, and d_{32} -Large of N_2 and CH_4 in

the Cold SBCR

Lines: Equation (6-5)

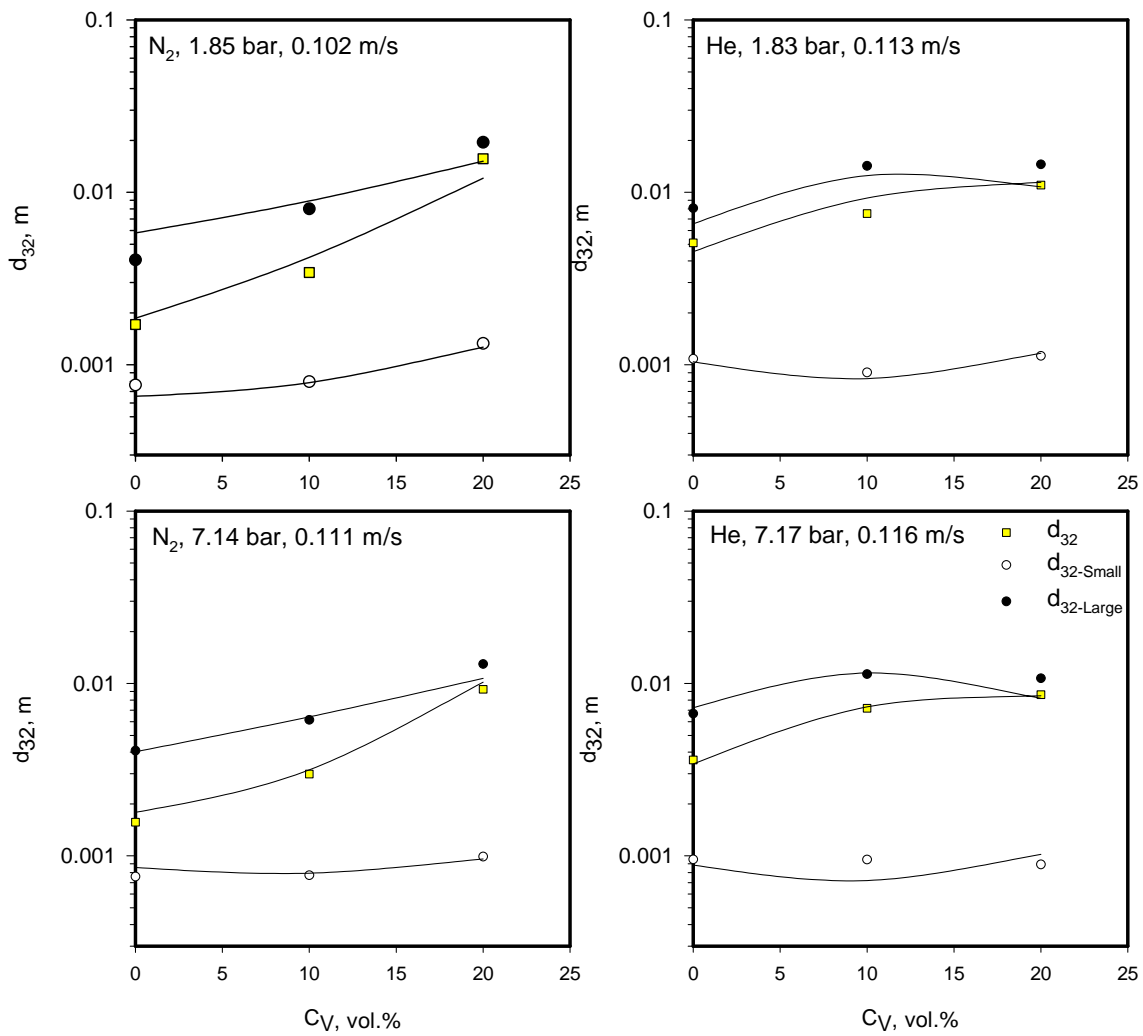


Figure 68 Effect of Alumina Powder Concentration on d_{32} , $d_{32-Small}$, and $d_{32-Large}$ of N_2 and

He in the Cold SBCR

Lines: Equation (6-5)

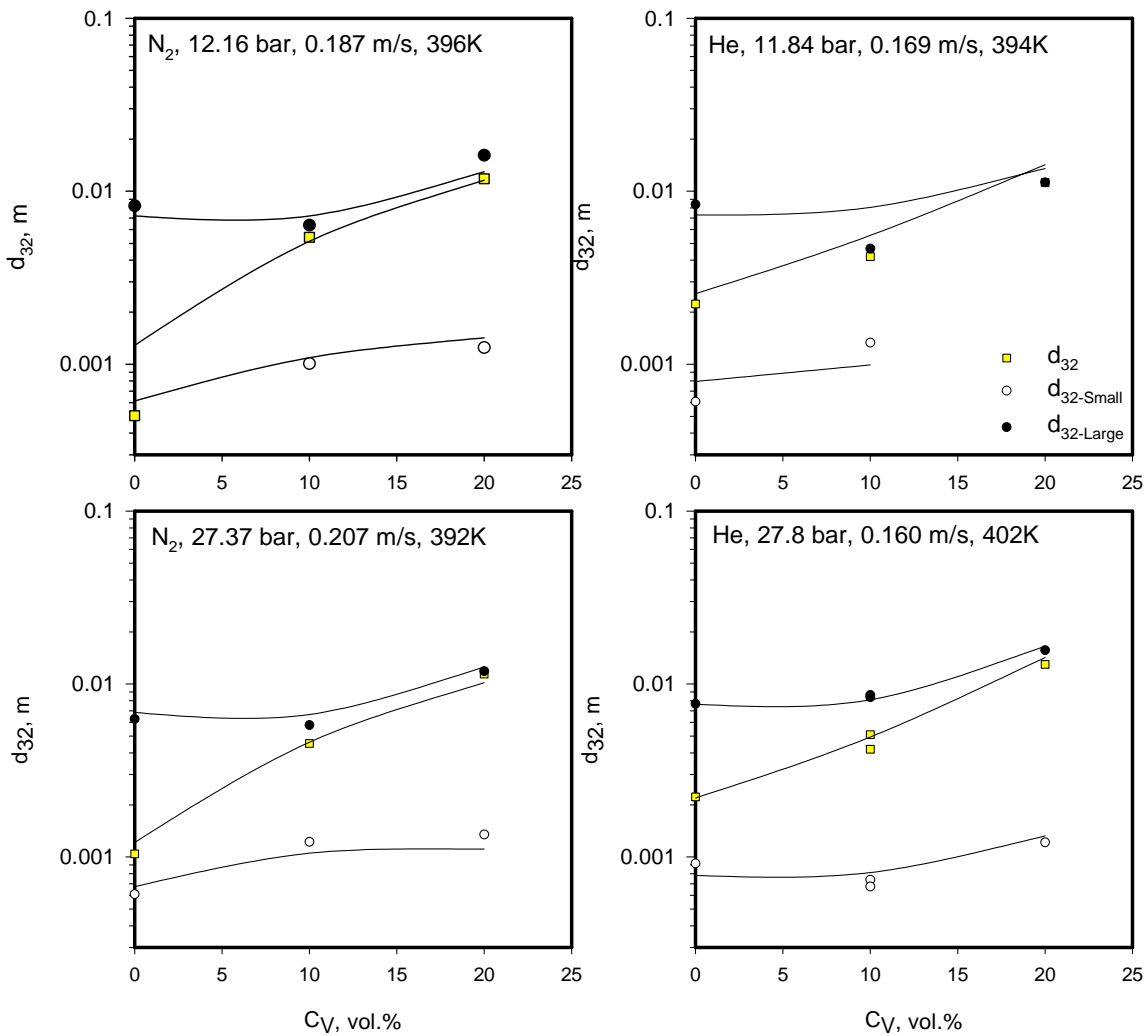


Figure 69 Effect of Alumina Powder Concentration on d_{32} , d_{32} -Small, and d_{32} -Large of N_2 and He in the Hot SBCR

Lines: Equation (6-6)

coefficient, k_L , and the gas-liquid interfacial area, a . A general correlation of k_L can be expressed as follows ⁽²⁰⁶⁾:

$$\frac{k_L}{U_F} Sc^n = const \quad (6-7)$$

Where U_F is the frictional velocity generated by the bubbles at the gas-liquid interface and Sc is the Schmidt Number. In the cold SBCR, the temperature was kept at ambient conditions during all experiments, and subsequently the kinematic viscosity and diffusivity in Sc could be considered constant. Hence, under these conditions, Equation (6-7) shows that k_L is mainly affected by U_F , however, since the superficial gas velocity was high enough to insure a fully-developed, churn-turbulent flow regime in all experiments, no significant changes in U_F values should be expected. Thus, the behavior of $k_L a$ in the cold SBCR could only be due to the alteration of the gas-liquid interfacial area. In the hot SBCR, however, the temperature and pressure were so high that the physical properties of the liquid phase should considerably change. It should therefore be determined if the behavior of $k_L a$ is dependent on the mass transfer coefficient, the gas-liquid interfacial area, or both.

The gas-liquid interfacial area, a , is defined as:

$$a = \frac{(\text{Surface Area})_{\text{Bubble}}}{(\text{Volume})_{\text{Liquid}}} = \frac{6\varepsilon_G}{d_{32}(1-\varepsilon_G)} \quad (6-8)$$

In the churn-turbulent flow regime, the gas bubbles can be split into small and large with their corresponding gas-liquid interfacial area of small (a_{Small}) and large (a_{Large}) gas bubbles as:

$$a_{\text{Small}} = \frac{6\varepsilon_{G-\text{Small}}}{d_{32-\text{Small}}(1-\varepsilon_G)} \quad (6-9)$$

$$a_{L \text{ arg e}} = \frac{6\varepsilon_{G-L \text{ arg e}}}{d_{32-L \text{ arg e}}(1-\varepsilon_G)} \quad (6-10)$$

The knowledge of the total gas holdup, ε_G and the Sauter-mean bubble diameter, d_{32} discussed in Sections 6.2 and 6.3, allows the calculation of the mass transfer coefficient k_L :

$$k_L = \frac{k_L a}{a} = \frac{(k_L a) d_{32}(1-\varepsilon_G)}{6\varepsilon_G} \quad (6-11)$$

Since all experiments were selected following the CCSD, similar to the gas holdup and Sauter-mean bubble diameter, $k_L a$ and k_L values were correlated with Equations (6-12) and (6-13) for the cold and hot SBCRs, respectively, as:

$$\text{Ln}(\Phi)_{\text{COLD}} = a_0 + \sum_{i=1}^3 a_i X_i + \sum_{\substack{i=1 \\ j \geq i}}^6 b_{i,j} X_i X_j + \sum_{i=1}^3 c_i \sqrt{1 + \exp(X_i^2)} + d_1 \exp(-1 - X_3) \quad (6-12)$$

$$\text{Ln}(\Phi)_{\text{HOT}} = a_0 + \sum_{i=1}^4 a_i X_i + \sum_{\substack{i=1 \\ j \geq i}}^{10} b_{i,j} X_i X_j + c_1 \exp(-1 - X_4) \quad (6-13)$$

Where the parameter Φ represents either $k_L a$ or k_L . The coefficients in Equations (6-12) and (6-13) for $k_L a$ in the cold and hot SBCRs are given in Tables 25 and 26, respectively.

The coefficients in Equation (6-12) and (6-13) for k_L in the cold and hot SBCRs are given in Tables 27 and 28, respectively.

Figures 70 a) and b) present a comparison between the experimental and predicted $k_L a$ and k_L values obtained in the cold and hot SBCRs respectively; and as can be seen all predicted values are in good agreement.

Table 25 Coefficients for Equation (6-12) used for $k_L a$ correlation in the cold SBCR

	<i>Glass beads system</i>				<i>Alumina system</i>	
	H ₂	CO	N ₂	CH ₄	He	N ₂
a ₀	-1.825	-1.369	-1.163	-1.551	-1.908	-1.972
a ₁	-	0.094	0.197	0.126	0.131	0.085
a ₂	0.176	-	-	0.163	0.149	0.098
a ₃	-	-0.348	-0.100	-	0.177	-
b ₁₂	-	-0.029	-0.025	-0.018	-	-0.047
b ₁₃	-	-	-	-0.051	0.029	-
b ₂₃	0.041	-	-	-0.021	-	-
b ₁₁	-0.096	-0.125	-0.050	-0.139	-0.036	-0.022
b ₂₂	-	-0.102	-0.098	-	-0.047	-0.125
b ₃₃	-0.385	-	-	0.062	-0.241	-
c ₁	0.088	0.091	-	0.094	-	-
c ₂	-0.026	0.105	0.096	-	-	0.071
c ₃	0.121	-0.056	-0.165	-0.196	-	-0.202
d ₁	0.794	-0.162	-	-	0.865	0.751
AARE, %	4	5	5	5	6	4

Table 26 Coefficients for Equation (6-13) used for $k_L a$ correlation in the hot SBCR

	He	N ₂
a ₀	-0.478	-0.4449
a ₁	0.111	0.14
a ₂	0.072	-
a ₃	0.178	0.1911
a ₄	-0.140	-0.1443
b ₁₂	-	-
b ₁₃	-	-0.0366
b ₁₄	-0.012	0.0429
b ₂₃	-	-
b ₂₄	0.034	-
b ₃₄	-0.027	-0.0293
b ₁₁	-0.038	-0.0461
b ₂₂	-0.024	-0.0414
b ₃₃	-	0.0256
b ₄₄	-	-
c ₁	-	-
AARE, %	9	11

Table 27 Coefficients for Equation (6-12) used for k_L correlation in the cold SBCR

	<i>Glass Beads System</i>				<i>Alumina System</i>	
	H ₂	CO	N ₂	CH ₄	He	N ₂
a ₀	-6.713	-6.358	-6.870	-7.559	-7.303	-7.718
a ₁	0.076	-	-0.074	-	0.014	-0.082
a ₂	0.102	-	-	0.088	0.162	-0.016
a ₃	1.185	0.511	0.896	1.064	1.889	-0.186
b ₁₂	-	-0.049	-	-	-	-0.036
b ₁₃	0.115	0.063	-	0.047	-	-0.051
b ₂₃	-	-	-	-	-	-
b ₁₁	-	-	0.341	-	0.172	-
b ₂₂	-	0.255	-0.097	-0.443	-	-
b ₃₃	-	0.514	-	0.558	-0.609	-
c ₁	-	-	-0.367	-0.065	-0.169	-
c ₂	-	-0.329	-	0.469	-	-
c ₃	-0.330	-0.444	-0.169	-0.733	-0.239	0.187
d ₁	1.387	-	0.777	1.339	3.163	-0.904
AARE, %	13	12	16	15	21	16

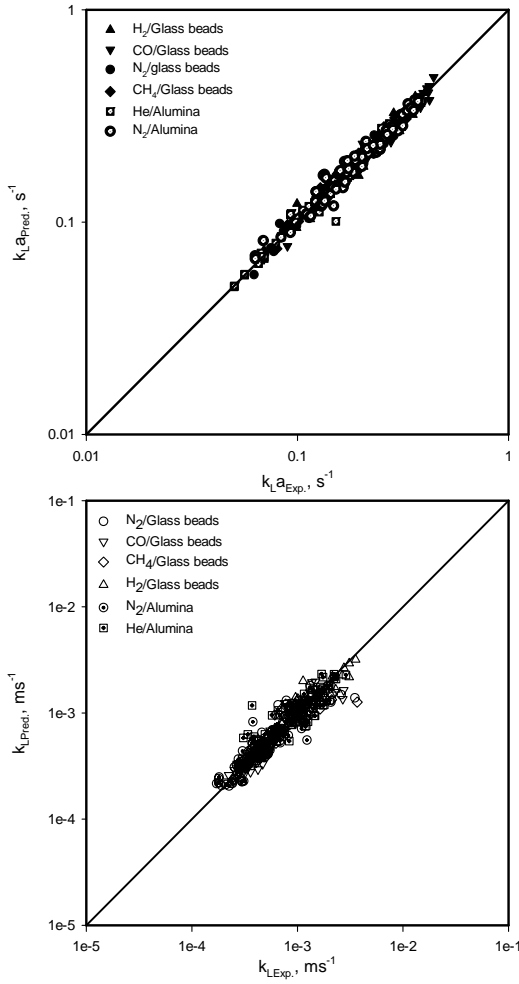
Table 28 Coefficients for Equation (6-13) used for k_L correlation in the hot SBCR

	He	N ₂
a ₀	-7.076	-7.588
a ₁	-0.081	-0.023
a ₂	-0.094	0.003
a ₃	0.105	0.031
a ₄	0.574	1.064
b ₁₂	0.100	-
b ₁₃	0.052	-0.026
b ₁₄	-0.031	0.028
b ₂₃	-	-
b ₂₄	-	-
b ₃₄	0.141	0.073
b ₁₁	0.045	-
b ₂₂	0.126	-
b ₃₃	0.066	0.128
b ₄₄	0.074	-0.228
c ₁	-	0.640
AARE, %	16	18

6.4.1 Effect of Pressure and Gas Velocity on $k_L a$

Figures 71 through 75 show the effects of pressure, gas velocity, and solid concentration on $k_L a$ for the five gases in Isopar-M/glass beads, alumina slurry obtained in the cold SBCR; and Figure 76 shows the effects of pressure and gas velocity on $k_L a$ values of N_2 and He in Isopar-M/alumina slurry obtained in the hot SBCR. As can be seen in these figures, $k_L a$ values increase with pressure and gas velocity. This increase of $k_L a$ can be observed at all solid concentrations used, however, the increase is more significant at lower pressure. For instance, at a gas superficial velocity of 0.1 m/s and a solid concentration of 7.6 vol.%, $k_L a$ values of H_2 increases by 25% when the pressure increases from 1.8 to 4.5 bar, while $k_L a$ values only increase by 7% when the pressure increases from 4.5 to 7.3 bar. This $k_L a$ behavior is similar to that observed by Inga⁽¹⁸⁹⁾ and Behkish et al.⁽⁷⁷⁾ for H_2 , CO, N_2 and CH_4 in hexanes liquid mixture. It should be mentioned that under similar operating conditions, the gas holdup and the Sauter mean bubble diameter (d_{32}) values were reported to vary faster at lower pressure, as discussed in Sections 6.2.1 and 6.3.2, respectively, leading to conclude that the increase of $k_L a$ with pressure was mainly due to the increase of the volume fraction of small gas bubbles^(126,77). Actually, in Figures 77 through 82 it can be seen that the gas-liquid interfacial area of the gases in the cold and hot SBCRs increases with pressure, mostly due to an increase of a_{Small} ; whereas a_{Large} appears to be almost independent of pressure, especially at high solid concentration. The effect of the operating variables on the mass transfer coefficients, k_L of the five gases in Isopar-M/glass beads, alumina in the cold and hot SBCRs is shown in Figures 83 through 88; and as can be seen the change of k_L with pressure over the entire range of solid concentration, gas velocity and temperature is insignificant.

a) Cold SBCR



b) Hot SBCR

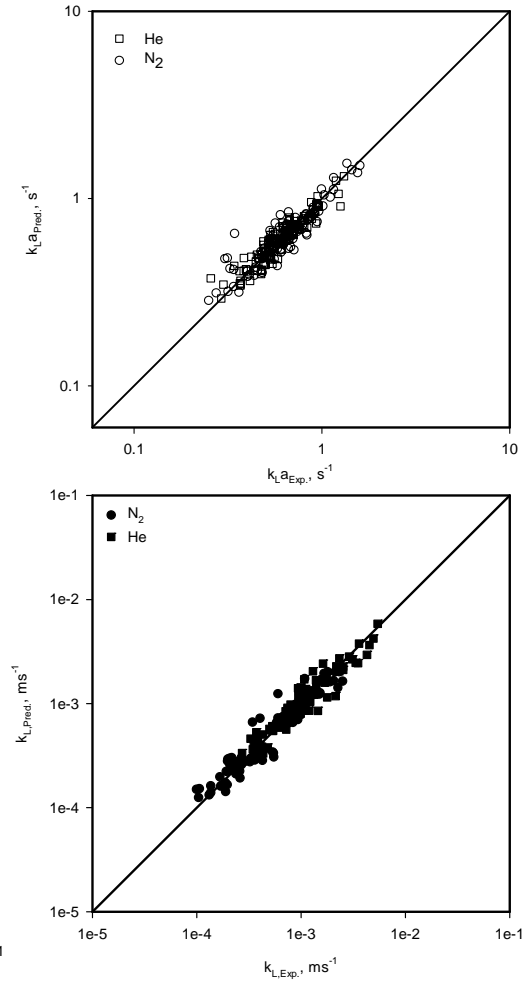


Figure 70 Comparison between the Experimental and Predicted $k_L a$ and k_L Values for the Gases Using Equation (6-12) and (6-13)

In fact, in the absence of solid particles, k_L actually decreases with pressure. For instance, in the case of H_2 at 0.135 m/s (Figure 83), when $C_V = 0$, k_L decreases over the entire range of pressure (2-7 bar) by 24%, whereas $k_{L,a}$ value under the same conditions (Figure 71) increases by almost 30%. Similar behavior was observed for the other gases. The decrease of k_L with pressure can be explained by the decrease of the size of the gas bubbles with pressure. Calderbank and Moo-Young⁽²⁰⁷⁾ and Marrucci⁽²⁰⁸⁾ reported that k_L is proportional to the bubble size, thus when the average bubble size decreases, the degree of turbulences decreases and a smaller k_L value can be expected⁽²⁰⁹⁾. Thus, the effect of pressure on $k_{L,a}$ values observed in this study concurs with the findings by several investigators^(17,41,45) who reported that increasing pressure was responsible for decreasing gas bubbles size, leading to the enhancement of the volumetric-liquid side mass transfer coefficients.

The increase of $k_{L,a}$ with superficial gas velocity, U_G , was found to be more important at lower than at higher pressures. For instance, Figure 74 shows that for CH_4 at 18 vol.% solid, $k_{L,a}$ values increases by 116% when the gas velocity increases from 0.08 to 0.16 m/s at 2 bar, whereas k_L values only increases by 57% when the gas velocity was increased from 0.08 to 0.16 m/s at 7.3 bar. Similar behavior of $k_{L,a}$ with U_G was observed for H_2 , CO, He, and N_2 , where the $k_{L,a}$ values increased by a factor greater than or equal to 100% at 1.7 bar, and by a factor less than or equal to 50% at 7.5 bar pressure. Figures 77 (a) through 81 (a) show that the gas-liquid interfacial area does not increase significantly with gas velocity, and in Figures 83 through 87, it can be seen that k_L of the gases increases with U_G , particularly for the lighter gases (i.e., H_2 , He and CH_4) than the heavier gases. For instance, at 7.6 vol.% of glass beads, k_L of H_2 increased by

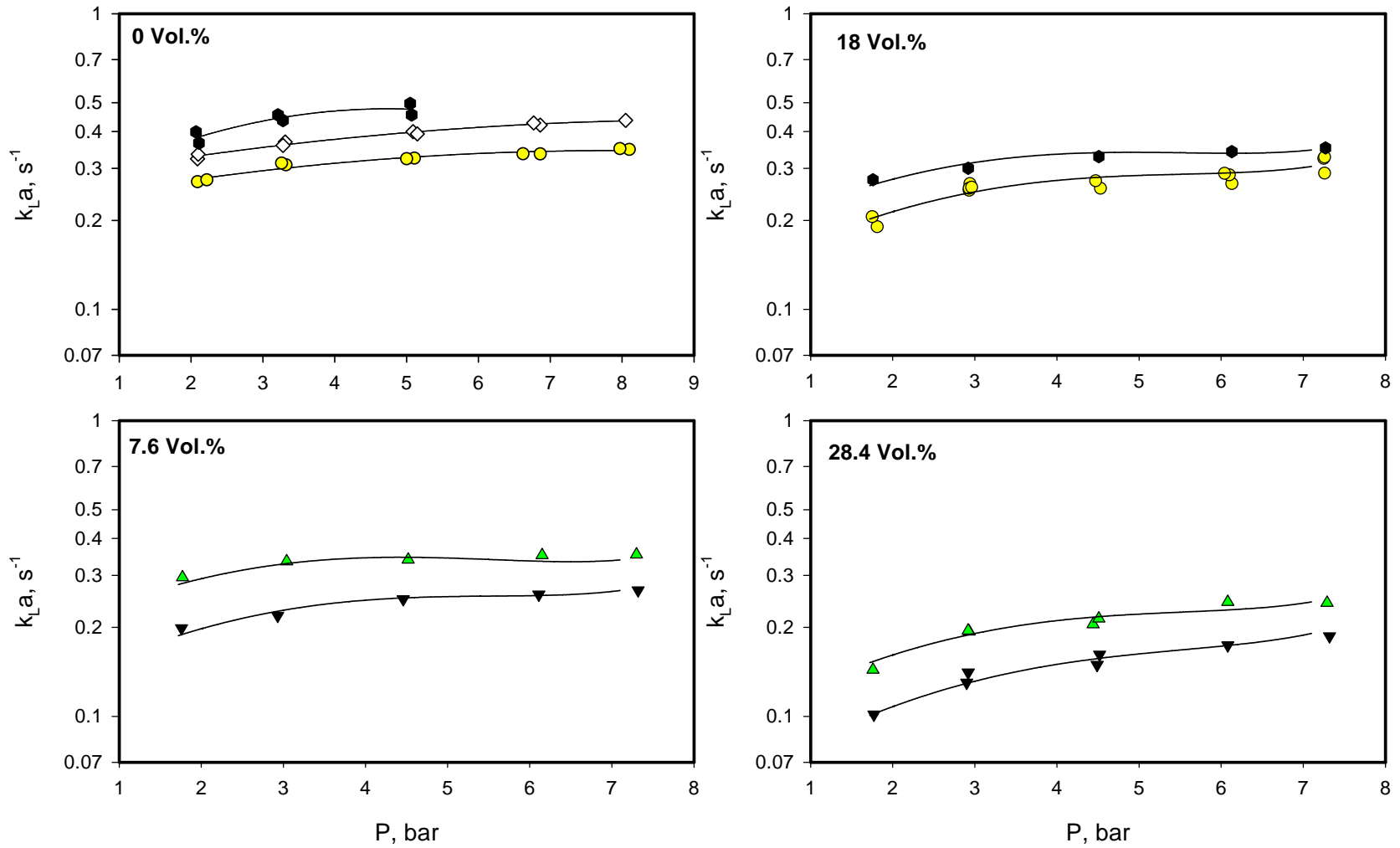


Figure 71 Effect of Operating Variables on $k_{L,a}$ of H₂/Isopar-M/Glass Beads in the Cold SBCR

● 0.135 m/s ◇ 0.164 m/s ● 0.200 m/s ▼ 0.100 m/s ▲ 0.170 m/s Lines: Equation (6-12)

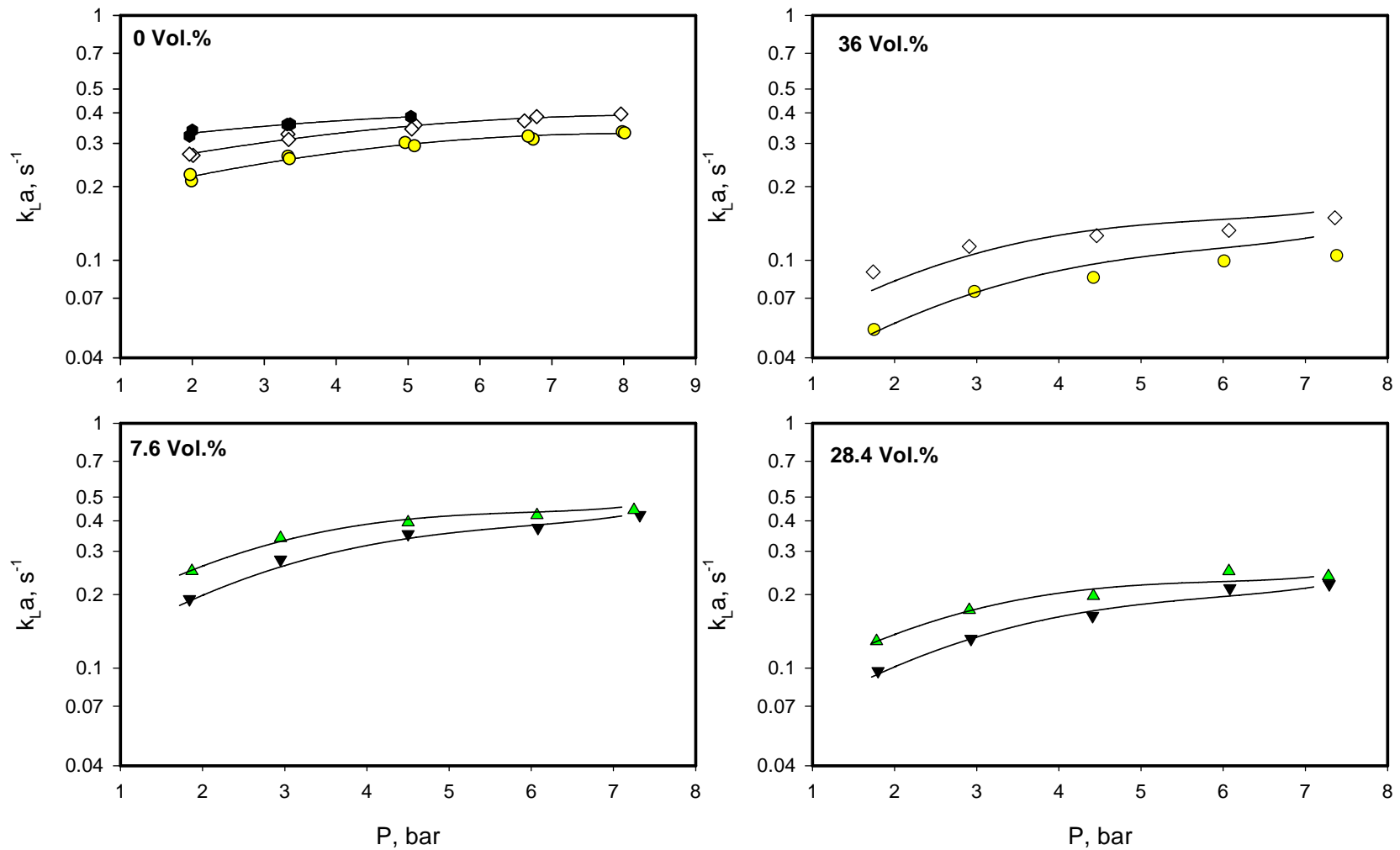


Figure 72 Effect of Operating Variables on k_{La} of CO/Isopar-M/Glass Beads in the Cold SBCR

● 0.085 m/s ▼ 0.093 m/s ▲ 0.130 m/s
◇ 0.122 m/s ● 0.141 m/s

Lines: Equation (6-12)

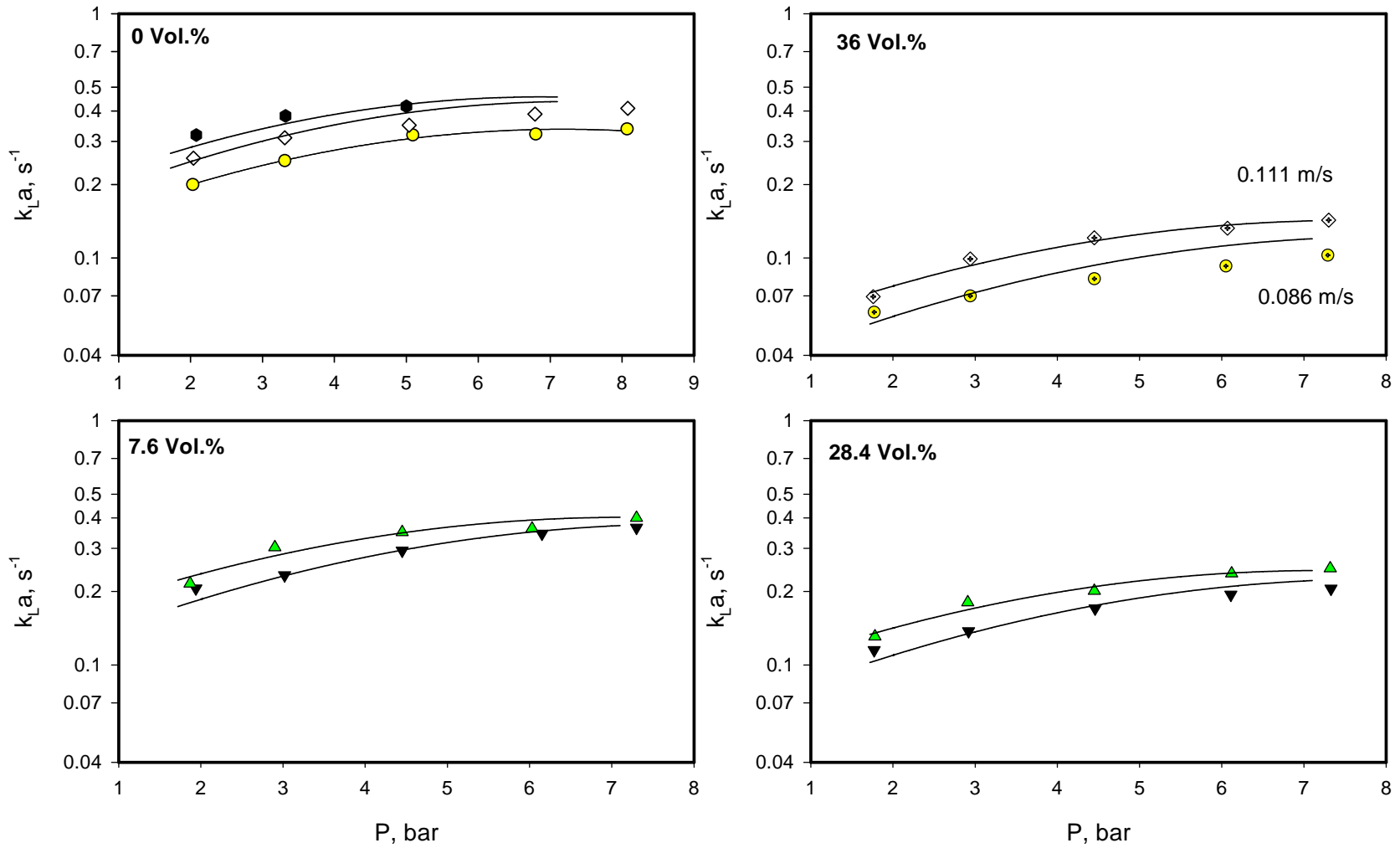


Figure 73 Effect of Operating Variables on $k_{L,a}$ of N_2 /Isopar-M/Glass Beads in the Cold SBCR



Lines: Equation (6-12)

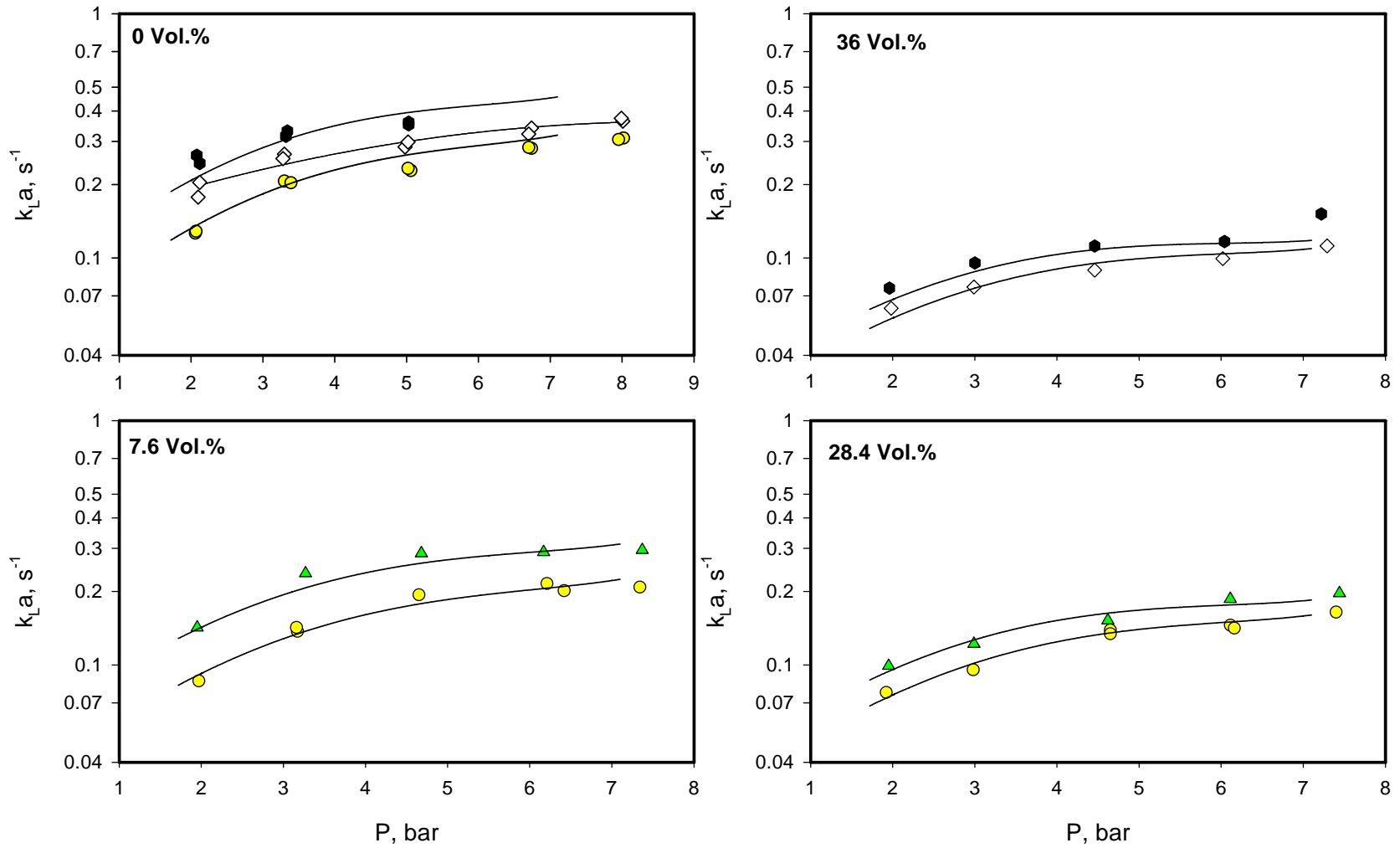


Figure 74 Effect of Operating variables on $k_{L,a}$ of CH₄/Isopar-M/Glass Beads in the Cold SBCR

- 0.099 m/s ◇ 0.122 m/s
- ▲ 0.140 m/s ● 0.160 m/s

Lines: Equation (6-12)

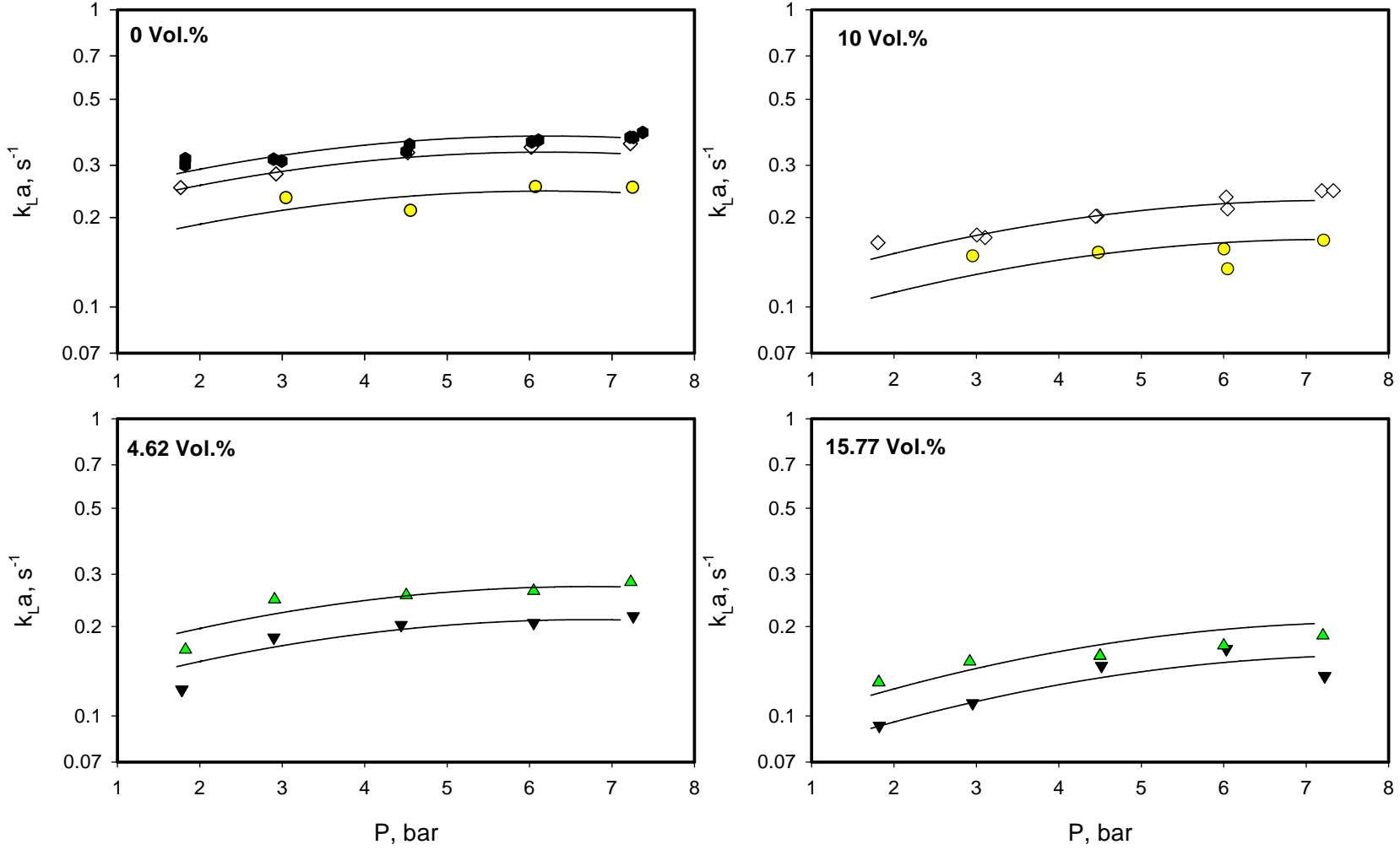


Figure 75 Effect of Operating variables on k_{La} of He/Isopar-M/Alumina in the Cold SBCR

● 0.086 m/s ◇ 0.114 m/s ● 0.150 m/s ▼ 0.098 m/s ▲ 0.134 m/s Lines: Equation (6-12)

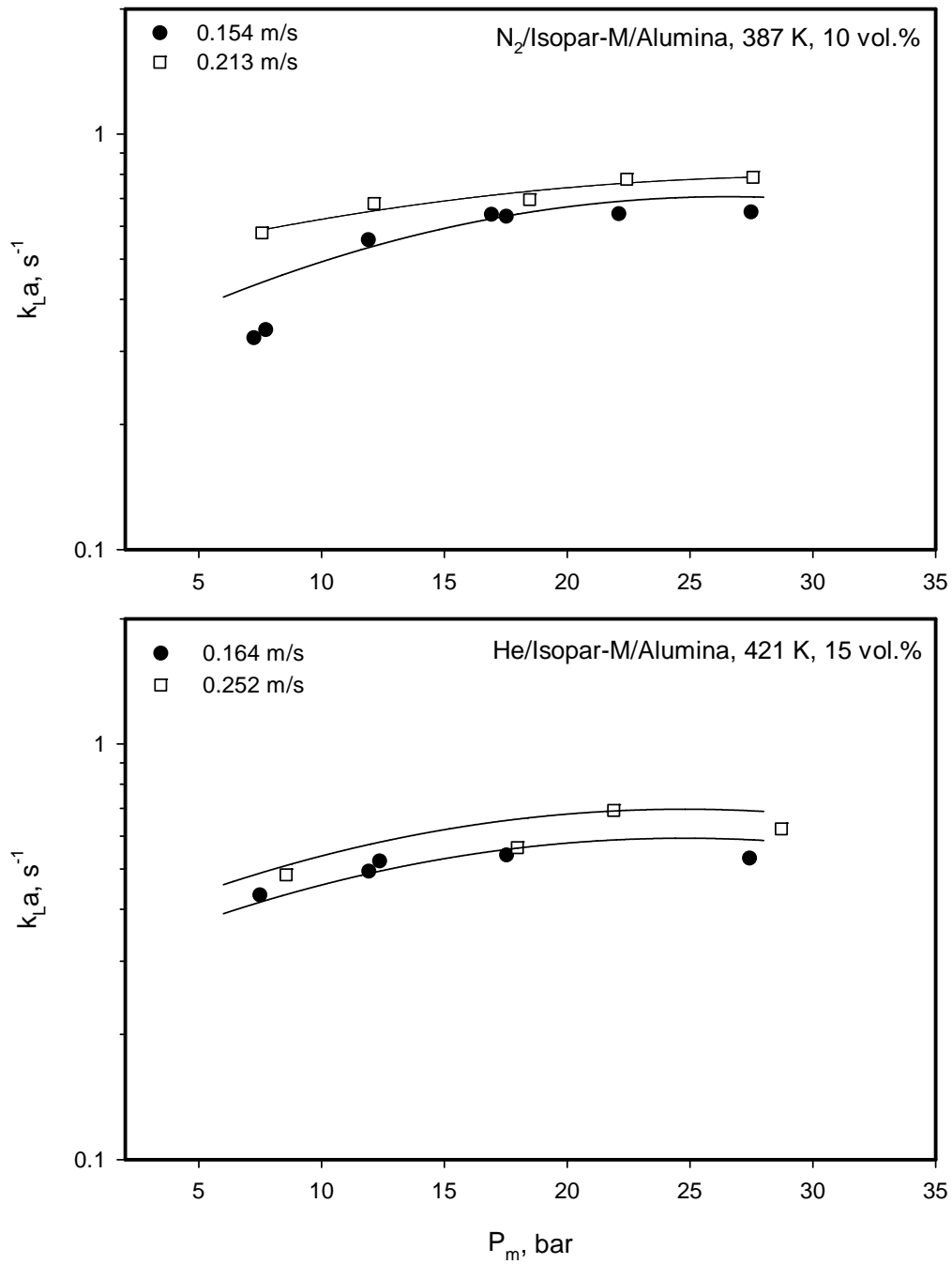


Figure 76 Effect of U_G on k_{La} of N₂ and He/Isopar-M/Alumina in the Hot SBCR

Lines: Equation (6-13)

an average of 33% over the entire range of pressure studied when U_G increases from 0.1 to 0.17 m/s. The k_L values of N_2 and CO, however, do not change when U_G is increased from 0.093 to 0.13 m/s. This behavior can be related to the larger bubble size formed with lighter gases, as shown in section 6.3.1. In Section 6.2.2, it was shown that an increase of U_G mostly affected $\varepsilon_{G-Large}$, by increasing their average bubble size, while $\varepsilon_{G-Small}$ was almost independent of U_G . Therefore, the increase of $k_L a$ with U_G can in part be due to the enhancement of k_L by the large gas bubbles formed at high gas velocity ^(207,208). This behavior clearly shows that under high pressures, the increase of the volume fraction of the small gas bubbles with increasing gas velocity is insignificant ^(126, 77) and the volume fraction of the large gas bubbles slightly contributes to the increase of the gas-liquid interfacial area.

6.4.2 Effect of Solid Concentration and Temperature on $k_L a$

Figures 71 through 75 show that $k_L a$ values gradually decrease in the glass beads concentration range from 7.6 to until 28.4 vol.% and then sharply drop at the highest solid concentration of 36 vol.%. This behavior can be explained considering the bubble size distribution in the reactor under these conditions. Although the volume fraction of gas bubbles is reduced at lower solid concentrations, this reduced volume mainly consists of a large population of small gas bubbles, contributing enormously to the gas-liquid interfacial area. When increasing solid concentration above certain value, however, the relative change of the volume fraction of small gas bubbles slightly decreases, whereas the population of these small bubbles sharply decreases due to coalescence, resulting in a sharp decrease of the gas-liquid interfacial area and subsequently $k_L a$. This behavior is even more pronounced at lower than at higher pressures, since high pressures

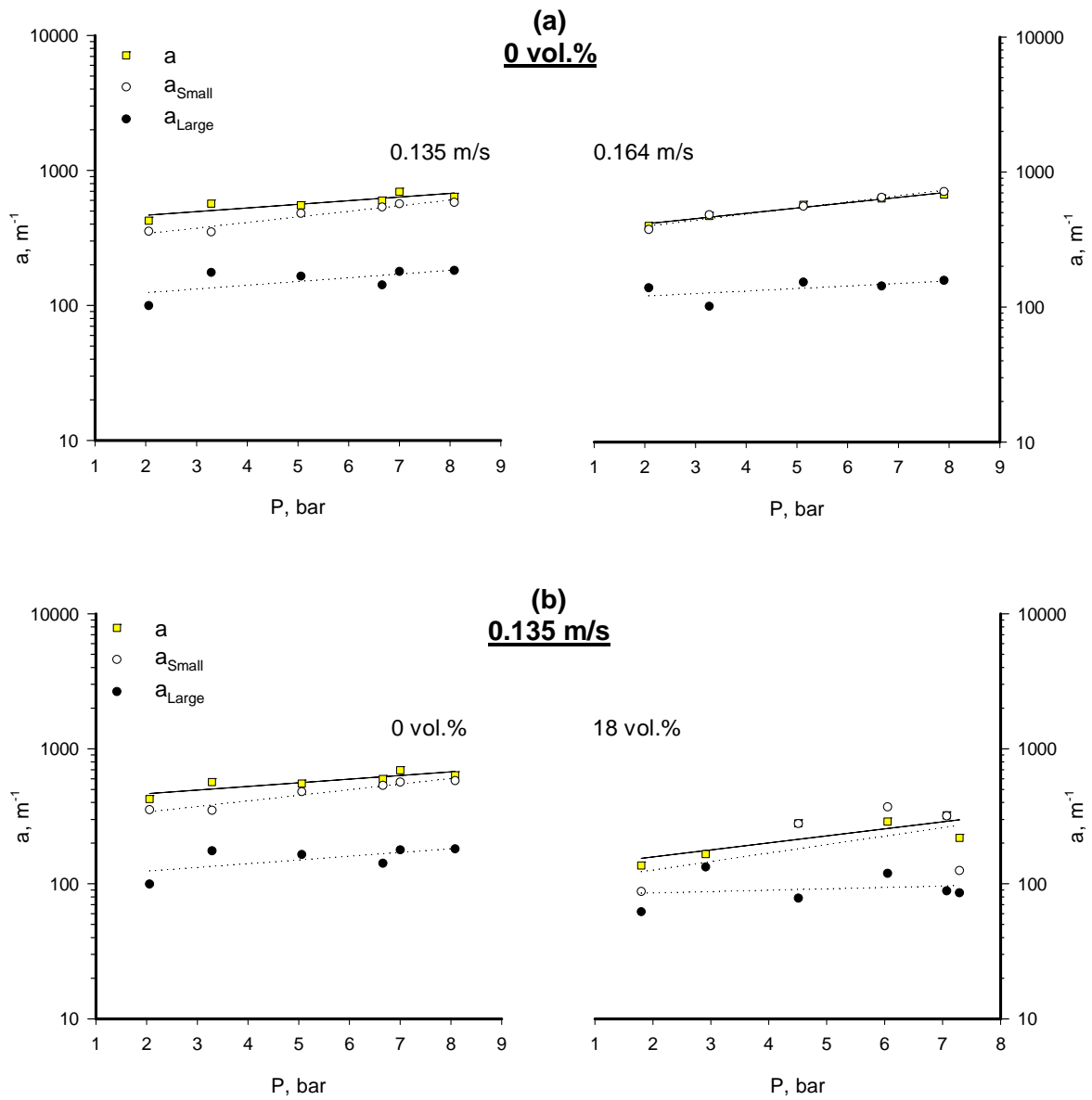


Figure 77 Effect of P , U_G , and C_V on a of H_2 /Isopar-M/Glass Beads in the Cold SBCR

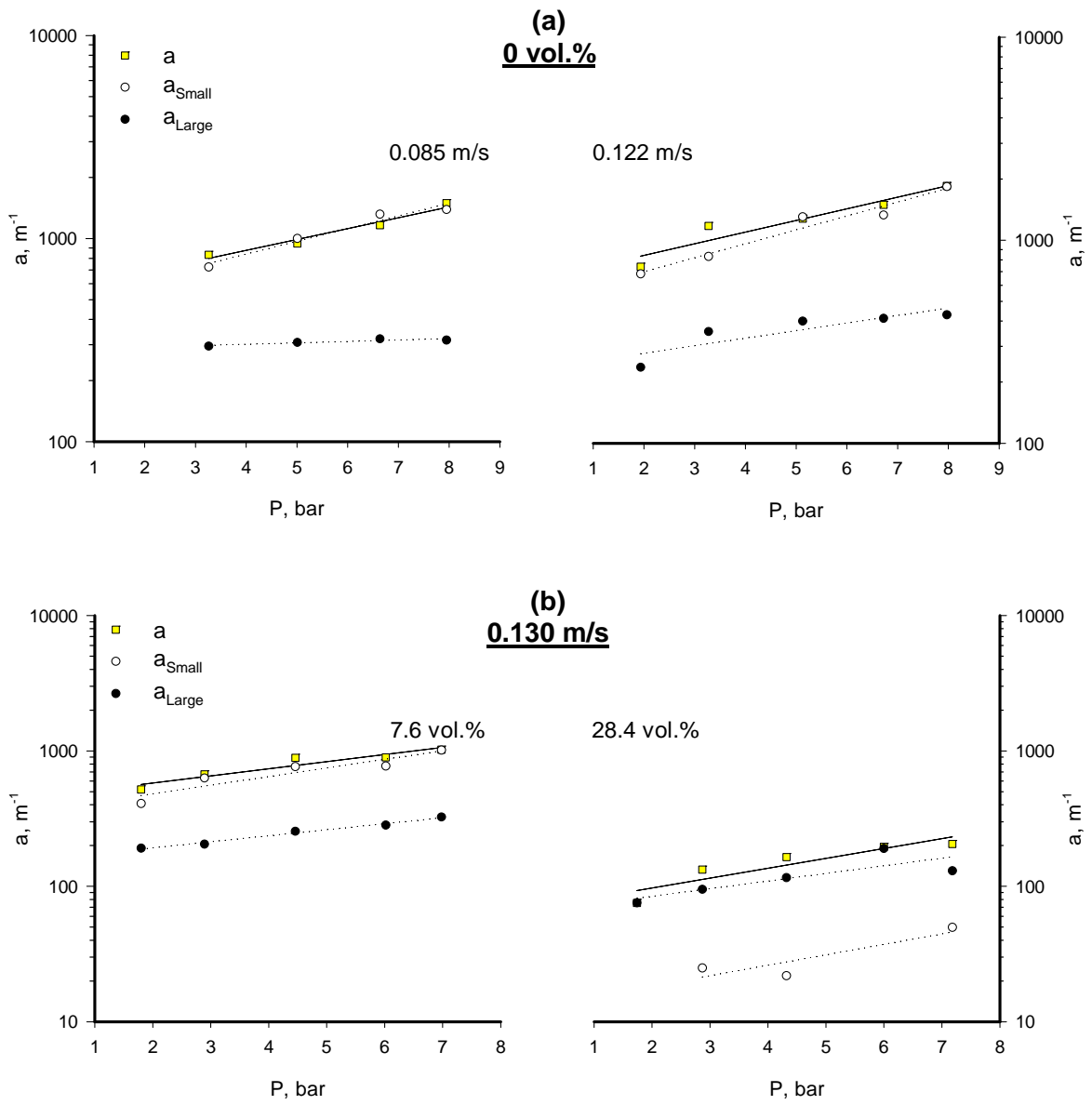


Figure 78 Effect of P, U_G , and C_V on a of CO/Isopar-M/Glass Beads in the Cold SBCR

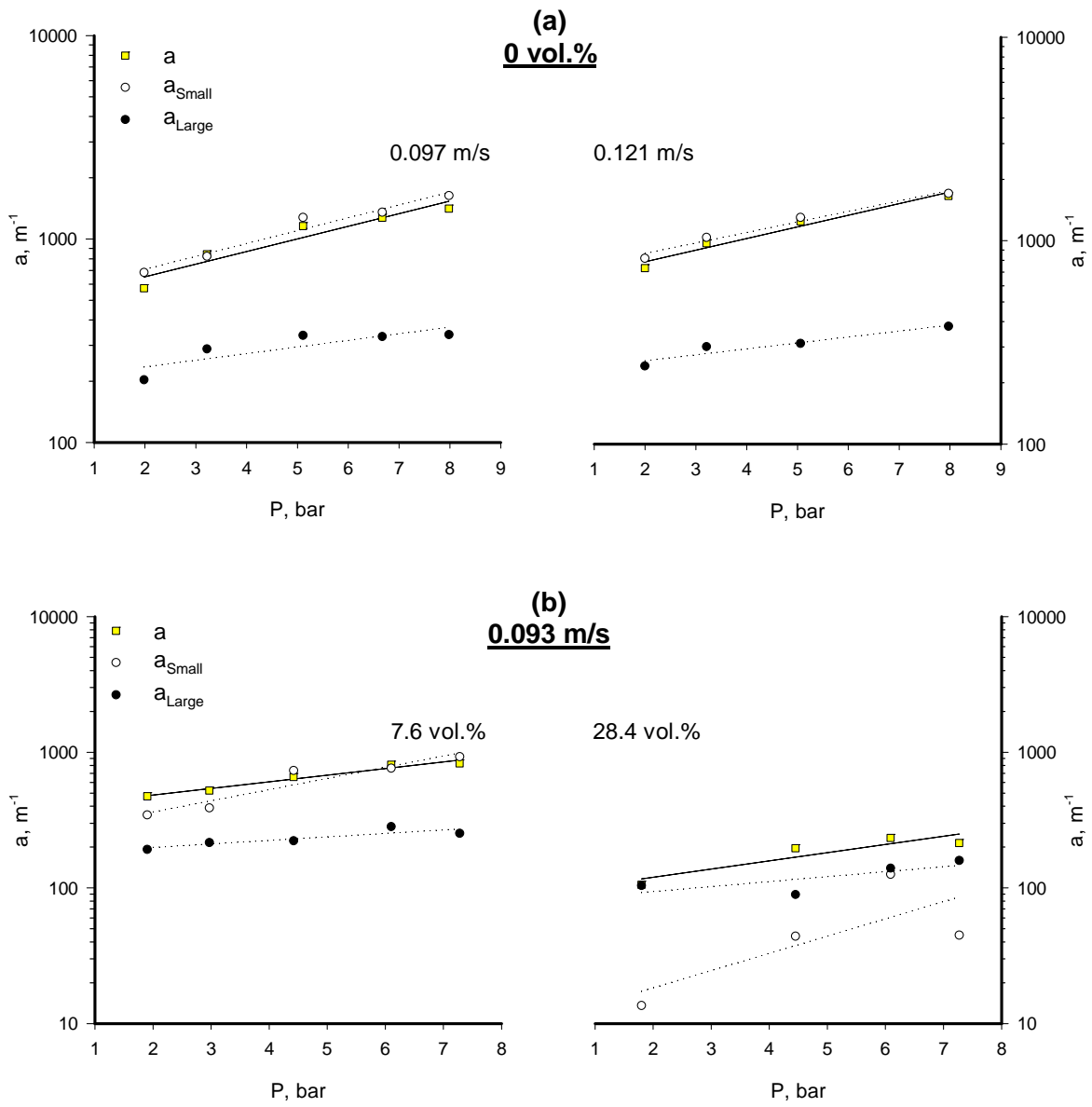


Figure 79 Effect of P, U_G , and C_V on a of N_2 /Isopar-M/Glass Beads in the Cold SBCR

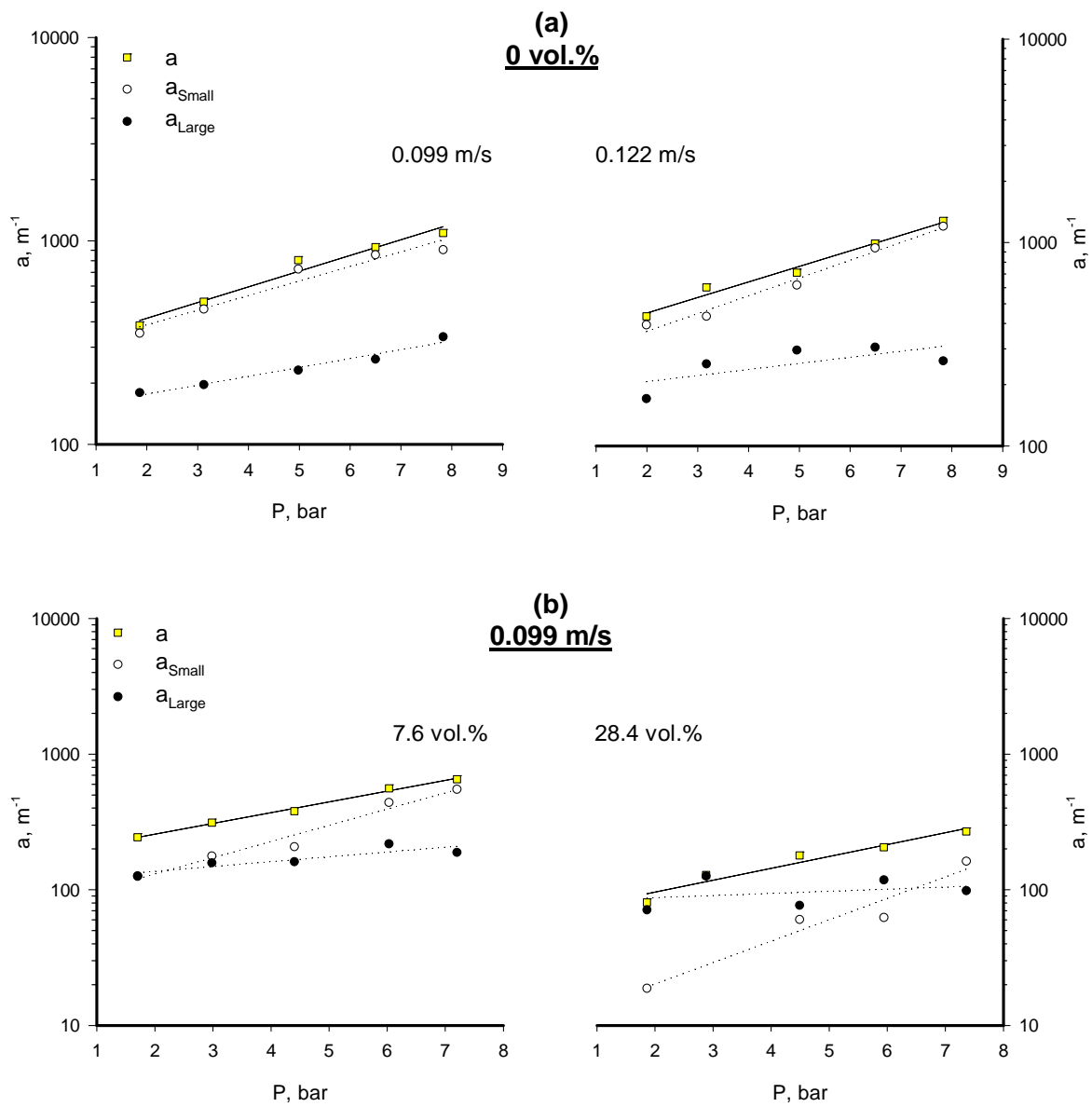


Figure 80 Effect of P, U_G , and C_V on a of CH_4 /Isopar-M/Glass Beads in the Cold SBCR

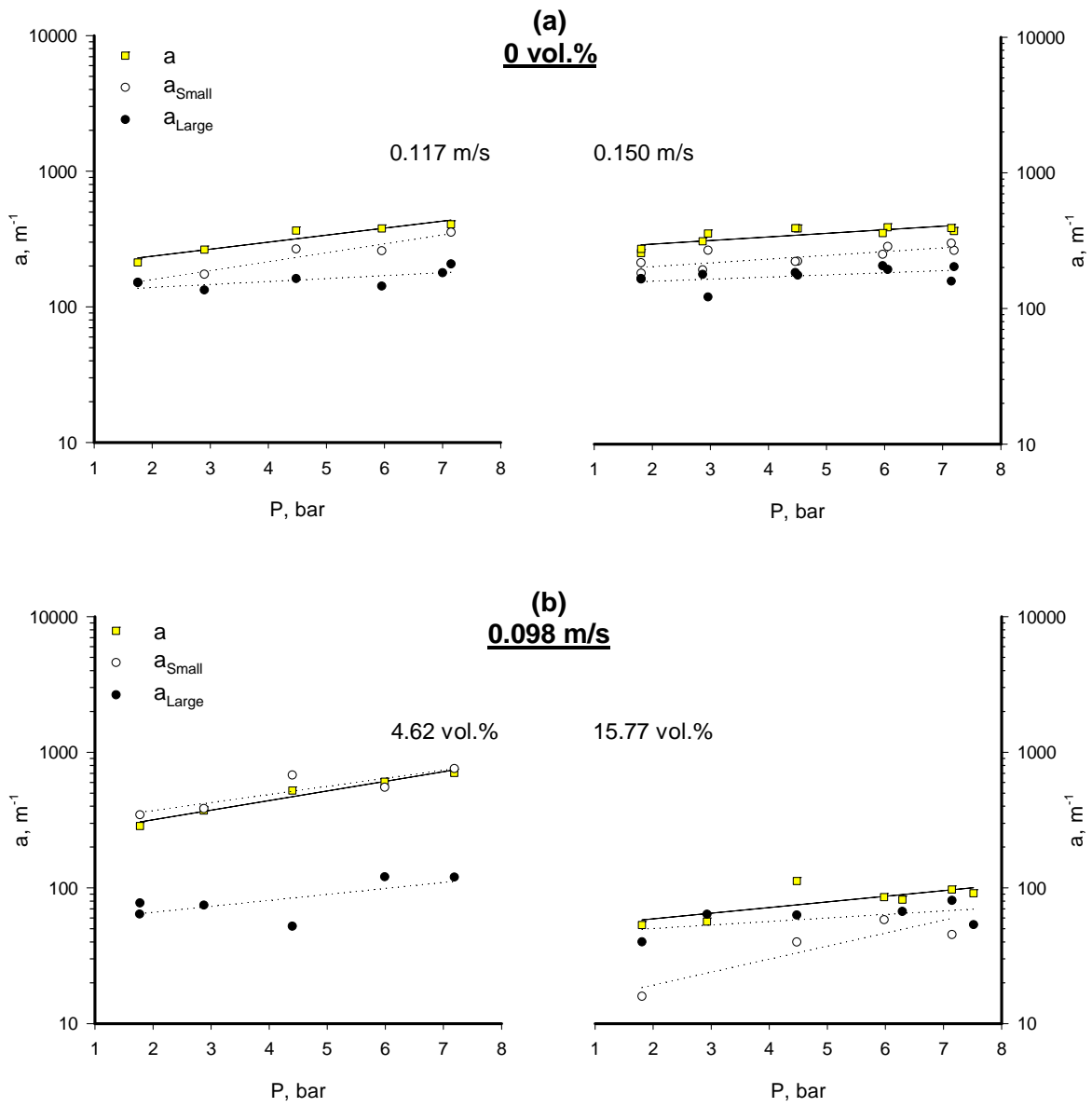


Figure 81 Effect of P, U_G , and C_V on a of He/Isopar-M/Alumina in the Cold SBCR

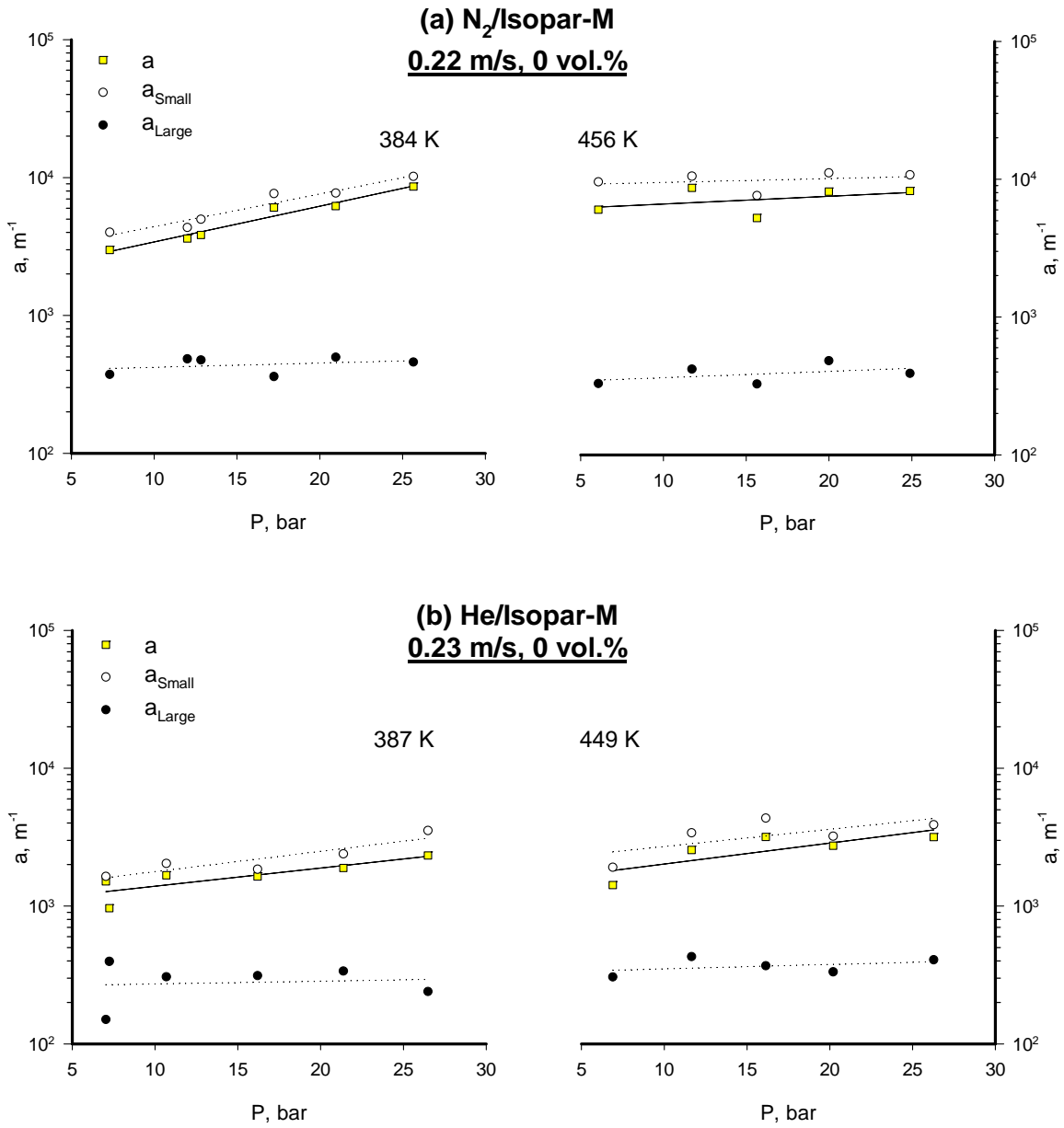


Figure 82 Effect of P and T on a of N₂ and He/Isopar-M/Alumina in the Hot SBCR

promote the formation of small gas bubbles with high gas-liquid interfacial area, i.e., high $k_L a$ values. Figure 89 shows the effect of alumina concentration on the $k_L a$ values of N_2 and He in Isopar-M obtained in the hot SBCR; and as can be seen $k_L a$ decreases as alumina concentration reaches 20 vol.%. The average decrease of $k_L a$ values from 0 to 20 vol.% is about 47 % for both N_2 and He, where the decrease from 0 to 10 vol.% is generally less significant than that from 10 to 20 vol.%. Accordingly, the smallest values of $k_L a$ would be expected at the highest solid concentration and the lowest system pressure. Actually, in Figures 77 (b) through 81 (b), it can be seen that when the solid concentration is less than 15 vol.%, a_{small} is generally greater than a_{large} , and when the solid concentration becomes greater than 15 vol.%, a_{small} becomes less than a_{large} . This behavior is mostly due to the dramatic reduction of the population of small gas bubbles as the solid loading increases above 15 vol.%, as it was shown in Section 6.3. This means that the knowledge of the holdup and size distribution of the small gas bubbles in SBCRs is important, since they are the ones contributing to the enhancement of the gas-liquid interfacial area, and therefore controlling the mass transfer behavior. Furthermore, in Figures 83 through 88, it can be seen that k_L increases slightly with C_V , which is due to an increase of gas bubbles size, but the decrease of $k_L a$ with C_V indicates that the gas-liquid interfacial area overwhelms the positive impact of k_L on $k_L a$. This finding is significant to commercial SBCRs, which often employ high catalyst loading and high pressure to achieve high yields^(8,77,204). High pressures in SBCRs are expected to increase $k_L a$ by creating large population of small gas bubbles of high gas-liquid interfacial area, whereas high catalyst loadings are likely to enhance gas bubbles coalescence, creating large gas bubbles of small gas-liquid interfacial area. Thus, high catalyst loading could overcome the positive contribution of pressure and strongly decrease the gas-liquid

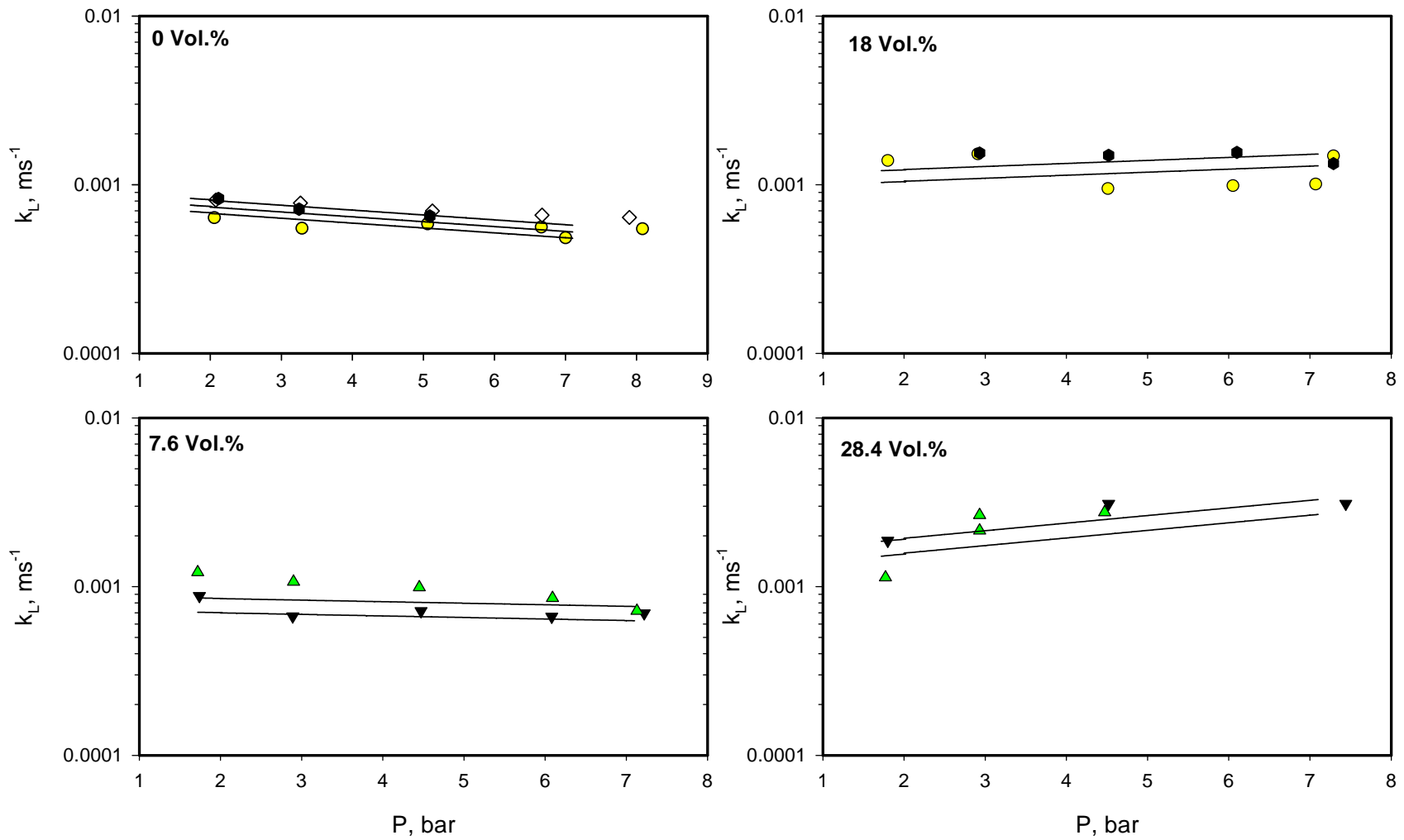


Figure 83 Effect of the Operating Variables on k_L of H_2 /Isopar-M/Glass Beads in the Cold SBCR

● 0.135 m/s
 ◇ 0.164 m/s
 ● 0.200 m/s
 ▼ 0.100 m/s
 ▲ 0.170 m/s
 Lines: Equation (6-12)

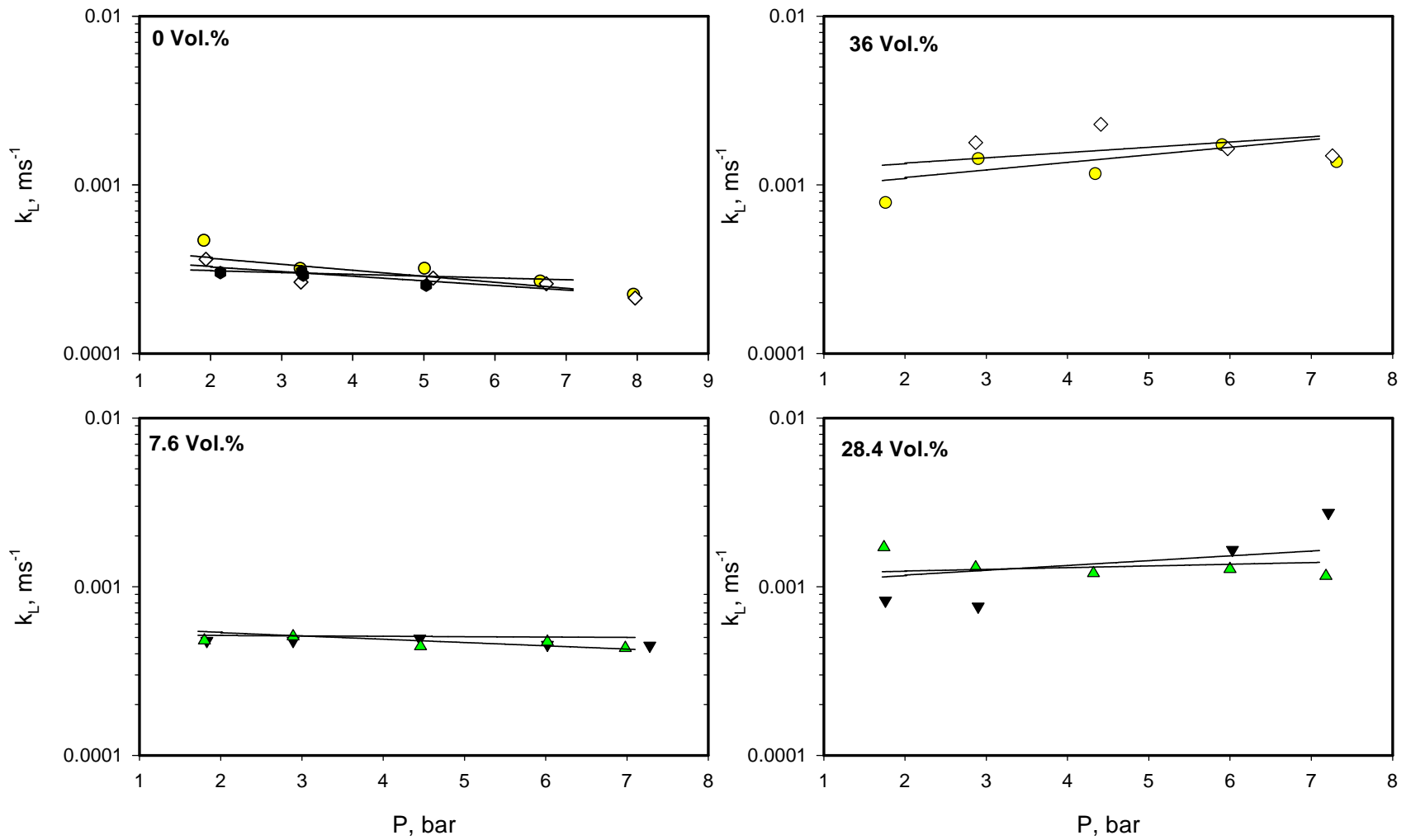


Figure 84 Effect of the Operating Variables on k_L of CO/Isopar-M/Glass Beads in the Cold SBCR

- 0.085 m/s
- ▼ 0.093 m/s
- ▲ 0.109 m/s
- ◇ 0.122 m/s
- 0.141 m/s

Lines: Equation (6-12)

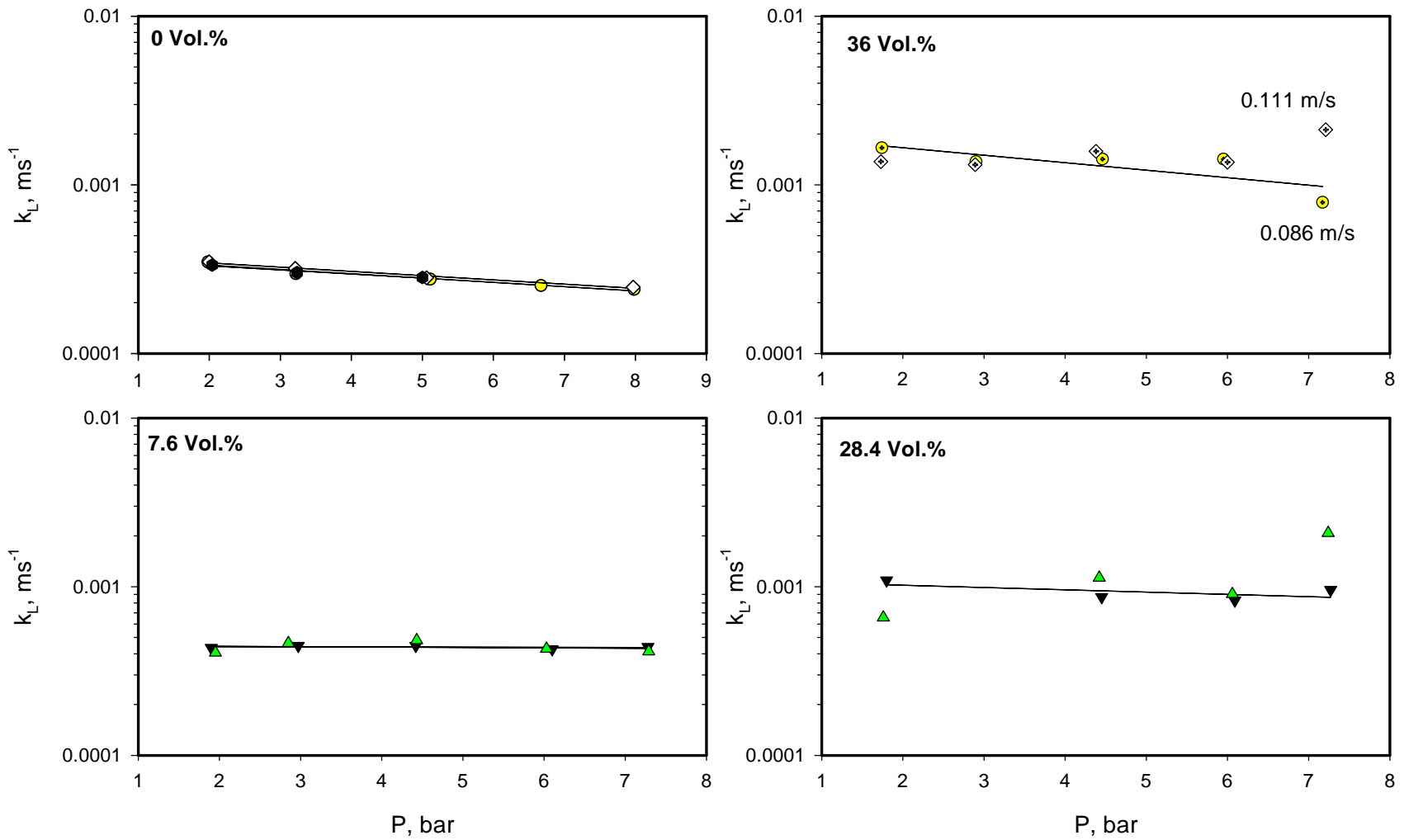


Figure 85 Effect of the Operating Variables on k_L of N_2 /Isopar-M/Glass Beads in the Cold SBCR

- 0.097 m/s
- ▼ 0.093 m/s
- ▲ 0.130 m/s
- ◇ 0.121 m/s
- 0.141 m/s

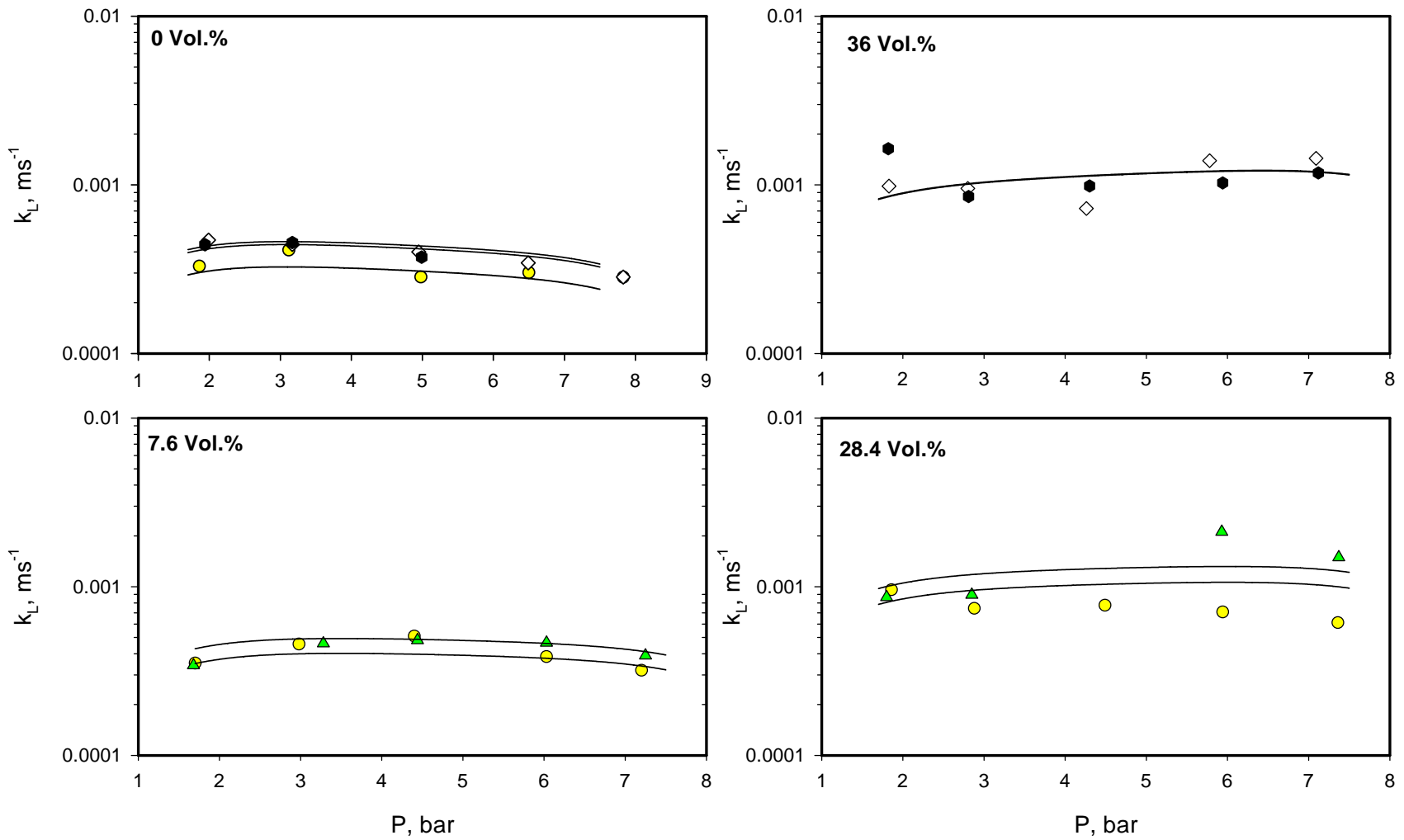


Figure 86 Effect of the Operating Variables on k_L of CH_4 /Isopar-M/Glass Beads in the Cold SBCR

0.099 m/s
 0.122 m/s
 0.140 m/s
 0.160 m/s
 Lines: Equation (6-12)

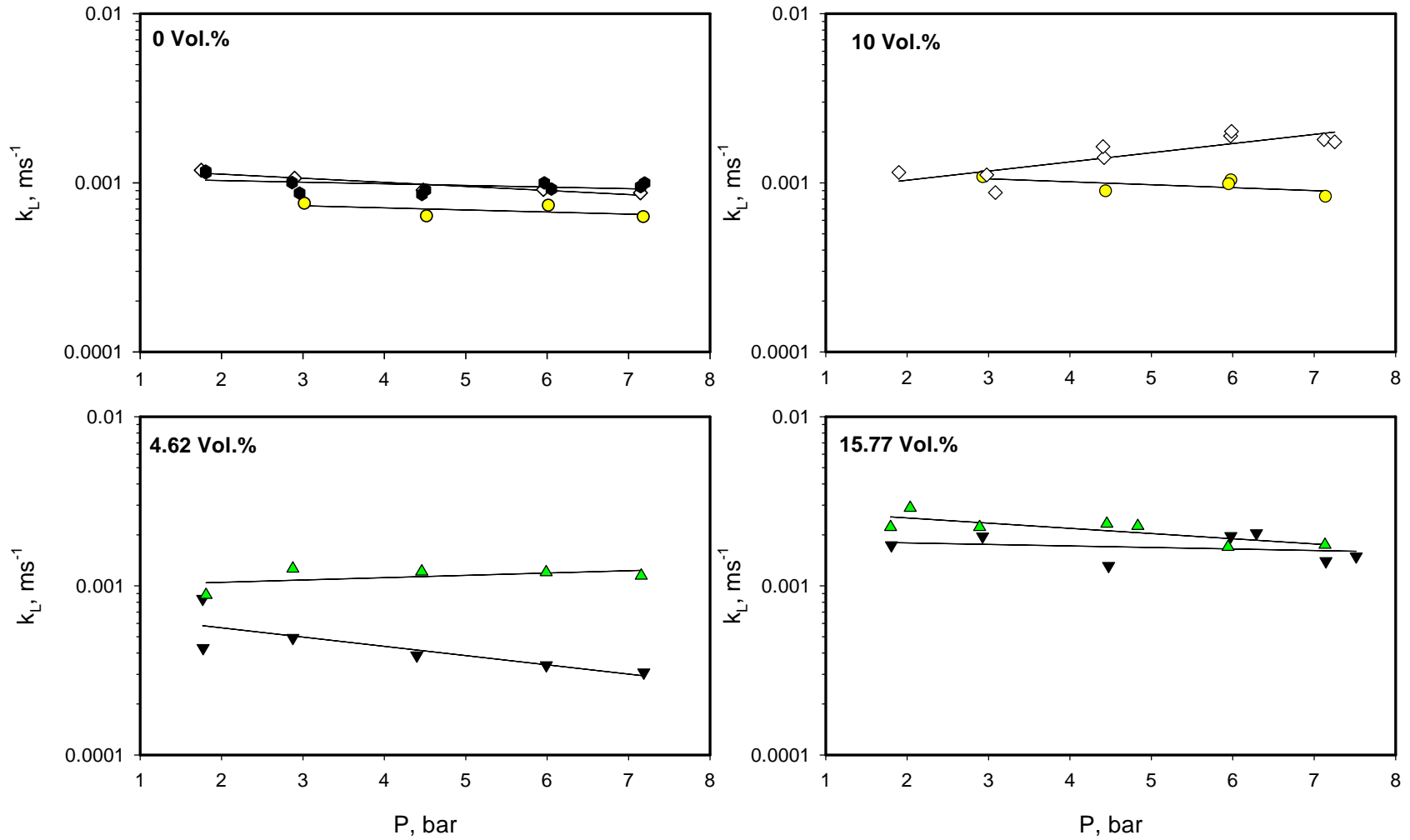


Figure 87 Effect of the Operating Variables on k_L of He/Isopar-M/Alumina in the Cold SBCR

● 0.086 m/s ◇ 0.114 m/s ● 0.150 m/s ▼ 0.098 m/s ▲ 0.134 m/s

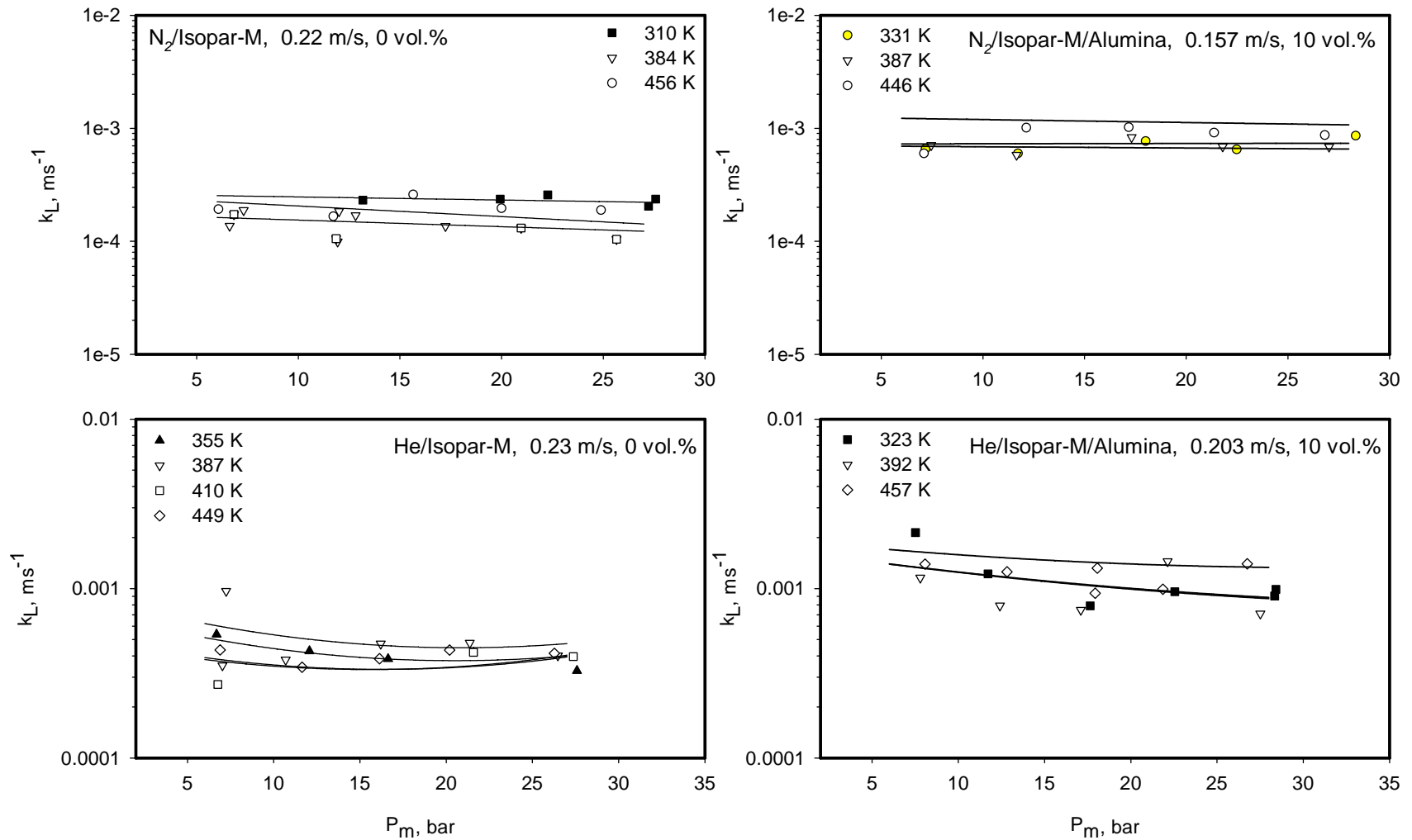


Figure 88 Effect of the Operating Variables on k_L of N_2 and $\text{He/Isopar-M/Alumina}$ in the Hot SBCR

Lines: Equation (6-13) for k_L

interfacial area and subsequently $k_L a$, leading to mass transfer limitations in the SBCR operating under such conditions.

Figure 90 shows the effect of temperature on $k_L a$ values for N_2 and He in Isopar-M containing 0 and 10 vol.% alumina powder; and as can be seen, $k_L a$ of both gases increases with temperature over the entire range of pressure and solid concentrations used. The behavior of $k_L a$ can be explained by the effect of temperature on a and k_L . The d_{32} values of the gases were found to decrease with temperature, as reported in Section 0, whereas ε_G values, presented in Section 6.2.3, appeared to increase with temperature and accordingly a from Equation (6-8) is expected to increase. Also, the diffusivity for N_2 and He, shown in Figure 9f), increases with temperature, and subsequently, k_L is expected to increase, due to its proportionality with the diffusivity to the power $0.5-1^{(2)}$.

Thus, both a and k_L increase with temperature and hence $k_L a$ values are expected to increase. Nevertheless, Figure 88 shows that temperature has a weak effect on k_L of N_2 and He. For instance, in the case of N_2 , k_L appears to decrease by 17% from 310 to 456 K at 20 bar in the absence of solid particles. This can be explained by the dependency of k_L on the bubble size, where increasing temperature decreases the surface tension and results in the formation of smaller gas bubbles, and consequently smaller k_L . In the case of He, the variation of k_L with temperature in the absence of solids, is even more insignificant. This suggests that the dependency of k_L on the bubble size is more important than diffusivity.

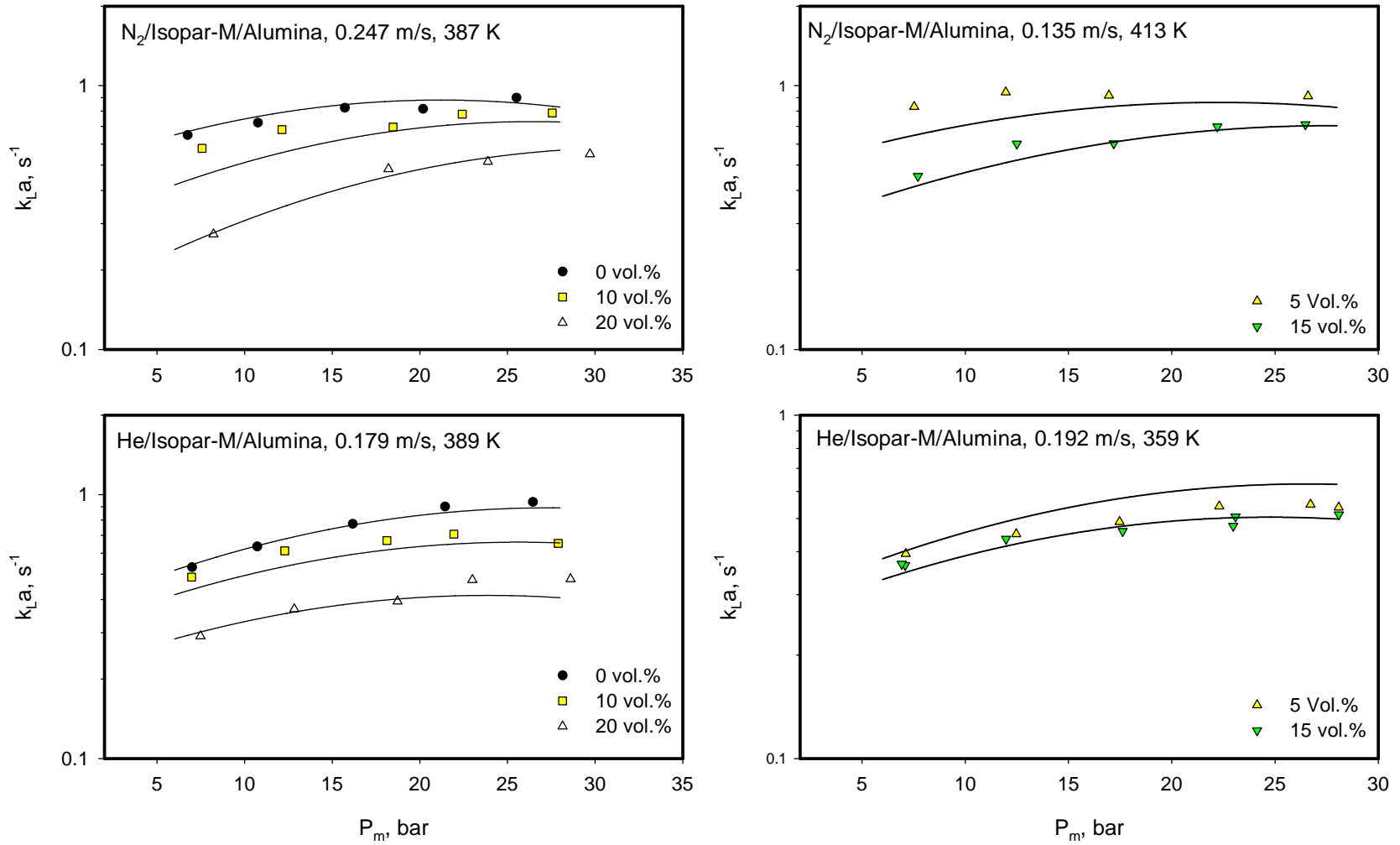


Figure 89 Effect of C_V and P on $k_{L,a}$ of N_2 and He/Isopar-M/Alumina in the Hot SBCR

Lines: Equation (6-13)

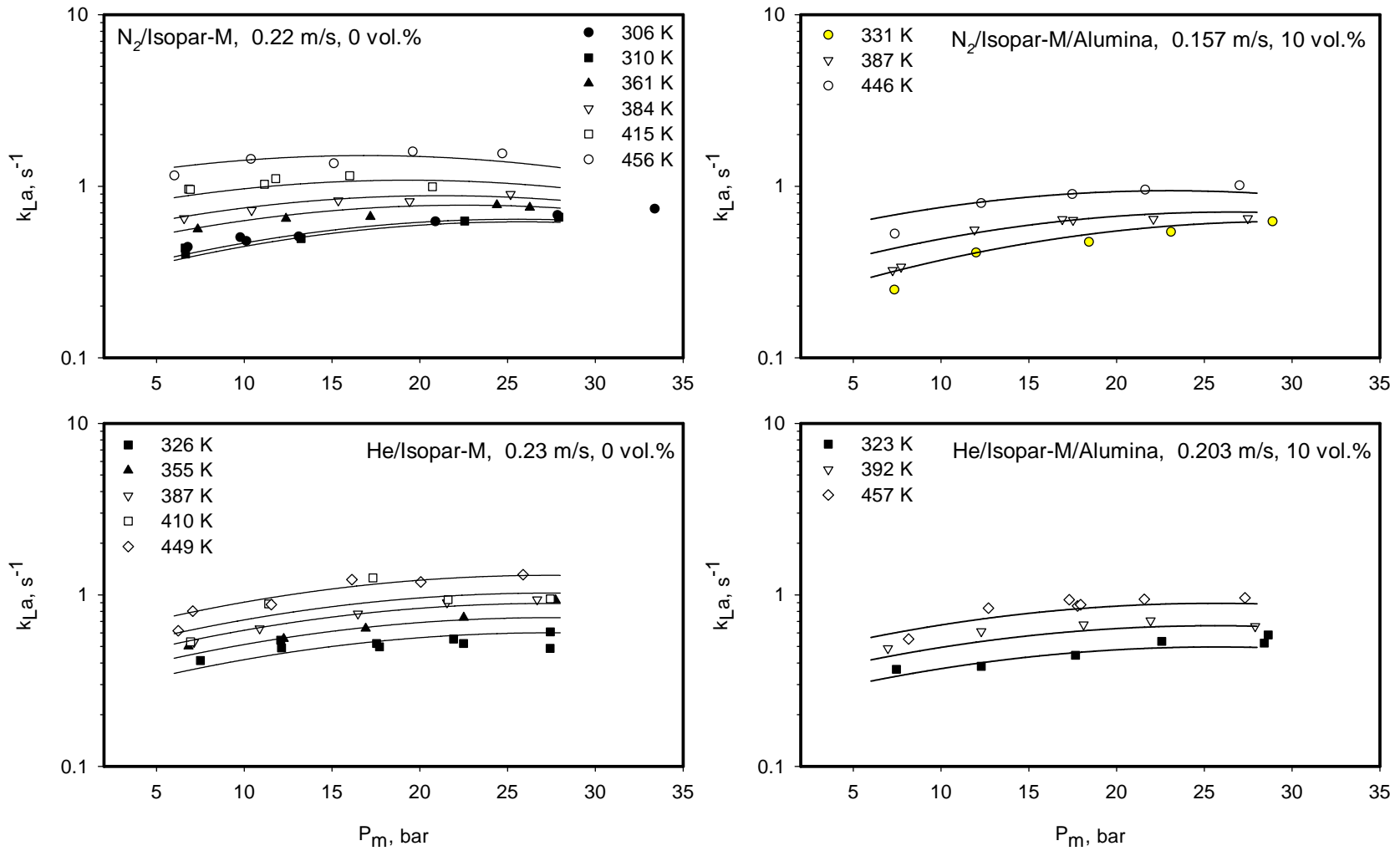


Figure 90 Effect of Temperature on k_{La} of N_2 and He/Isopar-M/Alumina in the Hot SBCR

Lines: Equation (6-13)

6.4.3 Effect of Gas Nature on $k_L a$

In order to explain the behavior of $k_L a$ for different gases, the diffusivities of the five gases were calculated using Equation (4-7) and the trend of the gas diffusivity in Isopar-M was found as follow:

$$(D_{AB})_{He} > (D_{AB})_{H_2} > (D_{AB})_{N_2} \approx (D_{AB})_{CO} > (D_{AB})_{CH_4}$$

The difference between the diffusivity of He and H₂ was about 8%. Similarly, the differences between the diffusivity of N₂ and CO, and N₂ and CH₄ were about 2 and 6%, respectively. According to the film-theory and the penetration-theory, k_L is proportional to the gas diffusivity to the power of 1 and 0.5, respectively^(2,77), which means that k_L should follow the above inequalities.

Figure 91 shows the effect of the gas nature on the $k_L a$, a , and k_L values of the five gases at 7 bar, 0.126, and as can be seen, $k_L a$, a , and k_L values of the heavier gases (CH₄, N₂ and CO) seems to follow the gas molecular weight, which is similar that of ε_G and $\varepsilon_{G-Small}$ of those gases as shown in Figure 51. $k_L a$ values of H₂, on the other hand, appear to be slightly smaller than those of He. The a values of H₂ are greater than those of He, which was attributed to the smaller $d_{32-Small}$ values of H₂ as shown in Figure 56. Figure 91 shows that the k_L values of H₂ are smaller than those of He, due to its smaller diffusivity in Isopar-M. Thus, it seems that the impact of k_L on $k_L a$ is more important than the effect of a for these two gases, resulting in a slightly smaller $k_L a$ values for H₂. Figure 92 shows the effect of gas nature on the $k_L a$ values of N₂ and He in the hot SBCR; and as can be seen, the $k_L a$ values of N₂ are greater than those of He at any given

operating conditions, which shows the behavior of k_{La} is similar to that of the gas holdup reported in Section 6.2.4.

6.4.4 Effect of Solid Nature on k_{La}

Figure 93 depicts the effect of solid nature on k_{La} values of N_2 in Isopar-M in the cold SBCR; and as can be seen, k_{La} values obtained with glass beads are greater than those obtained with alumina powder. This behavior can be due to the larger average particle size and higher density of alumina as shown in Section 4.3. Also as can be seen in Figure 12 using the correlation proposed by Riquarts ⁽⁹⁷⁾ for predicting the slurry viscosity, alumina particles yield a higher μ_{SL} when compared with that of glass beads. Therefore, stronger gas bubbles coalescence can be expected, which results in a smaller gas-liquid interfacial area. This can be seen in Figure 93, where for alumina slurries, the gas holdup values are lower, and the d_{32} values are higher than those obtained with glass beads slurries.

6.5 SOLID PHASE HYDRODYNAMICS IN THE COLD AND HOT SBCRS

6.5.1 Dispersion Model

The axial sedimentation-dispersion model described in Section 2.3.2, was used in this study to model the distribution of the solid particles in the cold and hot SBCRs. From section 2.3.2 the general solution to this model was given as:

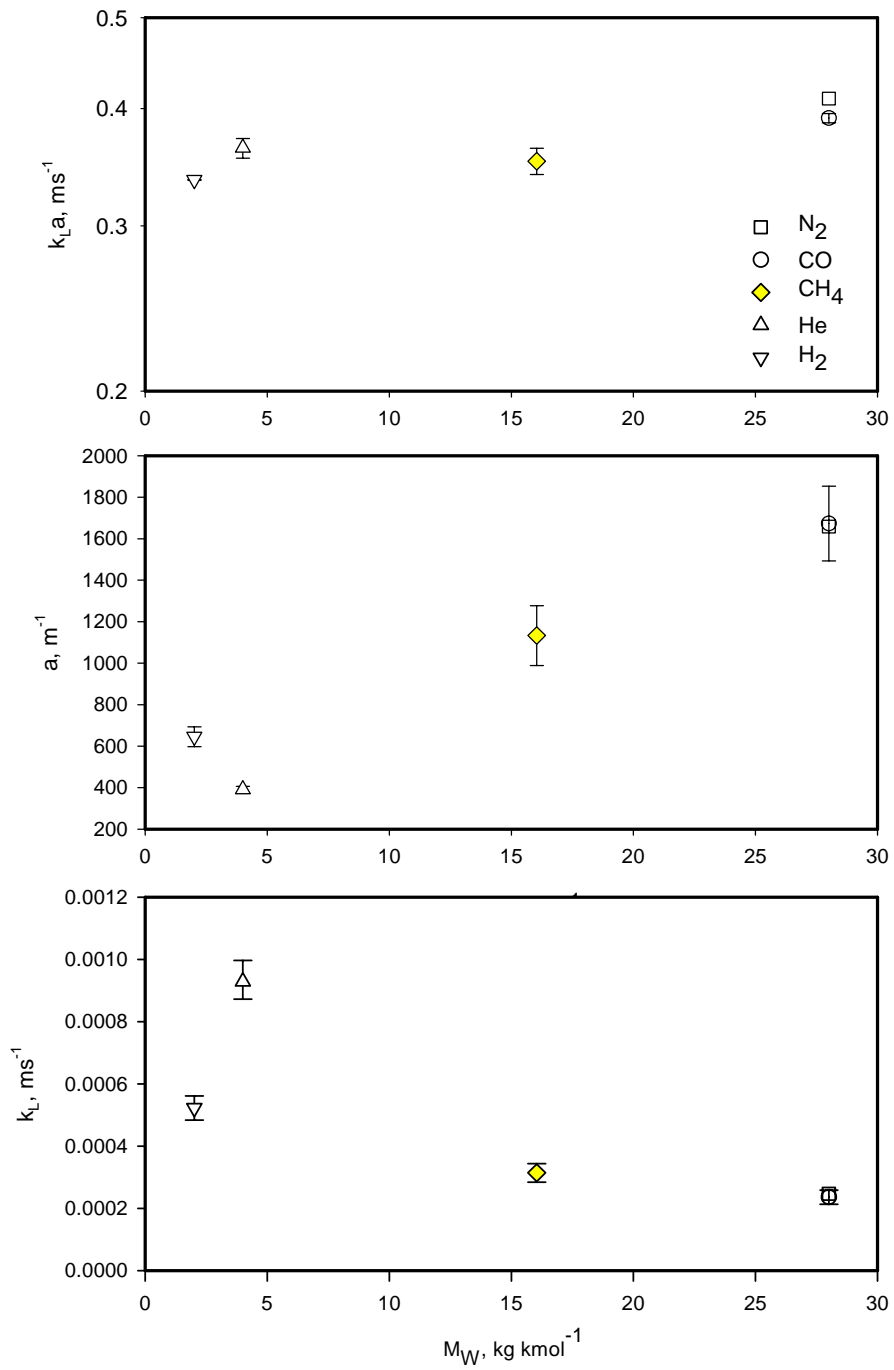


Figure 91 Effect of Gas Nature on $k_{L,a}$, a and k_L in Isopar-M in the Cold SBCR
 (7 bar, 0.126 m/s, 0 vol.%)

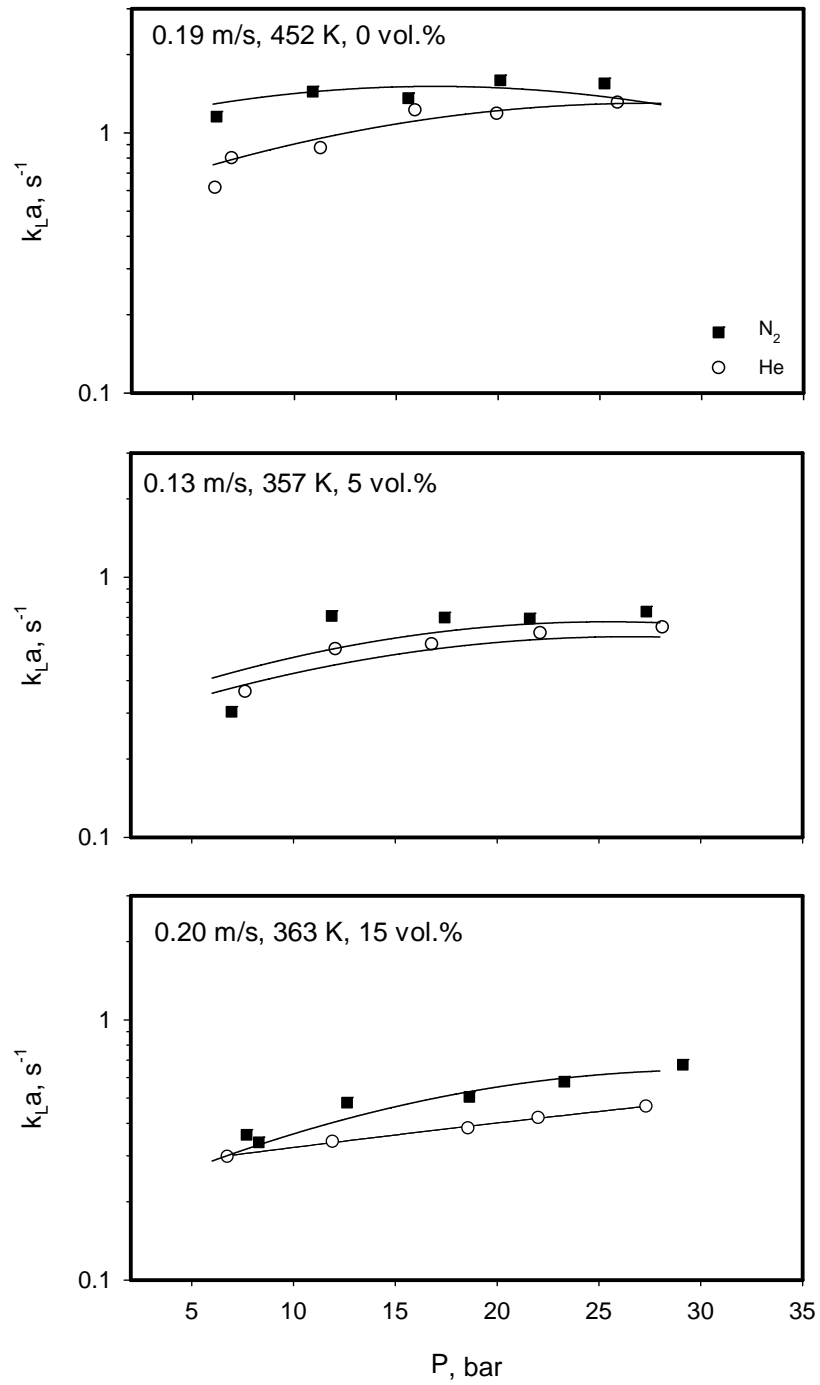


Figure 92 Effect of Gas Nature on $k_{L,a}$ of N_2 and He in Isopar-M/Alumina in the Hot SBCR

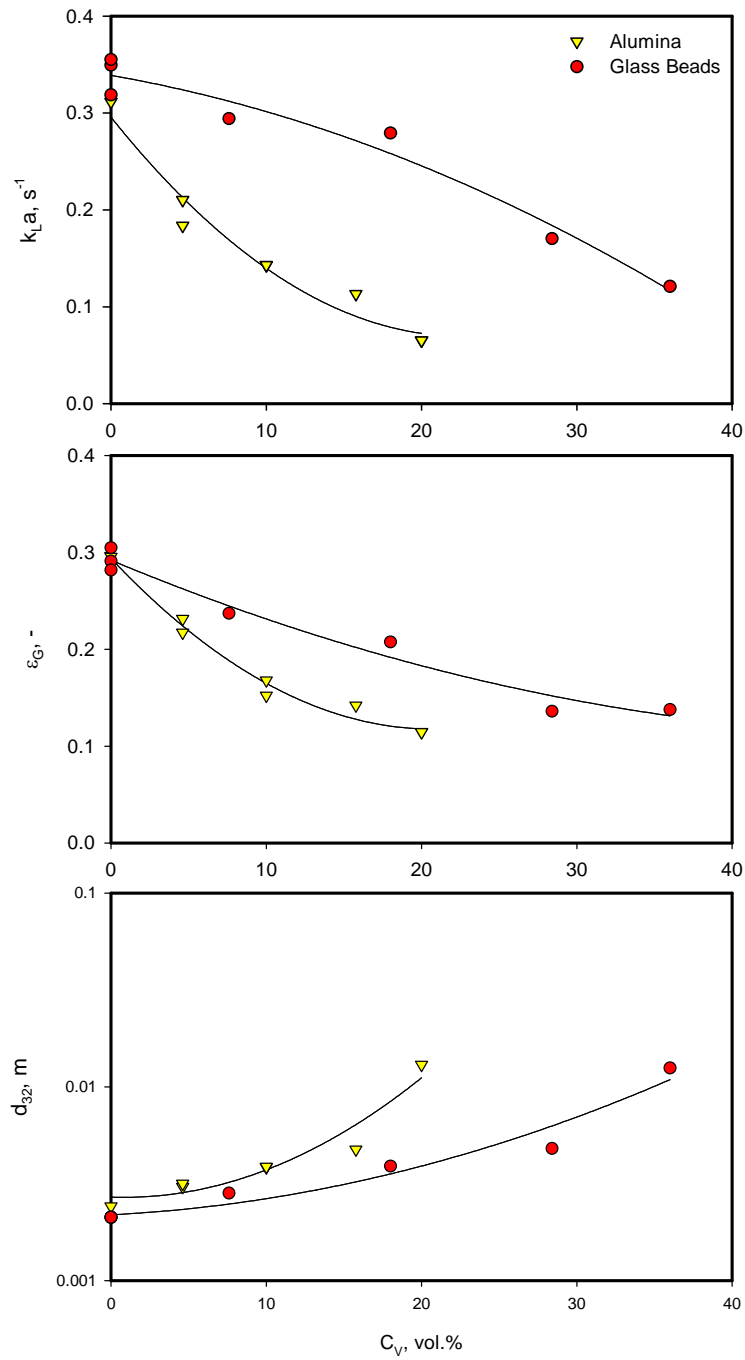


Figure 93 Effect of Solid Nature on k_{La} , ϵ_G , and d_{32} Values of N_2 /Isopar-M in the Cold

SBCR

(4.6 bar, 299 K, 0.11 m/s)

$$C_S(z) = C_1 + C_2 \exp\left(-\frac{U_p z}{D_S}\right) = C_1 + C_2 \exp(-Pe_z) \quad (6-14)$$

In Equation (6-14), Pe , the Peclet number for the particle is the quantity $(U_p z/D_S)$, since it has been reported that in batch operations, U_p/D_S cannot be separated^(210,211). To solve for the constants C_1 and C_2 in Equation (6-14), two sets of boundary conditions for an infinite and finite column are proposed:

Boundary Condition 1: Infinite Column

$$\begin{aligned} C_S &= C_{S1} && \text{at } z = z_1 \\ C_S &= 0 && \text{at } z = \infty \end{aligned}$$

Using these boundary conditions, Equation (6-14) becomes:

$$C_S(z) = C_{S1} \frac{\exp(-Pe_z)}{\exp(-Pe_{z_1})} \quad (6-15)$$

The quantity (U_p/D_S) can be obtained by fitting the experimental solid concentration profile. The solid concentrations at the bottom of the reactor, C_{S0} ($z = 0$), and at the expanded bed height of the reactor, C_{ST} ($z = H_T$) can be calculated from the following equations, respectively:

$$C_{S0} = C_{S1} \frac{1}{\exp(-Pe_{z_1})} \quad (6-16)$$

$$C_{ST} = C_{S1} \frac{\exp(-Pe_{H_T})}{\exp(-Pe_{z_1})} \quad (6-17)$$

The expanded bed height, H_T , at any given operating conditions can be estimated from the gas holdup with the following expression:

$$H_T = \frac{H_{SL}}{(1 - \varepsilon_G)} \quad (6-18)$$

where H_{SL} , the static slurry height, is 1.25 and 1.31 m in the cold and hot SBCR, respectively.

Boundary Condition 2: Finite Column

$$C_S = C_{S1} \quad \text{at } z = z_1$$

$$C_S = C_{SN} \quad \text{at } z = z_N$$

Where N in the last sampling port on the column (N = 3 for cold, and N = 4 for hot SBCR). Using these boundary conditions, Equation (6-14) becomes:

$$C_S(z) = C_{S1} - (C_{S1} - C_{SN}) \frac{\exp(-Pe_{z1}) - \exp(-Pe_z)}{\exp(-Pe_{z1}) - \exp(-Pe_{zN})} \quad (6-19)$$

The quantity (U_p/D_s) can be obtained by fitting Equation (6-19) to the experimental solid concentration profile. Furthermore, the solid concentrations at the bottom, C_{S0} , and at the expanded height, C_{ST} , can be calculated from the following equations, respectively:

$$C_{S0} = C_{S1} - (C_{S1} - C_{SN}) \frac{\exp(-Pe_{z1}) - 1}{\exp(-Pe_{z1}) - \exp(-Pe_{zN})} \quad (6-20)$$

$$C_{ST} = C_{S1} - (C_{S1} - C_{SN}) \frac{\exp(-Pe_{z1}) - \exp(-Pe_{H_T})}{\exp(-Pe_{z1}) - \exp(-Pe_{zN})} \quad (6-21)$$

6.5.2 Axial Solid Distribution in the Cold and Hot SBCR

Figures 94 and 95 show the effect of superficial gas velocity and gas nature on the axial solid concentration in the cold and hot SBCRs, respectively; and the fit line generated by Equations (6-15) through (6-17). All experiments were carried out at 7.5 and 17.5 bar using N_2 and He in the cold and hot SBCRs, respectively. The temperature in the hot SBCRs was maintained at 384

K for all experiment. As can be seen in these figures the axial solid concentration, $C_S(z)$, decreases with the reactor height at all U_G . The decrease of $C_S(z)$ with z seems to be more pronounced at lower slurry concentration. For instance when the average solid concentration in the cold SBCR is 142 kg m^{-3} (4.62 vol.%), the decrease of $C_S(z)$ with z is about 14-15% for both N_2 and He, whereas at higher slurry concentration of 644 kgm^{-3} (20 vol.%) the decrease of $C_S(z)$ with z is less than 2% for both gases, indicating that the degree of backmixing is stronger at higher solid concentration. Furthermore, it appears that the superficial gas velocity has a negligible effect on the axial solid concentration in the range of gas velocity studied (0.065-0.150 m/s, and 0.089-0.271 m/s in the cold and hot SBCRs, respectively). In general, as U_G increases the concentration profile becomes more uniform, which indicates that the solid dispersion in the reactor is enhanced. In fact Murray and Fan⁽¹⁵⁷⁾ reported that the solid dispersion coefficient, D_S increases with the superficial gas velocity, as can be seen in Equation (2-120).

Figures 94 and 95 show that the axial-sedimentation dispersion model fits the experimental data with an average absolute relative error (AARE) and standard deviation less than 1.5 and 2.5%, respectively.

It should be mentioned, however, that due to the limited number of experimental data points available, no conclusion can be drawn concerning the values and behavior of U_p/D_S .

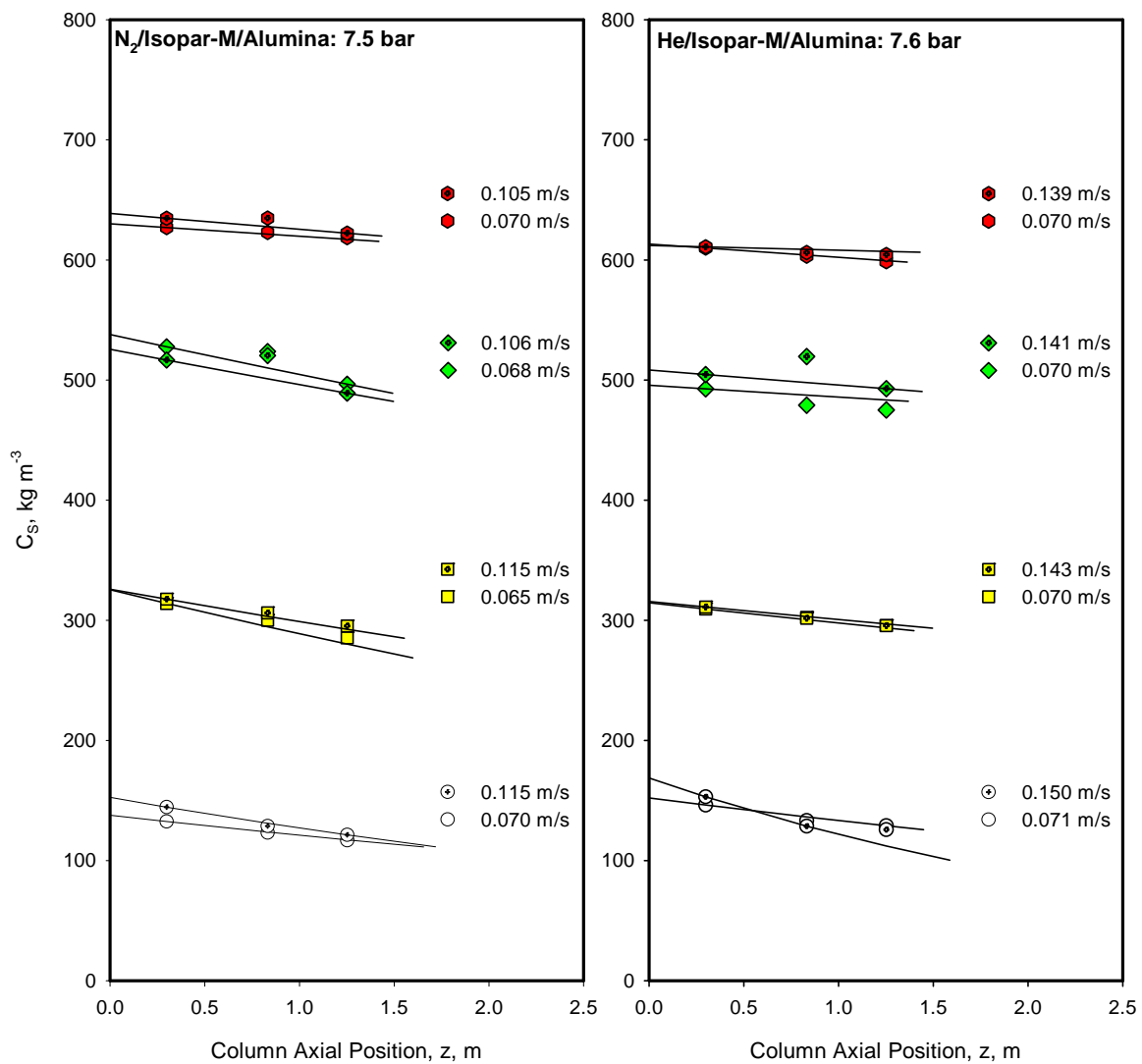


Figure 94 Axial Solid Distribution for N₂ and He in Isopar-M/Alumina in the Cold SBCR

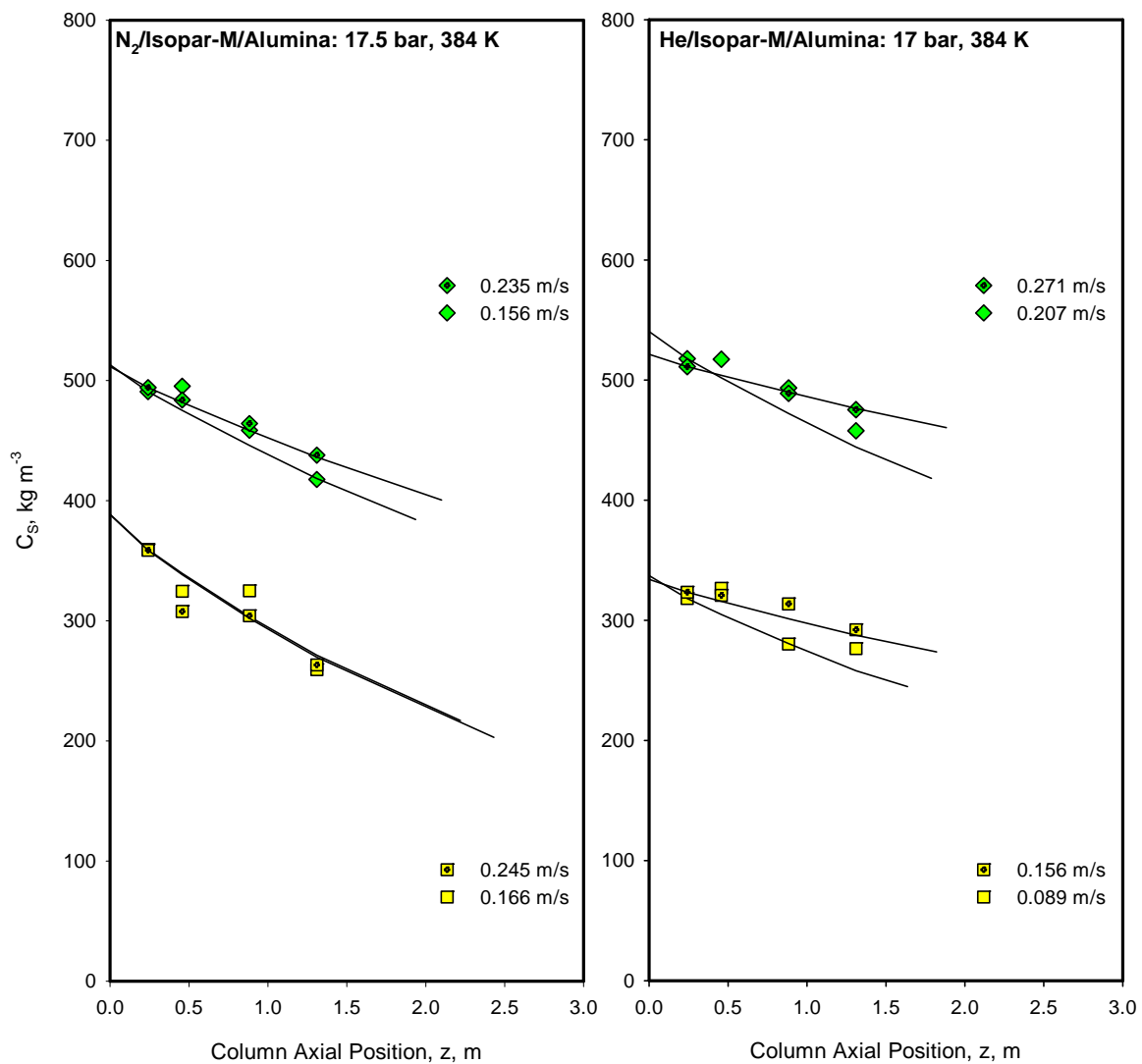


Figure 95 Axial Solid Distribution for N₂ and He in Isopar-M/Alumina in the Hot SBCR

7.0 CORRELATION OF THE HYDRODYNAMIC AND MASS TRANSFER DATA

In this study, two approaches were used to correlate the experimental hydrodynamic and mass transfer data obtained in the cold and hot SBCRs. The first method was to develop empirical correlations, and the second was to use Artificial Neural Network models. A comprehensive literature search, as listed in Tables 29 and 30 for Bubble Column Reactors (BCRs) and Slurry Bubble Column Reactors (SBCRs), respectively, was conducted to obtain the hydrodynamic and mass transfer data for different gases in various liquids and slurries operating under wide ranges of conditions in different size reactors provided with a variety of gas spargers.

7.1 EMPIRICAL CORRELATIONS

There are several empirical correlations available in the literature for the prediction of the hydrodynamic and mass transfer parameters in the bubble and slurry bubble column reactors, as listed in Tables 3, 4 and 10, but unfortunately these correlations have several limitations and accordingly they cannot be employed to simulate the behavior of industrial-size reactors. This is because most of these correlations were developed for aqueous, highly ionic systems in small-diameter reactors operating under atmospheric pressure and/or ambient temperature; the data were obtained with different gas spargers; and the majority of the solids were non-catalytic particles.

Table 29 Available literature data in BCRs used in the development of the correlations

<i>Author</i>	<i>Gas</i>	<i>Liquid</i>	<i>Operating variables</i>	<i>D_G, m</i>	<i>Sparger</i>	<i>Study</i>	<i>Symbols</i>
Bhaga et al. ⁽⁵⁶⁾	N ₂	n-octane + toluene, cumene + ams, toluene + ethanol, toluene + ams, toluene + cumene, toluene + ethylbenzene, acetone + benzene	P: atm. T: 298, 333 K U _G : 0.0213-0.035 m/s	0.0382	PfP	ε _G	○
Bukur and Daly ⁽²¹²⁾	O ₂	Wax	P: atm. T: 473, 538 K U _G : 0.01-0.15 m/s	0.229	PfP	ε _G	⊗
Camarasa et al. ⁽¹¹⁴⁾	Air	H ₂ O	P: atm. T: ambient U _G : 0.013-0.15 m/s	0.1	PoP	ε _G , d ₃₂	⊗
Chabot and Lasa ⁽⁸³⁾	N ₂	Paraffin oil	P: atm. T: 373, 448 K U _G : 0.022-0.146 m/s	0.2	PfP	ε _G	□
Daly et al. ⁽⁸⁹⁾	Air	Sasol wax	P: atm. T: 538 K U _G : 0.02-0.12	0.05	PfP	ε _G , d ₃₂	□
Dewes et al. ⁽¹⁷⁵⁾	Air	H ₂ O-0.8M sodium sulfate	P: 1-8 bar T: ambient U _G : 0.03-0.08 m/s	0.115	PfP	ε _G , k _L a	▣
Eickenbusch et al. ⁽¹⁰²⁾	Air	H ₂ O +Hydroxypropyl guar	P: atm. T: ambient U _G : 0.0095-0.09 m/s	0.19, 0.29, 0.6	PfP, R	ε _G , k _L a	△
Ellenberger and Krishna ⁽¹²⁷⁾	Air, Ar, He, SF ₆	Water, tetradecane, paraffin oil	P: atm. T: 298K U _G : 0.06-0.7 m/s	0.10, 0.19, 0.38	SP	ε _G -Large	▲
Grover et al. ⁽⁸⁴⁾	Air	H ₂ O	P: atm. T: 303-353 K U _G : 0.012-0.041 m/s	0.1	SP	ε _G	▲
Grund et al. ⁽¹⁹⁴⁾	Air	H ₂ O, methanol, toluene, ligroin	P: atm. T: 293 K U _G : 0.1025-0.1946 m/s	0.15	PfP	ε _G , ε _G -Large, d ₃₂ -Large, k _L a	▲
Halard et al. ⁽²¹³⁾	Air	H ₂ O-CMC sol.	P: atm T: ambient U _G : 0.02-0.05 m/s	0.76	R	ε _G , k _L a	▽
Hikita et al. ⁽¹⁸²⁾	Air, O ₂ , H ₂ , CO ₂ , CH ₄ , C ₃ H ₈	Water, +sucrose, +n-butanol, +methanol, +Na ₂ SO ₄ , +K ₂ SO ₄ , +K ₃ PO ₄ , +KNO ₃ , +CaCl ₂ , +AlCl ₃ , +KCl, +NaCl	P: atm. T: 298 K U _G : 0.042-0.38 m/s	0.10, 0.19	S-ON	k _L a	
Hyndman et al. ⁽²¹⁴⁾	Air, Ar	Water	P: atm. T: ambient U _G : 0.04-0.15 m/s	0.20	PfP	ε _G -Large	▼

Table 29 (Continued)

<i>Author</i>	<i>Gas</i>	<i>Liquid</i>	<i>Operating variables</i>	<i>D_G, m</i>	<i>Sparger</i>	<i>Study</i>	<i>Symbols</i>
Idogawa et al. ^(120,215)	Air, He, H ₂	Water, methanol, acetone, ethanol, isoamyl-alcohol+water, ethanol+water	P: 1-150 bar T: 293 K U _G : 0.005-0.050 m/s	0.05	S-ON, PfP, PoP	d ₃₂	
Jackson and Shen ⁽²¹⁶⁾	Air	Water+sodium sulfite	P:atm. T: 283-303 K U _G : 0.001-0.004 m/s	0.076, 1.800, 7.600	S-ON, M-ON	k _L a	
Jamialahmadi et al. ⁽¹⁵⁰⁾	Air	Water, +methanol, +ethanol, +propanol, +isopropanol, +glycerol, +potassium chloride	P: atm. T: 295 K U _G : 0.003-0.0086 m/s	0.1, Rect: 0.05x0.1	S-ON	d ₃₂	
Jiang et al. ⁽⁵³⁾	N ₂	Paratherm NF	P: 1-122 bar T: ambient U _G : 0.027-0.075 m/s	0.0508	R	ε _G , d ₃₂	▽
Jordan and Schumpe ⁽¹¹³⁾	N ₂ , He	Ethanol, decalin, 1-butanol, toluene	P: 1- 40 bar T: 293, 343 K U _G : 0.021-0.22 m/s	0.1	PfP	ε _G , k _L a	▽
Jordan et al. ⁽²⁰⁰⁾	N ₂ , He	Ethanol, decalin, 1-butanol, toluene	P: 1- 40 bar T: 293K U _G : 0.01-0.22 m/s	0.1	PfP, PoP	ε _G -Large, k _L a	▲
Kang et al. ⁽⁴²⁾	Air	Water+CMC	P: 1-6 bar T: ambient U _G : 0.02-0.20 m/s	0.152	M-ON	k _L a	
Kastanek et al. ⁽¹⁰¹⁾	Air	Water	P: atm. T: ambient U _G : 0.005-0.025 m/s	0.15, 0.30, 1.00	PfP	k _L a	
Kataoka et al. ⁽²¹⁷⁾	CO ₂	H ₂ O	P: atm. T: ambient U _G : 0.021-0.05 m/s	5.5	M-ON	ε _G , d ₃₂ , k _L a	◇
Laari et al. ⁽²¹⁸⁾	Air	H ₂ O	P: atm. T: ambient U _G : 0.018-0.038 m/s	0.98	S-ON	ε _G , k _L a	◇
Lau et al. ⁽⁸⁸⁾	Air	Paratherm NF	P: 1-42.4 bar T: 298, 365 K U _G : 0.019-0.039 m/s U _L : 0.0008-0.0032 m/s	0.1016	PfP	ε _G , k _L a	○
Lemoine et al. ⁽²⁰⁹⁾	N ₂ , air	Toluene, toluene+benzoic acid+benzaldehyde	P: 1.8-8.2 bar T: ambient U _G : 0.056-0.15 m/s	0.316	S	ε _G , ε _G -Large	○
Letzel et al. ^(17,41)	N ₂	H ₂ O	P: 1-9 bar T: ambient U _G : 0.12-0.2 m/s	0.15	PfP	ε _G , k _L a	○

Table 29 (Continued)

<i>Author</i>	<i>Gas</i>	<i>Liquid</i>	<i>Operating variables</i>	<i>D_G, m</i>	<i>Sparger</i>	<i>Study</i>	<i>Symbols</i>
Moujaes ⁽²¹⁹⁾	N ₂ , air	Tetraline, H ₂ O, Ethylene glycol	P: atm. T: 275-293 K U _G : 0.0152-0.1173 m/s	0.127, 0.3048, 1.8288	S-ON, M-ON	ε _G , k _L a	⊗
Özturk et al. ⁽⁴⁹⁾	Air, CO ₂ , N ₂ , He, H ₂	Xylene, p-xylene, toluene + ethanol, ligroin, ethylbenzene, ethylacetate, CCl ₄ , 1,4-dioxane, acetone, nitrobenzene, 1,2-dichloroethane, aniline Kerosene	P: atm. T: 293 K U _G : 0.03-0.082 m/s	0.095	S-ON	ε _G , k _L a	⊗
Pino et al. ⁽²²⁰⁾	Air	Kerosene	P: atm. T: 298 K U _G : 0.1-0.175	0.29	PfP	ε _G	▣
Pohorecki et al. ⁽⁸⁶⁾	N ₂	Cyclohexane	P: 11 bar T: 373-433 K U _G : 0.0035 m/s	0.304	M-ON	ε _G , d ₃₂	▣
Saxena et al. ⁽⁷⁹⁾	Air	H ₂ O	P: atm. T: 343, 353 K U _G : 0.01-0.3 m/s	0.305	BC	ε _G	▣
Schäfer et al. ⁽²²¹⁾	N ₂	Water, ethanol, cyclohexane, cyclohexanone, cyclohexanol	P: 1-45 bar T: 293-448 K U _G : 0.65-2.5 10 ⁻³ m/s	0.058	R, PoP	d ₃₂	▣
Shah et al. ⁽¹²⁵⁾	Air	H ₂ O + Ethanol	P: atm. T: ambient U _G : 0.1058-0.2083 m/s	0.1	SP	ε _G	▲
Shimizu et al. ⁽²²²⁾	Air	Water	P: atm. T: 298 K U _G : 0.008-0.033 m/s	0.155-0.200	PfP, R	k _L a	▲
Syeda et al. ⁽²²³⁾	Air	Methanol + propanol, ethyleneglycol + H ₂ O, propanol + H ₂ O	P: atm. T: ambient U _G : 0.32 m/s	0.09	PfP	ε _G	▲
Tarmy et al. ⁽⁴⁶⁾	N ₂	n-Heptane	P: 1.2-6.2 bar T: ambient U _G : 0.12 m/s	0.61	S-ON	ε _G	▲
Towell et al. ⁽²²⁴⁾	CO ₂	H ₂ O	P: atm. T: 300 K U _G : 0.07 m/s	0.407	S-ON	ε _G , k _L a	▼
Veera et al. ⁽²²⁵⁾	Air	H ₂ O	P: atm. T: ambient U _G : 0.06-0.29 m/s	0.385	PfP, S-ON	ε _G	⊗
Vermeer and Krishna ⁽¹⁹⁵⁾	Air	Turpentine 5	P: atm. T: 290 K U _G : 0.1-0.3 m/s	0.19	S	ε _G -Large, k _L a	⊕

Table 29 (Continued)

<i>Author</i>	<i>Gas</i>	<i>Liquid</i>	<i>Operating variables</i>	<i>D_G, m</i>	<i>Sparger</i>	<i>Study</i>	<i>Symbols</i>
Wezorke ⁽²²⁶⁾	Air	Mono-ethylene glycol	P: atm. T: ambient U _G : 0.11-0.41 m/s	0.44	S-ON	ε _G	▼
Wilkinson et al. ⁽⁴⁵⁾	N ₂	0.8M sodium sulfite+ H ₂ O, H ₂ O, mono-ethylene glycol, n-heptane	P: 1-20 bar T: 293K U _G : 0.03-0.28 m/s	0.15, 0.158, 0.23	R	ε _G , d ₃₂ , k _L a	▼
Zou et al. ⁽⁸⁷⁾	Air	H ₂ O, Ethanol	P: atm. T: 313-369.5 K U _G : 0.04-0.166 m/s U _L : 0.007 m/s	0.1	S-ON	ε _G	◆

Table 30 Available literature data in SBCRs used in the development of the correlations

<i>Author</i>	<i>Gas</i>	<i>Liquid</i>	<i>Solid</i>	<i>Operating variables</i>	<i>D_G, m</i>	<i>Sparger</i>	<i>Study</i>	<i>Symbols</i>
Choi et al. ⁽²²⁷⁾	Air	H ₂ O	Glass beads	P: atm. T: ambient U _G : 0.0205-0.08 m/s C _V : 3 vol.%	Rect: 0.456x0.153	PfP	ε _G , k _L a	⊙
Deckwer et al. ⁽¹¹⁾	N ₂	Wax	Al ₂ O ₃	P: 4 bar T: 523 K U _G : 0.0044-0.034 m/s C _V : 0-1.21 vol.%	0.1	SP	ε _G	◆
Gandhi et al. ⁽⁷³⁾	Air	H ₂ O	Glass beads	P: atm. T: ambient U _G : 0.05-0.26 m/s C _V : 10-35 vol.%	0.15	S	ε _G	⊙
Godbole ⁽²²⁸⁾	Air	H ₂ O, H ₂ O +CMC, H ₂ O +0.8 M sodium sulfite, H ₂ O +ethanol, H ₂ O +propanol, H ₂ O +butanol, H ₂ O +methanol, H ₂ O + glycerine, Sotrol-130	Polystyrene, coal, oil shell, sand	P: atm. T: 298 K U _G : 0.017-0.57 m/s, C _V : 0-26.3 vol.%	0.305	PfP	ε _G , k _L a	■
Inga ⁽¹⁸⁹⁾	H ₂ , CO, CH ₄ , N ₂	Hexanes	Iron Oxides	P: 1.26-7.67 bar T: ambient U _G : 0.06-0.35 m/s C _V : 0-21.76 vol.%	0.316	S	ε _G , ε _{G-Large} , d ₃₂ , d _{32-Large} , k _L a	⊙

Table 30 (Continued)

<i>Author</i>	<i>Gas</i>	<i>Liquid</i>	<i>Solid</i>	<i>Operating variables</i>	<i>D_G, m</i>	<i>Sparger</i>	<i>Study</i>	<i>Symbols</i>
Kluytmans et al. ⁽⁶³⁾	N ₂	H ₂ O	Carbon	P: atm. T: ambient U _G : 0.04-0.11 m/s C _V : 0-1.429x10 ⁻³ vol.%	0.3	PfP	ε _G	
Krishna et al. ⁽⁸⁾	Air	Paraffin oil	Silica	P: atm. T: ambient U _G : 0.085-0.2175 m/s C _V : 0-36 vol.%	0.38	SP	ε _G	
Li et al. ⁽²²⁹⁾	Air	H ₂ O	Glass beads	P: atm. T: ambient U _G : 0.05-0.3 m/s	0.28	S	ε _G	
Luo et al. ⁽⁴³⁾	N ₂	Paratherm NF	Alumina	P: 1-28.6 bar T: 301 K U _G : 0.04-0.333 m/s C _V : 0-19.1 vol.%	0.102	PfP	ε _G	
O'Dowd et al. ⁽¹⁶¹⁾	N ₂	H ₂ O	Glass beads	P: atm. T: ambient U _G : 0.031-0.194 m/s C _V : 4.17-10.74 vol.%	0.108	PfP	ε _G	
Sehabiague et al. ⁽²³⁰⁾	H ₂ , N ₂	Sasol wax, Isopar M	Alumina, Iron oxides	P: 1.7-30.0 bar T: 298-453 K U _G : 0.06-0.39 m/s C _V : 0-20 vol.%	0.29	S	ε _G , ε _{G-Large}	
Vandu and Krishna ⁽²³¹⁾	N ₂	Water, tetradecane, paraffin oil, ethanol, tellus oil	Silica	P: atm. T: ambient U _G : 0.01-0.42 m/s C _V : 0-25 vol.%	0.10, 0.15, 0.38, 0.63	S, PfP	k _L a	
This study	H ₂ , CO, CH ₄ , N ₂ , He	Isopar-M	Glass/Beads, Alumina	P: 6.5-30 bar T: 300-453 K U _G : 0.07-0.39 m/s C _V : 0-36 vol.%	0.316, 0.29	S	ε _G , ε _{G-Large} , d ₃₂ , d _{32-Large} , k _L a	

Statistical correlations have also been proposed for predicting the hydrodynamic and mass transfer parameters in two-phase and three-phase reactors and although they have been shown to enjoy high confidence levels ⁽²⁰⁹⁾, they are system-dependent and accordingly their application to predict and/or extrapolate the behavior of other gas-liquid-solid systems could be misleading ⁽²⁰⁹⁾. Thus, adequate correlations which can be used to predict the hydrodynamics and mass transfer parameters in multiphase reactors operating under wide ranges of industrial conditions are needed.

7.1.1 Gas Holdup Correlation

From the background presented in Section 2.0, it seems that any correlation to be developed for predicting the gas holdup in bubble columns and slurry bubble column reactors has to account for the impact of the mentioned criteria, including pressure, temperature, gas superficial velocity, temperature, solid concentration, particle density/concentration, reactor size, gas sparger characteristics, etc. In this study, the experimental total gas holdup (ϵ_G) data along with those obtained from the literature references listed in Tables 29 and 30, totaling 3881 data points were used to develop the following correlation:

$$\epsilon_G = 4.94 \times 10^{-3} \times \left(\frac{\rho_L^{0.415} \rho_G^{0.177}}{\mu_L^{0.174} \sigma_L^{0.27}} \right) U_G^{0.553} \left(\frac{P_T}{P_T - P_S} \right)^{0.203} \left(\frac{D_C}{D_C + 1} \right)^{-0.117} \Gamma^{0.053} \times \exp[-2.231C_V - 0.157(\rho_p d_p)] \quad (7-1)$$

Γ represents the effect of the gas sparger type, can be calculated from:

$$\Gamma = (K_d \times N_o d_o^\alpha) \quad (7-2)$$

$$\zeta = N_o \left(\frac{d_o}{D_c} \right)^2 \times 100 \quad (7-3)$$

In Equation (7-2), K_d is the distributor coefficient, N_o is the number of orifices in the sparger, and d_o is the diameter of the orifice. The values of K_d are given in Table 31 and the exponent α for several distributors can be found in Table 32. For perforated plates, however, the exponent α should be obtained from ζ , defined by Equation (7-3).

In the case of bubble column reactors, C_v , ρ_p , and d_p are zeros. Thus, Equation (7-1) considers the effects of gas-liquid-solid properties, liquid-phase composition, operating conditions, gas sparger type, and column diameter on the total gas holdup. Table 33 presents the ranges of the conditions of applicability of Equation (7-1).

Table 31 Values of K_d used in Equation (7-2)

<i>Distributor</i>	<i>K_d</i>
R, S	1.000
S-ON	1.205
PfP, M-ON	1.364
BC, PoP, SP	1.553

The importance of Equation (7-1) lies in the fact that it allows predicting the total gas holdup for a single-component as well as a multi-component gaseous system in liquids and/or slurries provided that the gas density under given operating conditions is known. For this purpose an Equation-of-State (EOS), such as Peng-Robinson EOS can be employed to determine the gas density which then can be used along with other needed variables in Equation (7-1) to predict the corresponding total gas holdup.

Table 32 Value of α used in Equation (7-2)

<i>Distributor</i>	$\zeta, \%$	α
PfP	< 0.055	0.017
PfP	≥ 0.055 and ≤ 0.3	0.303
PfP	> 0.3	0.293
M-ON		0.303
S-ON		0.134
R, S		0.015
BC		0.500
PoP, SP		0.650

Table 33 Upper and lower limits of the variables involved in Equation (7-1)

<i>Variables</i>	<i>Minimum value</i>	<i>Maximum value</i>
P_T , bar	1	150
P_S , bar	0	7
U_G , m/s	3.5×10^{-3}	0.574
C_V , vol.%	0	36
T , K	275	538
M_B , kg/kmol	18	730
M_A , kg/kmol	2	44
d_p , 10^{-6} m	5	300
ρ_P , kg/m ³	700	4000
ρ_G , kg/m ³	0.06	177.3
ρ_L , kg/m ³	633.4	1583
μ_L , 10^{-3} Pa s	0.189	398.8
σ_L , 10^{-3} N/m	8.4	75
D_C , m	0.0382	5.5

In order to determine the gas holdup corresponding to large bubbles ($\epsilon_{G\text{-large}}$), our experimental holdup data of large gas bubbles along with those obtained from the literature references given in Tables 29 and 30, totaling 1426 data points were used to develop the following correlation:

$$\epsilon_{G\text{-Large}} = \epsilon_G^{0.84} \left(1 - 3.04 \times 10^{-6} \frac{\rho_L^{0.97}}{\mu_L^{0.16}} e^{-4.59 C_V} \right) = \epsilon_G^{0.84} (F) \quad (7-4)$$

Figure 96 shows a comparison between predicted and experimental gas holdup values in this study along with those obtained from the literature references listed in Tables 29 and 30, and as can be seen the agreement between the predicted and experimental values is within an absolute average relative error (AARE) and a standard of deviation (σ) of 20 % for ε_G , and 23 and 27%, for $\varepsilon_{G-Large}$, respectively.

Thus, from the knowledge of the total gas holdup (ε_G), Equation (7-1) and the holdup of large gas bubbles, Equation (7-4), the holdup of small gas bubbles ($\varepsilon_{G-Small}$) can be deduced as:

$$\varepsilon_{G-Small} = \varepsilon_G - \varepsilon_{G-Large} \quad (7-5)$$

It should be noted that coupling Equations (7-1) and (7-4) leads to the following situations:

1. If ε_G is $\leq (F)^{25/4}$, small gas bubbles do not exist; and Equation (7-4) cannot be used to split ε_G into $\varepsilon_{G-Large}$ and $\varepsilon_{G-Small}$.
2. If, ε_G is $> (F)^{25/4}$ small and large gas bubbles coexist; and Equations (7-1) and (7-4) can be used.

7.1.2 Sauter-Mean Bubble Diameter Correlation

The d_{32} , $d_{32-Small}$ and $d_{32-Large}$ obtained in this study in the cold and hot SBCRs, along with the literature data, were used to develop the following correlation:

$$d_{32} = 37.19 \times \frac{\mu_L^{0.084} \sigma_L^{1.215} \rho_G^{0.018} T^{1.662}}{\rho_L^{1.516} M_A^{0.124}} U_G^{0.141} \left(\frac{D_C}{D_C + 1} \right)^{0.302} (1 - \varepsilon_G)^{1.556} \Gamma^{-0.017} \exp(2.81C_V + 2.77\rho_P d_P) \quad (7-6)$$

In Equation (7-6), Γ is defined in Equation (7-2). The $d_{32-Large}$ was also correlated as:

$$d_{32-Large} = d_{32}^{0.958} \left(1 - 10^{-5} \rho_L^{0.223} \mu_L^{0.034} \sigma_L^{8.600} U_G^{0.039} \varepsilon_G^{2.370} \varepsilon_{G-Large}^{2.740} \right) \quad (7-7)$$

Thus, $d_{32-Small}$ can be obtained from the following expression:

$$\frac{\varepsilon_G}{d_{32}} = \frac{\varepsilon_{G-small}}{d_{32-small}} + \frac{\varepsilon_{G-large}}{d_{32-large}} \quad (7-8)$$

The validity ranges of Equations (7-6) and (7-7) are shown in Table 34. Figure 96 shows the comparison between experimental and predicted d_{32} values.

7.1.3 Mass Transfer Correlation

The $k_L a$ values obtained in this study in the cold and hot SBCRs, along with the literature data given in the references listed in Tables 29 and 30, were used to develop the following correlation:

$$k_L a = 6.14 \times 10^4 \frac{\rho_L^{0.26} \mu_L^{0.12}}{\sigma_L^{0.52} \rho_G^{0.06}} \frac{\varepsilon_G^{1.21}}{U_G^{0.12} d_{32}^{0.05}} \frac{D_{AB}^{0.50}}{T^{0.68}} \Gamma^{0.11} \left(\frac{D_C}{D_C + 1} \right)^{0.40} \quad (7-9)$$

Γ is defined in Equation (7-2), Furthermore, the mass transfer coefficient, k_L , was correlated with Sherwood number as:

$$Sh = \frac{k_L d_{32}}{D_{AB}} = 0.187 Sc^{0.5} Bo^{-1.74} Ga^{1.09} Mo^{0.72} Fr^{-1.75} Re^{1.18} \left(\frac{\rho_G}{\rho_{SL}} \right)^{-0.21} \quad (7-10)$$

It should be noted that all dimensionless numbers in Equation (7-10) are based on the slurry physical properties (i.e., ρ_{SL} , μ_{SL}) and d_{32} . The validity ranges of Equations (7-9) and (7-10) are shown in Table 35. Figure 97 shows the comparison between experimental and predicted $k_L a$ and Sherwood number values.

Table 34 Upper and Lower limits of the variables involved in Equations (7-6) and (7-7)

<i>Variables</i>	<i>Minimum value</i>	<i>Maximum value</i>
P _T , bar	1	29.79
U _G , m/s	3.5x10 ⁻³	0.364
C _v , vol.%	0	36
T, K	293	530
M _A , kg/kmol	2	44
dp, 10 ⁻⁶ m	19	42.4
ρ _P , kg/m ³	2500	4000
ρ _G , kg/m ³	0.107	29.11
ρ _L , kg/m ³	633.4	1113
μ _L , 10 ⁻³ Pa s	0.189	21
σ _L , 10 ⁻³ N/m	8.4	75
D _C , m	0.1	5.5
ε _G , %	4.4	62.4

Table 35 Upper and lower limits of the variables involved in Equation (7-10)

<i>Variables</i>	<i>Minimum value</i>	<i>Maximum value</i>
Bo	0.18	1514.61
Ga	46.37	4.9x10 ⁷
Sc	48.43	12190.44
Mo	4x10 ⁻¹¹	9.3x10 ⁻³
Fr	0.20	2.53
Re	11.27	3637.35
ρ _G /ρ _{SL}	8.4x10 ⁻⁵	0.04

7.1.4 Comparison of the Data with the Available Literature Correlations

The literature correlations listed in Tables 3 and 4 along with Equation (7-1) were used to predict the total gas holdup data obtained in this study. Figure 98 shows a comparison between the predicted and experimental holdup of H₂ in Isopar-M/glass beads, and as can be clearly seen most of available literature correlations fail to predict the experimental gas holdup values of H₂ as a function of pressure in the presence of 7.6 vol.% of solid particles, whereas the predictions

using Equation (7-1) are in a very good agreement. This is because most of the correlations underemphasize the effect of the gas density. In this figure it can be seen that the largest deviation between the experimental and predicted H_2 holdup values was obtained with the correlation of Krishna and Sie⁽⁶⁾. In fact, an AARE of more than 150% between experimental and their predicted values is obtained.

This figure also shows the holdup of H_2 in Isopar-M up to 36 vol.% (64.3 wt.%) of glass beads, and those predicted using the correlations given in Table 4 proposed for SBCRs. As can be observed in this figure, literature correlations used do not predict the effect of solid concentration on the gas holdup of H_2 in Isopar-M/glass beads slurry, while Equation (7-1), shows the best fit.

Figure 99 shows the prediction of the k_{La} values of CH_4 in Isopar-M using the available correlations in Table 10, and as can be seen these correlations fail to predict the effect of pressure on the k_{La} values. For instance, the correlation proposed by Jordan and Schumpe⁽¹¹³⁾, was developed for high pressure systems, but in general an AARE of more than 48% between experimental and predicted values are observed. In this Figure it can be seen that Equation (7-9) fits the data within an AARE of less than 12%. Figure 99 also shows the experimental Sh number for CO in Isopar-M, and those predicted using the available literature correlations in Table 9, and in general a significant deviation between the experimental and predicted data can be observed. Yang et al.⁽¹⁸¹⁾ developed their correlation for H_2 and CO in paraffin oil/silica slurry, but their model shows an AARE of more than 32% compared to 12% obtained with Equation (7-10). Their model also ignores the effect of pressure on Sh number.

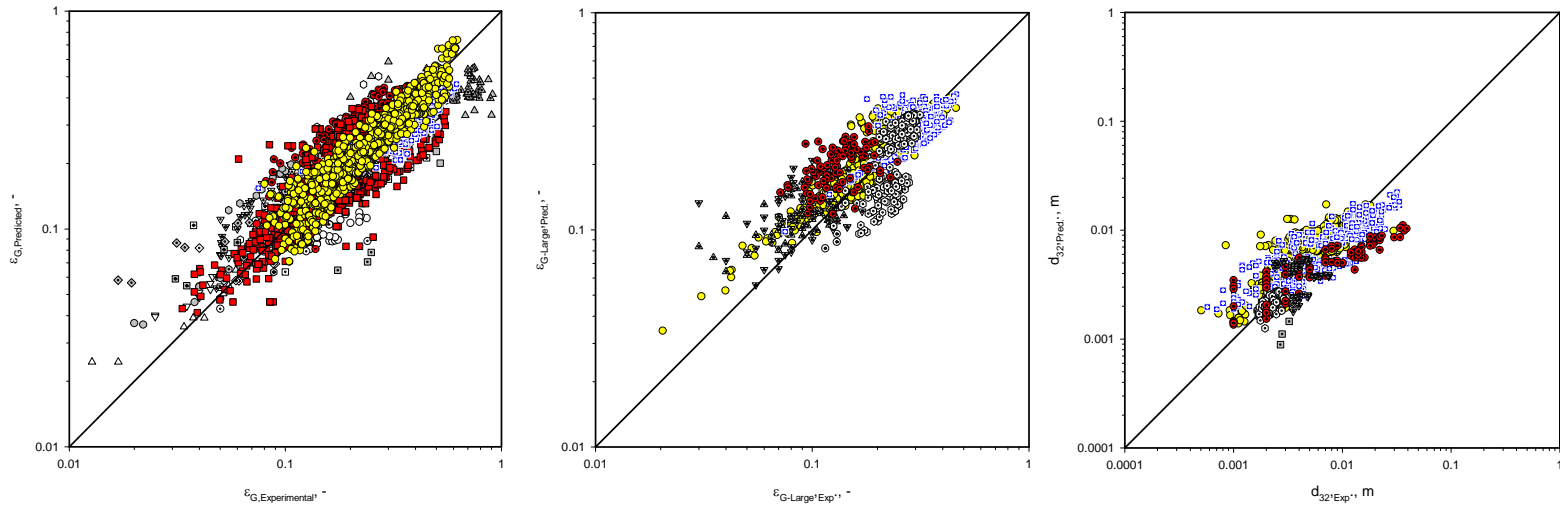


Figure 96 Comparison Between Experimental and Predicted ϵ_G , $\epsilon_{G-Large}$, and d_{32} Values from Equations (7-1), (7-4), and (7-6)

(Symbols are given in Tables 29 and 30)

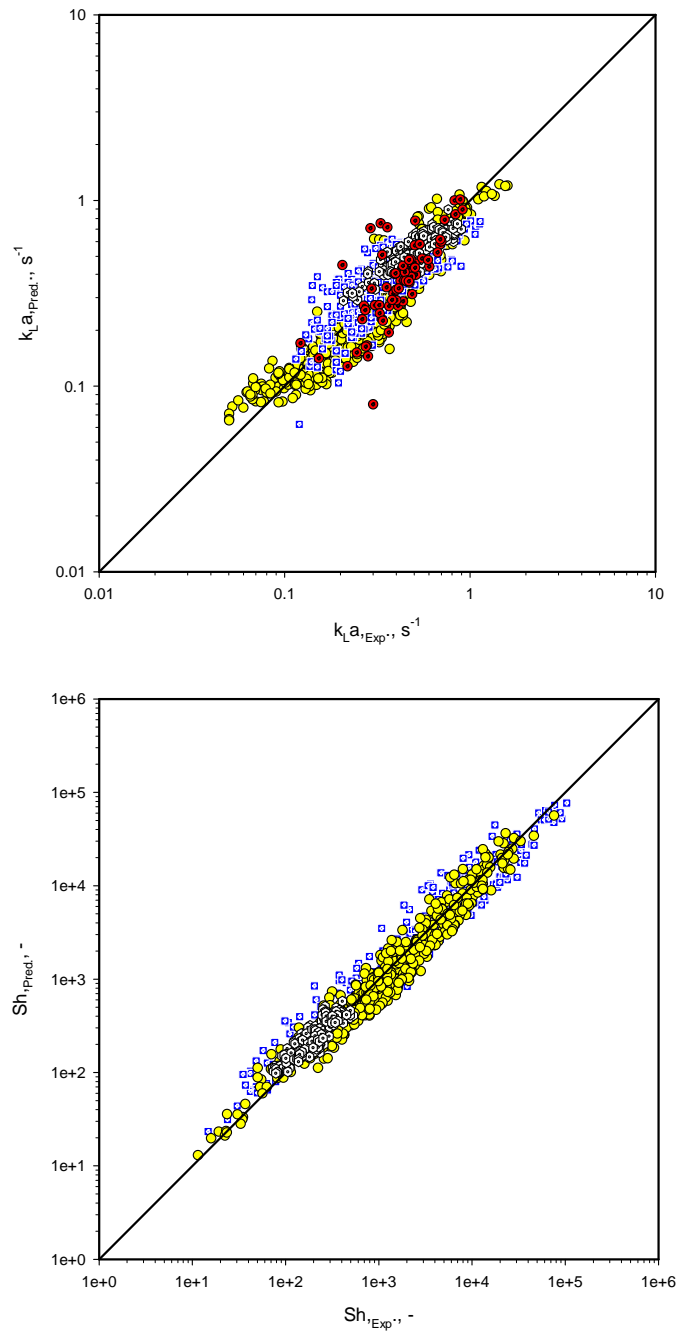


Figure 97 Comparison Between Experimental and Predicted $k_L a$ and Sherwood Values from Equations (7-9) and (7-10)
 (Symbols are given in Tables 29 and 30)

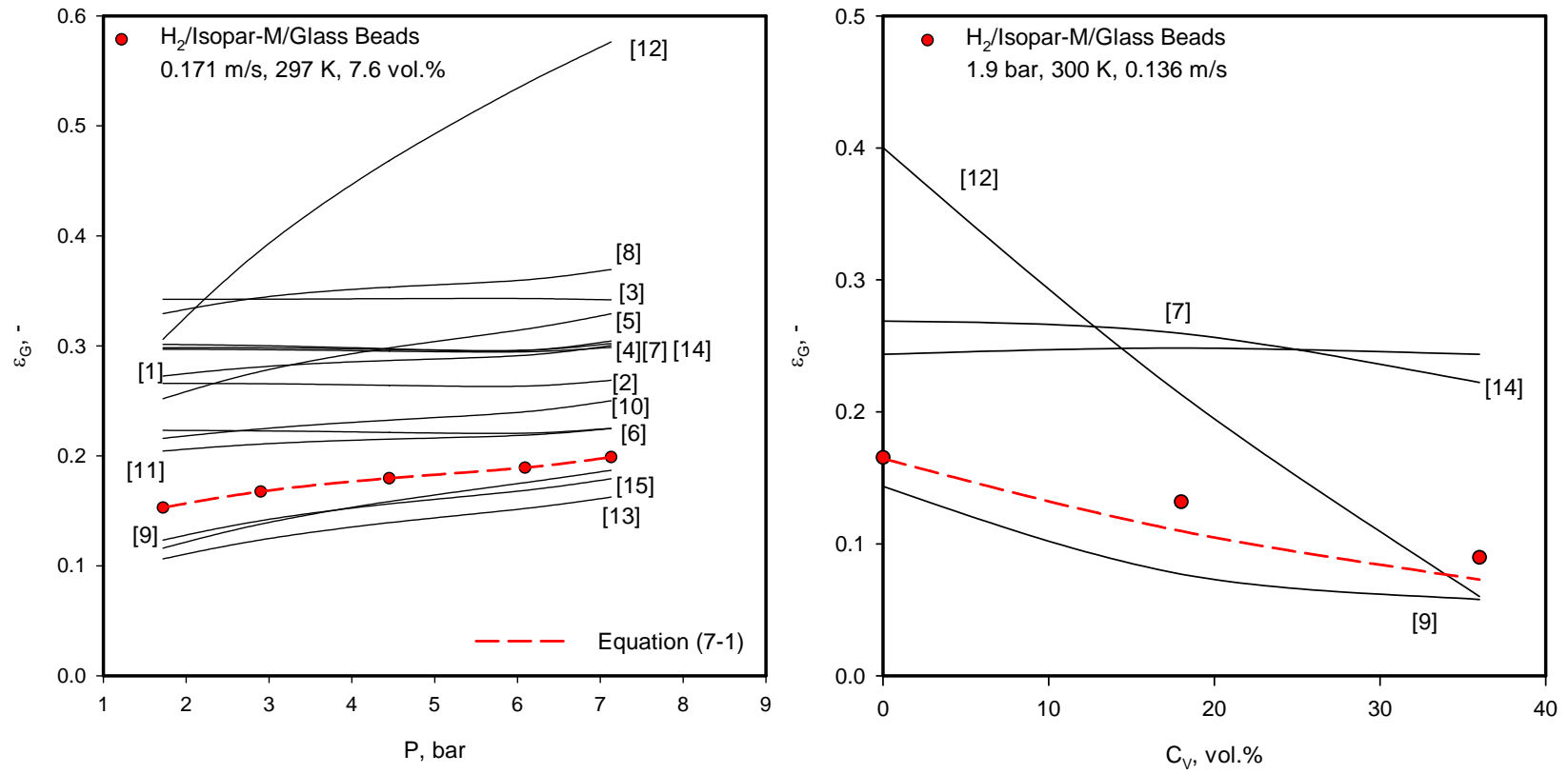


Figure 98 Prediction of the Holdup of H₂ in Isopar-M/Glass Beads Slurry using Available Literature Correlations and Equation (7-1)

[1] Hikita et al. ⁽³³⁾, [2] Bach and Pilhofer ⁽³²⁾, [3] Kumar et al. ⁽¹²¹⁾, [4] Hughmark ⁽³⁴⁾, [5] Reilly et al. ⁽¹²³⁾, [6] Zou et al. ⁽⁸⁷⁾, [7] Sauer and Hempel ⁽¹²⁴⁾, [8] Idogawa et al. ⁽¹²⁰⁾, [9] Fan et al. ⁽²⁸⁾, [10] Jordan and Schumpe ⁽¹¹³⁾, [11] Wilkinson et al. ⁽⁶¹⁾, [12] Krishna and Sie ⁽⁶⁾, [13] Urseanu et al. ⁽¹⁰³⁾, [14] Schumpe et al. ⁽⁶⁴⁾, [15] Reilly et al. ⁽⁴⁸⁾

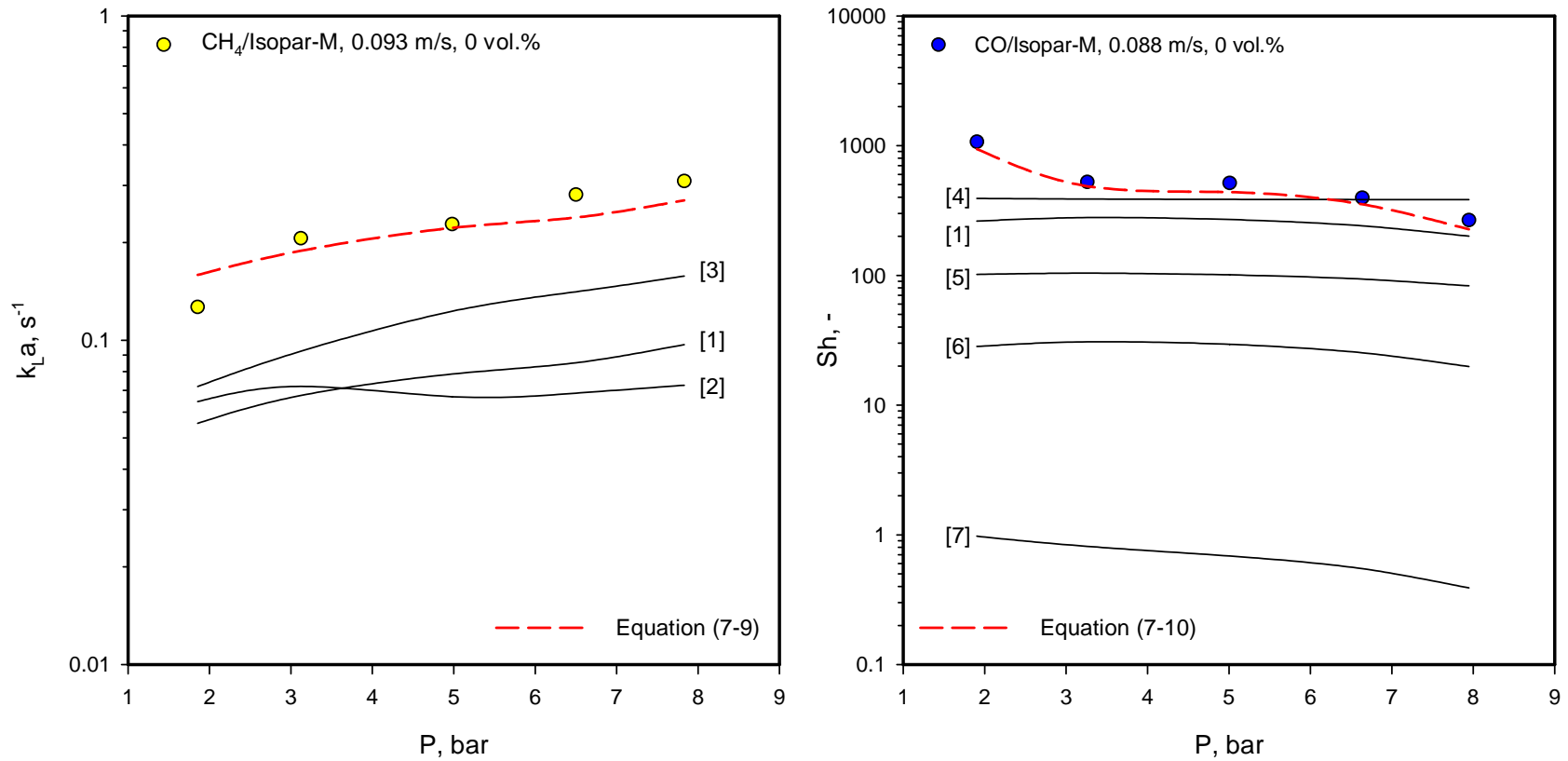


Figure 99 Prediction of k_{La} and Sh using Available Literature Correlations and Equations (7-9) and (7-10)

[1] Akita and Yoshida⁽³¹⁾, [2] Hikita et al.⁽¹⁸²⁾, [3] Jordan and Schumpe⁽¹¹³⁾, [4], Yang et al.⁽¹⁸¹⁾, [5] Neme et al.⁽⁵⁹⁾, [6], Fukuma et al.⁽¹⁸⁰⁾, [7] Miyahara et al.

7.2 ARTIFICIAL NEURAL NETWORK MODEL

Artificial Neural Network (ANN) models have been recently given an increasing attention in chemical engineering applications, including parameters prediction ⁽²³²⁾, modeling ⁽²³³⁾, process optimization ⁽²³⁴⁾, process simulation ⁽²³⁵⁾ and process control ⁽²³⁶⁾.

Unlike empirical correlations, ANNs are black boxes where no equations are a priori needed. For problems concerning control and prediction, Back Propagation Neural Network (BPNN) and radial basis function are employed, whereas for problems involving data clustering, adaptive resonance theory, network for binary signals and Kohonen self-organizing map are used. Since the purpose of this study is to predict the hydrodynamic and mass transfer parameters in industrial-scale BCRs and SBCRs, the BPNN previously described by Fausett ⁽²³⁷⁾ and recently used by Lemoine et al ⁽²³⁸⁾ was adopted. The details of the architecture, algorithm, and calculation of the output parameters of the BPNN models developed in this study are given in full in Appendix C. Shaikh and Al-Dahhan ⁽²³⁹⁾ developed an ANN for predicting gas holdup in bubble column reactors, where the effects of the operating variables along with the gas/liquid physical properties were represented by dimensionless numbers. Their ANN, however, was limited to BCRs and accordingly it cannot be employed for predicting the gas holdup in SBCRs. A comparison between experimental gas holdup data obtained in the cold and hot SBCR and those predicted using the ANN developed by Shaikh and Al-Dahhan ⁽²³⁹⁾ was performed; and as expected the deviation between the values was within an Average Absolute Relative Error

(AARE), standard of deviation (σ), and regression coefficient (R^2) of 58, 48 and 31 %, respectively.

7.2.1 Construction of the BPNNs

In this study, the following variables were selected to form the neurons of the input layer: superficial gas velocity (U_G); liquid physical properties: density (ρ_L), viscosity (μ_L), surface tension (σ_L), and molecular weight (M_B); gas physical properties: density (ρ_G), and molecular weight (M_A); solid physical properties: density (ρ_P), and particle size (d_p); solid concentration (C_V); liquid composition (X_W); reactor geometry: column diameter (D_C); and sparger design: open area per column cross-sectional area (ζ), and sparger type (S_T). The liquid composition X_W , is used when a mixture liquids is employed (i.e., Water +Alcohol, water + CMC, Organic + aqueous, etc.). X_W values lie between 50-100%, representing the weight fraction of the main liquid in the mixture. If the liquid is a mixture of hydrocarbons (i.e. wax, oil), however, X_W is considered to be 100%. The sparger open area, ζ is defined in Equation (7-3). The assigned values to the sparger type (S_T) are given in Table 36.

Table 36 Values of the sparger type (S_T)

<i>Sparger Type</i>	<i>S_T Value</i>
S-ON	0
PfP, M-ON	1/3
R, S	2/3
PoP, BC, SP	1

The data points obtained in this study and from the reference given in Tables 29 and 30 were used to develop and train the networks. The choice of the architecture, the number of

hidden layers and neurons as well as epoch (i.e. iteration), for the developed BPNNs was based on the minimization of the MSE as suggested by Lemoine et al. ⁽²³⁸⁾. In this study the feed-forward Back Propagation learning algorithm, as described by Lemoine et al. ⁽²³⁸⁾ has been selected for the learning and training of the experimental hydrodynamic and mass transfer data using the Pittnet software package developed at the University of Pittsburgh ⁽²³⁸⁾

7.2.2 Gas Holdup Prediction by BPNN

The BPNN selected for predicting the total gas holdup data had the following topology: [14,9-7,1], representing 14 input neurons, 9 and 7 neurons in the first and second hidden layer, respectively, and one output neuron. The BPNN developed for predicting the large gas bubbles holdup had the following topology: [14,8,1]. The maximum and minimum values of the input variables and the output parameters ε_G and $\varepsilon_{G-Large}$ can be found in Tables 37 and 38, respectively. The weight factors are given in Table 39 for ε_G and in Table 40 for $\varepsilon_{G-Large}$. The learning rate for the BPNNs was 0.25 and 10000 and 5000 iterations for the total gas holdup and large gas bubbles holdup, respectively, were used during the training and learning process. The AARE, σ , and R^2 of 16, 19 and 91 %, respectively for total gas holdup, and 10, 14 and 93%, respectively for large gas bubbles holdup were obtained with this BPNN. Figure 100 shows the comparison between the experimental and predicted ε_G and $\varepsilon_{G-Large}$ using the BPNNs.

7.2.3 Sauter-Mean Bubble Diameter Prediction by BPNN

The BPNNs selected for predicting the d_{32} and the $d_{32-Large}$ data have the following topology: [15,9-7,1], and [15,7-5,1], respectively. The maximum and minimum values of the input

Table 37 Ranges of the input and output parameters of the BPNN for total gas holdup (ϵ_G)

Input node #	1	2	3	4	5	6	7	8	9	10	11	12	13	14
	$U_{G,}$ $m\ s^{-1}$	$\rho_{L,}$ $kg\ m^{-3}$	$10^4 \times \mu_{L,}$ $Pa\ s$	$10^3 \times \sigma_{L,}$ Nm^{-1}	$M_{B,}$ $kg.kmol^{-1}$	$\rho_{G,}$ $kg\ m^{-3}$	$M_{A,}$ $kg\ kmol^{-1}$	$D_{C,}$ m	$\zeta,$ $\%$	$d_p,$ m	$\rho_{p,}$ $kg\ m^{-3}$	$X_{W,}$ $\%$	$C_{V,}$ $\%$	$S_{T,}$ $-$
<i>Min</i>	0.0035	633.42	1.89	8.416	18	0.0732	2	3.82×10^{-2}	9.66×10^{-3}	0	0	50	0	0
<i>Max</i>	0.5743	1583	3988	75	730	178.44	44	5.5	75	3×10^{-4}	4000	100	36	1
Output node #	1													
	$(\Pi) = Ln(\epsilon_G)$													
<i>Min</i>	-4.7749													
<i>Max</i>	-0.0943													

Table 38 Ranges of the input and output parameters of the BPNN for large bubbles holdup ($\epsilon_{G-Large}$)

Input node #	1	2	3	4	5	6	7	8	9	10	11	12	13	14
	$U_{G,}$ $m\ s^{-1}$	$\rho_{L,}$ $kg\ m^{-3}$	$10^4 \times \mu_{L,}$ $Pa\ s$	$10^3 \times \sigma_{L,}$ Nm^{-1}	$M_{B,}$ $kg.kmol^{-1}$	$\rho_{G,}$ $kg\ m^{-3}$	$M_{A,}$ $kg\ kmol^{-1}$	$\zeta,$ $\%$	$d_p,$ m	$\rho_{p,}$ $kg\ m^{-3}$	$\epsilon_{G,}$ $\%$	$X_{W,}$ $\%$	$C_{V,}$ $\%$	$S_{T,}$ $-$
<i>Min</i>	0.04	680	3.2	16.16	18	0.1	2	0.07	0	0	2.6	88	0	0
<i>Max</i>	0.75	1000	92.0	72.8	567.4	25.45	29	75	42.37×10^{-6}	4000	66	100	36	1
Output node #	1													
	$(\Pi) = \epsilon_{G-Large}$													
<i>Min</i>	0.015													
<i>Max</i>	0.463													

Table 39 Weights and biases for the [14,9-7,1] BPNN for ε_G

w_{Nm}	Input Nodes														
Hidden Layer 1	1	2	3	4	5	6	7	8	9	10	11	12	13	14	Bias
1	1.466	-4.199	3.260	-1.963	-4.411	-2.964	-1.895	0.884	-10.119	-4.897	0.134	-1.818	-1.020	-0.711	3.237
2	1.060	-9.229	6.266	9.948	0.067	2.070	-1.592	-0.010	1.735	-0.522	1.646	0.539	-0.987	-3.062	-1.933
3	14.179	0.493	-0.809	-0.654	-0.179	0.016	-0.043	-0.194	-2.033	-0.678	0.438	0.659	0.262	0.319	1.173
4	-1.642	2.841	11.051	-0.951	2.330	2.002	-0.302	-0.500	-1.970	-0.699	-0.594	3.369	4.599	0.979	-1.328
5	-0.276	10.573	-4.158	-7.788	-1.563	4.968	-2.343	-1.040	-8.910	5.061	0.826	-4.177	-0.360	-1.485	9.215
6	-1.339	-0.008	-3.241	0.719	-0.922	23.845	0.820	1.126	9.969	-1.814	0.186	3.651	1.759	0.685	-3.485
7	-0.610	-7.848	2.557	8.489	-0.255	-11.053	-0.432	14.458	-1.021	2.344	3.229	-5.482	3.564	-4.731	3.237
8	2.264	-2.157	-0.358	-12.222	1.451	-0.180	-0.036	3.274	6.136	-3.049	0.119	-5.298	3.696	-0.543	6.978
9	2.502	-3.565	-6.634	-1.483	-4.427	-1.089	-0.089	0.132	3.328	3.419	-1.183	1.545	0.883	1.320	-2.168

v_{mn}	Hidden layer 1									
Hidden layer 2	1	2	3	4	5	6	7	8	9	Bias
1	1.272	1.380	4.288	-5.433	0.614	-0.205	-6.026	1.038	-2.380	0.138
2	-0.026	1.467	-7.945	3.237	0.486	-0.001	-0.389	1.107	-4.560	0.236
3	1.651	-1.878	-5.529	-1.429	4.239	3.359	1.806	-0.700	1.403	-1.565
4	-7.056	8.627	1.443	-13.570	5.723	12.609	-7.700	5.924	2.876	-6.050
5	0.276	-0.248	-2.252	-1.128	-2.091	-0.612	0.324	-0.036	5.232	-1.612
6	4.422	0.765	-8.854	6.781	0.404	6.130	-1.051	-0.906	-9.425	-3.741
7	5.031	1.560	0.486	4.135	-5.799	1.564	-8.897	6.100	-1.252	-0.473

y_{nl}	Hidden Layer 2							
Output	1	2	3	4	5	6	7	Bias
1	2.417	-6.080	-2.336	2.084	-3.292	-1.915	-1.201	0.926

Table 40 Weights and biases for the [14,8,1] BPNN for ε_G -Large

w_{Nm} Hidden Layer 1	Input Nodes														Bias	
	1	2	3	4	5	6	7	8	9	10	11	12	13	14		
1	3.367	-1.136	2.763	5.584	-7.474	1.004	3.272	2.939	2.689	-6.765	0.724	-0.693	-9.702	1.243	0.128	
2	4.642	1.707	-4.601	3.549	-8.137	0.738	0.889	0.565	0.626	3.062	-2.220	1.030	-3.094	0.295	-3.356	
3	3.922	-7.681	-0.990	1.503	-0.199	-0.445	-0.100	0.866	-3.255	-2.943	2.874	-1.101	-5.067	1.678	-1.195	
4	1.696	-0.001	9.034	-1.939	-7.524	-0.142	-0.636	-1.213	-2.745	0.566	-4.374	0.240	10.339	-11.822	14.227	
5	1.551	-0.026	0.474	-0.435	0.126	0.160	0.081	-0.115	2.420	-2.923	-4.672	0.042	1.374	0.488	-1.095	
6	-3.178	1.454	3.932	-5.068	2.765	6.638	-1.018	-0.733	0.849	-1.594	2.898	0.284	7.183	-1.697	0.829	
7	5.157	-0.985	1.956	1.012	-0.723	-0.042	0.203	1.438	4.295	-2.617	4.696	-1.062	3.096	-8.217	1.592	
8	1.454	1.132	-0.886	-3.875	0.193	0.598	0.310	2.280	-0.511	-1.999	3.603	0.578	-1.276	9.864	-7.959	
y_{nl} Output	Hidden Layer 1								Bias							
1	-1.470	-1.652	-1.614	2.447	-2.946	-1.894	1.816	3.111	-1.528							

variables and output parameters d_{32} and $d_{32\text{-Large}}$, can be found in Table 41 and Table 42, respectively. The weight factors are given in Table 43 for d_{32} and in Table 44 for $d_{32\text{-Large}}$. The learning rate for the BPNNs was 0.25 and 10000 iterations were used. The AARE, σ , and R^2 of 17, 18 and 90 %, respectively for d_{32} , and 15, 12 and 95%, respectively for $d_{32\text{-Large}}$ were obtained with these networks. Figure 100 shows the comparison between experimental and predicted d_{32} values using the BPNN.

7.2.4 Volumetric Liquid-Side Mass Transfer Coefficient Prediction by BPNN

The BPNN selected for predicting $k_{L,a}$ has the following topology: [13,8-6,1]. The maximum and minimum values of the input variables and the output parameter $k_{L,a}$ can be found in Table 45. The weight factors are given in Table 46. The learning rate for the $k_{L,a}$ BPNN was 0.25 and 10000 iterations were used during the training and learning process. The AARE, σ , and R^2 of 16, 10 and 93 %, respectively, were obtained with this BPNN. Figure 100 shows the comparison between experimental and predicted $k_{L,a}$ values using the BPNN.

7.3 CASE STUDY: MODELING OF THE HYDRODYNAMIC AND MASS TRANSFER PARAMETERS IN FISCHER-TROPSCH SYNTHESIS

From the ranges of the data obtained, the developed models can be used to predict the hydrodynamic and mass transfer parameters in a large-scale slurry bubble column reactor operating under typical industrial conditions. In this study, the models were used to predict the total gas holdup, the holdup of large and small gas bubbles, the total, small and large Sauter-mean bubble diameters, and the volumetric mass transfer coefficient, in a large-scale SBCR

Table 41 Ranges of the input and output parameters of the BPNN for d_{32}

Input node #	1	2	3	4	5	6	7	8	9	10	11	12	13	14	15
	$U_{G,1}$ $m\ s^{-1}$	ρ_L , $kg\ m^{-3}$	$10^3 \times \mu_L$, $Pa\ s$	$10^3 \times \sigma_L$, Nm^{-1}	M_B , $kg.kmol^{-1}$	ρ_G , $kg\ m^{-3}$	M_A , $kg\ kmol^{-1}$	D_C , m	ζ , $\%$	d_p , m	ρ_P , $kg\ m^{-3}$	ϵ_G , $\%$	X_W , $\%$	C_V , $\%$	S_T , $-$
<i>Min</i>	0.00031	633.4	0.16	75	18	0.09	2	0.05	0.015	0	0	1	54.2	0	0
<i>Max</i>	0.36397	1113	44.3	8.4	730	223.77	44	5.5	75	42.37×10^{-6}	4000	62.4	100	36	1
Output node #	1														
	$(II) = \ln(d_{32})$														
<i>Min</i>	-7.59														
<i>Max</i>	-3.24														

Table 42 Ranges of the input and output parameters of the BPNN for $d_{32-Large}$

Input node #	1	2	3	4	5	6	7	8	9	10	11	12	13	14	15
	$U_{G,1}$ $m\ s^{-1}$	ρ_L , $kg\ m^{-3}$	$10^3 \times \mu_L$, $Pa\ s$	$10^3 \times \sigma_L$, Nm^{-1}	M_B , $kg.kmol^{-1}$	ρ_G , $kg\ m^{-3}$	M_A , $kg\ kmol^{-1}$	d_p , m	ρ_P , $kg\ m^{-3}$	ϵ_G , $\%$	d_{32} , m	$\epsilon_{G-Small}$, $\%$	$\epsilon_{G-Large}$, $\%$	X_W , $\%$	C_V , $\%$
<i>Min</i>	0.057	687.6	0.47	16	18	0.139	2	0	0	7.5	5.05×10^{-4}	0	2.0	88	0
<i>Max</i>	0.364	1000	9.2	72.8	567.4	29.1	29	42.37×10^{-6}	3218.3	62.43	0.0336	45.8	46.3	100	36
Output node #	1														
	$(II) = \ln(d_{32-Large})$														
<i>Min</i>	0.002														
<i>Max</i>	0.0591														

Table 43 Weights and biases for the [15,9-7,1] BPNN for d_{32}

w_{Nm}	<i>Input Nodes</i>															
<i>Hidden Layer 1</i>	1	2	3	4	5	6	7	8	9	10	11	12	13	14	15	Bias
1	3.998	7.604	2.385	-2.667	2.195	-1.569	-4.370	4.208	3.576	-1.255	-0.069	1.799	0.581	1.405	-8.841	2.167
2	-2.550	0.749	2.333	2.657	2.816	0.084	2.205	1.084	-0.286	-3.460	0.312	0.033	-2.111	3.377	12.982	-7.321
3	0.544	-5.000	8.170	-8.143	2.184	2.666	3.014	-3.629	-7.043	-3.780	7.724	3.147	-2.323	-8.972	-1.779	-1.135
4	2.281	-0.057	2.104	0.013	-3.901	-0.620	-3.117	6.903	-0.634	4.430	0.842	-5.356	-3.509	12.826	-1.451	-4.726
5	1.506	3.666	-4.440	-4.039	-1.026	-2.204	-0.579	5.316	-1.561	-2.979	-1.915	2.765	0.634	2.945	0.517	-2.505
6	-2.201	5.099	1.991	-1.237	-2.992	2.039	4.235	-3.128	-2.052	1.664	-3.291	3.463	-1.575	7.545	3.465	-3.769
7	2.413	-2.082	11.689	6.565	-0.012	-2.671	1.917	6.762	0.685	2.893	-0.301	2.464	-0.158	1.304	-5.323	-3.552
8	4.347	-0.983	0.744	-7.496	-10.177	-6.815	1.443	4.746	1.310	-0.205	-0.048	-2.561	2.505	0.196	-0.863	-1.436
9	1.220	-3.550	-5.478	-1.872	1.920	1.302	0.163	2.146	3.631	6.261	-3.084	2.218	-1.939	-2.923	-0.337	-0.535
v_{mn}	<i>Hidden Layer 1</i>									Bias						
<i>Hidden layer 2</i>	1	2	3	4	5	6	7	8	9	Bias						
1	-3.038	-0.326	2.485	-2.712	6.727	0.046	-2.627	-2.242	3.983	-3.290						
2	1.438	0.314	1.848	-4.670	-4.092	-0.842	-3.533	0.112	-2.245	0.017						
3	-6.237	1.592	-0.292	2.777	-0.484	-2.541	2.214	-9.922	-2.483	3.060						
4	-3.848	6.430	-3.056	3.445	-4.583	-0.471	-2.584	-0.524	4.523	-2.501						
5	2.686	0.052	0.496	-2.274	0.005	-0.766	1.229	1.397	-4.553	-4.552						
6	-2.801	4.226	-7.588	2.724	-3.414	-9.869	7.094	0.430	-4.609	1.197						
7	-1.130	-6.930	-5.117	-1.589	-0.340	-4.732	2.060	-6.585	6.572	-1.481						
y_{n1}	<i>Hidden Layer 2</i>							Bias								
<i>Output</i>	1	2	3	4	5	6	7	Bias								
1	-2.593	-3.113	-2.626	1.925	-4.526	2.909	-0.694	0.738								

Table 44 Weights and biases for the [15,7-5,1] BPNN for d_{32} -Large

w_{Nm} Hidden Layer 1	Input Nodes															
	1	2	3	4	5	6	7	8	9	10	11	12	13	14	15	Bias
1	-0.632	1.267	-1.522	-1.552	-1.015	0.229	0.356	0.931	-1.008	-0.085	8.598	-0.162	0.089	0.078	-5.308	0.312
2	1.133	0.595	0.240	-1.040	0.950	0.616	-1.404	0.441	-1.260	-1.674	5.044	-22.031	0.014	-0.813	2.816	-1.614
3	2.845	-1.296	1.458	0.357	0.579	-3.082	1.030	2.141	2.111	-1.346	13.299	0.838	8.359	-2.716	-0.311	-1.254
4	0.176	-3.432	0.377	6.100	0.860	-0.187	-0.041	1.586	-1.733	-0.377	5.289	0.650	0.791	0.243	1.499	-3.959
5	0.753	-0.148	1.408	-3.976	-3.890	0.968	-0.734	0.943	-3.148	1.502	-5.088	-0.498	-6.976	0.944	-4.135	4.065
6	-0.858	-0.948	5.203	-3.585	1.050	-1.524	4.107	-0.741	2.213	7.074	-14.702	1.128	3.765	2.045	7.364	-1.455
7	1.332	-0.365	-3.554	9.125	-0.756	0.694	-2.141	-1.918	3.011	-1.973	2.116	-8.478	-1.081	-1.649	2.567	-0.931
v_{mn} Hidden layer 2	Hidden Layer 1															
	1	2	3	4	5	6	7	Bias								
1	-0.757	-16.001	0.279	6.750	-2.706	1.588	7.401	1.092								
2	-3.820	1.797	-0.720	0.980	-4.953	3.920	-0.013	3.447								
3	-2.173	0.735	-13.254	-11.135	7.112	9.333	-2.611	6.634								
4	0.754	-0.752	1.264	3.284	0.251	-0.148	0.609	-4.354								
5	-3.495	-6.761	2.528	-4.502	3.898	-8.765	1.717	7.291								
y_{n1} Output	Hidden Layer 2															
	1	2	3	4	5	Bias										
1	0.234	0.464	-2.817	3.796	3.186	-2.527										

Table 45 Ranges of the input and output parameters of the BPNN for $k_L a$

Input node #	1	2	3	4	5	6	7	8	9	10	11	12	13
	$U_{G,1}$ m s^{-1}	ρ_L , kg m^{-3}	$10^3 \times \mu_L$, Pa s	$10^3 \times \sigma_L$, Nm^{-1}	$10^8 \times D_{AB}$, $\text{m}^2 \text{s}^{-1}$	ρ_G , kg m^{-3}	D_C , m	d_p , m	ρ_P , kg m^{-3}	ε_G , $\%$	d_{32} , m	X_W , $\%$	C_V , $\%$
<i>Min</i>	0.0017	680	0.31	16.2	0.0013	0.083	0.0508	0	0	0.8	0.0006	56.2	0
<i>Max</i>	0.4	1583	101.4	75	2.78	46	7.62	0.0003	4000	62.4	0.0336	100	36
Output node #	1												
	$(II) = \text{Ln}(k_L a)$												
<i>Min</i>	-6.908												
<i>Max</i>	0.465												

Table 46 Weights and biases for the [13,8-6,1] BPNN for $k_L a$

w_{Nm} Hidden Layer 1	Input nodes													
	1	2	3	4	5	6	7	8	9	10	11	12	13	Bias
1	-0.656	0.829	3.235	-4.440	-10.506	-0.924	-0.335	-10.772	-0.489	5.482	4.851	-4.641	1.089	2.347
2	-0.737	1.832	-17.814	-9.593	-11.598	-1.543	-3.898	4.372	-0.024	-0.793	-0.125	0.868	1.098	2.832
3	-1.046	-0.478	2.095	3.261	-24.007	-1.759	3.838	2.508	2.099	5.131	2.138	1.298	0.434	-5.312
4	3.530	-0.528	-4.336	-4.833	-3.391	2.963	5.425	-7.047	4.206	-6.124	-1.931	-0.809	3.999	4.330
5	-0.155	12.813	13.824	-1.067	3.937	-1.464	-7.809	0.705	3.470	-1.005	-9.263	-9.205	-0.787	9.524
6	-0.377	-1.895	-0.229	0.369	-0.266	0.211	-2.184	-4.491	1.015	-4.184	-0.853	6.149	0.173	-4.909
7	-4.661	-4.473	9.929	-2.940	-5.147	-3.023	15.544	3.419	-0.012	-1.905	-8.209	1.576	16.529	4.062
8	-0.810	5.350	-3.040	0.342	1.707	-1.260	-2.722	-0.578	3.097	1.722	-4.094	4.333	-1.035	-4.073
v_{mn} Hidden layer 2	Hidden Layer 1													
	1	2	3	4	5	6	7	8	Bias					
1	0.341	-3.681	-2.937	-6.359	2.008	-5.402	3.258	6.425	-3.861					
2	-8.134	-4.288	-1.085	3.023	-3.200	12.339	-3.586	-5.254	1.121					
3	0.013	-8.980	3.255	-2.802	-3.519	0.698	-1.604	3.617	-1.001					
4	11.526	-13.663	-8.489	13.993	4.829	0.323	7.365	3.306	-16.203					
5	4.221	-4.544	-12.717	-7.995	-7.810	3.003	0.266	3.265	4.707					
6	-1.276	-0.695	5.845	-8.476	8.079	5.406	3.883	-7.067	-1.312					
y_{n1} Output	Hidden Layer 2													
	1	2	3	4	5	6	Bias							
1	1.728	-1.357	2.680	1.251	1.627	-2.596	0.355							

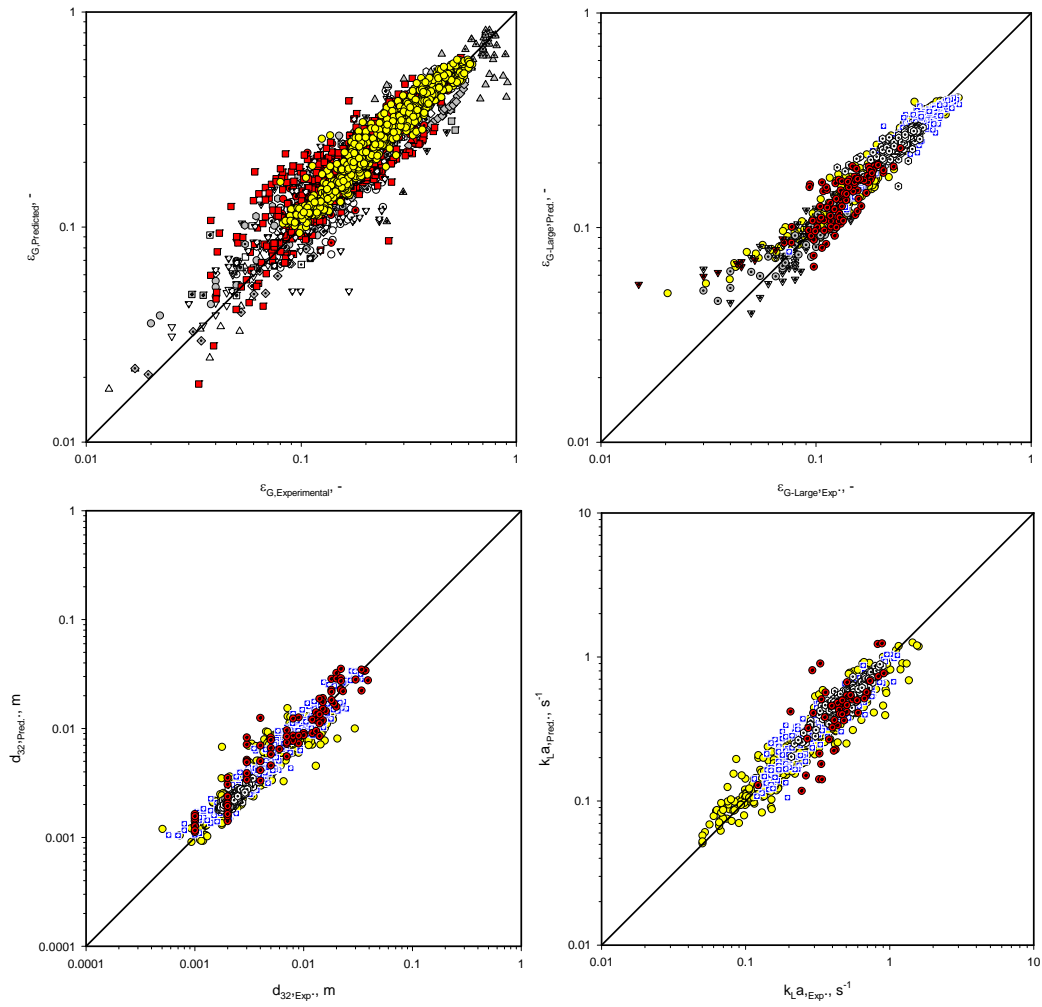


Figure 100 Comparison Between Experimental and Predicted ϵ_G , ϵ_G -Large, d_{32} , and $k_L a$

Values Using BPNN Models

(Symbols are given in Tables 29 and 30)

operating under typical Low-Temperature Fischer-Tropsch (LTFT) conditions. This is because of the importance of the Fischer-Tropsch (F-T) slurry technology expressed in terms of the numerous worldwide activities as summarized in Appendix A. It should be emphasized that industrial SBCRs are operated in the churn-turbulent flow regime which is characterized by strong gas-liquid-solid interactions and wide range of gas bubble sizes. The reactors are also preferred to operate with high catalyst loading in order to increase their productivity⁽²⁴⁰⁾, however, such a high catalyst loading is found to affect the reactor performance^(204,241). As shown in Sections 6.2 and 6.3, the gas bubbles in SBCRs are classified based on their behavior and/or size into small and large gas bubbles. Thus, the knowledge of the holdups of small and large gas bubbles is of prime importance in the design, modeling and scaleup of F-T SBCR. Since the BPNN models predicted the experimental data with much greater accuracy than the empirical correlations, the developed BPNN models were employed to predict the effects of operating conditions (pressure, temperature, superficial gas velocity, H₂/CO ratio, solid concentration), and reactor diameter as well as sparger/reactor open area on the hydrodynamic and mass transfer parameters. The conditions used in the simulation which correspond to low-temperature F-T synthesis are listed in Table 47.

7.3.1 Effect of P, T, and C_w on the Hydrodynamic and Mass Transfer Parameters

Figure 101 illustrates the effect of pressure (P) and temperature (T) on ϵ_G , d_{32} and $k_L a$ of H₂ and CO predicted with the BPNN in a 5-m ID SBCR provided with a multi-orifice distributor ($N_O = 1000$, $d_O = 0.05\text{m}$, and $\zeta = 10\%$) and operating under different temperatures with syngas (H₂/CO = 2:1), wax and 35 wt.% cobalt alumina-supported catalyst at 0.20 m/s superficial gas velocity.

Figure 101 shows that increasing pressure increases the total syngas holdup by about 19 - 21% over the temperature range used, which is in agreement with findings on the effect of pressure on the gas holdup at high temperature in this study and those reported in the literature ⁽⁴³⁾.

Table 47 Conditions Selected for the modeling of the hydrodynamics and mass transfer parameters in Low-Temperature Fischer-Tropsch (LTFT) Synthesis using SBCRs

<i>Operating Conditions</i>	
Pressure, bar	20 - 50
Temperature, K	443 - 563
Superficial gas velocity, m/s	0.1 - 0.4
Solid concentration, wt. %	10 - 50
<i>Gas/Liquid Solid system</i>	
Gas	
H ₂	M _A = 2.02 kg/kmol
CO	M _A = 28.01 kg/kmol
H ₂ /CO ratio	1 (Iron Oxide) 2 (Cobalt)
Liquid	
Wax (<i>n</i> -C ₁₇ -C ₇₉)	M _B = 567.4 kg/kmol
– Density	ρ _L (493K) = 706 kg/m ³ ρ _L (513K) = 696 kg/m ³
– Viscosity	μ _L (493K) = 4.41x10 ⁻³ Pa s μ _L (513K) = 4.04x10 ⁻³ Pa s
– Surface Tension	σ _L (493K) = 1.8x10 ⁻² N/m σ _L (513K) = 1.7x10 ⁻² N/m
– Composition	X _W = 100 %
Solid	
Alumina Powder	Support for cobalt catalyst
– Density	ρ _P = 3218.3 kg/m ³
– Particle size	d _P = 42x10 ⁻⁶ m
Iron Oxide	Catalyst
– Density	ρ _P = 4000 kg/m ³
– Particle size	d _P = 40 x10 ⁻⁶ m
<i>Reactor Geometry</i>	
Column diameter	0.1 – 5 m
Height/Diameter	4 - 20
Sparger type	M-ON (d _O = 0.01- 0.05 m)
Column open area, ζ	0.5 - 10%

This increase of the total syngas holdup with pressure at 35 wt% cobalt alumina-supported catalysts in wax can be mainly attributed to the increase of the small gas bubbles holdup, since $\epsilon_{G\text{-Large}}$ seems to be unaffected by pressure as can be seen in Figure 102, which is in line with the findings by Jordan et al.⁽²⁰⁰⁾. Therefore, the increase of the gas density or gas momentum at constant gas velocity is responsible for shrinking the gas bubbles leading to an increase of the small gas bubbles population. Consequently, it can be seen in Figure 101 that the d_{32} values of the syngas increase by about 3.5 - 7.1%, and therefore the $k_L a$ values for H₂ and CO increase with pressure over the entire range of temperature studied due to an increase of the gas-liquid interfacial area.

Figure 101 also shows that increasing temperature decreases the total syngas holdup by about 24-25% over the pressure range used. The effect of temperature on ϵ_G can be attributed to a change of the physical properties and the foaming characteristics of the liquid phase. When surface tension and viscosity decrease with temperature, smaller gas bubbles are formed and hence $\epsilon_{G\text{-Small}}$ increases⁽⁶¹⁾. The reduction of the stability of the froth with temperature, however, is responsible for the reduction of $\epsilon_{G\text{-Small}}$, resulting in smaller total gas holdup, as shown in Section 6.2.3. Thus, the decrease of the total syngas holdup with increasing temperature in wax containing 35 wt% cobalt alumina-supported catalysts in Figure 101 can mainly be related to the fact that the decrease of the surface tension and viscosity is less significant than that of the reduction of the froth stability of wax, resulting in a reduction of $\epsilon_{G\text{-Small}}$, since $\epsilon_{G\text{-Large}}$ seems to be almost independent of temperature as can be seen in Figure 102.

It should be noted that the $k_L a$ values of H₂ appears to be higher than those of CO. Since the gas holdup and Sauter-mean bubble diameters are determined by the mixture density, the

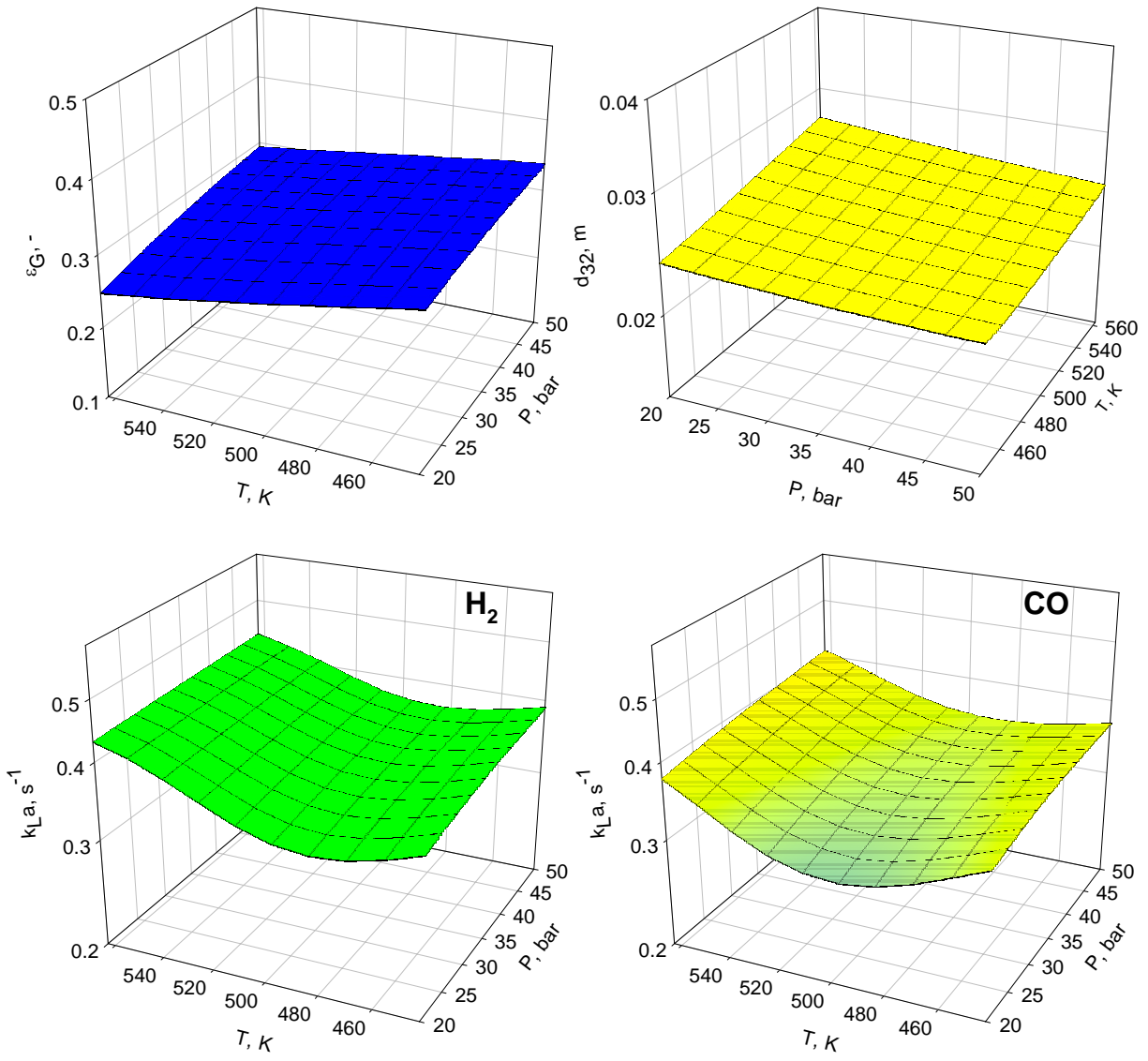


Figure 101 Effect of P and T on Predicted ϵ_G , d_{32} and k_{La} of Syngas in Wax/Alumina Using

BPNNs

$H_2/CO = 2$, 0.20 m/s, 35 wt.%, 5 m ID, M-ON, $d_o=0.05m$, $N_o=1000$ ($\zeta=10\%$)

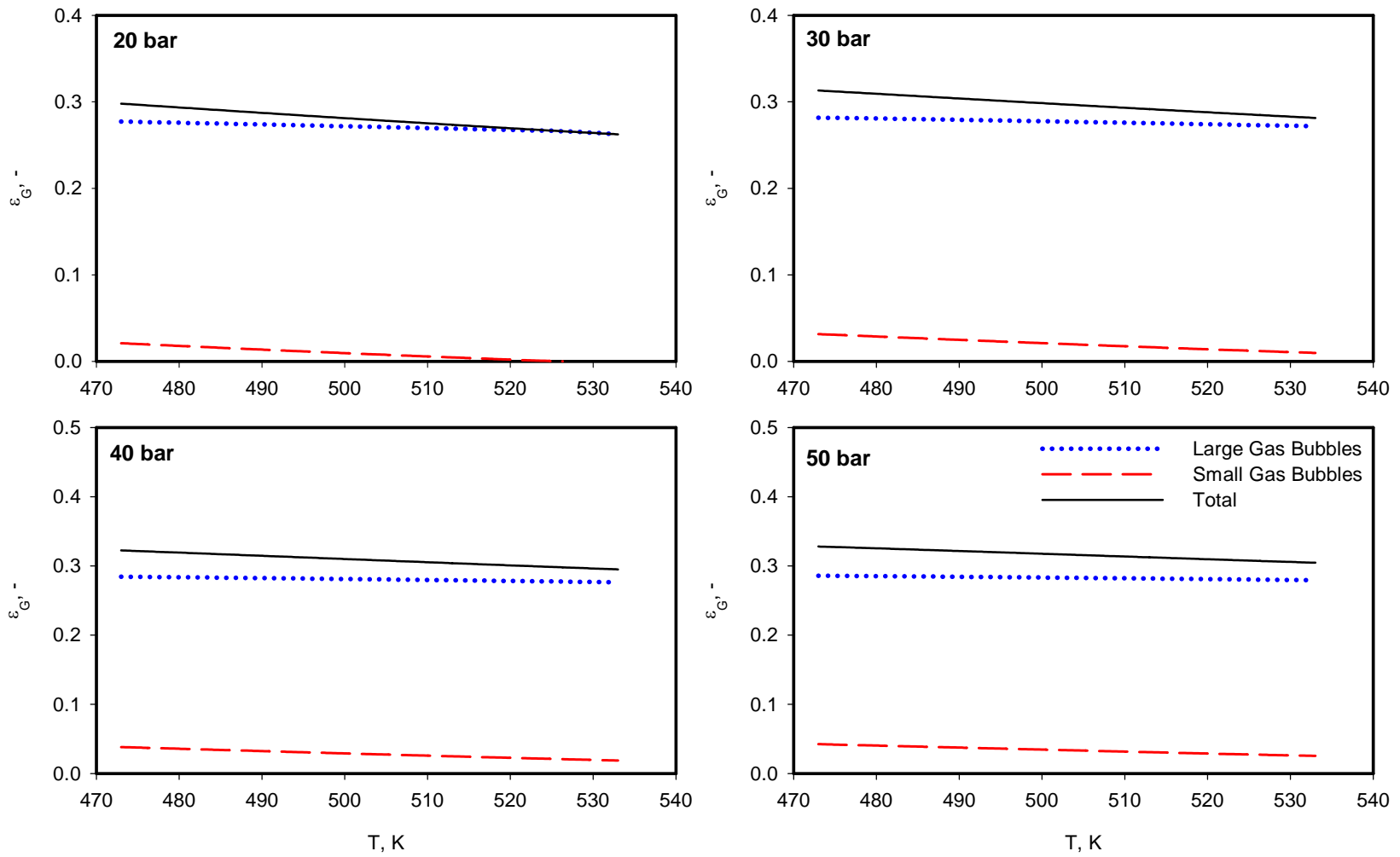


Figure 102 Effect of P and T on ϵ_G , $\epsilon_{G\text{-Small}}$ and $\epsilon_{G\text{-Large}}$ of the Syngas in wax/Alumina

$H_2/CO = 2$, 0.20 m/s, 35 wt.%, 5 m ID, M-ON, $d_o=0.05\text{m}$, $N_o=1000$ ($\zeta=10\%$)

gas-liquid interfacial area for both H₂ and CO in the mixture would be the same, and consequently larger than that obtainable with pure H₂ gas only. Thus, with similar gas-liquid interfacial area, the only variable affecting the k_La of H₂ and CO would be the mass transfer coefficient, k_L, or gas diffusivity. The k_La values of H₂ are therefore expected to be higher than those of CO since H₂ has a higher diffusivity than CO.

Figure 103 shows the effects of temperature and catalyst loading (C_w) on ε_G, d₃₂ and k_La predicted in a 5-m ID SBCR provided with a multi-orifice distributor (N_O = 1000, d_O = 0.05m, and ζ = 10%) and operating with syngas (H₂/CO = 2:1) and wax/cobalt catalyst slurry at 30 bar and 0.20 m/s superficial gas velocity. As can be seen in this figure the syngas holdup increases with temperature in the absence of catalyst which can be again related to the decrease of the wax surface tension and viscosity, resulting in the formation of small bubbles⁽⁶¹⁾. When the catalyst concentration is increased from 0 to 50 wt%, however, the total syngas holdup is decreased by 38 and 45% at 443 and 553 K, respectively. This decrease of the total gas holdup with increasing catalyst loading can be attributed to the increase of slurry viscosity and decrease of the froth stability, which led to gas bubbles coalescence and to the decrease of the small gas bubbles holdup (ε_{G-Small}) as can be clearly observed in Figure 104. This behavior is in agreement with a number of literature findings^(6,8,77,126).

Similarly in Figure 103 it can be seen that d₃₂ of syngas increase by more than 200% from 0 to 50 wt.%, indicating a strong coalescence tendency of syngas bubbles in wax/alumina-supported cobalt catalyst slurry. Consequently, the combined effect of the catalyst loading on the gas holdup and the Sauter-mean bubble diameter of the syngas, yield an increase of the k_La

values. The increase of k_{La} from 0 to 50 wt.% was about 23 – 48 % over the entire range of temperature studied.

Figure 104 also shows that the holdup of large gas bubbles ($\epsilon_{G-Large}$) remains unaffected with increasing catalyst concentration from 0 to ~ 30 wt.%; and at catalyst concentrations > 30 wt.%, the $\epsilon_{G-Small}$ starts approaching zero, and consequently the gas-liquid interfacial area will drive the process into a mass transfer-controlled regime. This predicted gas holdup behavior agrees well with the findings by Inga and Morsi⁽²⁰⁴⁾, who reported that the F-T synthesis with iron catalyst would move from a kinetically-controlled to a mass transfer-controlled regime at concentration range of 37-40 wt.%.

7.3.2 Effect of U_G and D_C on the Hydrodynamic and Mass Transfer Parameters

Figure 105 illustrates ϵ_G , d_{32} and k_{La} values predicted with the BPNN for syngas ($H_2/CO = 2:1$) in wax containing 50 wt.% of alumina-supported cobalt catalyst at 30 bar and 513 K; and as can be seen ϵ_G increases with the superficial gas velocity for all reactor diameters used. The total gas holdup appears to increase linearly until U_G values of 0.05-0.07 m/s, and then at velocities greater than these values, it becomes smaller. These values of U_G (0.05-0.07m/s) appear to be close to the transition velocity values of 0.045-0.103 as reported by Sarrafi et al.⁽¹⁵⁾. For two different reactor diameters of 1.15 and 5.0 m operating with 50 wt.% alumina-supported catalyst in wax, it seems that increasing U_G from 0.01 to about 0.1 m/s, increases ϵ_G by more than 225 and 390% respectively, whereas increasing U_G from 0.20 to 0.40 m/s increases ϵ_G by 33 and 44% in the 1.15 and 5 m ID reactor, respectively. This means that increasing U_G above about 0.25 m/s

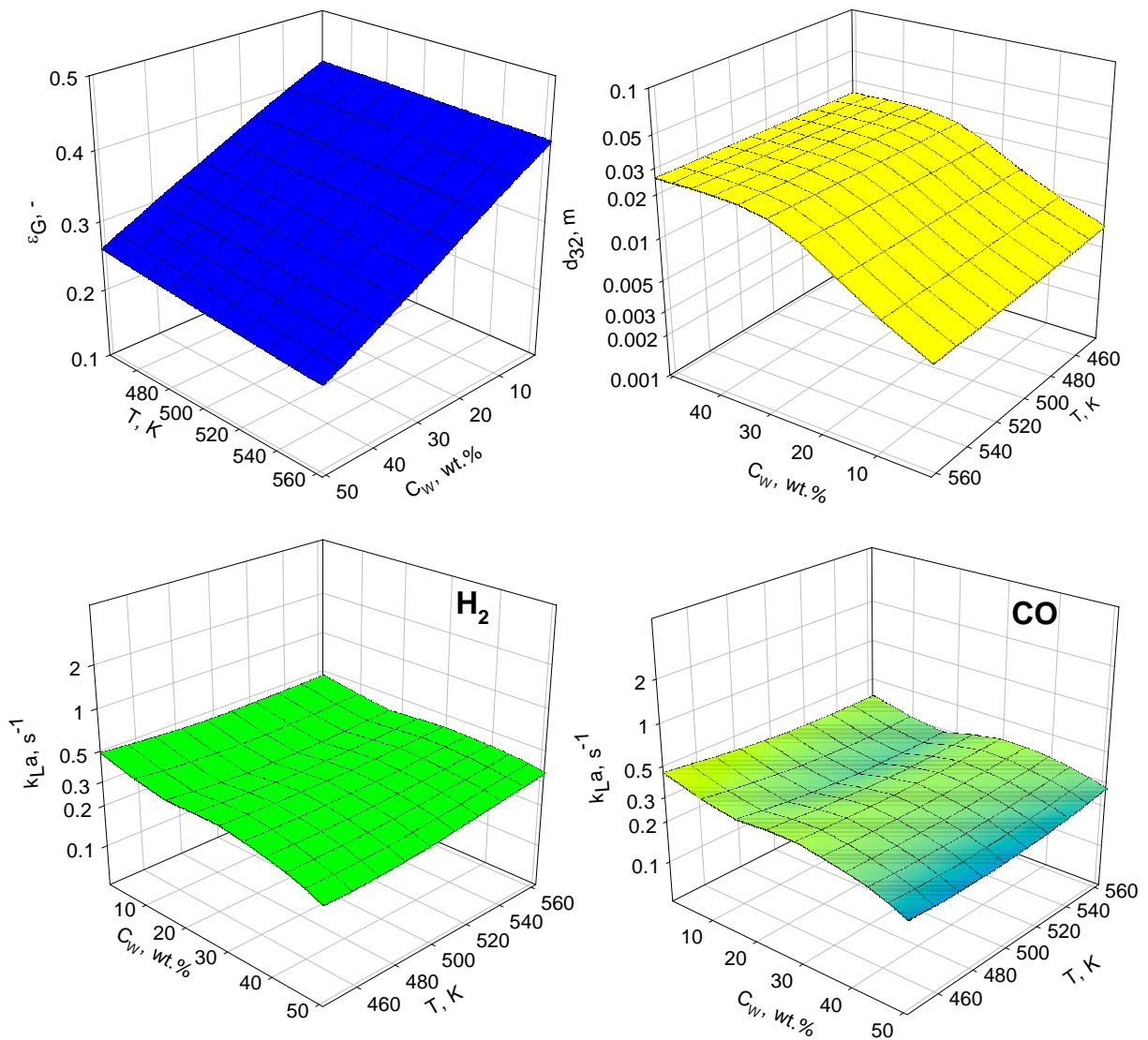


Figure 103 Effect of T and C_w on Predicted ϵ_G , d_{32} and k_{La} of Syngas in Wax/Alumina

Using BPNNs

H₂/CO = 2, 30 bar, 0.20 m/s, 5 m ID, M-ON, d_o=0.05m, N_o=1000 (ζ =10%)

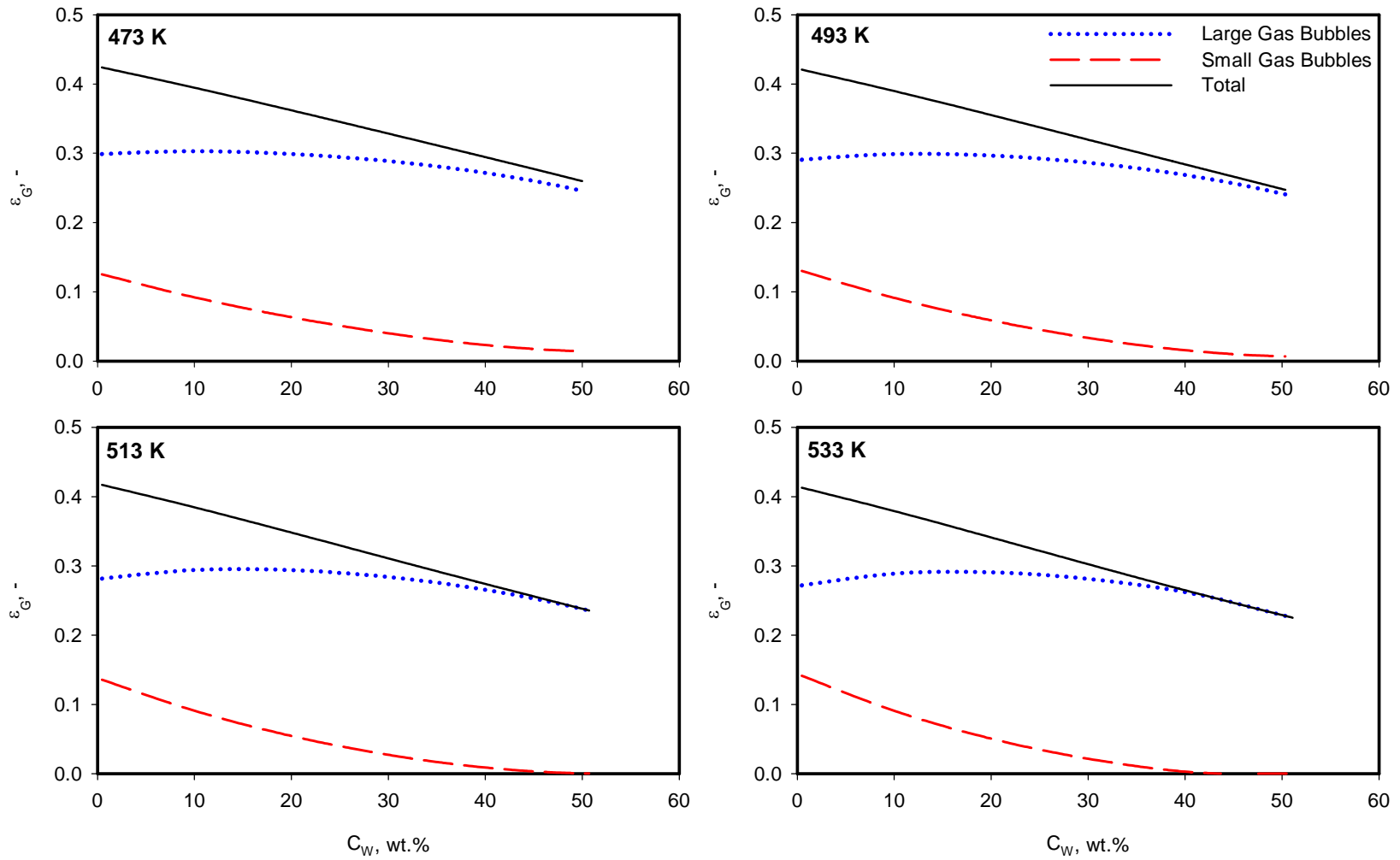


Figure 104 Effect of T and C_w on ϵ_G , $\epsilon_{G\text{-Small}}$ and $\epsilon_{G\text{-Large}}$ of the Syngas in wax/Alumina

$H_2/CO = 2$, 30 bar, 0.20 m/s, 5 m ID, M-ON, $d_o=0.05\text{m}$, $N_o=1000$ ($\zeta=10\%$)

does not significantly increase the total gas holdup. Also, increasing U_G was reported to decrease the syngas conversion ⁽⁶⁾. Similarly, the increase of $k_L a$ with U_G in the 5m ID column, from 0.20 to 0.40 m/s was about 30%, compared to a 400% increase from 0.01 to 0.1 m/s. Thus, there is no incentive to operate SBCRs at very high superficial gas velocity, since the relatively low increase of ϵ_G and the decrease of syngas conversion will not balance the cost of the power requirements associated with feeding the syngas at high U_G . Therefore, a U_G value between 0.1 and 0.25 m/s would be adequate for catalyst suspension, fluids dispersion, and syngas conversion in SBCRs.

Figure 105 also shows the effect of column diameter (D_C) on ϵ_G , d_{32} and $k_L a$ values of syngas ($H_2/CO = 2:1$) in wax containing 50 wt.% of alumina-supported cobalt catalyst; and as can be seen the ϵ_G values appear to first decrease and then level off after a D_C of about 0.7 m. Furthermore, the d_{32} values of syngas in Figure 105 appear to increase and then level off at the same D_C of 0.7. This predicted D_C value at which the total gas holdup becomes independent are greater than 0.15 m which was suggested by a number of investigators ^(23,61,101). Vandu and Krishna ⁽²³¹⁾ reported that at superficial gas velocity of 0.1 m/s, the gas holdup of air in water decreased by about 41% when D_C was increased from 0.1 to 0.63 m ID. Thus, these BPNN predictions clearly shows the important impact of reactor diameter on the total gas holdup and accordingly gas holdup data obtained in small diameter reactors would not be adequate for modeling large-scale (< 0.7 m ID) SBCRs. In general, the decrease of the total gas bubbles holdup in SBCRs operating in the churn-turbulent flow regime as shown in Figure 105 can be related to the decrease of the large gas bubbles holdup ⁽⁸⁾, a reduction in foaming characteristics ⁽⁶⁵⁾ and a change in the liquid backmixing ⁽³⁵⁾. Thus, increasing the SBCR diameter appears to reduce the probability of the gas bubbles coalescence, leading to fewer large gas bubbles being

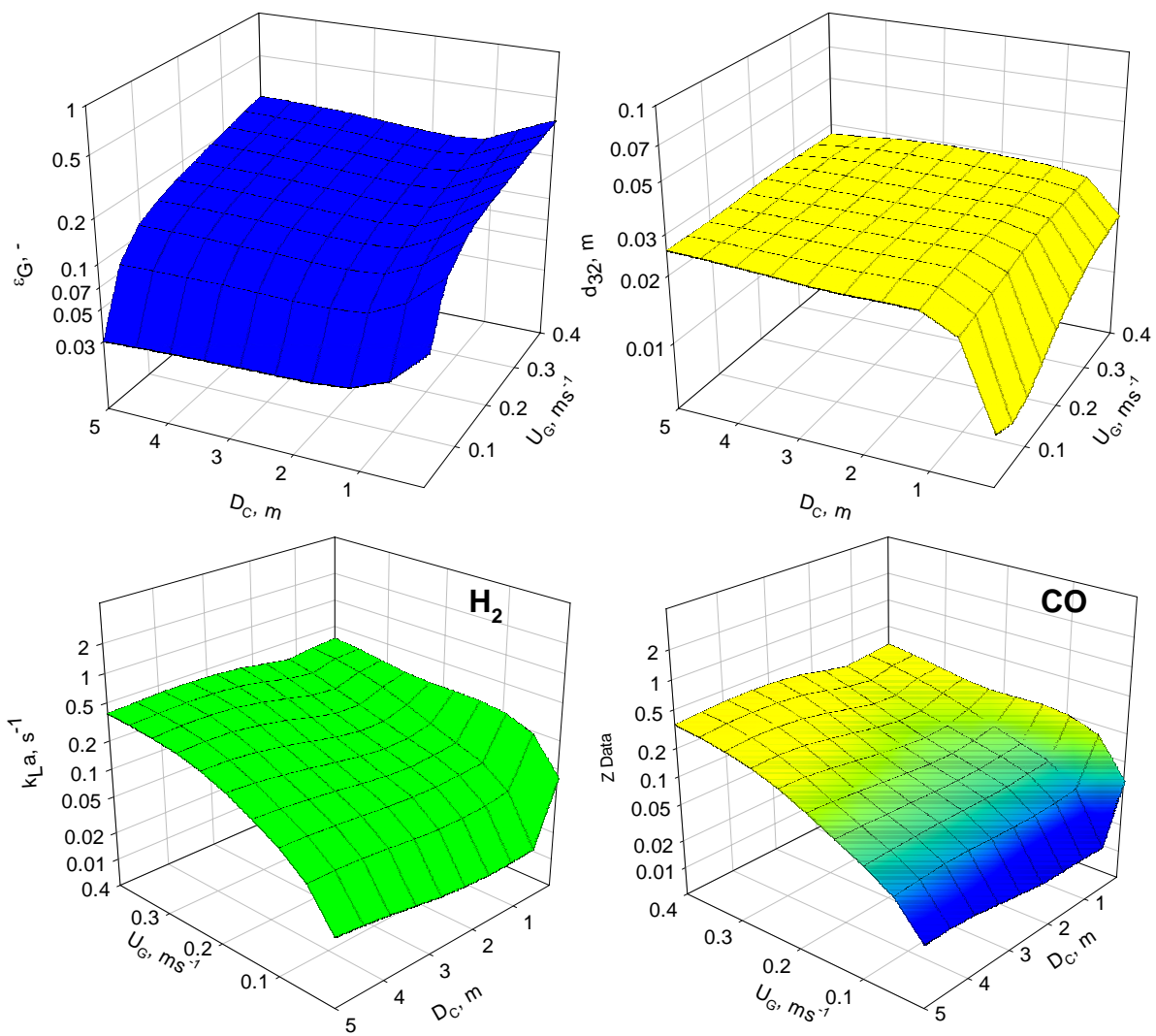


Figure 105 Effect of U_G and D_C on ϵ_G , d_{32} and k_{La} of the Syngas in Wax/Alumina

$H_2/CO = 2$, 30 bar, 513 K, 50 wt.%, M-ON, $d_0=0.05m$, $N_0=300$ ($\zeta=3\%$)

formed. This would affect the total gas holdup and the recirculation pattern in the slurry in which the smaller gas bubbles are entrained. Furthermore, the combined effect of ε_G and d_{32} results in a decrease of $k_L a$ values of the syngas with D_C until 0.7 m ID and then $k_L a$ seems to level off as well. It should be noted, however, that the decrease of ε_G and $k_L a$ values (and the decrease of d_{32}) of the syngas was more noticeable at lower superficial gas velocity than higher, which also coincides with the findings in the literature ⁽²³¹⁾. This is due to the fact that at higher superficial gas velocity, the reactor operates in a fully developed hydrodynamic regime.

7.3.3 Comparison between Coal-to-Liquid (CTL) and Gas-to-Liquid (GTL) Processes

In the F-T synthesis, the syngas is either derived from coal or natural gas which is then catalytically converted to liquid hydrocarbons. The conversion of the syngas from coal, referred to as Coal-to-Liquid (CTL) uses iron oxides catalyst, whereas the conversion of syngas from natural gas, known as Gas-to-Liquid (GTL) often employs a cobalt-based catalyst ^(242,243). The syngas in the CTL process has a H_2/CO of about 1:1 due to the Water-Gas-Shift (WGS) reaction between CO and H_2O , which produces H_2 ⁽²⁴⁴⁾, whereas that in the GTL process has H_2/CO of about 2:1 due to the absence of the WGS reaction ⁽²⁴⁵⁾. Figure 106 presents the total syngas holdup for H_2/CO ratios of 1:1 and 2:1 in wax using a 5 m ID SBCR operating at 30 bar and 513 K with iron oxide and alumina-supported cobalt catalysts at 50 wt.%. Under these conditions, the densities of the syngas with H_2/CO of 2:1 and 1:1 are about 7.5 and 10.6 kg/m³, respectively, and the densities of the slurry with cobalt-based and iron catalyst and iron are 1144 and 1186 kg/m³. As can be seen in this figure the total gas holdup values of the H_2/CO ratio of 2:1 and cobalt-based catalyst are systematically lower than those obtained with H_2/CO ratio of 1:1 and

iron oxides catalyst. Actually, the syngas holdup values in wax/cobalt slurry are about 19 % lower than those predicted in wax/iron slurry at 50 wt%. This behavior can be attributed to the greater density and momentum of the syngas with iron catalyst when compared with those of the H₂-rich syngas with cobalt catalyst. As can be seen, the d_{32} values of the H₂/CO of 2:1 are also slightly higher than those in Iron oxide system. Similarly, the $k_L a$ values obtained in the alumina-supported cobalt catalyst are lower. In fact, at 0.20 m/s, increasing the syngas ratio from 1:1 to 2:1 (changing from CTL to GTL), decreases the $k_L a$ values by about 17%.

Figure 106 shows that in a 5 m ID column SBCR operating under typical LTFT conditions (30 bar, 513 K, and 0.2m/s) the total syngas holdup, Sauter-mean syngas bubble diameter and $k_L a$ of H₂ and CO were 16%, 0.026 m, 0.252 and 0.183 s⁻¹, respectively for wax/alumina-supported cobalt catalyst, and 23%, 0.026m, 0.290 and 0.255 s⁻¹, respectively for wax/Iron oxide catalyst.

7.3.4 Effect of the Number of Orifices in the Gas Sparger on ϵ_G

The open areas (ζ) of different multiple-orifice nozzle (M-ON) gas spargers used by numerous investigators ^(42,86,101,217,219) were reported to be < 10%. In this study, the effect of open area as defined by Equation (7-3) was represented by varying the number of the orifices (N_O), and to insure an axial mixing, the orifice diameter (d_o) was calculated while maintaining a Weber number, defined in Equation (2-13), for gas flow through the orifice greater than or equal 2. Figure 107 shows the effects of number of orifices (N_O) in a multiple-orifice nozzle gas sparger ($d_o = 0.05$ m) on the total syngas holdup in wax containing cobalt alumina-supported catalyst at different loadings in a SBCR (5 m ID) operating under the following conditions: 30 bar, 513 K,

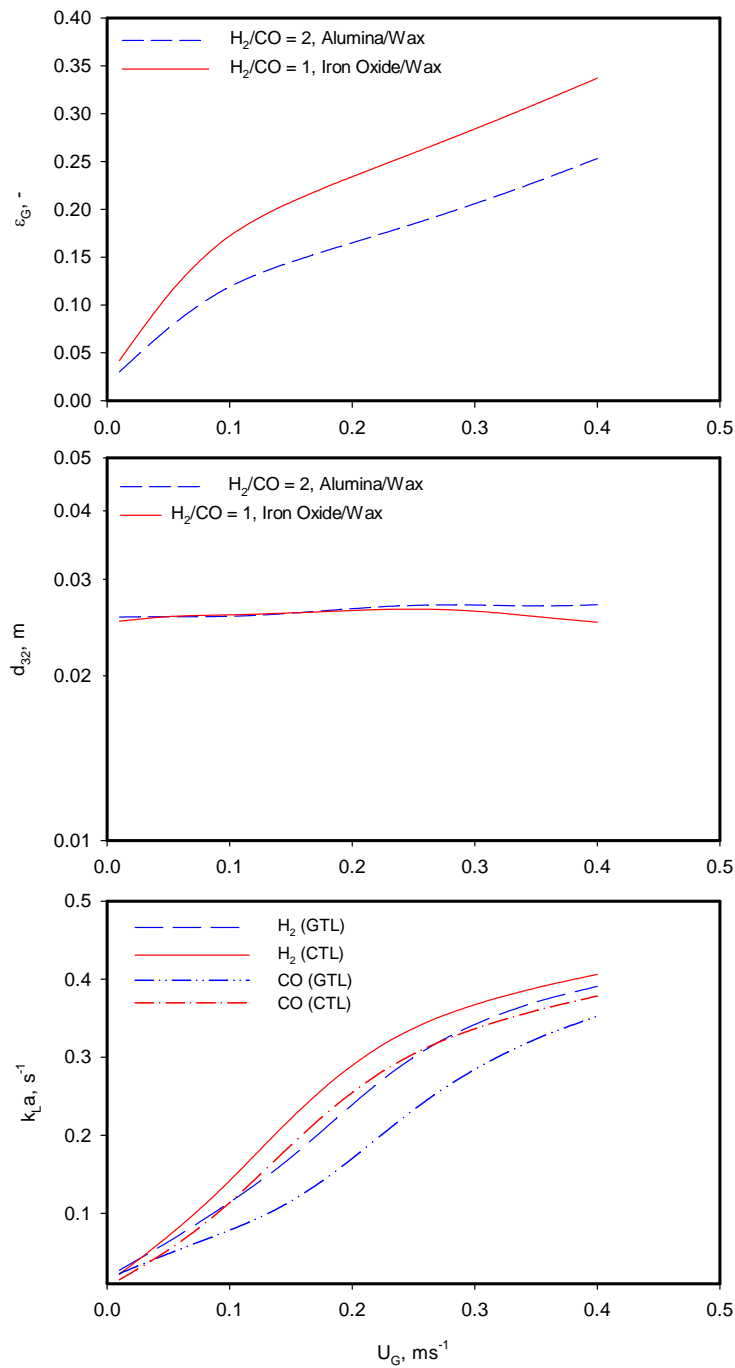


Figure 106 Effect of H_2/CO Ratio on ϵ_G , d_{32} and k_{La} of the Syngas in Wax/Alumina and Wax/Iron Oxide

30 bar, 513 K, 50 wt.%, M-ON, $d_o=0.05\text{m}$, $N_o=300$ ($\zeta=3\%$)

0.2 m/s, and $H_2/CO = 2:1$. As can be seen in this figure, ϵ_G increases with increasing the number of orifices, which can be related to the increase of the holdup of small gas bubbles in the reactor at constant superficial gas velocity ($U_G = 0.2$ m/s). This is because increasing the number of the orifices at constant U_G decreases the gas velocity generated at the orifice ($U_{G,O}$) and at a constant d_O , the average bubbles size at the orifice is expected to decrease as reported by a number of investigators^(31,107,112,246). Thus, decreasing the average bubbles size generated at the orifice under such conditions resulted in the increase of the holdup of small gas bubbles, which led to the increase of the total syngas holdup as mentioned earlier.

Figure 107 also shows that increasing N_O from 200 to 1000 orifices increases the total syngas holdup by about 61% at catalyst loadings less than 5 wt%, and by only 14% at high catalyst loading of 58 wt%. This behavior can be attributed to the increase of slurry viscosity with catalyst loading which led to the coalescence of several small gas bubbles and the decrease of their holdup, resulting in the modest decrease of the total syngas holdup. Thus, it can be concluded that increasing the number of orifices mostly affects the behavior of small bubbles which were reported to re-circulate with the slurry^(6,126).

7.3.5 Effect of the Gas Sparger Type on ϵ_G

Equation (7-1) was used to predict the effect of gas distributor-type on the total gas holdup in SBCR, operating under typical Fisher-Tropsch conditions. Two different gas distributors, a multiple-orifice nozzle and a spider-type gas distributor were used. Since the diameter (d_O) and the number (N_O) of orifices affect the total gas holdup, the diameter of the orifice was fixed at a

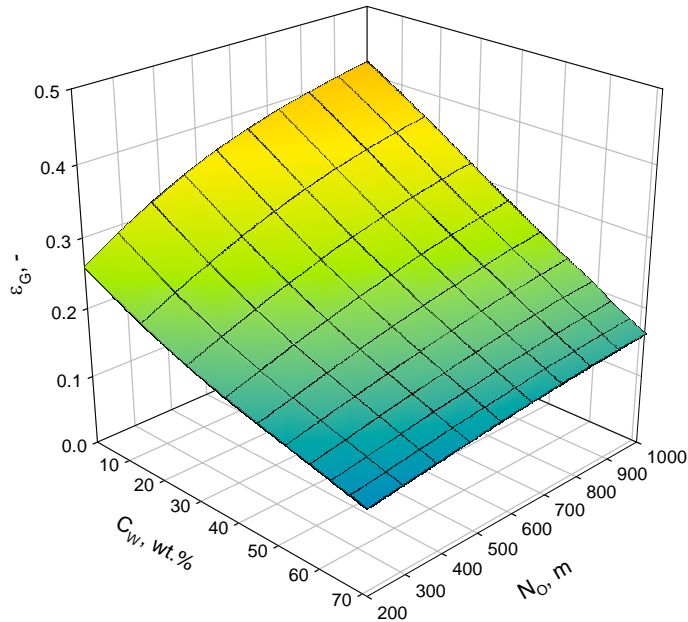


Figure 107 Effect of N_O and C_W on ϵ_G of Syngas in wax/Alumina

$H_2/CO = 2:1$, 30 bar, 513 K, 0.2 m/s, 5 m ID, M-ON, $d_o = 0.05$ m

given value, whereas the number of orifices was calculated based on the orifice Weber number for gas in Equation (2-13). Under the conditions studied, an arbitrary $We_G = 10$ at the minimum superficial gas velocity used was assumed to calculate the number of orifices (N_O) from Equation (7-11):

$$N_o = \sqrt{\frac{\rho_G U_{G,\min}^2 D_C^4}{10 d_o^3 \sigma_L}} \quad (7-11)$$

Figure 108 illustrates that for the multiple-orifice nozzle and the spider-type gas distributor the ϵ_G decreases with increasing orifice diameter. For instance ϵ_G appears to decrease by 4.3% and 6.7 % and by 5.3 and 8.2 % for the multiple-orifice nozzle and spider-type distributor with increasing the orifice diameter from 0.01 to 0.02 and from 0.01 to 0.03 m,

respectively. Although these increases seem insignificant, the trend indicates that large gas bubbles are formed with the larger orifice diameter and consequently lower total gas holdup was predicted.

Figure 108 also shows that the total gas holdup obtained with the spider-type distributor is consistently greater than that with a multiple-orifice nozzle which can be attributed to the more even gas distribution achieved with the spider-type sparger. This difference between the gas holdups by the two distributors, however, is about 5.5% and 3.8 % for 0.01 and 0.03 m orifice diameter, respectively which is small.

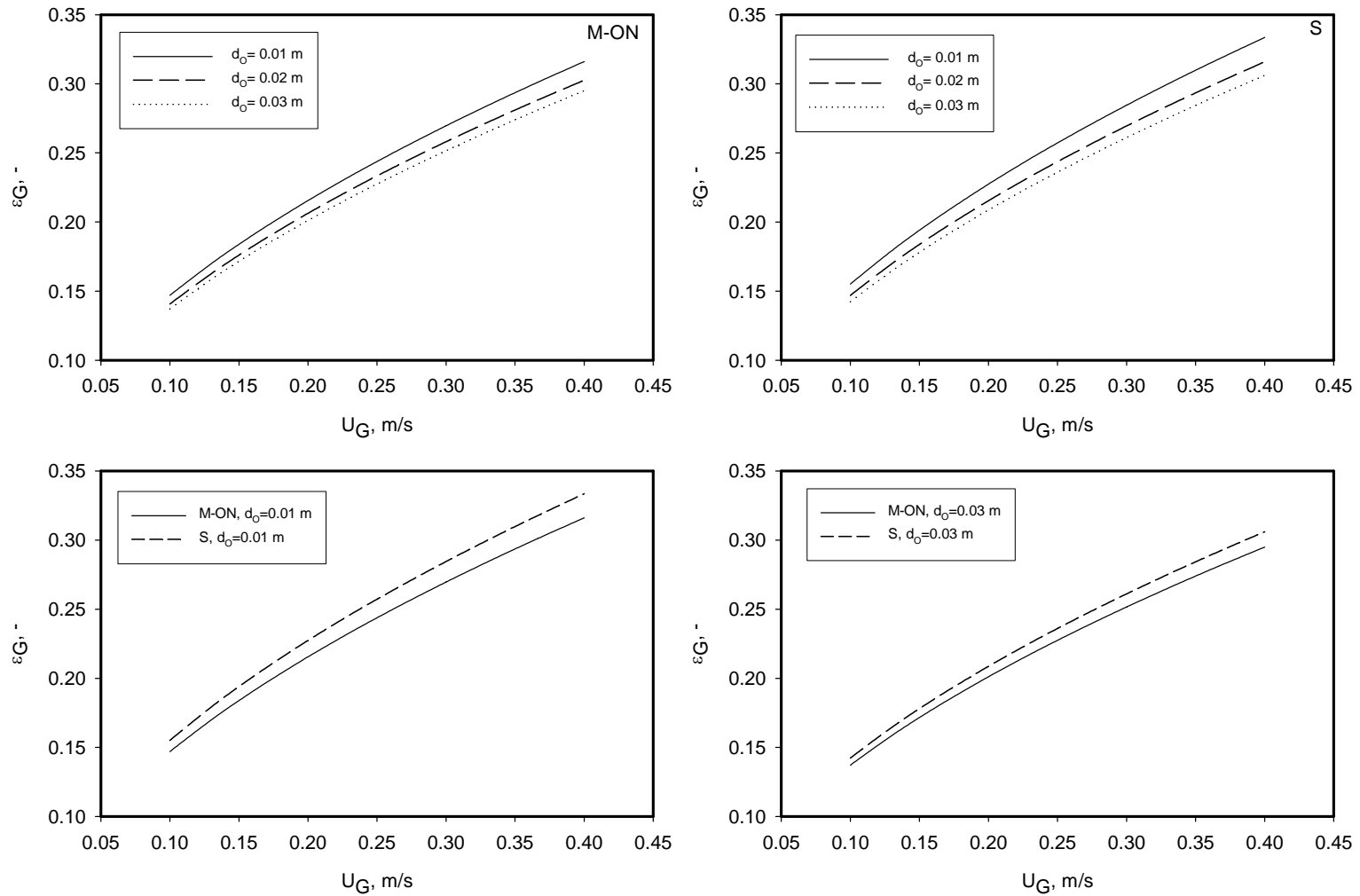


Figure 108 Effect of Gas Sparger on the Total Gas Holdup of Syngas in Wax using Equation (7-1)

$H_2/CO = 2:1$, 30 bar, 513 K, 30 vol.%, 5 m ID

8.0 CONCLUSIONS

This study led to the following conclusions:

1. The equilibrium solubilities of H₂, He, CO, N₂, and CH₄ were determined in a 4-liter agitated reactor, and it was found that C* values followed Henry's Law.
2. In the Cold and hot SBCRs, the Central Composite Statistical Design approach was successfully employed to determine the effect of operating variables, gas and solid nature on the hydrodynamics and mass transfer parameters.
3. The study of the hydrodynamic led to the following conclusions:
 - a. ϵ_G increased with pressure, superficial gas velocity, and gas molecular weight; and decreased with increasing solid concentration;
 - b. ϵ_G increased with temperature at solid concentrations, $C_V < 15$ vol.% and above that it decreased with temperature;
 - c. ϵ_G was higher in the glass beads/Isopar-M slurry than in the alumina/Isopar-M slurry;
 - d. ϵ_G of N₂/Isopar-M/glass beads compared well with the comparable liquid/solid system in the literature;
 - e. d_{32} decreased with pressure, slightly increased with superficial gas velocity, and significantly increased with solid concentration;
 - f. d_{32} decreased with temperature at solid concentrations < 15 vol.% and above that it increased with temperature;

- g. d_{32} of the He, CH₄, N₂ and CO decreased with increasing the gas molecular weight. The d_{32} values of H₂, however, were smaller than those of He; and
 - h. d_{32} values were smaller in the glass beads/Isopar-M slurry than in the alumina/Isopar-M slurry.
4. Using the Dynamic Gas Disengagement technique, the gas holdup and bubble sizes were split into the small and large gas bubbles, and the following conclusions could be derived:
- a. $\epsilon_{G\text{-Small}}$ increased with pressure and temperature and decreased with solid concentration; and at $C_V > 15$ vol.% $\epsilon_{G\text{-Small}}$ completely disappeared;
 - b. $\epsilon_{G\text{-Large}}$ was independent of pressure, temperature and solid concentrations < 15 vol.%; but decreased at $C_V > 15$ vol.%;
 - c. $d_{32\text{-Small}}$ decreased with solid concentration; and at $C_V > 15$ vol.% it completely disappeared;
 - d. $d_{32\text{-Small}}$ of the He, CH₄, N₂ and CO decreased with the gas molecular weight. The $d_{32\text{-Small}}$ values of H₂ were smaller than those of He;
 - e. $\epsilon_{G\text{-Large}}$ increased with superficial gas velocity;
 - f. $d_{32\text{-Large}}$ significantly increased with solid concentration above 15 vol.%, and
 - g. $d_{32\text{-Large}}$ values of the gases decreased with gas molecular weight.
5. The study of the mass transfer parameters led to the following conclusions:
- a. $k_L a$ increased with pressure, superficial gas velocity, temperature, and decreased with solid concentration;

- b. The large gas-liquid bubbles interfacial area, a_{Large} , was independent of pressure and solid concentration;
 - c. The small gas-liquid bubbles interfacial area, a_{Small} increased with pressure and gas velocity and decreased with solid concentration;
 - d. The mass transfer coefficient, k_L , decreased with pressure and temperature, and increased with superficial gas velocity and solid concentration;
 - e. $k_L a$ values of the CH_4 , N_2 and CO increased with gas molecular weight. $k_L a$ values of H_2 , however, were slightly smaller than those of He;
 - f. a values of He, CH_4 , N_2 , and CO increased with gas molecular weight; however, a values of H_2 were greater than those of He; and
 - g. k_L values of He, CH_4 , N_2 , and CO decreased with gas molecular weight; however, k_L values of H_2 were smaller than those of He.
6. The study of the solid phase dispersion led to the following conclusions:
- a. The solid concentration $C_S(z)$ decreased with reactor height; and the decrease was more pronounced at lower solid concentration;
 - b. In the range of superficial gas velocity studied, $C_S(z)$ was not significantly affected by U_G ;
 - c. The axial dispersion-sedimentation model was used to fit the experimental $C_S(z)$ data. The model was solved with the infinite reactor boundary conditions; and
 - d. The scarcity of experimental data could not lead to a tangible conclusion on the U_P/D_S values.

7. The experimental ϵ_G , $\epsilon_{G\text{-Small}}$, $\epsilon_{G\text{-Large}}$, d_{32} , $d_{32\text{-Small}}$, $d_{32\text{-Large}}$, k_{La} and k_L , along with published literature data were correlated using empirical and Neural Network models. The models were used to predict the hydrodynamic and mass transfer parameters of the Low-Temperature Fischer-Tropsch synthesis in large scale slurry bubble column reactors operating under typical industrial conditions. The modeling led to the following conclusions:

- a. ϵ_G , and $\epsilon_{G\text{-Small}}$ increased with pressure and decreased with solid concentration;
- b. $\epsilon_{G\text{-Small}}$ approached zero above 35-40 wt% catalyst;
- c. $\epsilon_{G\text{-Large}}$ was independent of pressure, and solid concentration below 35-40 wt%;
- d. d_{32} increased with pressure and decreased with solid concentration;
- e. k_{La} increased with pressure and decreased with solid concentration;
- f. No significant effect of the column diameter was found above $D_C = 0.7$ m;
- g. ϵ_G increased with number of orifices in the gas sparger. This increase was more pronounced at lower solid concentration;
- h. ϵ_G decreased with increasing gas distributor's orifice diameter. The gas holdups obtained with spider-type gas sparger were consistently greater than those obtained with multiple-orifice nozzle;
- i. ϵ_G and k_{La} values obtained with H_2/CO (2:1) in wax/alumina-supported cobalt catalyst were lower than those obtained with H_2/CO (1:1) in wax/iron oxide catalyst;
- j. d_{32} values obtained with H_2/CO (2:1) in wax/alumina-supported cobalt catalyst were higher than those obtained with H_2/CO (1:1) in wax/iron oxide catalyst; and

- k. Under typical LTFT of 30 bar, 513 K, 0.2m/s and 50 wt.%, in a 5 m ID SBCR equipped with a multiple orifice nozzles ($d_o = 0.05$ m ID, $N_o = 300$, $\zeta = 3\%$), ε_G , d_{32} and $k_L a$ values of syngas were 16%, 0.026 m, and 0.259 s^{-1} , respectively for wax/alumina-supported cobalt catalyst, and 23%, 0.026m, and 0.314 s^{-1} , respectively for wax/Iron oxide catalyst.

APPENDIX A

CURRENT TREND IN THE SLURRY PHASE FISCHER-TROPSCH PROCESS

Fischer-Tropsch synthesis is the hydrogenation of carbon monoxide over a metal catalyst. Zimmerman et al. ⁽²⁴⁷⁾ proposed the following mechanism for the formation FT products:



Although, this process have been successfully commercialized in South Africa since 1955 using Arge technology ⁽²⁴⁸⁾, the continual advances in the field of kinetics and reaction engineering drove the FT process to adopt new technologies, including better and improved reactors, unique catalysts for higher productivities and selectivities, and enhanced kinetic modeling ⁽²⁴⁹⁾.

The first step in the FT process is the production of the synthesis gas, which is usually carried out by the gasification of coal or the conversion of natural gas. The manufacture of the synthesis gas is of prime importance, since it comprises the most capital-intensive part of the Fischer-Tropsch commercial process ⁽²⁵⁰⁾. Recently, a lot of attentions have been given to the conversion of natural gas, mainly because of the large worldwide reserve, which was estimated

to be between 113 to 138x10¹² m³ (STP) in 1996 ^(251,252). Figure A-1 illustrates the basic steps involved in the GTL process.

Fischer-Tropsch synthesis is currently carried out in three different reactors, namely the fluidized bed, the multitubular fixed bed, and the slurry bed reactor. The fluidized bed and multitubular fixed bed reactors have been successfully used for FT process over the past years, operating mainly with iron catalyst ⁽²⁵³⁾. In fact, at the present time the largest multitubular fixed bed reactors for FT process are those employed by SASOL in South Africa using iron catalyst, and that by Shell in Malaysia using cobalt catalyst for Gas-to-Liquid (GTL) process that converts natural gas to wax ⁽²⁴⁸⁾. The commission in 1993 of the slurry phase process by SASOL for low-temperature FT process brought the question of competitiveness between the multitubular fixed bed and slurry bubble column reactors. Despite the fact that the new slurry phase process employs iron catalyst, SASOL is considering using this technology for GTL process with cobalt catalyst ⁽²⁴⁸⁾. On the other hand, Shell is confident that their multitubular fixed bed technology is as competitive as the slurry process and arguably attributes the basis of comparison of the two technologies on the reactor/catalyst combination ⁽²⁵⁰⁾. In this respect, if the product selectivity based on the catalyst as a function of volumetric productivity were enhanced, there would be less limitation imposed on the scaleup criteria. However, it should be noted that the Fischer-Tropsch reaction is very exothermic and requires rigorous heat removal and temperature control. This imposes strict conditions on the type of industrial reactors to be used. Since slurry bubble columns have better heat removal and temperature control, their capital cost would be significantly lower and hence more competitive than multitubular fixed bed reactors. Following the commission of SASOL's slurry phase technology in 1993, more investments in the slurry

process have been carried out, and most of these were for direct application in the field of GTL technology as can be seen in Table A-1.

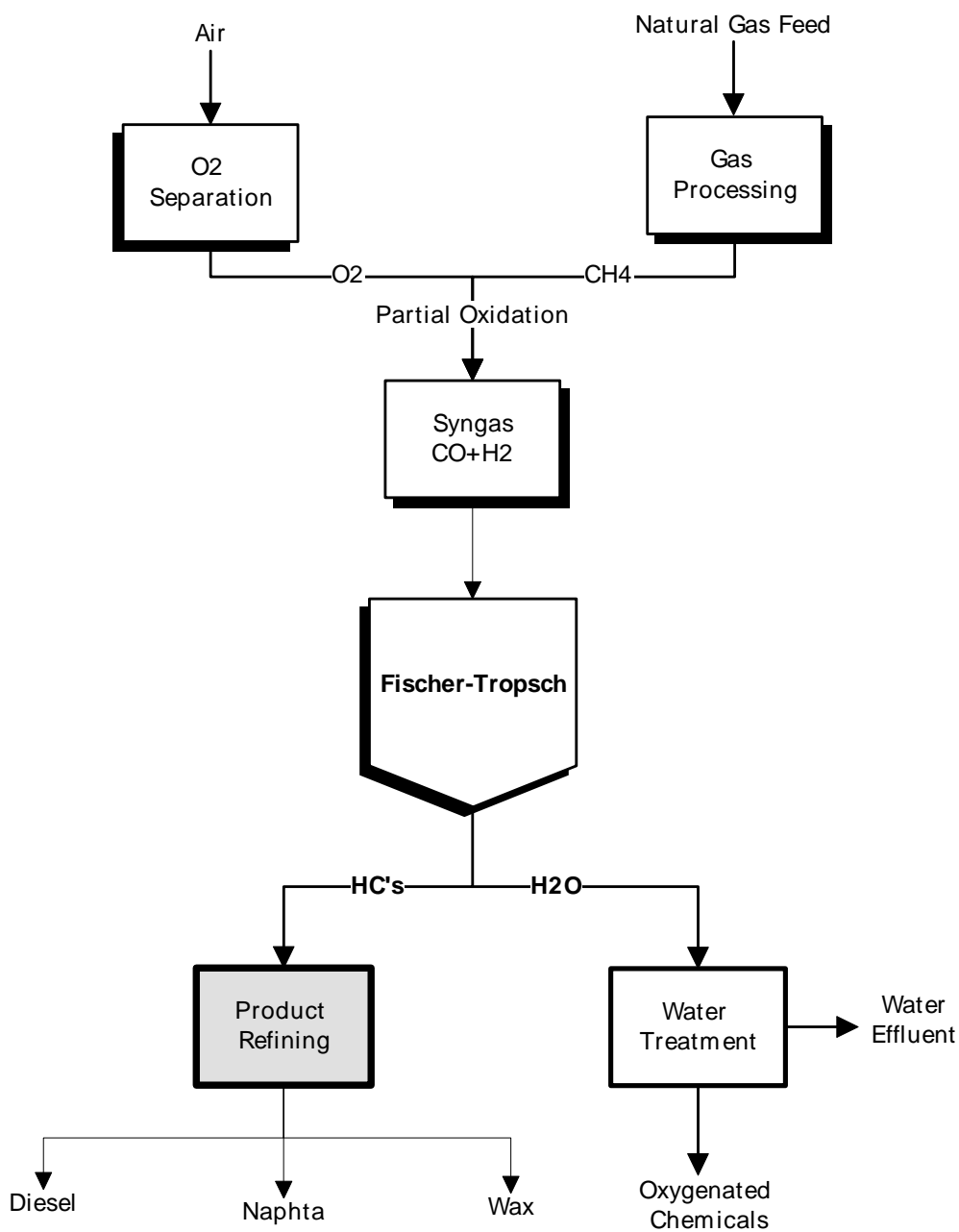


Figure A-1 The Gas-To-Liquid (GTL) Process ⁽²⁵⁴⁾

Table A-1 Existing and planned GTL plants in the world ⁽²⁵⁵⁾

<i>Plant name</i>	<i>Country Location</i>	<i>Capacity (B/D)</i>	<i>Start date</i>	<i>Status</i>	<i>Type</i>	<i>FT Process</i>
Shell (Argentina)	Argentina	75000	2007	Potential	Commercial	SMDS
Australia GTL SasolChevron	Australia	30000	2006	Potential	Commercial	Sasol
Shell (Australia)	Australia	75000	2007	Potential	Commercial	SMDS
Sweetwater GTL	Burrup peninsula	11500	2005	Potential	Commercial	Syntroleum
GTL Bolivia	Bolivia	10000	2006	Potential	Commercial	Rentech
Repsol/Syntroleum	Bolivia	103500	N/A	Potential	Commercial	Syntroleum
Synergy/Stone Canyon Resources	Canada Calgary	4	2000	Existing	Pilot	SynGen
ENAP	Chile	10000	2006	Potential	Commercial	Syntroleum
Shell/EGPC	Egypt	75000	2005	Potential	Commercial	SMDS
Sicor	Ethiopia	20000	N/A	Planned	Commercial	N/A
Pertamina	Indonesia	16500	N/A	Potential	Commercial	Rentech
Shell (Indonesia)	Indonesia	75000	2007	Potential	Commercial	SMDS
Nakangan	Iran	35000	2006	Potential	Commercial	N/A
IFP/ENI	Italy	20	2001	Existing	Pilot	IFP/ENI
JNOC Tomakomai	Japan Hokkaido	7	2002	Existing	Pilot	JNOC-TRC
NKK Corp	Japan	0	1999	Existing	Pilot	NKK
Shell MDS	Malaysia Bintulu	12500	1993	Existing	Commercial	SMDS
Shell (Malaysia)	Malaysia	75000	2007	Potential	Commercial	SMDS
NZ Synfuels	New Zealand New Plymouth	12000	1985	Closed	Commercial	N/A
Escravos GTL	Nigeria Escravos.	34000	2005	Future	Commercial	Sasol
Syntroleum/BPZ	Peru Talara Basin	5000	2003	Planned	Commercial	Syntroleum
ConocoPhillips/QP	Qatar	80000	2009	Project	Commercial	ConocoPhillips
ExxonMobil/QP	Qatar	115000	N/A	Planned	Commercial	Exxon AGC 21
Oryx GTL	Qatar Ras Laffan	100000	2009	Future	Commercial	Sasol
QP/SasolChevron II	Qatar Ras Laffan	130000	2010	Future	Commercial	Sasol
Shell (Qatar)	Qatar	140000	2008	Future	Commercial	SMDS
Ivanhoe (Qatar)	Qatar	185000	N/A	Potential	Commercial	Syntroleum
Yakutsk	Russia	0	N/A	Potential	Commercial	Syntroleum
Forest Oil	South Africa	12500	2006	Potential	Commercial	Non Av.
SASOL I	South Africa Sasolburg	5600	1955	Existing	Commercial	Sasol
SASOL II/III	South Africa Secunda	124000	1980	Existing	Commercial	Sasol
MossGass	South Africa Mossel Bay	24000	1992	Existing	Commercial	Sasol

Table A-1 (Continued)

<i>Plant name</i>	<i>Country Location</i>	<i>Capacity (B/D)</i>	<i>Start date</i>	<i>Status</i>	<i>Type</i>	<i>FT Process</i>
Orobos steel facility	Sweden	N/A	N/A	Potential	Commercial	Rentech
Petro SA	South Africa Mossel Bay	1000	2003	Future	Pilot	Statoil
GTL Trinidad	Trinidad Point Lisas	10000	2003	Future	Commercial	N/A (Based on DOE Research)
BP Nikiski	USA Alaska, Nikiski	300	2002	Existing	Pilot	BP/Kvaerner
Conoco (Ponca)	USA Ponca City	400	2002	Existing	Pilot	Conoco
Exxon Mobil (Baton Rouge)	USA Baton Rouge	300	1993	Existing	Pilot	Exxon AGC 21
DOE	USA LaPorte	35	1992	Existing	Pilot	N/A
Synfuels	USA Texas	12	2000	Existing	Pilot	N/A
Rentech Colorado	USA Colorado	1	1992	Existing	Pilot	Rentech
ANGTL	USA Alaska	50000	2006	Potential	Commercial	Sasol
Syntroleum	USA Tulsa, OK	2	1990	Existing	Pilot	Syntroleum
ARCO/Syntroleum Cherry Point	USA Cherry Point	70	1999	Closed	Pilot	Syntroleum
Syntroleum/Marathon Tulsa	USA Tulsa, OK	70	2003	Future	Pilot	Syntroleum
Williams/EI	USA Pittsburgh	15	2003	Planned	Pilot	Williams GasCatSM
PDVSA	Venezuela	15000	2007	Potential	Commercial	Intevep
PDVSA	Venezuela	100	2003	Planned	Pilot	N/A

APPENDIX B

CALCULATION OF THE PHYSICAL PROPERTIES OF THE GAS-LIQUID

Gas Viscosity:

Table B-1 Parameters for correlation of gas viscosity in Equation (4-1)

Component	A (x10 ⁷)	B (x10 ⁹)	C (x10 ¹³)	$\mu_{298K}(10^6)$ kg m ⁻¹ s ⁻¹
H ₂	21.87	22.20	-37.50	8.47
N ₂	30.43	49.89	-109.30	16.95
CO	32.28	47.47	-96.48	16.52
CH ₄	15.96	34.39	-81.40	11.19
He	53.20	53.04	-165.4	19.66

Liquid Viscosity:

The calculation of the liquid viscosity at high pressure is as follow:

$$\frac{\mu_L^P}{\mu_L^0} = \frac{1 + D_\mu \left(\frac{\Delta P_r}{2.118} \right)^{E_\mu}}{1 + C_\mu \omega \Delta P_r} \quad (\text{B-1})$$

Where μ_L^0 and μ_L^P are the viscosity of the ungasged liquid at the atmospheric and operating pressure, respectively

$$C_\mu = -0.07921 + 2.1616 T_r - 13.4040 T_r^2 + 44.1706 T_r^3 - 84.8291 T_r^4 +$$

$$96.1209 T_r^5 - 59.8127 T_r^6 + 15.6719 T_r^7 \quad (\text{B-2})$$

$$D_\mu = \frac{0.3257}{(1.0039 - T_r^{2.573})^{0.2906}} - 0.2086 \quad (\text{B-3})$$

$$E_\mu = 0.9991 - \frac{4.674 \times 10^{-4}}{(1.0523 T_r^{-0.03877} - 1.0513)} \quad (\text{B-4})$$

It should be mentioned that Equation (B-1) through (B-4) are calculated for all components of Isopar-M. The required parameters are given in Table B-2.

Table B-2 Parameters for calculation of liquid viscosity at high pressure

Component	Tc, K	P _C , bar	ω, -
<i>n</i> -C ₁₁	638.8	19.65603	0.535
<i>n</i> -C ₁₂	658.2	18.2381	0.575
<i>n</i> -C ₁₃	675.8	17.22415	0.619
<i>n</i> -C ₁₄	692.4	15.39924	0.581
<i>n</i> -C ₁₅	706.8	15.19825	0.706
<i>n</i> -C ₁₆	720.6	14.1853	0.742

It should be noted that all component are considered to be *normal* (*n*-C) rather than *iso* (*i*-C). The viscosity of the mixture can be estimated by the following equation from the API Technical Data Book:

$$\mu_m^P = \left(\sum x_i (\mu_i^P)^{1/3} \right)^3 \quad (\text{B-5})$$

Surface Tension:

The Surface tension of Isopar-M was calculated using the Parachor contribution group method as shown:

$$\sigma_{mix}^{1/4} = \sum [P_i] \left(\frac{\rho_L}{(M_B)_{Liq}} x_i - \frac{\rho_{vap.}}{(M_B)_{vap.}} y_i \right) \quad (B-6)$$

Where x_i and y_i are the composition of the i th component in the liquid and gas phase, respectively. $(M_B)_{Liq}$ and $(M_B)_{vap.}$ are the molecular weight of the liquid in the liquid and vapor phase, respectively. It should be mentioned, however, that the ρ_L and ρ_V in Equation (B-6) are in g/cm^3 and σ_{mix} is in dynes/cm. The values for the Parachor contribution group $[P_i]$ are given in Table B-3. If the vapor pressure of the liquid is too low (as it is in the case of Isopar-M) the vapor term in Equation (B-6) can be neglected.

Table B-3 Group contributions in Equation (B-6)

Component	[P]
<i>i</i> -C ₁₁	468.8
<i>n</i> -C ₁₁	471
<i>i</i> -C ₁₂	508.8
<i>n</i> -C ₁₂	511
<i>i</i> -C ₁₃	548.8
<i>n</i> -C ₁₃	551
<i>i</i> -C ₁₄	588.8
<i>n</i> -C ₁₄	594.6
<i>i</i> -C ₁₅	628.8
<i>n</i> -C ₁₅	634.9
<i>i</i> -C ₁₆	672.4

APPENDIX C

ARTIFICIAL NEURAL NETWORK

Introduction

An artificial neural network is an information-processing system that has certain similarities with the biological neural networks from the brain. The mathematical model of the neural biology is based on the assumptions that:

- Information processing occurs at many simple element called neurons
- The information travels between neurons over connection links
- Each connection link has an associated weight, which amplifies, or not the signal

Each neuron applies an activation function, usually non-linear, to its input to determine the output signal, as shown in the following figure.

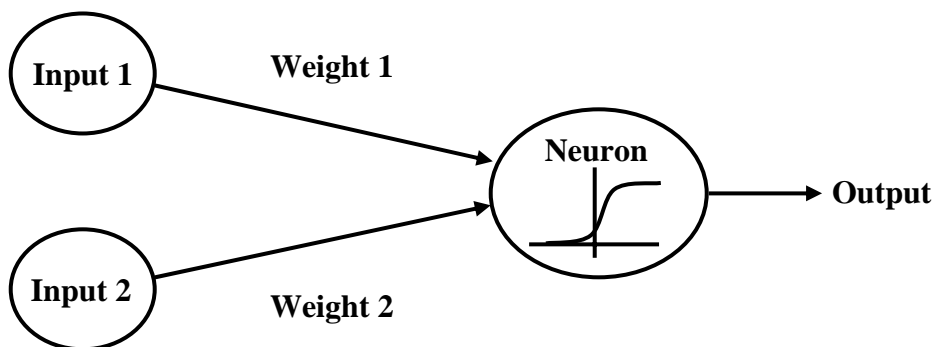


Figure C-1 Schematic of a Simple Artificial Neural Network

Artificial neural networks consist of the following characteristics:

- Architecture: pattern of connections between the neurons.
- Learning Algorithm: iterative procedure to determine the weights between connections.
- Activation function at the neurons.

Due to their iterative learning abilities, neural networks are able to optimize, correlate and predict with high accuracy in a short period of time a considerable amount of experimental data.

Table C-1 lists some of the available literature works on the use of ANN in multi-phase reactors. In this table it can be seen that there are many different learning algorithms employed, among others, Back Propagation (BP), Quasi-Newtonian (QN), and Conjugate-Gradient Optimization (CGO) account for the main ones.

Architecture and Algorithm of the BPNN

The architecture of the BPNN consists of one input layer, one or two hidden layers, and one output layer where each layer of the network is made of a number of neurons as shown in Figure C-2. The process variables (operating conditions; gas-liquid-solid properties; reactor size, etc.) are the neurons in the input layer. The output layer consists of one neuron which is the predicted parameter. The hidden and output layers have additional neuron called the bias. Every neuron in a specific layer is connected with all other neurons to the adjacent layers. The connection between each neuron has a certain weight associated with it. The neurons in each layer are also used to amplify the information received by means of an activation function.

In the learning algorithm of the BPNN, information is fed forward from the input to the hidden layers where the weight-carrying information is then amplified through an activation function inside the neuron. The output of the neurons in the hidden layers is fed to the output layer; and after passing through the activation function, the predicted value is computed. The mean square error (MSE) is calculated between the predicted and experimental values so that the network can adjust the weights between each neuron and repeat the process until the desired MSE is achieved. The algorithm of the feed-forward BPNN is shown in Figure C-3, and is the same used by Lemoine et al. ⁽²³⁸⁾ for predicting mass transfer in agitated reactors using over 4000 data points.

It is important to mention that over-training of the ANN with the sole purpose of achieving low MSE value could make it exclusive to the data used for its training and development. Such a network would give erroneous predictions of the untrained data and thus, cannot be used for modeling purposes. To avoid such a problem, the ANN developed in this study was validated using experimental data values which were not used in the training of the network.

Activation function of the BPNN

The most common activation functions used in ANNs are known to be linear, sigmoid, Gaussian, logarithmic, or hyperbolic tangent functions ^(256,257). In this study, the activation function Equation (C-1) is a sigmoid, which similar to that employed by Lemoine et al. ⁽²³⁸⁾ as:

$$F(x) = \frac{1}{1 + e^{-x}} \quad (C-1)$$

In this equation, x is the weighted sum of a neuron in a corresponding layer.

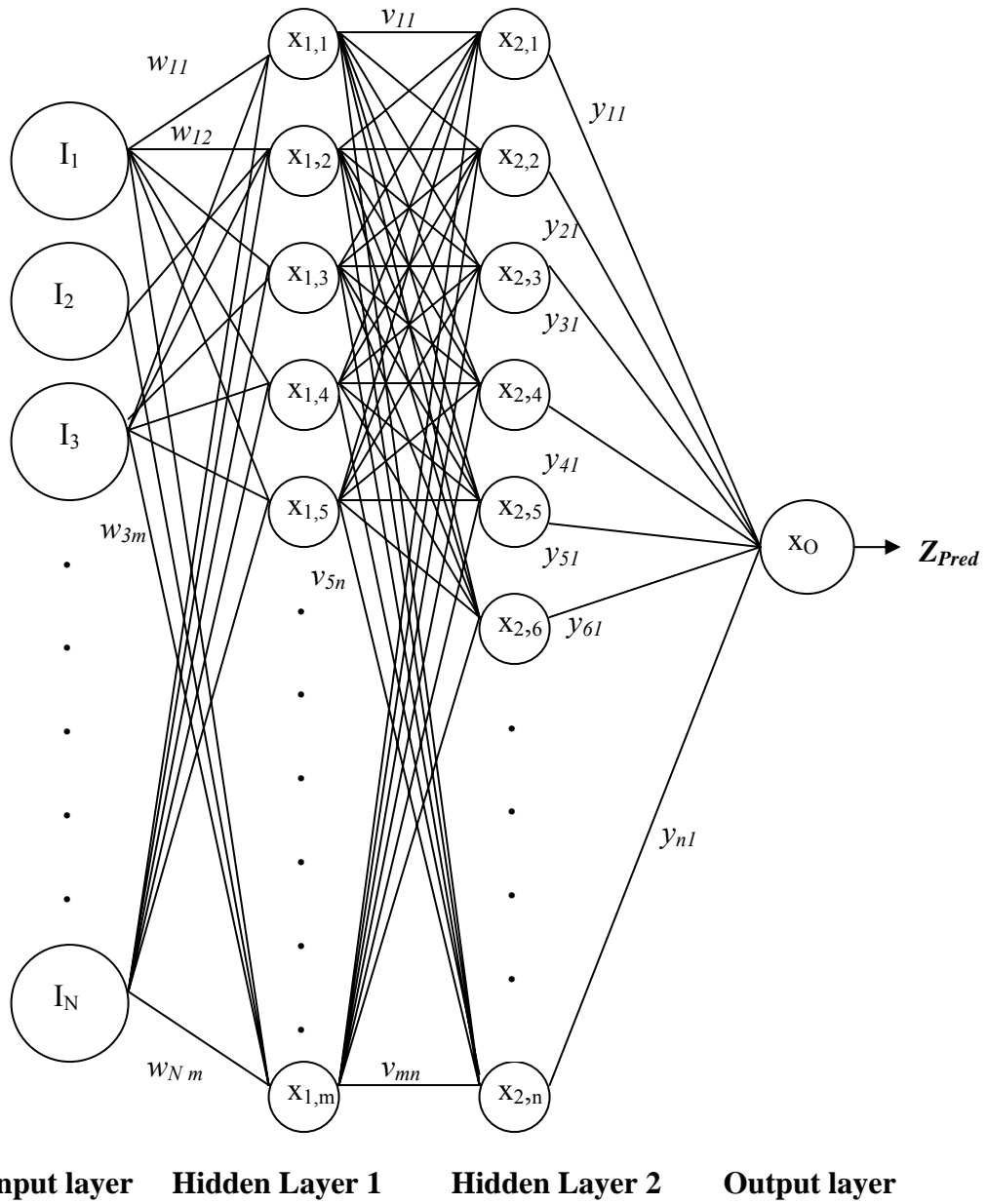


Figure C-2 Architecture of the Back Propagation Neural Network Model

Calculation of the Output

The calculation of the output parameter requires normalization of the input variables ⁽²³⁸⁾:

$$\text{Normalized value} = \frac{\text{Actual value} - \text{Minimum value}}{\text{Maximum value} - \text{Minimum value}} \quad (\text{C-2})$$

The maximum and minimum values in Equation (C-2) are those of the variables in the input nodes of the BPNNs listed in Tables 37, 38, 41, 42, and 45.

The weighted sum to the i th neuron in the first hidden layer is expressed by:

$$x_{1,i} = b_{1,i} + \sum_{k=1}^N (w_{ki} I_k) \quad (\text{C-3})$$

Where $b_{1,i}$ is the bias for the i th neuron in the first hidden layer and I_k is the normalized value of the k th neuron in the input layer; w is the weight factor between the input and first hidden layer neurons; and N is the number of neurons in the input layer.

Similarly, the weighted sum to the j th neuron in the second hidden layer is:

$$x_{2,j} = b_{2,j} + \sum_{i=1}^m (v_{ij} F_{1,i}) \quad (\text{C-4})$$

$F_{1,i}$ is the output value of the activation function of the i th neuron in the first hidden layer using the corresponding weighted sum ($x_{1,i}$) from Equation (C-3). Also, v is the weight factor between the first and second hidden layer neurons.

The weighted sum of the output layer was expressed as:

$$x_o = b_{z,1} + \sum_{j=1}^n (y_{j1} F_{2,j}) \quad (\text{C-5})$$

Where, $F_{2,j}$ is the output from the activation function of the j th neuron in the second hidden layer using the corresponding weighted sum ($x_{2,j}$) in Equation (C-4); and y is the weight factor between the neurons in the second hidden layer and the output neuron.

The output (Z_{pred}) is calculated by inserting Equation (C-5) into Equation (C-1); and subsequently the value of the correlated parameter (Π) is obtained from the following relationship:

$$(\Pi) = (Z_{\text{pred}})(\text{maximum value} - \text{minimum value}) + \text{minimum value} \quad (\text{C-6})$$

The maximum and minimum values in Equation (C-6) are those of the parameter (Π) listed in Tables 37, 38, 41, 42, and 45, for ε_G , $\varepsilon_{G\text{-Large}}$, d_{32} , $d_{32\text{-Large}}$, and k_{La} , respectively..

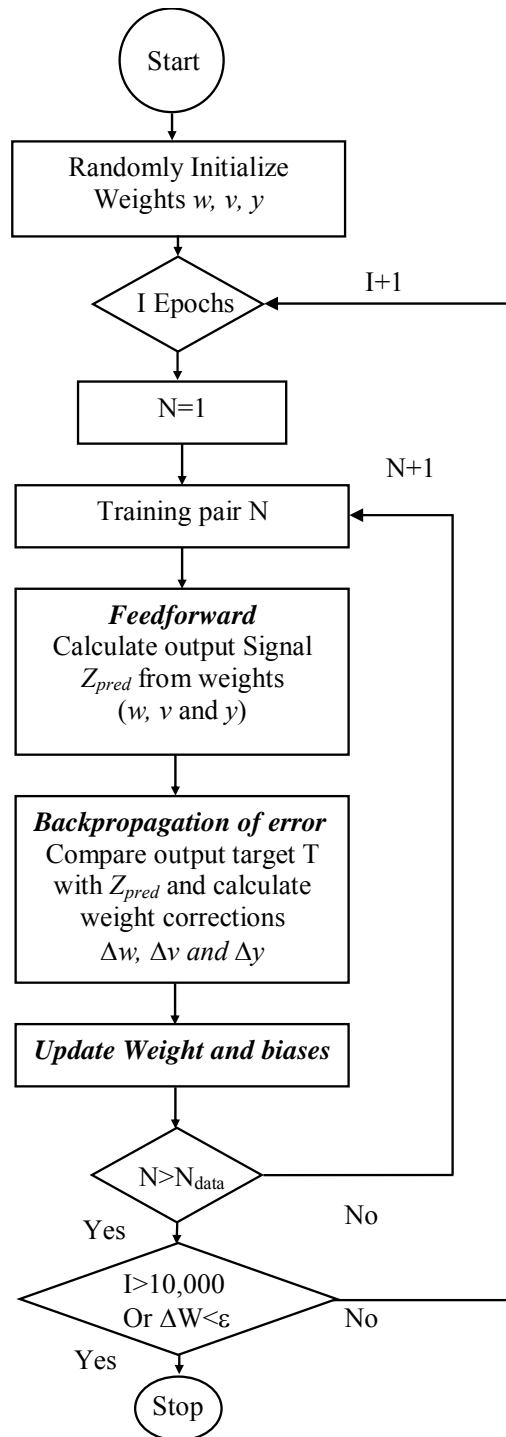


Figure C-3 The Algorithm of the BPNN Model

Table C-1 Use of neural network in multi-phase reactors

<i>Authors</i>	<i>System studied</i>	<i>Reactor type</i>	<i>Purpose and output parameters</i>	<i>Type of Network and Topology [ILN-HLN-OLN]</i>
Chouai et al. (258)	Oxalic acid + H ₂ O Tributylphosphate+ dodecane + H ₂ O	Liquid-liquid extraction column	Prediction: pH, conductivity	QN-FF [11-9-2]
Larachi et al. (259)	$780 \leq \rho_L \leq 1623$ $8.9 \times 10^{-4} \leq \mu_L \leq 0.0719$ $0.025 \leq \sigma_L \leq 0.073$ $1.145 \leq \rho_G \leq 1.159$ $1290 \leq \rho_S \leq 7510$	3-Phase fluidized beds	Prediction: U_{Lmf} , Re_L	QN-FF [8-6-1], [5-9-1]
Otawara et al. (260)	Air-H ₂ O-glass beads	2-D, 3-phase fluidized bed	Prediction: Temporal intervals of bubble and solid passage.	BP-FB [I_n - N_h - I_{n+1}] ($3 \leq N_h \leq 15$)
Qi et al. (261)	O ₂ -Benzene-V ₂ O ₅	Fixed-bed	Prediction: overall heat transfer coefficient	QN-FF, 3 ILN and 1 OLN
Reisener et al. (262)	Electrolyte solution	Gas sparged	Prediction: mass transfer coefficient, k	CGO-FF [3-4-1], [3-10-1]
Sharma et al. (263)	H ₂ /CO SiO ₂ -Al ₂ O ₃	Fixed bed	Modeling: %conv., liq. Conc., SS conc ^(*) . CH ₄ , SS conc. Oxygenates, SS conc. Hydrocarbons.	BP-FF, 5 Networks of 3 ILN and 1 OLN each. (1 or 2 HLN)
Tendulkar, et al. (264)	H ₂ O ₂ -Phenol-Ti-based zeolite catalyst	Fixed bed	Predictive control: phenol flow rate, Temperature	BP-FF [4-5-2]
Utomo et al. (265)	Air-H ₂ O	2-D, Bubble column	Prediction: mean bubble diameter, local ε_G	BP-FF 3 networks [2- N_h -2] $N_h = 4, 8, 10$
Yang et al. (266)	$0 \leq P_g/V_L \leq 55000$ $0.8 \leq \mu_L \leq 70.2$	Stirred tank	Prediction: $k_L a$	BP and CGO-FF [6-11-1]

Table C-1 (Continued)

<i>Authors</i>	<i>System studied</i>	<i>Reactor type</i>	<i>Purpose and output parameters</i>	<i>Type of Network and Topology [ILN-HLN-OLN]</i>
Alvarez et al. ⁽²⁶⁷⁾	CO ₂ , Sucrose and CMC	Bubble column	Prediction: $k_L a$	BP-FF
Belfares et al. ⁽²⁶⁸⁾	790 ≤ ρ_L ≤ 1200 5.5x10 ⁻⁴ ≤ μ_L ≤ 26.6x10 ⁻³ 0.029 ≤ σ_L ≤ 0.073 8x10 ⁻² ≤ ρ_G ≤ 4.3 8.8x10 ⁻⁶ ≤ μ_G ≤ 1.82x10 ⁻⁵	Packed-bubble column	Prediction: Pe	QN-FF [6-11-1]
Carsky and Kuwornoo ⁽²⁶⁹⁾	1x10 ⁻⁴ ≤ d_p ≤ 3.36x10 ⁻³ 400 ≤ T (°C) ≤ 900	Fluidized-bed Spouted-bed Hot-rod (fixed bed)	Prediction: Pyrolysis Yield of tar (wt.%), Yield of volatiles (wt.%), Yield of char (wt.%)	BP-FF [47-16-3]
García-Ochoa and Gómez Castro ⁽²⁵⁶⁾	O ₂ , H ₂ O-Xanthan gum solution	Baffled stirred tank	Prediction: $k_L a$	BP-FF [13-4-1]
Iliuta et al. ⁽²⁷⁰⁾	805 ≤ ρ_L ≤ 1450 6.32x10 ⁻⁴ ≤ μ_L ≤ 4.72x10 ⁻² 1.06x10 ⁻² ≤ σ_L ≤ 7.77x10 ⁻² 0.937 ≤ ρ_G ≤ 57.46 5.4x10 ⁻⁴ ≤ d_p ≤ 2.64x10 ⁻²	Trickle beds	Prediction: Sh_G , Sh_L , $ad_h/(1-\epsilon)$	QN-FF [7-13-1], [7-8-1], [8-11-1]
Leib et al. ⁽²⁷¹⁾	Propylene oxidation process	Fluidized bed	Simulation: u_{sb} , y_i , y_{4-6} , w_i , w_{4-6} , ($i = 1$ to 3)	BP-FF [11-8-9]
Leib et al. ⁽²⁷²⁾	Liquid-phase Fischer-Tropsch system	Slurry bubble column	Simulation: C_G , C_L , U_G	BP-FF [6-5-3]
Nikravesh et al. ⁽²⁷³⁾	Nonisothermal system	CSTR	Process control: h and E_0	BP-FF
Parisi and Laborde ⁽²⁷⁴⁾	Steam reforming of CH ₄	Fixed-bed	Modeling: global reaction rate	BP-FF [6-5-1]

(*) SS conc.: Steady state concentration, [g/Nm³ of H₂+CO]

BIBLIOGRAPHY

1. Jager B., Kelfkens R.C., Steynberg A.P. "A Slurry Bed Reactor for Low Temperature Fischer-Tropsch," Studies in Surface Science and Catalysis, Vol. 81, (1994), pp. 419.
2. Nigam, K.D.P., Schumpe A., Three-Phase Sparged Reactors, (Gordon and Breach Publishers, Amsterdam, The Netherlands, 1996)
3. "LPMeOH begins operation". Power Generation, Vol. 18, (1997), pp.1.
4. Jager, B. Espinoza, R., "Advances in Low Temperature Fischer-Tropsch Synthesis," Catalysis Today, Vol. 23, (1995), pp.17-28.
5. Knott D. "Gas to Liquids Projects Gaining Momentum as Process List Grows." Oil & Gas Journal, Vol.95, (1997), pp. 16-21.
6. Krishna, R., Sie, S.T., "Design and Scale-Up of the Fischer-Tropsch Bubble Column Slurry Reactor," Fuel Processing Technology, Vol. 64, (2000), pp. 73-105.
7. Yakobson, D.L., "Fischer-Tropsch Technology: GTL's Place in the Drive Towards Cleaner Fuels," Gas Tech 2000 Conference, Nov. 15, 2000. Houston, TX.
8. Krishna, R., de Swart, J.W.A., Ellenberger, J., Martina, G., B., Maretto, C. "Gas Holdup in Slurry Bubble Columns: Effect of Column Diameter and Slurry Concentrations," AIChE Journal, Vol. 43, (1997), pp.311-316.
9. Fox, J.M., "Fischer-Tropsch Reactor Selection" Catalysis Letter, Vol. 7, (1990), pp. 281.
10. Saxena, S.C., Chen, Z.D., "Hydrodynamics and Heat Transfer of Baffled and Unbaffled Slurry Bubble Column", Rev. Chem. Eng., Vol. 10, (1994), pp.193.
11. Deckwer, W.D., Louisi, Y., Zaidi, A., Ralek, M., "Hydrodynamic Properties of The Fischer-Tropsch Slurry Process", Industrial and Engineering Chemistry Process Design and Development, Vol. 19, (1980), pp.699-708.

12. Guy, C., Carreau, J.P., Paris, J., "Mixing Characteristics and Gas Holdup of a Bubble Column" The Canadian Journal of Chemical Engineering, Vol. 64, (1986), pp. 23.
13. Wallis, G.B., One Dimensional Two Phase Flow, (McGraw Hill, New York, 1969)
14. Magaud, F., Souhar, M., Wild, G., Boisson, N., "Experimental Study of Bubble Column Hydrodynamics," Chemical Engineering Science, Vol. 56, (2001), pp.4597-4607.
15. Sarrafi, A., Jamialahmadi, M., Müller-Steinhagen, H., Smith, J.M., "Gas Holdup in Homogeneous and Heterogeneous Gas-Liquid Bubble Column Reactors," The Canadian Journal of Chemical Engineering, Vol. 77, (1999), pp. 11-21.
16. Krishna, R., Urseanu, M.I., de Swart, J.W.A., Ellenberger, J., "Gas Holdup in Bubble Columns: Operation with Concentrated Slurries Versus High Viscosity Liquid," The Canadian Journal of Chemical Engineering, Vol. 78, (2000), pp. 442-448.
17. Letzel, H.M., Schouten, J.C., Van den Bleek, C.M., Krishna, R. "Influence of Elevated Pressure on the Stability of Bubbly Flows," Chemical Engineering Science, Vol. 52, (1997), pp.3733-3739.
18. Lin, T.J., Tsuchiya, K., Fan, L.S. "On the Measurements of Regime Transition in High-Pressure Bubble Columns," The Canadian Journal of Chemical Engineering, Vol. 77, (1999), pp. 370-375.
19. Anderson, J.L., Quinn, J.A., "The Transition to Slug Flow in Bubble Columns," Chemical Engineering Science, Vol. 25, (1970), pp. 338-340.
20. Hills, J.H., "The Operation of a Bubble Column at High Throughputs I. Gas Holdup Measurements," Chemical Engineering Journal, Vol.12, (1976), pp.89-99.
21. Miller D.N., "Gas Holdup and Pressure Drop in Bubble Column Reactors," Industrial and Engineering Chemistry Process Design and Development, Vol. 19, (1980), pp. 371-377.
22. Schumpe, A., "Die Chemische Bestimmung von Phasengrenzflächen in Blasensäulen bei ungleichmäßigen blasengrößen," (Ph.D. dissertation, Universität Hannover, 1981).
23. Shah, Y.T., Kelkar, B.G., Godbole, S.P., Deckwer, W.D. "Design Parameters Estimations for Bubble Column Reactors," AIChE, Journal, Vol. 28, (1982), pp. 353-379.

24. Oshinowo, T., Charles, M.E., "Vertical Two-Phase Flow. Part I. Flow Pattern Correlations", The Canadian Journal of Chemical Engineering, Vol. 52, (1974), pp. 25-35.
25. Vial, Ch., Laine, R., Poncin, S., Midoux, N., Wild, G. "Influence of Gas Distribution and Regime Transition on Liquid Velocity and Turbulence in a 3-D Bubble Column," Chemical Engineering Science, Vol. 56, (2001), pp. 1085-1093.
26. Lee, D.J., McLain, B.K., Cui, Z., Fan, L.S. "Pressure Effect on the Flow Fields and the Reynolds Stresses in a Bubble Column," Industrial and Engineering Chemistry Research, Vol. 40, (2001), pp. 1442-1447.
27. Chen, R.C., Reese, J., Fan, L.S. "Flow Structure in a 3-D Bubble Column and Three-Phase Fluidized Bed," AIChE Journal, Vol. 40, (1994), pp. 1093-1104.
28. Fan, L.S., Yang, G.Q., Lee, D.J., Tsuchiya, K., Luo, X. "Some Aspects of High-Pressure Phenomena of Bubbles in Liquid and Liquid-Solid Suspensions," Chemical Engineering Science, Vol. 54, (1999), pp. 4681-4709.
29. Shah, Y.T., Gas-Liquid-Solid Reactor Design. (McGraw-Hill: New York, 1979)
30. Wu, Y., Ong, B.C., Al-Dahhan, M.H. "Prediction of Radial Gas Holdup Profiles in Bubble Column Reactors," Chemical Engineering Science, Vol. 56, (2001), pp.1207-1210.
31. Akita, K., Yoshida, F., "Gas Holdup and Volumetric Mass Transfer Coefficient in Bubble Columns", Industrial Engineering Chemistry Process Design and Development, Vol. 12, (1973), pp. 76-80.
32. Bach, H.F., Pilhofer, T., "Variations of Gas Hold-Up in Bubble Columns with Physical Properties of Liquids and Operating Parameters of Column", German Chemical Engineering, Vol.1, (1978), pp. 270-275.
33. Hikita, H., Asai, S., Tanigawa, K., Segawa, K., Kitao, M., "Gas Hold-Up in Bubble Columns", The Chemical Engineering Journal, Vol.20 (1980), pp. 59-67.
34. Hughmark, G.A., "Holdup and Mass Transfer in Bubble Columns", Industrial Engineering Chemistry Process Design and Development, Vol. 6 (1967), pp. 218-221.
35. Deckwer, W.,-D., Bubble Column Reactor, (John Wiley and Sons, Chichester, 1992).

36. Krishna, R., Ellenberger, J., "Gas Holdup in Bubble Column Reactors Operating in the Churn-Turbulent Flow Regime," AICHE Journal, Vol. 42, (1996), pp. 2627-2634.
37. Deckwer, W.-D., Burckhart, R., Zoll, G., "Mixing and Mass Transfer in Tall Bubble Columns," Chemical Engineering Science, Vol. 29, (1974), pp.2177-2188.
38. Oyevaar, M.H., Bos, R., Westerterp, K.R., "Interfacial Areas and Gas Hold-Ups in Gas-Liquid Contactors at Elevated Pressures from 0.1 to 8.0 MPa," Chemical Engineering Science, Vol. 46, (1991), pp. 1217-1231.
39. Smith, G.B., Gamblin, B.R., Newton, D., "X-Ray Imaging of Slurry Bubble Column Reactors: The Effects of System Pressure and Scale," Chemical Engineering Research and Design, Vol. 73, (1995), pp. 632.
40. Kojima, H., Sawai, J., Suzuki, H. "Effect of Pressure on Volumetric Mass Transfer Coefficient and Gas Holdup in Bubble Column," Chemical Engineering Science, Vol. 52, (1997), pp. 4111-4116.
41. Letzel, H.M., Schouten, J.C., Krishna, R., Van den Bleek, C.M. "Gas Holdup and Mass Transfer in Bubble Column Reactors Operated at Elevated Pressure," Chemical Engineering Science, Vol. 54, (1999), pp. 2237-2246.
42. Kang Y., Cho, Y.J., Woo, K.J., Kim, S.D. "Diagnosis of Bubble Distribution and Mass Transfer in Pressurized Bubble Columns with Viscous Liquid Medium," Chemical Engineering Science, Vol. 54, (1999), pp. 4887-4893.
43. Luo, X., Lee, D.J., Lau, R., Yang, G., Fan, L.S. "Maximum Stable Bubble Size and Gas Holdup in High-Pressure Slurry Bubble Columns," AICHE Journal, Vol. 45, (1999), pp.665-680.
44. Stegeman, D., Knop, P.A., Wijnands, A.J.G., Westerterp, K.R., "Interfacial Area and Gas holdup in a Bubble Column Reactor at Elevated Pressure," Industrial and Engineering Chemistry Research, Vol. 35, (1996), pp. 3842-3847.
45. Wilkinson, P.M., Haringa, H., Van Dierendonck, L.L. "Mass Transfer and Bubble Size in a Bubble Column Under Pressure," Chemical Engineering Science, Vol. 49, (1994), pp. 1417-1427.
46. Tarmy, B., Chang, M., Coualoglou, C., Ponzi, P. "Hydrodynamic Characteristics of Three Phase Reactors," The Chemical Engineer, Vol. 407, (1984), pp. 18-23.

47. Wilkinson, P.M., Van Dierendonck, L.L. "Pressure and Gas Density Effects on Bubble Break-Up and Gas Hold-Up in Bubble Columns," Chemical Engineering Science, Vol. 45, (1990), pp. 2309-2315.
48. Reilly, I.G., Scott, D.S., de Bruijn, T.J.W. and MacIntyre, D. "The Role of Gas Phase Momentum in Determining Gas Holdup and Hydrodynamic Flow Regimes in Bubble Column Operations," The Canadian Journal of Chemical Engineering, Vol. 72, (1994), pp. 3-12.
49. Öztürk, S.S., Schumpe, A., Deckwer, W.D., "Organic Liquids in a Bubble Column: Holdups and Mass Transfer Coefficients," AIChE Journal, Vol. 33, (1987), pp.1473-1480.
50. Clark, K.N., "The Effect of High Pressure and Temperature on Phase Distributions in a Bubble Column," Chemical Engineering Science, Vol. 45, (1990), pp. 2301-2307.
51. Pohorecki, R., Moniuk, W., Zdrojkowski, A. "Hydrodynamics of a Bubble Column Under Elevated Pressure," Chemical Engineering Science, Vol 54, (1999), pp. 5187-5193.
52. Kemoun, A., Ong, B.C., Gupta, P., Al-Dahhan, M.H., "Gas Holdup in Bubble Columns at Elevated Pressure Via Computed Tomography," International Journal of Multiphase Flow, Vol. 27, (2001), pp. 929-946.
53. Jiang, P., Lin, T.J., Luo, X., Fan, L.S., "Flow Visualization of High Pressure (21 MPa) Bubble Column: Bubble Characteristics," Transaction of Institute of Chemical Engineering, Vol. 73, (1995), pp. 269-274.
54. Therning, P., Rasmuson, A., "Liquid Dispersion, Gas Holdup and Frictional Pressure Drop in a Packed Bubble Column at Elevated Pressures," Chemical Engineering Journal, Vol. 81, (2001), pp. 331-335.
55. Soong, Y., Harke, F.W., Gamwo, I.K., Schehl, R.R., Zarochak, M.F. "Hydrodynamic Study in a Slurry Bubble-Column Reactor," Catalysis Today, Vol. 35, (1997), pp. 427-434.
56. Bhaga, D., Pruden, D.D., Weber, M.E. "Gas Holdup in a Bubble Column Containing Organic Liquid Mixtures," The Canadian Journal of Chemical Engineering, Vol. 49, (1971), pp.417-420.
57. Godbole, S.P., Schumpe, A., Shah, Y.T., Carr, N.L. "Hydrodynamics and Mass Transfer in Non-Newtonian Solutions in a Bubble Column," AIChE Journal, Vol. 30, (1984), pp. 213-220.

58. Yasunishi, A., Fukuma, M., Muroyama, K. "Measurement of Behavior of Gas Bubbles and Gas Holdup in a Slurry Bubble Column by a Dual Electroresistivity Probe Method," Journal of Chemical Engineering of Japan, Vol. 19, (1986), pp. 444-449.
59. Neme, F., Coppola, L., Böhm, U. "Gas Holdup and Mass Transfer in Solid Suspended Bubble Columns in Presence of Structured Packings," Chemical Engineering Technology, Vol. 20, (1997), pp. 297-303.
60. Crabtree, J.R., Bridgwater, J. "Bubble Coalescence in Viscous Liquids," Chemical Engineering Science, Vol. 26, (1971), pp. 839-851.
61. Wilkinson, P.M., Spek, A.P., van Dierendonck, L.L., "Design Parameters Estimation for Scale-Up of High-Pressure Bubble Columns," AIChE Journal, Vol. 38, (1992), pp. 544-554.
62. Kantak, M.V., Hesketh, R.P., Kelkar, B.G., "Effect of Gas and Liquid Properties on Gas Phase Dispersion in Bubble Columns," Chemical Engineering Journal, Vol. 59, (1995), pp. 91-100
63. Kluytmans, J.H.J., van Wachem, B.G.M., Kuster, B.F.M., Schouten, J.C., "Gas Holdup in a Slurry Bubble Column: Influence of Electrolyte and Carbon Particles," Industrial and Engineering Chemistry Research, Vol. 40, (2001), pp. 5326-5333.
64. Schumpe, A., Saxena, A.K., Fang, L.K. "Gas/Liquid Mass Transfer in a Slurry Bubble Column," Chemical Engineering Science, Vol. 42, (1987), pp. 1787-1796.
65. Pino, L.Z., Solari, R.B., Siquier, S., Antonio Estevez, L., Yopez, M.M. "Effect of Operating Conditions on Gas Holdup in Slurry Bubble Columns with a Foaming Liquid," Chemical Engineering Communication, Vol. 117, (1992), pp. 367-382.
66. Yamashita, F. "Effect of Foam Layer on Gas Holdup in a Bubble Column," Journal of Chemical Engineering of Japan, Vol. 28, (1995), pp. 837-840
67. Kara, S., Balmohan, G., Shah, Y.T., Carr, N.L. "Hydrodynamics and Axial Mixing in a Three-Phase Bubble Column," Industrial Engineering Chemistry Process Design and Development, Vol. 21, (1982), pp. 584-594
68. Koide, K., Takazawa, A., Komura, M., Matsunaga, H. "Gas Holdup and Volumetric Liquid-Phase Mass Transfer Coefficient in Solid-Suspended Bubble Columns," Journal of Chemical Engineering of Japan, Vol. 17, (1984), pp. 459-466.

69. Kojima, H., Anjyo, H., Mochizuki, Y. "Axial Mixing in Bubble Column with Suspended Solid Particles," Journal of Chemical Engineering of Japan, Vol. 19, (1986), pp. 232-234.
70. de Swart, J.W.A., Krishna, R. "Influence of Particles Concentration on the Hydrodynamic of Bubble Column Slurry Reactors," Chemical Engineering Research and Design, Vol. 73, (1995), pp. 308-313.
71. Krishna, R., van Baten J.M., Urseanu, M.I., Ellenberger, J., "Design and Scale up of a Bubble Column Slurry Reactor for Fischer-Tropsch Synthesis," Chemical Engineering Science, Vol.56, (2001), pp. 537-545.
72. Lee, D.J., Luo, X., Fan, L.S. "Gas Disengagement Technique in a Slurry Bubble Column Operated in Coalesced Bubble Regime," Chemical Engineering Science, Vol. 54, (1999), pp. 2227-2236.
73. Gandhi, B., Prakash, A., Bergougnou, M.A. "Hydrodynamic Behavior of Slurry Bubble Column at High Solids Concentrations," Powder Technology, Vol. 103, (1999), pp. 80-94.
74. de Swart, J.W.A., Van Vliet, R.E., Krishna, R. "Size, Structure and Dynamics of "Large" Bubbles in a Two-Dimensional Slurry Bubble Column,". Chemical Engineering Science, Vol. 51, (1996), pp. 4619-4629.
75. Banisi, S., Finch, J.A., Laplante, A.R., Weber, M.E., "Effect of Solid Particles on Gas Holdup in Flotation Columns-II. Investigation of Mechanisms of Gas Holdup Reduction in Presence of Solids," Chemical Engineering Science, Vol. 50, (1995), pp. 2335-2342.
76. Sada, E., Kumazawa, H., Lee, C.H., "Chemical Absorption in a Bubble Column Loading Concentrated Slurry," Chemical Engineering Science, Vol. 38, (1983), pp. 2047-2051.
77. Behkish, A., Men, Z., Inga, J.R., Morsi, B.I., "Mass Transfer Characteristics in a Large-Scale Slurry Bubble Column Reactor with Organic Liquid Mixtures," Chemical Engineering Science, Vol. 57, (2002), pp. 3307-3324.
78. Gopal, J.S., Sharma, M.M., "Mass Transfer Characteristics of Low H/D Bubble Columns", The Canadian Journal of Chemical Engineering, Vol. 61, (1983) pp. 517-526.
79. Saxena, S.C., Rao, N.S., Thimmapuram, P.R., "Gas Phase Holdup in Slurry Bubble Column for Two- and Three-Phase Systems", The Chemical Engineering Journal, Vol.49 (1992), pp. 151-159.

80. Colmenares, A., Sevilla, M., Goncalves, J.J., Gonzales-Mendizabel, D., "Fluid-Dynamic Study in a Bubble Column with Internals," Int. Comm. Heat Mass Transfer, Vol. 28, (2001), pp. 389-398.
81. Quicker, G., Schumpe, A., Deckwer, W.D., "Gas-Liquid Interfacial Areas in a Bubble Column with Suspended Solids," Chemical Engineering Science, Vol. 39, (1984), pp. 179-183.
82. de Bruijn, T.J.W., Chase, J.D., Dawson, W.H. "Gas Holdup in a Two Phase Vertical Tubular Reactor at High Pressure," The Canadian Journal of Chemical Engineering, Vol. 66, (1988), pp. 330-333.
83. Chabot, J., Lasa, H.I. "Gas Holdups and Bubble Characteristics in a Bubble Column Operated at High Temperature," Industrial Engineering Chemistry Research, Vol. 32, (1993), pp. 2595-2601.
84. Grover, G.S., Rode, C.V., Chaudhari, R.V. "Effect of Temperature on Flow Regime and Gas Holdup in a Bubble Column," The Canadian Journal of Chemical Engineering, Vol. 64, (1986), pp. 501-504.
85. Lin, T.-J., Tsuchiya, K., Fan, L.S., "Bubble Flow Characteristics in Bubble Columns at Elevated Pressure and Temperature," AIChE Journal, Vol. 44, (1998), pp. 545-560.
86. Pohorecki, R., Moniuk, W., Zdrojkowski, A., Bielski, P. "Hydrodynamics of a Pilot Plant Bubble Column Under Elevated Temperature and Pressure," Chemical Engineering Science, Vol. 56, (2001), pp. 1167-1174.
87. Zou, R., Jiang, X., Li, B., Zu, Y., Zhang, L. "Studies on Gas Holdup in a Bubble Column Operated at Elevated Temperature," Industrial and Engineering Chemistry Research, Vol. 27, (1988), pp. 1910-1916.
88. Lau, R., Peng, W., Velazquez-Vargas, G., Yang, G.Q., Fan, L.S., "Gas-Liquid Mass Transfer in High-Pressure Bubble Columns", Industrial and Engineering Chemistry Research, Vol. 43, (2004), pp. 1302-1311.
89. Daly, J.G., Patel, S.A., Bukur, D.B., "Measurement of Gas Holdups and Sauter Mean Bubble Diameters in Bubble Column Reactors by Dynamic Gas Disengagement Method", Chemical Engineering Science, Vol. 47 (1992), pp. 3647-3654.

90. Ishibashi, H., Onozaki, M., Kobayashi, M., Hayashi, J. I., Itoh, H., Chiba, T. "Gas Holdup in Slurry Bubble Column Reactors of a 150 t/d Coal Liquefaction Pilot Plant Process," Fuel, Vol. 80, (2001), pp. 655-664.
91. Bukur, D.B., Patel, S.A., Daly, J.G., "Gas Holdup and Solids Dispersion in a Three-Phase Slurry Bubble Column", AIChE Journal, Vol. 36 (1990), pp. 1731-1735.
92. Yang, G.Q., Luo, X., Lau, R., Fan, L.S. "Heat-Transfer Characteristics in Slurry Bubble Columns at Elevated Pressures and Temperatures," Industrial and Engineering Chemistry Research, Vol. 39, (2000), pp. 2568-2577.
93. Thomas D.G. "Transport Characteristics of Suspension: VIII. A Note on Viscosity of Newtonian Suspensions of Uniform Spherical Particles," Journal of Colloid Science, Vol. 20, (1965), pp. 267-277.
94. Guth, E., Simha, H. "Viscosity of Suspensions and Solutions: III Viscosity of Sphere Suspensions," Kolloid-Z, Vol. 74, (1936), pp. 266-275.
95. Barnea, E., Mizrahi, J. A. "Generalized Approach to the Fluid Dynamics of Particulate System. Part 1 General Correlation for Fluidization and Sedimentation in Solid Multiparticle Systems," The Chemical Engineering Journal, Vol. 5, (1973), pp. 171-189.
96. Roscoe, R. "The Viscosity of Suspension of Rigid Spheres," British Journal of Applied Physics., Vol. 3, (1952), pp. 267.
97. Riquarts, H. P., "Disperse Zweiphasenstroemungen: Berechnungsgrundlagen und deren Anwendung," (Habilitationsschrift, TU Muenchen, 1978).
98. Vand, V., "Viscosity of Solutions and Suspensions. I. Theory," Journal of Physical Chemistry, Vol. 52, (1948), pp.277-299.
99. Thorat, B.N., Kataria, K., Kulkarni, A.V., Joshi, J.B. "Pressure Drop Studies in Bubble Columns," Industrial and Engineering Chemistry Research, Vol. 40, (2001), pp. 3675-3688.
100. Yamashita, F., "Effect of Clear Liquid Height and Gas Inlet Height on Gas Holdup in a Bubble Column," Journal of Chemical Engineering of Japan, Vol. 31, (1998), pp. 285-288.
101. Kastanek, F., Zahradnik, J., Kratochvil, J., Cermak, J., "Modeling of Large-Scale Bubble Column Reactors for Non-Ideal Gas-Liquid Systems," edited by L. K. Doraiswamy, R. A.

- Mashelkar, Frontier in Chemical Reaction Engineering, (John Wiley & Sons, New Delhi, India, Vol. 1, 1984, pp.330-344).
102. Eickenbusch, H., Brunn, P.O., Schumpe, A., "Mass Transfer into Viscous Pseudoplastic Liquid in Large-Diameter Bubble Columns," Chemical Engineering and Proceedings, Vol. 34, (1995), pp. 479-485.
 103. Urseanu, M.I., Guit, R.P.M., Stankiewicz, A., van Kranenburg, G., Lommen, J.H.G.M., "Influence of Operating Pressure on the Gas Hold-Up in Bubble Columns for High Viscous Media", Chemical Engineering Science, Vol. 58, (2003), pp. 697-704.
 104. Fair, J.R., Lambright, A.J., Anderson, J.W. "Heat Transfer and Gas Holdup in a Sparged Contactor," Industrial & Engineering Chemistry Process Design and Development, Vol. 1, (1962), pp. 33-36.
 105. Yoshida, F., Akita, K. "Performance of Gas Bubble Columns: Volumetric Liquid-Phase Mass Transfer Coefficient and Gas Holdup," AIChE Journal, Vol. 11, (1965), pp. 9-13.
 106. Moustiri, S., Hebrard, H., Thakre, S.S., Roustan, M., "A Unified Correlation for Predicting Liquid Axial Dispersion Coefficient in Bubble Columns," Chemical Engineering Science, Vol. 56, (2001), pp. 1041-1047.
 107. Koide, K., Morooka, S., Ueyama, K., Matsuura, A., Yamashita, F., Iwamoto, S., Kato, Y., Inoue, H., Shigeta, M., Suzuki, S., Akehata, T., "Behavior of Bubbles in Large Scale Bubble Column," Journal of Chemical Engineering of Japan, Vol. 12 (1979), pp. 98-104.
 108. Smith, J.S., Burns, L.F., Valsaraj, K.,T., Thibodeaux, L.J. "Bubble Column Reactors for Wastewater Treatment. 2. The Effect of Sparger Design on Sublation Column Hydrodynamic in the Homogeneous Flow Regime," Industrial and Engineering Chemistry Research, Vol. 35, (1996), pp. 1700-1710.
 109. Tsuchiya, K., Haryono, M. H., Tomida, T., "Performance of a Hollow-Fiber Spiral Disk for Effective Gas Dispersion Toward High Mass Transfer Rate," Industrial and Engineering Chemistry Research, Vol. 35, (1996), pp. 613-620.
 110. Elgozali, A., Linek, V., Fialova, M., Wein, O., Zahradnik, J. "Influence of Viscosity and Surface Tension on Performance of Gas-Liquid Contactors with Ejector Type Gas Distributor," Chemical Engineering Science, Vol. 57, (2002), pp. 2987-2994.

111. Bouaifi, M., Hebrard, G., Bastoul, D., Roustan, M., "A Comparative Study of Gas Holdup and Mass Transfer Coefficients in Stirred Gas-Liquid Reactors and Bubble Columns," Chemical Engineering and Proceeding, Vol. 40, (2001), pp. 97-111.
112. Heijnen, J.J., Van't Riet, K. "Mass Transfer and Heat transfer Phenomena in Low Viscosity Bubble Columns Reactors," Chemical Engineering Journal, Vol. 28, (1984), pp. B21-B42.
113. Jordan, U., Schumpe, A., "The Gas Density Effect on Mass Transfer in Bubble Columns with Organic Liquids," Chemical Engineering Science, Vol. 56, (2001), 6267-6272.
114. Camarasa, E., Vial, C., Poncin, S., Wild, G., Midoux, N., Bouillard, J., "Influence of Coalescence Behavior of the Liquid and Gas Sparging on Hydrodynamics and Bubble Characteristics in a Bubble Column," Chemical Engineering and Proceeding, Vol. 38, (1999), pp. 329-344.
115. Schügerl, K., Lücke, J., Oels, U., "Bubble Column Bioreactors," Adv. Biochem. Eng., Vol. 7 (1977), pp. 1-84.
116. Arnold, D.S., Plank, C.A., Schoenborn, E.M. "Performance of Plate Distillation Columns," Chemical Engineering Progress, Vol. 48, (1952), pp. 633-642.
117. Mersmann, A. "Design and Scale-up of Bubble and Spray Columns," Ger. Chem. Eng. Vol. 1, (1978), pp. 1-11
118. Neubauer, G., (PhD. Dissertation, TU Munich SFB 153, 1977)
119. Chen, C.M., and Leu, L.P., "Hydrodynamics and Mass Transfer in Three-Phase Magnetic Fluidized Beds," Powder Technology, Vol. 117, (2001), pp. 198-206.
120. Idogawa K., Ikeda, K., Fukuda, T., Morooka, S. "Effect of Gas and Liquid Properties on the Behavior of Bubbles in a Column Under High Pressure," International Chemical Engineering, Vol. 27, (1987), pp. 93-99
121. Kumar, A., Degaleesan, T.E., Laddha, G.S., Hoelscher, H.E., "Bubble Swarm Characteristics in Bubble Columns", The Canadian Journal of Chemical Engineering, Vol. 54 (1976), pp. 503-508.
122. Sotelo, J.L., Benitez, F.J., Beltran-Heredia, J., Rodriguez, C. "Gas Holdup and Mass Transfer Coefficient in Bubble Columns. 1. Porous Glass-Plate Diffusers," International Chemical Engineering, Vol. 34, (1994), pp. 82-89.

123. Reilly, I.G., Scott, D.S., de Bruijn, T.J.W., Jain, A., Piskorz, J., "A Correlation for Gas Holdup in Turbulent Coalescing Bubble Columns", The Canadian Journal of Chemical Engineering, Vol. 64, (1986), pp. 705-717.
124. Sauer, T., Hempel, D.C., "Fluid Dynamics and Mass Transfer in a Bubble Column with Suspended Particles", Chemical Engineering and Technology, Vol. 10 (1987), pp. 180-189.
125. Shah, Y.T., Joseph, S., Smith, D.N., Ruether, J.A., "Two-Bubble Class Model for Churn-Turbulent Bubble-Column Reactor," Industrial & Engineering Chemistry Process Design and Development, Vol. 24, (1985), pp. 1096-1104.
126. Inga, J.R., Morsi, B.I., "Effect of Operating Variables on the Gas Holdup in a Large-Scale Slurry Bubble Column Reactor Operating with Organic Liquid Mixture," Industrial and Engineering Chemistry Research, Vol. 38, (1999), pp. 928-937.
127. Ellenberger, J., Krishna, R. "A Unified Approach to the Scale-Up of Gas-Solid Fluidized Bed and Gas-Liquid Bubble Column Reactors," Chemical Engineering Science, Vol. 49, (1994), pp. 5391-5411.
128. Prince, M.J., Blanch, H.W., "Bubble Coalescence and Break-Up in Air-Sparged Bubble Columns," AIChE Journal, (1990), Vol. 36, pp. 1485-1499.
129. Davidson, J.F., and Schuler, B.O.G. "Bubble Formation at an Orifice in an Inviscid Liquid," Trans. Ins. Chem. Eng., Vol. 38, (1960), pp. 330-342.
130. Tsuge, H., Tanaka, Y., Hibino, S.I., "Effects of the Physical Properties of Gas on the Volume of Bubble Formed from a Submerged Single Orifice," The Canadian Journal of Chemical Engineering, Vol. 59, (1981), pp. 569-572.
131. Hooper, A. P., "A Study of Bubble Formation at a Submerged Orifice Using the Boundary Element Method," Chemical Engineering Science, Vol. 41, (1986), pp. 1879-1890.
132. Tan, R. B.H., Harris, I. J., "A Model for Nonspherical Bubble Growth at a Single Orifice," Chemical Engineering Science, Vol. 41, (1986), pp. 3175-3182.
133. Wilkinson, P.M., Van Dierendonck, L.L., "A Theoretical Model for the Influence of Gas Properties and Pressure on Single-Bubble Formation at an Orifice," Chemical Engineering Science, Vol. 49, (1994), pp.1429-1438.
134. Massimilla, L., Solimando, A., Squillace, E., "Gas Dispersion in Solid-Liquid Fluidized Beds," British Chemical Engineering, Vol. 6, (1961), pp. 232-238.

135. Marrucci, G., "A Theory of Coalescence," Chemical Engineering Science, Vol. 24, (1969), pp. 975-985.
136. Sagert, N.H., Quinn, M.J., "Influence of High-Pressure Gases on the Stability of Thin Aqueous Films," Journal of Colloid and Interface Science, Vol. 61 (1977), pp. 279-286.
137. Taylor, G.I., "The Instability of Liquid Surfaces When Accelerated in a Direction Perpendicular to Their Planes," Proceedings of the Royal Society of London, Vol. A201 (1950), pp. 192.
138. Bellman, R., Pennington, R.H. "Effects of Surface Tension and Viscosity on Taylor Instability," Quarterly Journal of Applied Mathematics, Vol. 12, (1953), pp. 151-162.
139. Walter, J.F., Blanch, H.W., "Bubble Break-Up in Gas-Liquid Bioreactors: Break-Up in Turbulent Flows," The Chemical Engineering Journal, Vol. 32, (1986), pp. B7-B17.
140. Levich, V.G., Physicochemical Hydrodynamics, (Prentice Hall, Englewood Cliffs, NJ, 1962)
141. Hinze, J.O, "Fundamental of the Hydrodynamics Mechanism of Splitting in Dispersion Processes", AIChE Journal, Vol. 1 (1955), pp.289-295.
142. Lapidus, L., Elgin, J.C., "Mechanics of Vertical-Moving Fluidized Systems," AIChE Journal, Vol. 3, (1957), pp. 63-68.
143. Davies, R.M., Taylor, G.I., "The Mechanics of Large Bubbles Rising Through Extended Liquids and Through Liquids in Tubes," Proc. Roy. Soc. London, A200, (1950), pp.375-390.
144. Tsuchiya, K., Furumoto, A., Fan, L.S., Zhang, J., "Suspension Viscosity and Rise Velocity in Liquid-Solid Fluidized Beds," Chemical Engineering Science, Vol. 52, (1997), pp. 3053-3066.
145. Mendelson, H.D. "The Prediction of Bubble Terminal Velocity from Wave Theory," AIChE Journal, Vol. 15 (1967), pp. 250-253.
146. Clift, R., Grace, J.R., Weber, M., Bubbles, Drops and Particles, (London, Academic Press, 1987), pp. 173.

147. Lehrer, I.H., "A Rational Terminal Velocity Equation for Bubbles and Drops at Intermediate and High Reynolds Numbers," Journal of Chemical Engineering of Japan, Vol. 9, (1976), pp. 237-240.
148. Thorsen, G., Stordalen, R.M., Terjesen, S.G., "On the Terminal Velocity of Circulating and Oscillating Liquid Drops," Chemical Engineering Science, Vol. 23, (1968), pp. 413-426.
149. Marrucci, G., Apuzzo, G., Astarita, G., "Motion of Liquid in Non-Newtonian Systems," AIChE Journal, Vol. 16, (1970), pp. 538-541.
150. Jamialahmadi, M., Branch, C., Müller-Steinhagen, H. "Terminal Bubble Rise Velocity in Liquids," Trans Inst. Chem. Eng., Vol. 72, (1994), pp. 119-122.
151. Fukuma, M., Muroyama, K., Yasunishi, A. "Properties of Bubble Swarm in a Slurry Bubble Column," Journal of Chemical Engineering of Japan, Vol. 20, (1987), pp. 28-33.
152. Fan, L.S., Tsuchiya, K. "Bubble Wake Dynamics in Liquids and Liquid-Solid Suspensions," (Stoneham: Butterworth-Heinemann Series in Chemical Engineering, 1990), pp. 50.
153. Maneri, C.C., "New Look at Wave Analogy for Prediction of Bubble Terminal Velocities," AIChE Journal, Vol. 41, (1995), pp. 481-487.
154. Tomiyama, A., Kataoka, I., Sakaguchi, T., "Drag Coefficients of Bubbles (1st Report, Drag Coefficients of a Single Bubble in a Stagnant Liquid)," Nippon Kikai Gakkai Ronbunshu B Hen, Vol. 61, (1995), pp. 2357-2364.
155. Krishna, R., Urseanu, M.I., van Baten, J.M., Ellenberger, J., "Rise Velocity of a Swarm of Large Gas Bubbles in Liquids," Chemical Engineering Science, Vol. 54, (1999), pp. 171-183.
156. Luo, X., Zhang, J., Tsuchiya, K., Fan, L.S., "On the Rise Velocity of Bubbles in Liquid-Solid Suspensions at Elevated Pressure and Temperature," Chemical Engineering Science, Vol. 52, (1997), pp. 3693-3699.
157. Murray, P., Fan, L.S., "Axial Solid Distribution in Slurry Bubble Columns," Industrial and Engineering Chemistry Research, Vol. 28, (1989), pp. 1697-1703.
158. Smith, D.N., Ruether, J.A., "Dispersed Solid Dynamics in a Slurry Bubble Column," Chemical Engineering Science, Vol. 40, (1985), pp. 741-754.

159. Kato, Y., Nishiwaki, A., Fukuda, T., Tanaka, S., "The Behavior of Suspended Solid Particles and Liquid in Bubble Columns," Journal of Chemical Engineering of Japan, Vol. 5, (1972), pp. 14-20.
160. Reilly, I.G., Scott, D.S., de Bruijn, T.J.W., MacIntyre, D., Piskorz, J., "Axial Solid Concentrations in Three-Phase Bubble Columns," Chemical Engineering Science, Vol. 45, (1990), pp. 2293-2299.
161. O'Dowd, W., Smith, D.N., Ruether, J.A., Saxena, S.C., "Gas and Solids Behavior in a Baffled and Unbaffled Slurry Bubble Column," AIChE Journal, Vol. 33, (1987), pp. 1959-1970.
162. Zhang, K. "Axial Solid Concentration Distribution in Tapered and Cylindrical Bubble Columns," Chemical Engineering Science, Vol. 86, (2002), pp. 299-307.
163. Perry, R.H.; Green, D.W., Perry's Chemical Engineers' Handbook, (New York: McGraw-Hill, 7th Edition, 1997)
164. Letterman, R.D., Water Quality and Treatment : A Handbook of Community Water Supplies, (New York : McGraw-Hill, 1999)
165. Maude, A.D., Whitmore, R.L., "A Generalized Theory of Sedimentation," British Journal of Applied Physics, Vol. 9, (1958), pp. 477-482.
166. Cova, D.R. "Catalyst Suspension in Gas-Agitated Tubular Reactors," Industrial & Engineering Chemistry Process Design and Development, Vol. 5, (1966), pp. 20-25.
167. Suganuma, T., Yamanishi, T. "Behavior of Solid Particles in Bubble Column," Kagaku Kogaku, Vol. 30, (1966), pp. 1136-1140.
168. Fillion, B., and Morsi, B.I., "Gas-Liquid Mass Transfer and Hydrodynamic Parameters in a Soybean Oil Hydrogenation Process under Industrial Conditions," Industrial and Engineering Chemistry Research, Vol. 39, (2001), pp. 2157-2169.
169. Doraiswamy, L.K., Sharma, M.M., Heterogeneous Reactions: Analysis, Examples, and Reactor Design, (John Wiley and Sons, New York, 1984) pp. 227.
170. Lewis, W.K. and Whitman, W.G., "Principles of Gas Absorptions," Industrial Engineering Chemistry, Vol. 16, (1924), pp. 1215-1220.

171. Fogler, S.H., Elements of Chemical Reaction Engineering, (Prentice Hall PTR, Englewood Cliffs, New Jersey, 1992) pp. 608-609.
172. Satterfield, C.N., Mass Transfer in Heterogeneous Catalysis, (MIT Press, Cambridge, MA, 1970) pp. 33-47
173. Bauer, M., and Eigenberger, G., "Multiscale Modeling of Hydrodynamics, Mass Transfer and reaction in Bubble Column Reactors," Chemical Engineering Science, Vol. 56, (2001), pp. 1067-1074.
174. Salvacion, J.L., Murayama, M., Ohtaguchi, K., Koide, K., "Effects of Alcohols on Gas Holdup and Volumetric Liquid-Phase Mass Transfer Coefficient in Gel-Particle-Suspended Bubble Column," Journal of Chemical Engineering of Japan, Vol. 28, (1995), pp. 434-441.
175. Dewes, I., Kuksal, A., Schumpe, A. "Gas Density Effect on Mass Transfer in Three-Phase Sparged Reactors," Chemical Engineering Research and Design, Vol. 73, (1995), pp. 697-700.
176. Muller, F.L., Davidson, F. "On the Effects of Surfactants on Mass Transfer to Viscous Liquids in Bubble Columns," Chemical Engineering Research and Design, Vol. 73, (1995), pp. 291-296.
177. Vásquez, G., Cancela, M.A., Riverol, C., Alvarez, E., Navaza, J.M., "Application of the Dankwerts Method in a Bubble Column. Effects of Surfactants on Mass Transfer Coefficient and Interfacial Area," Chemical Engineering Journal, Vol. 78, (2000), pp. 13-19.
178. Vásquez, G., Cancela, M.A., Riverol, C., Alvarez, E., Navaza, J.M., "Determination of Interfacial Areas in a Bubble Column by Different Chemical Methods," Industrial and Engineering Chemistry Research, Vol., 39, (2000), pp. 2541-2547.
179. Miyahara, T., Hamanaka, H., Takino, T., Akagi, Y., "Gas Holdup Gas-Liquid Interfacial Area and Mass Transfer Coefficient in External-Loop Airlift Bubble Column Containing Low Density Particles," Journal of Chemical Engineering of Japan, Vol. 30, (1997), pp. 958-961.
180. Fukuma, M., Muroyama, K., Yasunishi, A., "Specific Gas-Liquid Interfacial Area and Liquid-Phase Mass Transfer Coefficient in a Slurry Bubble Column," Journal of Chemical Engineering of Japan, Vol. 20, (1987), pp. 321-324.

181. Yang, W., Wang, J., Jin, Y., "Mass Transfer Characteristics of Syngas Components in Slurry System at Industrial Conditions," Chemical Engineering Technology, Vol. 24, (2001), pp. 651-657.
182. Hikita, H., Asai, S., Tanigawa, K., Segawa, K., Kitao, M., "The Volumetric Liquid-Phase Mass Transfer Coefficient in Bubble Columns", The Chemical Engineering Journal, Vol. 22 (1981), pp. 61-69.
183. Alvarez, E., Sanjuro, B., Cancela, A., Navaza, J.M., "Mass Transfer and Influence of Physical Properties of Solutions in a Bubble Column," Trans IChemE, Vol. 78, (2000), pp. 889-893.
184. Kawase, Y., Halard, B., Moo-Young, M., "Theoretical Prediction of Volumetric Mass Transfer Coefficients in Bubble Columns for Newtonian and Non-Newtonian Fluids," Chemical Engineering Science, Vol. 42, (1987), pp. 1609-1617.
185. Dewes, I., and Schumpe, A., "Gas Density Effect on Mass Transfer in the Slurry Bubble Column," Chemical Engineering Science, Vol. 52, (1997), pp. 4105-4109
186. Karandikar, B.M., "An Experimental Study of Gas Liquid Mass Transfer at Fischer-Tropsch Reaction Conditions," (unpublished Ph.D. dissertation, University of Pittsburgh, 1986).
187. Reid, R.C., Prausnitz, J.M., Poling, B.E., The Properties of Gases and Liquids, (New York, Mac Graw-Hill Book Company, 1987)
188. Wilke, C.R., Chang, P., "Correlations of Diffusion Coefficients in Dilute Solutions," AIChE Journal, Vol. 1, (1955), 264-270.
189. Inga, J.R. "Scale-up and Scale-down of Slurry Bubble Column Reactor, a New Methodology", (unpublished Ph.D. Dissertation, University of Pittsburgh, 1996).
190. Kim, S.S., "Development of a Selective Agglomeration Process Using Light Hydrocarbons for Fine Coal Beneficiation" (unpublished Ph.D. Dissertation, University of Pittsburgh, 1993).
191. Li, J., Tekie, Z., Mohammad, A., Morsi, B.I., "Statistical Assessment of Gas Liquid Mass Transfer in Slurry-Phase Propylene Polymerization Process," The Canadian Journal of Chemical Engineering, Vol. 74, (1996), 77-83.

192. Tekie, Z., Li, J., Morsi, B.I., "Mass Transfer Parameters of O₂ and N₂ in Cyclohexane under Elevated Pressures and Temperatures: A Statistical Approach," Industrial and Engineering Chemistry Research, Vol. 36, (1997), pp. 3879-3888.
193. Inga, J.R., and Morsi, B.I., "Effect of Catalyst loading on Gas/Liquid Mass Transfer in a Slurry Reactor: a Statistical Experimental Approach," The Canadian Journal of Chemical Engineering, Vol. 75, (1997), pp. 872-800.
194. Grund, G., Schumpe, A., Deckwer, W.-D., "Gas-Liquid Mass Transfer in a Bubble Column With Organic Liquids," Chemical Engineering Science, Vol. 47, (1992), pp. 3509-3516
195. Vermeer, D.J., Krishna, R. "Hydrodynamics and Mass Transfer in Bubble Columns Operating in the Churn-Turbulent Regime," Industrial and Engineering Chemistry Process Design and Development, Vol. 20 (1981), pp. 475-482.
196. Sriram, K., Mann, R., "Dynamic Gas Disengagement: A New Technique for Assessing the Behaviour of Bubble Columns," Chemical Engineering Science, Vol. 32 (1977), pp. 571-580.
197. Schumpe, A., Grund, G., "The Gas Disengagement Technique for Studying Gas Holdup Structure in Bubble Columns," The Canadian Journal of Chemical Engineering, Vol. 64 (1986), pp. 891-896.
198. Deshpande, N.S., Dinkar, M., Joshi, J.B., "Disengagement of the Gas Phase in Bubble Columns," International Journal of Multiphase Flow, Vol. 21 (1995), pp. 1191-1201.
199. Patel, S.A., Daly, J.G., Bukur, D.B., "Holdup and Interfacial Area Measurements Using Dynamic Gas Disengagement," AIChE Journal, Vol. 35 (1989), pp. 931-942.
200. Jordan, U., Saxena, A. K., Schumpe, A., "Dynamic Gas Disengagement in a High-Pressure Bubble Column," The Canadian Journal of Chemical Engineering, Vol. 81 (2003), pp. 491-498.
201. Chang, M.Y., Morsi, B.I., "Mass Transfer in a Three Phase Reactor Operating at Elevated Pressures and Temperatures", Chemical Engineering Science, Vol. 47 (1991), pp.1779-1790.
202. Chang, M.Y., Morsi, B.I., "Mass Transfer Characteristics of Gases in n-Decane at Elevated Pressures and Temperatures in Agitated Reactors", Chemical Engineering Journal, Vol. 47 (1991), pp.33-45.

203. Alghamdi, K., "Mass Transfer Characteristics in a Slurry Agitated Reactor with Organic Liquid Mixtures Under High Pressure and Temperature," (unpublished M.S. Dissertation, University of Pittsburgh, 2001).
204. Inga, J.R., and Morsi, B.I., "A Novel Approach for the Assessment of Rate-Limiting Step in Fischer-Tropsch Slurry Process," Energy and Fuels, Vol. 10, (1996), pp. 566-572.
205. Raje, A., Inga, J.R., Davis, B., "Fischer-Tropsch Synthesis: Process Considerations Based on Performance of Iron-based Catalysts," Fuel, Vol. 76, (1997), pp. 273-280.
206. Cockx, A., Roustan, M., Line, A., Hebrard, G., "Modeling of Mass Transfer Coefficient k_L in Bubble Columns", Chemical Engineering Research and Design, Vol. 73 (1995), pp. 627-631.
207. Calderbank, P.H., Moo-Young, M.B., "The Continuous Phase Heat- and Mass-Transfer Properties of Dispersions," Chemical Engineering Science, Vol. 16, (1961), pp. 39-54.
208. Marrucci, G., "Rising Velocity of a Swarm of Spherical Bubbles," Industrial & Engineering Chemistry Fundamentals, Vol. 4, (1965), pp. 224-225.
209. Lemoine, R., Behkish, A., Morsi, B.I., "Hydrodynamic and Mass Transfer Characteristics in Organic Liquid Mixtures in a Large-Scale Bubble Column Reactor for Toluene Oxidation Process," Industrial and Engineering Chemistry Research, Vol. 43, (2004), pp. 6195-6212.
210. Imafuku, K., Wang, T.-Y., Koide, K., Kubota, H., "The Behavior of Suspended Solid Particles in the Bubble Column," Journal of Chemical Engineering of Japan, Vol. 1., (1968), pp. 153-158.
211. Badgajar, M.N., "Hydrodynamics and Solids Mixing in a Bubble Column with Aqueous and Organic Liquids," (unpublished M.S. Dissertation, University of Pittsburgh, 1985).
212. Bukur, D.B., Daly, J.G., "Gas Hold-Up in Bubble Columns for Fischer-Tropsch Synthesis", Chemical Engineering Science, Vol. 42, (1987), pp. 2967-2969.
213. Halard, B., Kawase, Y., Moo-Young, M., "Mass Transfer in a Pilot Plant Scale Airlift Column with Non-Newtonian Fluids," Industrial and Engineering Chemistry Research, Vol. 28 (1989), pp. 243-245.

214. Hyndman, C.L., Larachi, F., Guy, C., "Understanding Gas-Phase Hydrodynamics in Bubble Columns: A Convective Model Based on Kinetic Theory," Chemical Engineering Science, Vol. 52 (1997), pp. 63-77.
215. Idogawa, K., Ikeda, K., Fukuda, T., Morooka, S., "Behavior of Bubbles of the Air-Water System in a Column Under High Pressure," International Chemical Engineering, Vol. 26, (1986), pp. 468-474.
216. Jackson, M. L., Shen, C.C., "Aeration and Mixing in Deep Tank Fermentation Systems," AIChE Journal, Vol. 24, (1978), pp. 63-71.
217. Kataoka, H., Takeuchi, H., Nakao, K., Yagi, H., Tadaki, T., Otake, T., Miyauchi, T., Washimi, K., Watanabe, K., Yoshida, F., "Mass Transfer in a Large Bubble Column," Journal of Chemical Engineering of Japan, Vol. 12 (1979), pp. 105-110.
218. Laari, A., Kallas, J., Palosaari, S., "Gas-Liquid Mass Transfer in Bubble Columns with a T-Junction Nozzle for Gas Dispersion," Chemical Engineering Technology, Vol. 20 (1997), pp. 550-556.
219. Moujaes, S.F., Internal R&D Task Summary Report: Large-Scale Dissolver Cold-Flow Modeling, (DOE report # DOE/OR/03054-20, 1984).
220. Pino, L.R.Z., Yopez, M.M., Saez, A.E., "Hydrodynamics of a Semibatch Slurry Bubble Column with a Foaming Liquid," AIChE Journal, Vol. 36 (1990), pp. 1758-1762.
221. Schäfer, R., Merten, C., Eigenberger, G., "Bubble Size Distributions in a Bubble Column Reactor Under Industrial Conditions," Experimental Thermal and Fluid Science, Vol. 26, (2002), pp. 595-604
222. Shimizu, K., Takada, S., Minekawa, K., Kawase, Y., "Phenomenological Model for Bubble Column Reactors: Prediction of Gas Hold-Ups and Volumetric Mass Transfer Coefficients," Chemical Engineering Science, Vol. 78, (2000), pp. 21-28.
223. Syeda, S. R., Afacan, A., Chuang, K.T., "Prediction of Gas Hold-Up in a Bubble Column Filled with Pure and Binary Liquids," The Canadian Journal of Chemical Engineering, Vol. 80 (2002), pp. 44-50.
224. Towell, G.D., Strand, C.P., Ackerman, G.H., "Mixing and Mass Transfer in Large-Diameter Bubble Columns," Proc. AIChE-Inst. Chem. Eng., Vol. 10 (1965), pp. 97-105.

225. Veera, U. P., Kataria, K.L., Joshi, J.B., "Gas Hold-Up in Foaming Liquids in Bubble Columns," Chemical Engineering Journal, Vol. 84 (2001), pp. 247-256.
226. Wezorke, H., "Einfluss von Grössblasen in Blasensäulenreaktoren," (Ph.D. Dissertation, University of Dortmund, Germany, 1986).
227. Choi, K.H., Chisti, Y., Moo-Young, M., "Comparative Evaluation of Hydrodynamic and Gas-Liquid Mass Transfer Characteristics in Bubble Column and Airlift Slurry Reactors," Chemical Engineering Journal, Vol 62 (1996), pp. 223-229.
228. Godbole, S.P., "Study of Hydrodynamic and Mass Transfer Characteristics of Multiphase Bubble Column Reactor," (unpublished Ph.D. Dissertation, University of Pittsburgh, 1983).
229. Li, H., Prakash, A., Margaritis, A., Bergougnou, M.A., "Effect of Micron-Sized Particles on Hydrodynamics and Local Heat Transfer in a Slurry Bubble Column," Powder Technology, Vol. 133 (2003), pp. 177-184.
230. Sehabiague, L., Behkish, A., Lemoine, R., Heintz, Y., Morsi, B.I., "Hydrodynamic and Mass Transfer Parameters of Slurry Bubble Column Reactors Operating Under Fischer-Tropsch Conditions," Presented at the Annual AIChE meeting, Austin, TX, Nov 7-12, (2004).
231. Vandu, C.O., Krishna, R., "Volumetric Mass Transfer Coefficients in Slurry Bubble Columns Operating in the Churn-Turbulent Flow Regime," Chemical and Engineering Processing, Vol. 43, (2004), pp. 987-995.
232. Thibault, J., Grandjean, B.P.A. "A Neural Network Methodology for Heat Transfer Data Analysis," International Journal of Heat and Mass Transfer, Vol. 34, (1991), pp. 2063-2070.
233. Fullana, M., Trabelsi, F., Recasens, F. "Use of Neural Net Computing for Statistical and Kinetic Modeling and Simulation of Supercritical Fluid Extractors," Chemical Engineering Science, Vol. 55, (2000), pp.79-95.
234. Nascimento, C.A.O., Giudici, R. "Neural Network Based Approach for Optimization Applied to an Industrial Nylon-6,6 Polymerization Process," Computers and Chemical Engineering, Vol. 22, (1998), pp. 595-600.
235. Henrique, H.M., Lima, E.L., Seborg, D.E. "Model Structure Determination in Neural Network Models," Chemical Engineering Science, Vol. 55, (2000), pp. 5457-5469.

236. Wilson, J.A., Zorzetto, F.M. "A Generalized Approach to Process State Estimation Using Hybrid Artificial Neural Network/Mechanistic Models," Computers and Chemical Engineering, Vol. 21, (1996), pp. 951-963.
237. Fausett, L., Fundamentals of Neural Networks: Architectures, Algorithms and Applications, (Prentice Hall Inc., Englewood Cliffs, New Jersey, 1994)
238. Lemoine, R., Fillion, B., Behkish, A., Smith, A.E., Morsi, B.I., "Prediction of the Gas-Liquid Volumetric Mass Transfer Coefficients in Surface-Aeration and Gas-Inducing Reactors Using Neural Networks", Chemical Engineering and Processing, Vol. 42, (2003), pp. 621-643.
239. Shaikh, A., Al-Dahhan, M., "Development of an Artificial Neural Network Correlation for Prediction of Overall Gas Holdup in Bubble Column Reactors", Chemical Engineering and Processing, Vol. 42, (2003), pp. 599-610.
240. Maretto, C., Krishna, R., "Modeling of a Bubble Column Slurry Reactor for Fischer-Tropsch Synthesis," Catalysis Today, Vol. 52, (1999), pp. 279-289.
241. Satterfield, C. N., Huff, G. A., "Effects of Mass Transfer on Fischer-Tropsch Synthesis in Slurry Reactors", Chemical Engineering Science, Vol. 35, (1980), pp.195-202
242. Van der Laan, G.P., "Kinetics, Selectivity and Scale Up of the Fischer-Tropsch Synthesis", (PhD dissertation, University of Groningen, The Netherlands, 1999).
243. Davis, P., Howard Weil Energy Conference, New Orleans, LA, March (2004), (<http://www.sasol.com>)
244. Dry, M.E., "Advances in Fischer-Tropsch Chemistry", Industrial & Engineering Chemistry Product Research and Development, Vol. 15, (1976), pp. 282-288 .
245. Yates, I. C., Satterfield, C. N., "Intrinsic kinetics of the Fischer-Tropsch synthesis on a cobalt catalyst", Energy Fuels, Vol. 5 (1991), 168-173.
246. Davidson, J. K., Harrison, D., Fluidized Particles, (Cambridge University Press, London, 1963).
247. Zimmerman, W., Bukur, D., Ledakowicz, S., "Kinetic Model of Fischer-Tropsch Selectivity in the Slurry Phase", Chemical Engineering Science, vol. 47, (1992), pp. 2707-2712.

248. Espinoza, R.L., Steynberg, A.P., Jager, B., Vosloo, A.C., "Low Temperature Fischer-Tropsch Synthesis from a SASOL Perspective," Applied Catalysis A: General, Vol. 186, (1999), pp. 13-26.
249. Schulz, H., "Short History and Present Trends of Fischer-Tropsch Synthesis," Applied Catalysis A: General, Vol. 186, (1999), pp. 3-12.
250. Geerlings, J.J.C., Wilson, J.H., Kramer, G.J., Kuipers, H.P.C.E., Hoek, A., Huisman, H.M., "Fischer-Tropsch Technology – From Active Site to Commercial Process," Applied Catalysis A: General, Vol. 186, (1999), pp. 27-40.
251. Jess, A, Popp, R., Hedden, K., "Fischer-Tropsch Synthesis with Nitrogen-Rich Syngas. Fundamentals and Reactor Design Aspect," Applied Catalysis A: General, Vol. 186, (1999), pp. 321-342.
252. Wender, I, "Reactions of Synthesis Gas," Fuel Processing Technology, Vol. 48, (1996), pp. 189-297.
253. Steynberg, A.P., Espinoza, R.L., Jager, B., Vosloo, A.C., "High-Temperature Fischer-Tropsch Synthesis in Commercial Practice," Applied Catalysis A: General, Vol. 186, (1999), pp. 41-54.
254. "Conoco Gas Solutions Offers New GTL Technology for Economic Development of "Stranded" Gas Reserves", <http://www.conoco.com> , (2002)
255. LNG Center, <http://gmaiso.free.fr/lng/index.php3?suj=gtl&page=gtlsearch>
256. García-Ochoa, F., Gómez Castro, E., "Estimation of Oxygen Mass Transfer Coefficient in Stirred Tank Reactors Using Artificial Neural Networks", Enzyme and Microbial Technology, Vol. 28, (2001), pp. 560-569.
257. Hussain, M.A., "Review of the Application of Neural Networks in Chemical Process Control-Simulation and Online Implementation", Artificial Intelligence Engineering, Vol. 13, (1999), pp. 55-68.
258. Chouai, A., Cabassud, M., Le Lann, M.V., Gourdon, C., Casamatta, G. "Use of Neural Networks for Liquid-Liquid Extraction Column Modeling: An Experimental Study," Chem. Eng. and Processing, Vol. 39, (2000), pp. 171-180.

259. Larachi, F., Iliuta, I., Rival, O., Grandjean, B.P.A. "Prediction of Minimum Fluidization Velocity in Three-Phase Fluidized Reactors," Industrial and Engineering Chemistry Research, Vol. 39, (2000), pp. 563-572.
260. Otawara, K., Fan, L.T., Tsutsumi, A., Yano, T., Kuramoto, K., Yoshida, K. "An Artificial Neural Network as a Model for Chaotic Behavior of a Three-Phase Fluidized Bed," Chaos, Solitons and Fractals, Vol. 13, (2002), pp. 353-362.
261. Qi, H., Zhou, X.G., Liu, L.H., Yuan, W.K., "A Hybrid Neural Network-First Principles Model for Fixed-Bed Reactor," Chemical Engineering Science, Vol.54, (1999), pp. 2521-2526.
262. Reisener, J., Reuter, M.A., Krüger, J. "Modeling of the Mass Transfer in Gas-Sparged Electrolysers with Neural Nets," Chemical Engineering Science, Vol. 48, (1993), pp.1089-1101.
263. Sharma, B.K., Sharma, M.P., Roy, S.K., Kumar, S., Tendulkar, S.B., Tambe, S.S., Kulkarni, B.D. "Fischer-Tröpsch Synthesis with Co/SiO₂-Al₂O₃ Catalyst and Steady-State Modeling Using Artificial Neural Networks," Fuel, Vol. 77, (1998), pp. 1763-1768.
264. Tendulkar, S.B., Tambe, S.S., Chandra, I., Rao, P.V., Naik, R.V., Kulkarni, B.D. "Hydroxylation of Phenol to Dihydroxybenzenes: Development of Artificial Neural-Network-Based Process Identification and Model Predictive Control Strategies for a Pilot Plant Scale Reactor," Industrial and Engineering Chemistry Research, Vol. 37, (1998), pp. 2081-2085.
265. Utomo, M.B., Sakai, T., Uchida, S., Maezawa, A. "Simultaneous Measurement of Mean Bubble Diameter and Local Gas Holdup Using Ultrasonic Method with Neural Network," Chemical Engineering Technology, Vol. 24, (2001), pp. 493-500.
266. Yang, H., Fang, B.S., Reuss, M., "k_La Correlation Established on the Basis of Neural Network Model," The Canadian Journal of Chemical Engineering, Vol. 77, (1999), pp. 838-843.
267. Alvarez, E., Correa, J.M., Riverol, C., Navaza, J.M., "Model Based in Neural Networks for the Prediction of the Mass Transfer Coefficients in Bubble Columns. Study in Newtonian and Non-Newtonian fluids," International Communication on Heat and Mass Transfer, Vol. 27, (2000), pp. 93-98.

268. Belfares, L., Cassanello, M., Grandjean, B.P.A., Larachi, F., "Liquid Back-Mixing in Packed-Bubble Column Reactors: A State-Of-The-Art Correlation," Catalysis Today, Vol. 64, (2001), pp. 321-332.
269. Carsky, M., Kuwornoo, D.K., "Neural Network Modeling of Coal Pyrolysis," Fuel, Vol. 80, (2001), pp. 1021-1027.
270. Iliuta, I., Larachi, F., Grandjean, B.P.A., Wild, G., "Gas-Liquid Interfacial Mass Transfer in Trickle-Bed Reactors: State-Of-The-Art Correlations," Chemical Engineering Science, Vol. 54, (1999), pp. 5633-5645
271. Leib, T.M., Mills, P.L., Lerou, J.J., "Fast Response Distributed Parameters Fluidized Bed Reactor Model for Propylene Partial Oxidation Using Feed-Forward Neural Network Methods," Chemical Engineering Science, Vol. 51 (1996), pp. 2189-2198.
272. Leib, T.M., Mills, P.L., Lerou, J.J., Turner, J.R., "Evaluation of Neural Networks for Simulation of Three-Phase Bubble Column Reactors," Chemical Engineering Research and Design, Vol. 73 (1995), pp. 690-696.
273. Nikraves, M., Farrell, Stanford, T.G., "Control of Nonisothermal CSTR with Time Varying Parameters via Dynamic Neural Network Control (DNNC)," Chemical Engineering Journal, Vol. 76, (2000), pp. 1-16.
274. Parisi, D.R., Laborde, M.A., "Modeling Steady-State Heterogeneous Gas-Solid Reactors Using Feedforward Neural Networks," Computers and Chemical Engineering, Vol. 25, (2001), pp. 1241-1250.